



**HAL**  
open science

# Modeling, fabrication and characterization of resonant piezoelectric nano mechanical systems for high resolution chemical sensors

Paul Ivaldi

► **To cite this version:**

Paul Ivaldi. Modeling, fabrication and characterization of resonant piezoelectric nano mechanical systems for high resolution chemical sensors. Micro and nanotechnologies/Microelectronics. Université de Grenoble, 2014. English. NNT : 2014GRENT109 . tel-01192918

**HAL Id: tel-01192918**

**<https://theses.hal.science/tel-01192918>**

Submitted on 3 Sep 2015

**HAL** is a multi-disciplinary open access archive for the deposit and dissemination of scientific research documents, whether they are published or not. The documents may come from teaching and research institutions in France or abroad, or from public or private research centers.

L'archive ouverte pluridisciplinaire **HAL**, est destinée au dépôt et à la diffusion de documents scientifiques de niveau recherche, publiés ou non, émanant des établissements d'enseignement et de recherche français ou étrangers, des laboratoires publics ou privés.

## THÈSE

Pour obtenir le grade de

## DOCTEUR DE L'UNIVERSITÉ DE GRENOBLE

Spécialité : **Micro et Nano Electronique**

Arrêté ministériel : 7 août 2006

Présentée par

**Paul Ivaldi**

Thèse dirigée par **Emmanuel Defaÿ**  
et codirigée par **Sébastien Hentz**

Préparée au sein du **Laboratoire des Composants Micro  
Capteurs – CEA/LETI – DCOS/SCMS/LCMC**

dans l'**École Doctorale Electronique Electrotechnique et  
Traitement du Signal**

# Micro-Poutres Résonantes à Base de Films Minces de Nitrure d'Aluminium Piézoélectriques, Application aux Capteurs de Gaz Gravimétriques

Thèse soutenue publiquement le 13 mai 2014

devant le jury composé de :

**Skandar Basrour**

Professeur (CNRS-TIMA), *Président*

**Isabelle Dufour**

Professeur (CNRS-IMS), *Rapporteur*

**Liviu Nicu**

Chargé de recherche (CNRS-LAAS), *Rapporteur*

**Emmanuel Defaÿ**

Ingénieur de recherche (CEA-LETI), *Directeur de thèse*

**Sébastien Hentz**

Ingénieur de recherche (CEA-LETI), *Encadrant CEA - invité*

**Alain Ramond**

Président, docteur ingénieur (YZATEC), *invité*



*à Martial et Denise*

*à Pallavi et Saraswati*

# Table of Content

---

<b>TABLE OF CONTENT</b> .....	<b>III</b>
<b>TABLE OF FIGURES</b> .....	<b>VI</b>
<b>TABLE OF TABLES</b> .....	<b>X</b>
<b>RESUME DETAILLE EN FRANÇAIS</b> .....	<b>XI</b>
<b>GENERAL INTRODUCTION</b> .....	<b>1</b>
<b>CHAPTER 1: MICRO TECHNOLOGY BASED GAS CHEMO SENSORS</b> .....	<b>8</b>
1.1. <b>MICRO / NANO GAS CHEMO-SENSORS</b> .....	<b>9</b>
1.1.1. <i>Figures of merit</i> .....	<b>9</b>
1.1.2. <i>Chemical functionalization</i> .....	<b>12</b>
1.1.3. <i>Physical transducers overview</i> .....	<b>14</b>
1.1.3.1.    Electro-chemical transducers.....	<b>15</b>
1.1.3.2.    Thermal transducers.....	<b>18</b>
1.1.3.3.    Optical transducers .....	<b>18</b>
1.1.3.4.    Mechanical transducers.....	<b>19</b>
1.2. <b>GRAVIMETRIC SENSORS</b> .....	<b>20</b>
1.2.1. <i>Working principle and architecture</i> .....	<b>20</b>
1.2.2. <i>Mechanical resonators</i> .....	<b>23</b>
1.2.3. <i>Performance modeling</i> .....	<b>26</b>
1.2.3.1.    Sensitivity.....	<b>26</b>
1.2.3.2.    Resolution.....	<b>28</b>
1.3. <b>CONCLUSION</b> .....	<b>34</b>
<b>CHAPTER 2: PIEZOELECTRIC MICRO / NANO CANTILEVERS RESONATORS</b> .....	<b>35</b>
2.1. <b>CANTILEVER RESONATORS FOR SENSING APPLICATIONS</b> .....	<b>36</b>
2.1.1. <i>Historical overview</i> .....	<b>36</b>
2.1.2. <i>Transduction principles</i> .....	<b>37</b>
2.2. <b>PIEZOELECTRIC TRANSDUCTION</b> .....	<b>43</b>
2.2.1. <i>Generalities</i> .....	<b>43</b>
2.2.2. <i>Piezoelectric materials</i> .....	<b>45</b>
2.2.3. <i>Thermodynamic approach of piezoelectricity</i> .....	<b>46</b>
2.2.4. <i>Piezoelectric flexural cantilever resonators</i> .....	<b>48</b>

## Table of Content

---

2.3.	ANALYTICAL MODELING AND DESIGN OPTIMIZATION .....	52
2.3.1.	<i>Analytical input/output relationship for a piezoelectric cantilever</i> .....	52
2.3.2.	<i>Frequency loops</i> .....	56
2.3.3.	<i>Design optimization</i> .....	58
2.3.3.1.	Preliminaries .....	58
2.3.3.2.	Optimization without constraints.....	60
2.3.3.3.	Optimization with constraints.....	66
2.4.	CONCLUSION .....	68
<b>CHAPTER 3: SENSING DEVICES FABRICATION AND CHARACTERIZATION .....</b>		<b>69</b>
3.1.	SUB-100 NM PIEZOELECTRIC FILMS .....	70
3.1.1.	<i>Choice of the piezoelectric material</i> .....	70
3.1.2.	<i>50 nm AlN films development</i> .....	71
3.1.2.1.	DC pulsed Reactive Magnetron Sputtering .....	71
3.1.2.2.	Results .....	73
3.2.	MICRO-CANTILEVERS FABRICATION .....	75
3.2.1.	<i>Process</i> .....	75
3.2.2.	<i>Static deflection control</i> .....	80
3.3.	ELECTRICAL CHARACTERIZATION .....	82
3.3.1.	<i>Electrical setup: active probes</i> .....	82
3.3.2.	<i>Results and analytical fit</i> .....	85
3.4.	NANO-CANTILEVERS ARRAYS .....	88
3.4.1.	<i>Process</i> .....	88
3.4.2.	<i>Results</i> .....	91
3.5.	CONCLUSION .....	92
<b>CHAPTER 4: SENSING PERFORMANCES CHARACTERIZATION .....</b>		<b>94</b>
4.1.	NOISE CHARACTERIZATION .....	95
4.1.1.	<i>Allan deviation</i> .....	95
4.1.2.	<i>Open Loop Characterization</i> .....	97
4.1.3.	<i>Frequency loops</i> .....	100
4.1.3.1.	Phase Locked Loop .....	100
4.1.3.2.	Self Oscillating loop .....	102
4.2.	GAS SENSING EXPERIMENTS .....	103
4.2.1.	<i>Experimental setup</i> .....	104
4.2.2.	<i>Results</i> .....	109
4.2.2.1.	First experiments on blank devices .....	109
4.2.2.2.	DMMP sensing .....	110
4.3.	CONCLUSION .....	113

## **Table of Content**

---

<b>GENERAL CONCLUSION .....</b>	<b>115</b>
<b>BIBLIOGRAPHY.....</b>	<b>121</b>
<b>APPENDIX A: FEM MODELING OF PIEZOELECTRIC CANTILEVER .....</b>	<b>140</b>
B.1    MODEL DESCRIPTION .....	140
B.2    RESULTS .....	144

# Table of Figures

---

FIGURE 0- 1: EXAMPLE OF COMMERCIAL GAS ANALYZER SYSTEMS WITH CORRESPONDING PRICES .....	2
FIGURE 0- 2: GENERAL ARCHITECTURE OF A GAS CHEMO-SENSOR .....	3
FIGURE 0- 3: EVOLUTION OF THE MEMS MARKET PER APPLICATIONS FIELD, 2010 TO 2011: REAL FIGURES - 2012 TO 2016: PROSPECTION BY YOLE DEVELOPMENT [20].....	5
FIGURE 1- 1: GAS SENSOR CHARACTERISTIC CURVES AND FOM. THE FIGURES ARE REPRODUCED AND MODIFIED FROM [52] WHERE THE GAS CHEMO-SENSOR IS BASED ON A CAPACITIVE MEMBRANE ULTRASONIC TRANSDUCER (CMUT) COATED WITH POLY-ISOBUTYLENE (PIB).....	12
FIGURE 1- 2: SCHEMATIC AND WORKING PRINCIPLE OF A METAL-OXIDE GAS SENSOR. IN PRESENCE OF A REDUCING GAS THE ENERGY BARRIER AND THE DEPLETION LAYER AT TWO GRAINS BOUNDARY IS REDUCED LEADING TO A LOWER RESISTIVITY OF THE FILM. ....	16
FIGURE 1- 3: EXAMPLE OF (A) SINGLE WALL CARBON NANOTUBES AND (B) GRAPHENE BASED GAS SENSOR. IMAGES REPRODUCED FROM [85] AND [88] .....	17
FIGURE 1- 4: CROSS SECTIONAL AND SEM VIEW OF A $\mu$ -TCD DETECTOR OF THE $\mu$ -CHEMLAB™. OPTICAL VIEW OF THE FLUIDIC PART OF THE $\mu$ -CHEMLAB™ CONTAINING THE PUMPS, THE MICRO-GC AND THE $\mu$ -TCD DETECTOR. IMAGES REPRODUCED FROM [95] .....	19
FIGURE 1- 5: PRINCIPLE OF OPERATION OF A TOLUENE OF DI NITRO TOLUENE (DNT) STATIC GAS SENSOR. UPON THE ADSORPTION OF THE TARGETED MOLECULES, THE BENZENE THIOLS POLARIZE AND START ATTRACTING EACH OTHER, CREATING A COMPRESSIVE SURFACE STRESS THAT BENDS THE CANTILEVER. IMAGE REPRODUCED FROM [105].....	20
FIGURE 1- 6: PRINCIPLE OF OPERATION OF A RESONANT GAS CHEMO-SENSOR OR GRAVIMETRIC SENSOR. IMAGE REPRODUCE FROM [106] .....	21
FIGURE 1- 7: GENERAL ARCHITECTURE OF A GRAVIMETRIC SENSOR. THE MECHANICAL RESONATOR IS REPRESENTED AS A 3-PORTS SYSTEM: ACTUATION PORT (ELECTRICAL SIGNAL $\rightarrow$ FORCE), GRAVIMETRIC PORT (MASS $\rightarrow$ FREQUENCY SHIFT TRANSDUCTION) AND DETECTION PORT (DISPLACEMENT $\rightarrow$ ELECTRICAL). FIGURE REPRODUCED FROM [106].....	22
FIGURE 1- 8: SCHEMATIC OF A WIRELESS SAW SENSOR. THE ELECTROMAGNETIC SIGNAL IS TRANSFORMED INTO A SURFACE ACOUSTIC WAVE THANKS TO THE SINGLE PHASE UNIDIRECTIONAL TRANSDUCER (SPUDT). NOTE THAT THE SUBSTRATE IS PIEZOELECTRIC (LiNbO <sub>3</sub> ). ONCE GENERATED, THE ACOUSTIC SIGNAL REFLECTS ON THREE ACOUSTIC REFLECTORS R <sub>1</sub> , R <sub>2</sub> AND R <sub>3</sub> BEFORE BEING TRANSDUCED BACK INTO ELECTROMAGNETIC WAVES. THE DELAY BETWEEN THE DIFFERENT “ECHOES” DEPENDS ON THE MASS LOADING IN THE SENSITIVE COATING. FIGURE REPRODUCED FROM [10]. .....	25
FIGURE 1- 9: (A) SCHEMATICS OF A CAPACITIVE MEMBRANE ULTRASONIC TRANSDUCER (CMUT) (B) INTEGRATION OF CMUT IN COLLECTIVELY ADDRESSED ARRAY. IMAGE REPRODUCED FROM [52].....	26
FIGURE 1- 10: GRAPHICAL ILLUSTRATION OF THE RELATIONSHIPS BETWEEN (A) PHASE NOISE AND AMPLITUDE NOISE AND (B) FREQUENCY NOISE AND PHASE NOISE USED IN THE ROBBINS FORMULA. ....	31

## Table of Figures

---

FIGURE 2- 1: EXAMPLE OF PIEZOELECTRIC FLEXURAL CANTILEVER DESIGNS (A) SINGLE PORT OUT OF PLANE FLEXURAL CANTILEVER (ONLY ONE PIEZOELECTRIC LAYER IS USED BOTH FOR ACTUATION AND DETECTION) WITH ADDITIONAL ELASTIC LAYER (B) TWO PORTS OUT OF PLANE FLEXURAL CANTILEVER (C) TWO PORT IN-PLANE CANTILEVER (FREE FREE DESIGN) .....	41
FIGURE 2- 2: (A) 3D VIEW OF ALN CRYSTALLOGRAPHIC CELL. YELLOW ATOMS REPRESENT THE POSITIVELY CHARGED ALUMINUM ATOMS WHILE THE GREY ATOMS REPRESENT THE NEGATIVELY CHARGED NITROGEN ATOMS. THE PERMANENT POLARIZATION DIRECTION IS GIVEN BY THE C-AXIS PERPENDICULAR TO THE HEXAHEDRONS PLANES. 2D PIEZOELECTRIC CRYSTAL (B) DIRECT LONGITUDINAL EFFECT, (C) DIRECT TRANSVERSAL (D) REVERSE LONGITUDINAL (E) REVERSE TRANSVERSAL .....	45
FIGURE 2- 3: (A) SCHEMATIC OF THE CANTILEVER STRUCTURE UNDER STUDY (B) BUTTERWORTH-VAN DYKE EQUIVALENT CIRCUIT OF THE PIEZOELECTRIC BIMORPH; (C) CAPACITIVE HALF BRIDGE ARCHITECTURE: OUT OF PHASE SIGNALS ARE APPLIED TO THE CANTILEVER AND A DUMMY CAPACITOR WITH CAPACITANCE EQUAL TO THE CANTILEVER STATIC CAPACITANCE. THE OUTPUT SIGNAL IS TAKEN AT THE COMMON PORT OF THE CANTILEVER AND DUMMY CAPACITOR WHERE THE BACKGROUND SIGNAL IS CANCELLED OUT. (D) EQUIVALENT CIRCUIT OF THE HALF BRIDGE SETUP, THE OUTPUT SIGNAL CAN BE DERIVED BY APPLYING KIRSHOFF'S LAWS AT POINT O. ....	53
FIGURE 2- 4: ARCHITECTURE OF A SELF OSCILLATING LOOP. THE GAIN AND PHASE SHIFT OF THE ELECTRONIC AMPLIFIER ARE ADJUSTED SUCH THAT THE OPEN LOOP TRANSFER FUNCTION $G=1$ . IN THIS CASE THE ELECTRONIC AMPLIFIER COMPENSATES EXACTLY FOR THE DIFFERENT SIGNAL LOSS IN THE LOOP AND THE WHOLE SYSTEM OSCILLATES NATURALLY. THE FREQUENCY COUNTER MEASURES THE FREQUENCY OF THE SIGNAL IN THE LOOP USING ANOTHER TIME REFERENCE .....	57
FIGURE 2- 5: ARCHITECTURE OF A PHASE LOCKED LOOP RESONANCE FREQUENCY MEASUREMENT SETUP. THE VOLTAGE CONTROL OSCILLATOR (VCO) DELIVERS A SIGNAL TO THE DEVICE WITH A FREQUENCY FIXED BY THE CONTROLLING SIGNAL $V_c$ WHICH, IN TURN, IS FIXED BY THE PHASE DIFFERENCE BETWEEN THE VCO SIGNAL AND THE OUTPUT SIGNAL FROM THE CANTILEVER AND THE CONTROLLER TRANSFER FUNCTION .....	58
FIGURE 2- 6: SMLOD AS A FUNCTION OF THE SiN LAYER THICKNESS AND FOR DIFFERENT ALN LAYER THICKNESSES AND FOR TWO CAPACITANCE MATCHING CASES: (A) $CL = 100 \text{ pF} > C0$ FOR ALL ALN THICKNESSES (B) $CL = 1 \text{ pF} < C0$ FOR ALL ALN THICKNESSES. FOR COMPARISON WITH EXPERIMENTAL RESULTS, THE REMAINING PARAMETERS ARE COMMON FOR THE TWO FIGURES: BOTTOM AND TOP ELECTRODE THICKNESS : 100 NM AND 25 NM (RESPECTIVELY), LENGTH AND WIDTH: <b>80 <math>\mu\text{m}</math></b> AND <b>40 <math>\mu\text{m}</math></b> (RESPECTIVELY), THE ACTUATION VOLTAGE, QUALITY FACTOR, MEASUREMENT BANDWIDTH AND AMPLIFIER WHITE NOISE ARE 750 mV, 100, 0.1 Hz AND <b>5 nV/Hz</b> (RESPECTIVELY). THE STATIC CAPACITANCE OF THE CANTILEVER $C0$ VARIES FROM 28 pF FOR 10 NM THICK ALN FILM DOWN TO 1.4 pF FOR 200 NM THICK ALN FILMS .....	61
FIGURE 2- 7: OPTIMUM SiN THICKNESS AS A FUNCTION OF THE ALN THICKNESS DEFINED BY THE EQUATION $\partial \delta m_{surf} / \partial t_{SiN} = 0$ AND CALCULATED, FOR THIS GRAPH, WITH A BOTTOM AND TOP Pt ELECTRODE OF THICKNESS EQUAL TO 10 NM. ....	64

## Table of Figures

---

FIGURE 2- 8: ULTIMATE SMLOD REACHED THANKS TO OUR DESIGN RULES AS A FUNCTION OF THE MINIMUM ALN THICKNESS ALLOWED BY THE TECHNOLOGY. FOR THIS GRAPH PARAMETERS ARE: ACTUATION VOLTAGE, QUALITY FACTOR, MEASUREMENT BANDWIDTH AND AMPLIFIER WHITE NOISE EQUAL TO 750 mV, 100, 0.1 Hz AND 5 nV/Hz (RESPECTIVELY). MINIMUM PT LAYER THICKNESS (TOP AND BOTTOM): 10 NM. THE LENGTH AND WIDTH ARE CHOSEN SUCH THAT $C_{0min} = CL2$ AND $L/W = 10$ (THIS ELIMINATES $W, L$ AND $CL$ FROM THE SMLOD FORMULA), THE SiN LAYER THICKNESS IS TAKEN AT ITS OPTIMUM VALUE (C.F. FIGURE 2- 7) .....	64
FIGURE 2- 9: OPTIMUM LENGTH AND OPTIMUM RESONANCE FREQUENCY ACCORDING TO OUR DESIGN RULES. PARAMETERS FOR THIS GRAPH ARE THE SAME AS IN FIGURE 2- 8 .....	65
FIGURE 3- 1: GROWTH MODE AND CORRESPONDING CRYSTALLINE STRUCTURE. IMAGE REPRODUCED AND MODIFIED FROM [204] .....	72
FIGURE 3- 2: VARIATION OF ALN $e_{31, eff}$ WITH FILM THICKNESS .....	75
FIGURE 3- 3: MICRO-CANTILEVERS MASK LAYOUT (A) VIEW OF THE COMPLETE PATTERNS CONTAINING ALL THE CANTILEVER DESIGNS (B) DETAILS OF ONE PARTICULAR CANTILEVER. THE FIRST MASK LEVEL IN GREEN IS USED TO PATTERN THE TOP ELECTRODE AND THE <b>AlN</b> LAYER. THE SECOND MASK IS THE NEGATIVE OF THE GREY PATTERNS AND IS USED TO ETCH AN ACCESS TO THE Si SUBSTRATE THROUGH THE BOTTOM ELECTRODE AND THE <b>Si3N4</b> STRUCTURAL LAYER. 76	76
FIGURE 3- 4: CHOSEN MATERIAL STACKS FOR MICRO-CANTILEVERS FABRICATION .....	77
FIGURE 3- 5: MICRO-CANTILEVERS FABRICATION PROCESS FLOW .....	78
FIGURE 3- 6: OPTIMIZATION OF THE ANNEALING AND RELEASE PROCESS STEPS. (A) DOWNWARD DEFLECTED CANTILEVER ANNEALED AT 500 °C, (B) SLIGHTLY UPWARD DEFLECTED CANTILEVER ANNEALED AT 700 °C, (C) ZOOM ON A CRACK OF THE <b>Pt</b> BOTTOM ELECTRODE AT THE CANTILEVER ANCHOR, (D) FULLY OPTIMIZED CANTILEVER. ....	82
FIGURE 3- 7: FREQUENCY RESPONSE OF 80 $\mu\text{m}$ LONG PZT CANTILEVER RESONATOR. THE OBSERVED FOUR RESONANCE PEAKS CORRESPOND TO THE FIRST FOUR FLEXURAL MODES OF THE CANTILEVER. THEORETICAL RESONANCE FREQUENCIES ARE 92 kHz, 578 kHz, 1.62 MHz AND 3.17 MHz. ....	84
FIGURE 3- 8: CUSTOM MADE SET-UP FOR MICRO-CANTILEVER CHARACTERIZATION. ....	85
FIGURE 3- 9: FIRST FLEXURAL MODE ELECTRICAL RESPONSE AND ANALYTICAL FIT. ....	87
FIGURE 3- 10: NON LINEAR ELECTRICAL RESPONSE OF THE FIRST RESONANT MODE FOR DIFFERENT DRIVING VOLTAGE .....	87
FIGURE 3- 11: SEM IMAGE OF AN ARRAY OF Th/PZT NANO-CANTILEVER ARRAY. THE CANTILEVERS ARE 2.8 $\mu\text{m}$ long 1 $\mu\text{m}$ WIDE, INCLUDE A STACK <b>Si</b> (160 nm) / <b>AlSi</b> (25 nm) AND ARE DISTRIBUTED OVER 20 ROWS AND 140 COLUMN. ....	89
FIGURE 3- 12: NANO-CANTILEVERS FABRICATION PROCESS FLOW .....	90
FIGURE 3- 13: SEM MICROGRAPH OF THE PZT FABRICATED NANO-CANTILEVERS. (A) ARRAY OF NANO-CANTILEVER (B) ZOOM ON A SINGLE CANTILEVER IN THE ARRAY (C) TILTED VIEW OF A SINGLE CANTILEVER IBE ETCHED WITH AN ANGLE OF 90° REVEALING THE PRESENCE OF ETCHING RESIDUES ON THE CANTILEVER SIDES (D) ZOOM ON THE RESIDUES (E) TILTED VIEW OF A SINGLE NANO-CANTILEVER IBE ETCHED WITH AN ANGLE OF 45° (F) ZOOMED ON A EDGE WITH A LARGE SLOPE OF 40° WITH RESPECT TO THE SUBSTRATE. ....	90

## Table of Figures

---

FIGURE 4- 1: ELECTRICAL SETUP SCHEMATIC FOR OPEN LOOP ALLAN DEVIATION MEASUREMENT METHOD. ....	98
FIGURE 4- 2: OPEN LOOP ALLAN DEVIATION RESULTS. AS EXPECTED THE DOMINANT NOISE SOURCE IS THE ELECTRONIC NOISE, WHICH CREATES $\tau - 1/2$ ASYMPTOTES THAT SHIFT DOWNWARDS WITH INCREASING INPUT POWER. THE MINIMUM ALLAN DEVIATION VALUE IS $10 - 8$ FOR $\tau = 10$ s AND FITS WELL WITH THE ANALYTICALLY PREDICTED VALUE OF $1.6 \cdot 10 - 8$ USING EQUATION (1.2-18) . ....	99
<b>FIGURE 4- 3:</b> (A) DIGITAL PLL ALLAN DEVIATION MEASUREMENT AND SETUP. (B) ALLAN DEVIATION CURVES OF THE DIGITAL PLL SETUP. THIS FIGURE FURTHER SUPPORTS THE VALIDITY OF THE OPEN LOOP ALLAN DEVIATION MEASUREMENT METHOD THANKS TO THE SUPERPOSITION OF THE VIOLET (OPEN LOOP) AND BLUE (CLOSED LOOP) CURVES OBTAINED RESPECTIVELY WITH THE OPEN LOOP SETUP AND THE PLL SETUP FOR THE SAME CANTILEVER AND THE SAME INPUT SIGNAL AMPLITUDE $V_{in} = 100$ mV. ....	101
<b>FIGURE 4- 4:</b> (A) SELF OSCILLATING LOOP SETUP SCHEMATICS, (B) ALLAN DEVIATION CURVES USING THE OPEN LOOP SETUP . ....	103
FIGURE 4- 5: GAS SENSING EXPERIMENT SETUP: (A) PICTURE OF THE GAS TEST BENCH AT CALTECH WITH THE DEVICE CHAMBER (B) SCHEMATIC OF THE OPERATING PRINCIPLE (MFC STANDS FOR MASS FLOW METER). ....	108
FIGURE 4- 6: FIRST DMMP VAPOR DETECTION MEASUREMENT WITH AN UNCOATED CANTILEVER AND UN-OPTIMIZED SETUP. ....	110
FIGURE 4- 7: DMMP VAPOR DETECTION EXPERIMENT WITH AN UNCOATED AND A DKAP COATED CANTILEVER AND FOR DMMP VAPORS CONCENTRATION FROM 10 PPM DOWN TO 25 PPB . ....	112
FIGURE 4- 8: FREQUENCY SHIFT VERSUS DMMP CONCENTRATION (SENSITIVITY GRAPH) FOR OUR CANTILEVER RESONATOR GAS SENSING SETUP FOR AN UN-COATED (BLANK) AND A DKAP COATED CANTILEVER . ....	112
FIGURE A- 1: FEM PROBLEM DEFINITION (A) MATERIALS: BLUE PT, GREY ALN AND GREEN SiN (B) BOUNDARIES CONDITIONS: BLUE MECHANICALLY FIXED, GREEN ELECTRICAL PORT "TOP ELECTRODE", RED ELECTRICAL PORT "BOTTOM ELECTRODE", ALL OTHER BOUNDARY ARE MECHANICALLY FREE AND ELECTRICALLY INSULATED (C) TYPICAL MESH WITH MEDIUM DENSITY OBTAINED BY EXTRUDING A RECTANGULAR MESH OF THE BOTTOM SiN BOUNDARY THROUGH THE THICKNESS OF THE DIFFERENT LAYERS. ....	142
FIGURE A- 2: RESULTS OF FEM CONVERGENCE STUDY FOR FIRST RESONANCE MODE FREQUENCY. ....	144
FIGURE A- 3: FEM HARMONIC ANALYSIS: OUTPUT VOLTAGE OF THE CAPACITIVE BRIDGE VS FREQUENCY. ....	145
FIGURE A- 4: FEM HARMONIC ANALYSIS: OUTPUT VOLTAGE OF THE CAPACITIVE BRIDGE VS FREQUENCY. ....	146

# Table of Tables

---

TABLE 1- 1: DMMP SENSING PERFORMANCES FOR DIFFERENT GRAVIMETRIC GAS CHEMO-SENSORS IN THE LITERATURE. (A) DATA PROVIDED IN THE REFERENCED ARTICLE, (B) DATA CALCULATED FROM THE INFORMATIONS IN THE REFERENCED ARTICLE (C) DATA NOT AVAILABLE (D) MEASURED (E) CALCULATED FROM THE SMLOD WITH A PARTITION COEFFICIENT OF **105** AND FUNCTIONALIZATION THICKNESS EQUAL TO ONE TENTH OF THE DEVICE THICKNESS..... 33

TABLE 2- 1: COMPARISON TABLE BETWEEN THE DIFFERENT ACTUATION TECHNIQUES FOR CANTILEVERS..... 43

TABLE 2- 2: COMPARISON TABLE BETWEEN THE DIFFERENT DETECTION TECHNIQUES OF CANTILEVERS ..... 43

TABLE 3- 1: RELEVANT MATERIAL PROPERTIES FOR ULTRATHIN PIEZOELECTRIC FILMS IN THE LITERATURE..... 71

TABLE 3- 2: INFLUENCE OF THE TYPE AND THICKNESS OF THE BOTTOM ELECTRODE AND OF THE PRESENCE OF A SEED LAYER ON ***e31, eff*** OF 50 NM THICK ALN FILMS ..... 75

TABLE 3- 3: CALCULATED STRESS AND CORRESPONDING ANNEALING TEMPERATURE FOR NULL STATIC DEFLECTION ..... 81

TABLE 4- 1: LINKS BETWEEN THE POWER LAW MODELS FOR PHASE AND FREQUENCY NOISE AND ALLAN DEVIATION. THIS TABLE IS REPRODUCED FROM [38]. IN THIS FREQUENCY LAW MODEL PHASE NOISES ARE CATEGORIZED ACCORDING TO THEIR ASYMPTOTIC BEHAVIOR WITH RESPECT TO FREQUENCY: ***f0, f – 1, f – 2*** AND SO ON. THE COEFFICIENTS ***b0, b – 1, b – 2, b – 3*** AND ***b – 4*** GIVE THE ASYMPTOTIC NOISE PSD LEVEL. PM AND FM STAND FOR PHASE MODULATION AND FREQUENCY MODULATION RESPECTIVELY. ***fH*** IS THE LOW PASS FILTER CUT-OFF FREQUENCY OF THE REQUIRED FILTER TO AVOID THE ALLAN DEVIATION TO DIVERGE IN WHITE PM AND FLICKER PM NOISES CASES. .... 96

TABLE 4- 2: CHEMICAL PROPERTIES OF DMMP <sup>(A)</sup> DATA TAKEN FROM [220]. <sup>(B)</sup> DATA USED BY CALTECH SCIENTIST AND IN OUR EXPERIMENTS..... 105

TABLE 4- 3: COMPARISON OF OUR PIEZOELECTRIC CANTILEVER RESONATOR BASED GAS SENSOR PERFORMANCES WITH OTHER MICRO/NANO RESONATOR BASED GAS SENSOR. (A) DATA PROVIDED IN THE REFERENCED ARTICLE, (B) DATA CALCULATED FROM THE INFORMATIONS IN THE REFERENCED ARTICLE (C) DATA NOT AVAILABLE (D) MEASURED (E) CALCULATED FROM THE SMLOD WITH A PARTITION COEFFICIENT OF **105** AND FUNCTIONALIZATION THICKNESS EQUAL TO ONE TENTH OF THE DEVICE THICKNESS. .... 113

# Résumé détaillé en Français

## 1. Introduction

Les capteurs de gaz ont aujourd'hui trouvé de nombreuses applications dans des marchés aussi diverses que l'environnement, la sécurité, la défense, l'agroalimentaire, l'industrie, l'automobile et le médical... Le marché de la mesure de gaz a ainsi été récemment évalué à 3.9 Milliards de dollars [1] avec une croissance de 5 à 10% par ans pour les dix prochaines années supportée principalement par l'émergence de nouvelles applications

Parmi ces nouvelles applications, la possibilité de diagnostiquer le cancer du poumon, à un stade bien plus précoce que ce qui est possible avec les techniques de diagnostic actuelles (biopsie), a retenu toute notre attention. En effet, l'équipe du Dr Philips [2] a récemment démontré que certains Composés Organiques Volatiles (COV) présents (ou absents) dans l'haleine de patients pouvaient être utilisés comme marqueurs de la maladie et ce dès les premiers stades de développement. Toutefois, le nombre important de COV marqueurs ainsi que leur concentration extrêmement faible impose l'utilisation de techniques de mesure très fines telle que la chromatographie en phase gazeuse couplée à la spectrométrie de masse. Très récemment, deux équipes de chercheurs [3][4] ont montré que des capteurs de gaz utilisant des éléments sensibles nanométriques offraient des performances suffisantes pour remplacer les spectromètres de masse et ainsi rendre possible le développement d'outils de diagnostic ayant un coût compatible avec une généralisation grand publique.

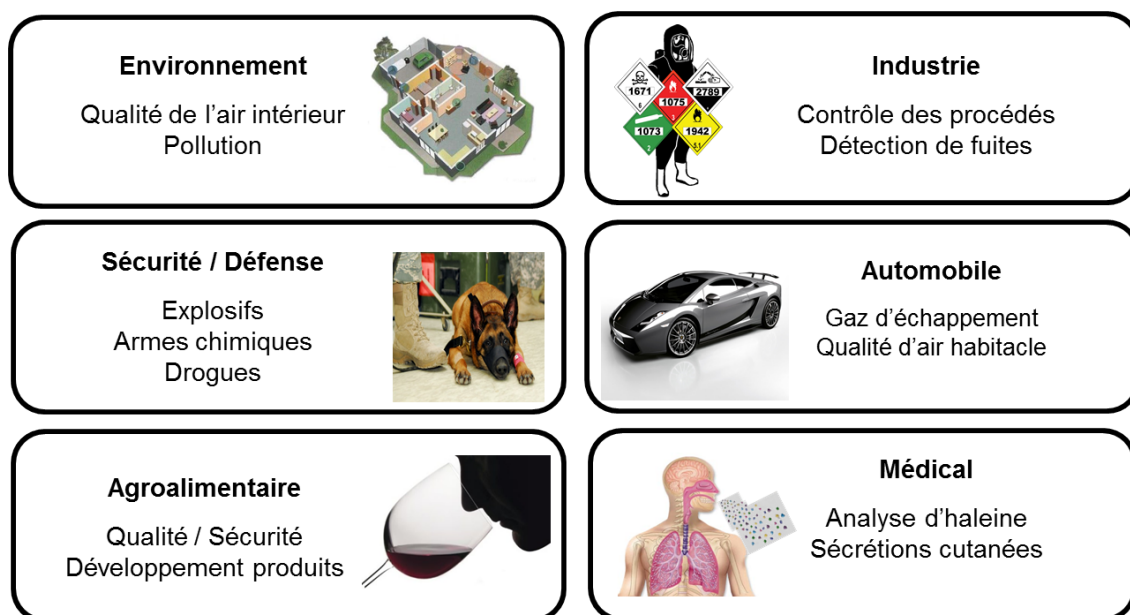


Figure RF- 1 : Exemples d'application capteur gaz (par domaine)

En réalité, la capacité à réaliser des mesures à la fois qualitative et quantitative de mélange gazeux complexes et de faible concentration est commune à de nombreuses applications émergentes. Ainsi pour comparer les différentes technologies de capteur de gaz, il est intéressant de classer leurs performances en fonction d'un critère qualitatif, la sélectivité (capacité du capteur à reconnaître une molécule particulière dans un mélange gazeux complexe), et d'un critère quantitatif, la résolution (la plus petite concentration détectable). De manière non exhaustive, nous pouvons distinguer cinq familles de capteur de gaz selon leur mode d'opération :

- Electrochimique :

Les capteurs de gaz électrochimiques utilisent les variations de potentiel ou de conductivité électrique consécutives à l'adsorption d'une molécule sur la surface du capteur. Ces dispositifs sont déjà largement répandus avec, par exemple, les capteurs à oxyde métallique semi-conducteurs, produits à plusieurs millions de pièces chaque année, et utilisés comme éléments sensibles dans les détecteurs de fumée. Fort de ce succès, la technologie électrochimique s'est développée pour offrir toujours plus de sélectivité et de résolution : transistors à effet de champs (Chem-FET), polymères conducteurs et, plus récemment, des dispositifs à base de nano-fils et nanotubes de carbone. Si les performances obtenues avec ces dispositifs semblent excellentes, leur stabilité dans le temps et la consommation électrique nécessaire sont encore un frein à leur succès commercial.

- Thermique :

Les capteurs de gaz thermiques utilisent soit la chaleur dégagée par une réaction chimique spécifique (pellistors, thermopile), soit les variations de conductivité thermique du gaz consécutives à une modification de leur composition chimique (Thermal Conductivity Detector ou TCD). Les pellistors et les thermopiles offrent des performances et ne sont utilisés que dans des applications très spécifiques industrielles ou de laboratoire. Au contraire les capteurs de conduction thermique sont largement diffusés. Leur très faible sélectivité et relativement haute résolution en font d'excellents candidats comme éléments sensibles dans les chromatographes. Le manque de sélectivité étant ainsi compensé par un module près-analytique (la colonne de chromatographie) très efficace. Les capteurs TCD sont de plus assez simples à mettre en œuvre et peuvent être facilement miniaturisés.

- Ionisation :

Les capteurs gaz à ionisation utilisent les produits de réaction d'ionisation du gaz soit par voie optique (Photo Ionisation Detector, PID) soit par combustion (Flame Ionisation Detector, FID). Les espèces chimiques ionisées comportent une charge électrique et sont donc plus faciles à compter, manipuler, concentrer. Ces capteurs de gaz équipent en particulier les systèmes de spectrométrie de masse, encore une fois grâce à leur excellente résolution et faible sélectivité. Toutefois, ils sont difficilement miniaturisables et requièrent des alimentations électriques incompatibles avec le développement de système de mesure de gaz autonome.

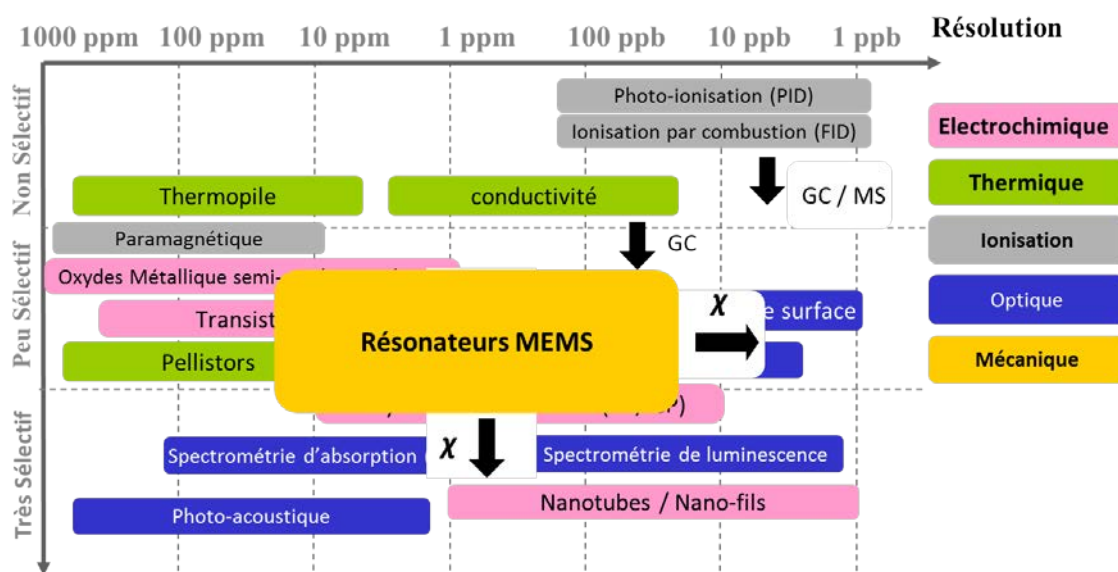


Figure RF- 2 : Classification des différentes technologies de capteur de gaz en fonction de leur sélectivité et de leur résolution

- Optique :

Les capteurs de gaz optiques permettent d'accéder aux meilleures performances en termes de sélectivité grâce à la signature optique spectrale unique des liaisons moléculaires. Les spectromètres utilisent des sources lumineuses de forte intensité et des filtres optiques très sélectifs permettant d'obtenir des spectres hautement résolus en fréquence et des rapports signal à bruit excellents. Toutefois pour des raisons de dissipation d'énergie, de complexité du système et plus simplement de disponibilité des technologies, ces instruments sont difficilement miniaturisables et/ou autonome en énergie.

Récemment, plusieurs systèmes optiques miniaturisés ont été démontrés. Il s'agit, par exemple, des capteurs à résonance de plasmon de surface et des capteurs à fibre optique qui fonctionnent grâce à la réponse spectrale des molécules gazeuses mais sur la modification de l'indice optique d'un élément sensible suite à l'adsorption de molécules gazeuses à la surface cet élément sensible. Les niveaux de résolution atteints avec ces dispositifs semblent très prometteurs. Toutefois, la sélectivité de ces capteurs dépend l'affinité de surface de l'élément sensible avec telle ou telle molécule gazeuse. L'utilisation de couches dites de fonctionnalisation, permettant de modifier les propriétés chimiques de la surface de façon à cibler une molécule particulière se heurte à la difficulté de trouver une couche de fonctionnalisation ayant les propriétés chimiques désirées sans pour autant modifier les propriétés optiques de la surface.

- Mécanique :

Il existe deux grandes familles de capteurs de gaz à transduction mécanique selon qu'ils opèrent de façon statique ou dynamique. Les capteurs de gaz mécaniques statiques sont généralement constitués de micro-poutres (encastrées-libres ou encastrées-encastrées) qui sont sensibles à la variation des contraintes mécaniques de surface engendrées par l'adsorption d'une molécule gazeuse. Ces contraintes engendrent une déformation

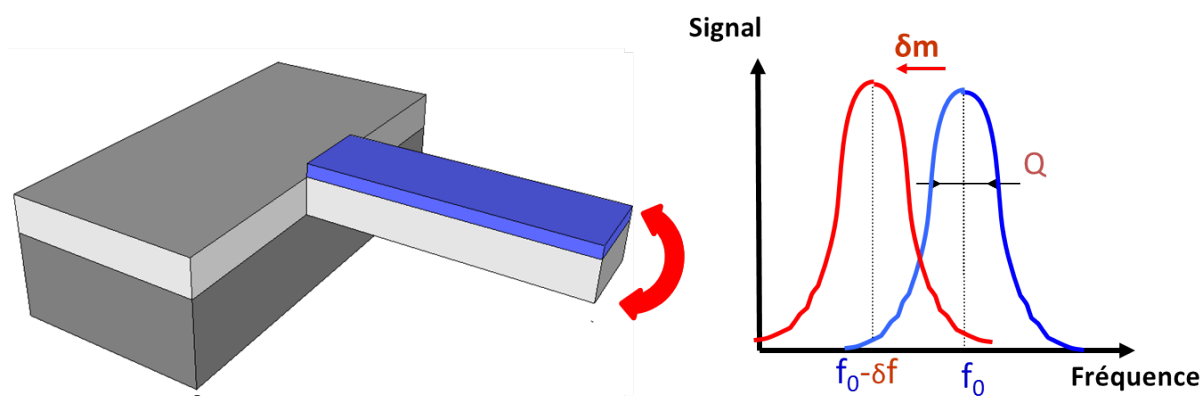


Figure RF- 3 : Principe de mesure de gaz avec un résonateur mécanique : la masse adsorbée sur la surface de la poutre, proportionnelle à la concentration de l'analyte dans le gaz environnant, augmente la masse totale vibrante et entraîne une diminution de la fréquence de résonance.

mécanique de la structure, typiquement une flexion, qui peut être mesurée facilement, c'est à dire avec un budget énergétique faible (de l'ordre du  $\mu\text{W}$ ) et avec une excellente précision. A l'instar des capteurs de gaz optiques intégrés, cette technologie est très sensible au choix de la couche de fonctionnalisation qui doit avoir à la fois les bonnes propriétés chimiques pour garantir une bonne sélectivité et les bonnes propriétés mécaniques pour engendrer les contraintes désirées.

Les capteurs de gaz mécaniques dynamiques reposent sur la sensibilité de la fréquence de résonance mécanique d'une structure aux variations de la masse de celle-ci. Ainsi, lorsque des molécules de gaz sont adsorbées sur la surface de l'élément sensible, la masse vibrante augmente et la fréquence de résonance diminue d'une quantité proportionnelle à la masse adsorbée. L'avantage de cette technique de détection réside à la fois dans l'extrême sensibilité de la fréquence de résonance aux variations de masse, et ce d'autant plus que les résonateurs sont miniaturisés; et dans le grand nombre de couches de fonctionnalisation compatibles avec ce mode de détection. Les microbalances à quartz (QMB), historiquement les premiers représentants de cette famille de capteurs, connaissent un succès commercial certain notamment pour le contrôle de procédés de dépôt de couche mince (évaporation, pulvérisation). De nombreux autres types de résonateurs sont en cours de développement atteignant des niveaux de maturité suffisants pour être commercialisés : capteur à ondes acoustiques de bulk (BAW) ou de surface (SAW), résonateurs en mode de contours, résonateurs en mode de flexion... Ces derniers dispositifs ont récemment été utilisés pour démontrer des performances en résolution massiques extrêmes. Ainsi des nano-poutres résonantes en silicium ou en nanotubes de carbone permettent de détecter la présence de quelques atomes de Xénon sur leur surface, c'est à dire des variations de masse de l'ordre du yocto-gramme ( $10^{-24}\text{g}$ ) [5], [6]!

Si la réduction agressive des dimensions des résonateurs permet d'atteindre de telles performances en détection de masse; la même stratégie de design pour améliorer la résolution en concentration pour des mesures de gaz n'est pas évidente. En effet elle se heurte au fait que la masse adsorbée, supposée uniformément répartie sur la surface du capteur, diminue lorsque le résonateur

est miniaturisé. Nous nous proposons donc d'évaluer la résolution de ces capteurs selon un critère original, baptisé Surface Masse Limit of Détection (SMLOD) ou résolution en masse par unité de surface du résonateur.

Plus précisément, la masse de molécules gazeuses absorbées (analyte)  $m_g$  sur la surface du résonateur est relié à leur concentration  $C_g$  dans le gaz environnement par:

$$m = \rho_g K V_{AS} C_g$$

où  $\rho_g$ ,  $V_{AS}$  et  $K$  sont respectivement la densité massique de l'analyte gazeuse, le volume de la couche de fonctionnalisation, et le coefficient de partition du couple analyte / couche de fonctionnalisation. Ce dernier paramètre caractérise l'équilibre chimique entre la phase gazeuse et la phase adsorbé de l'analyte et prend en compte les phénomènes d'adsorption et de diffusion des molécules de l'analyte sur la surface / à l'intérieur de la couche de fonctionnalisation.

La plus petite concentration mesurable avec un capteur de gaz résonant est donc relié à la plus petite masse mesurable  $\delta m_{min}$  avec ce même capteur, elle-même reliée à la plus petite variation relative de fréquence de résonance  $\left(\frac{\delta f}{f_0}\right)_{min}$  par :

$$\delta c_{min} = \frac{\delta m_{min}}{\rho_g K V_{AS}} = \frac{2M}{\rho_g K V_{AS}} \left(\frac{\delta f}{f_0}\right)_{min}$$

où  $M$  est la masse du résonateur. En écrivant  $M = \rho t S$  et  $V_{AS} = t_f S$  avec  $S$  la surface du résonateur,  $\rho$  la masse volumique de du résonateur et  $t$  et  $t_f$  l'épaisseur du résonateur et de la couche de fonctionnalisation respectivement, on a :

$$\delta c_{min} = \frac{2\rho t}{\rho_g K t_f} \left(\frac{\delta f}{f_0}\right)_{min}$$

le terme  $\rho_g K t_f$  ne dépend que du couple analyte / couche de fonctionnalisation et peut-être omis pour l'évaluation des performances capteurs d'un résonateur particulier. Le facteur de mérite permettant de prédire la résolution pour une mesure gaz d'un résonateur mécanique est donc la plus petite masse par unité de surface de résonateur que l'on puisse mesurer (SMLOD):

$$\delta m_{surf} = 2\rho t \left(\frac{\delta f}{f_0}\right)_{min}$$

La plus petite variation relative de fréquence de résonance mesurable  $\left(\frac{\delta f}{f_0}\right)_{min}$  peut être déterminée par une étude du bruit en fréquence d'un système en boucle fermée en fréquence à l'intérieur de laquelle le résonateur opère. Plusieurs topologies de boucle de fréquence peuvent être utilisées. Les plus fréquentes sont les boucles auto-oscillantes dans lesquels le signal de sortie du résonateur est réinjecter à l'entrée après amplification et déphasage de sorte que les pertes énergétiques dans le résonateurs soient exactement compensées par l'amplification ; et la boucle à verrouillage de phase (PLL) dans laquelle le résonateur est constamment excité à sa fréquence de résonance à l'aide d'un oscillateur à fréquence variable piloté par un comparateur de phase garantissant que la phase du signal de sortie du résonateur par rapport au signal d'entrée soit constante. Dans ces deux cas et dans l'hypothèse d'un bruit dominant blanc, on peut montrer que la densité spectrale de bruit en fréquence est inversement proportionnelle au facteur de qualité  $Q$  du résonateur et au rapport signal à bruit  $\frac{\langle V_{noise} \rangle}{V_{out}}$ , ainsi :

$$\delta m_{surf} = 2\rho t \left(\frac{\delta f}{f_0}\right)_{min} = \frac{\rho t \langle V_{noise} \rangle}{Q V_{out}}$$

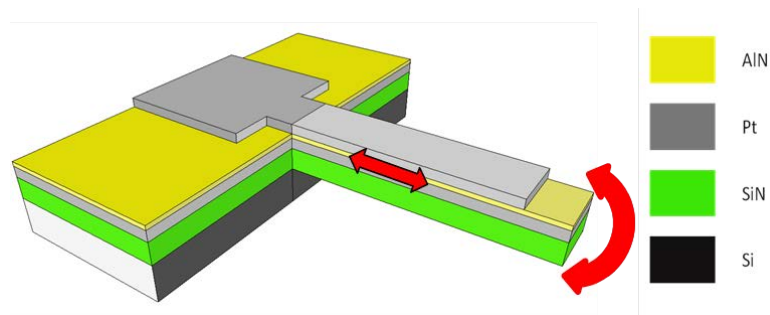


Figure RF- 4 : Fonctionnement d'une poutre piézoélectrique, la couche piézoélectrique crée un stress longitudinal qui, par réaction des autres couches de matériaux, entraîne le fléchissement de la poutre

Cette dernière équation montre que le design optimum pour un capteur de gaz résonant est celui qui garantit à la fois une épaisseur faible du résonateur, un haut facteur de qualité et un important rapport signal à bruit. Cela impose une contrainte forte sur l'efficacité de la méthode de transduction électromécanique choisie pour l'actionner et détecter les mouvements mécaniques du résonateur.

Nous nous intéresserons dans ce travail aux poutres résonantes encastrées libres à transduction piézoélectrique. Ces dispositifs sont constitués d'une structure suspendue contenant au moins trois couches de matériaux différents, deux métalliques servant d'électrodes de part et d'autre de la couche de matériau piézoélectrique. Une couche supplémentaire dite couche élastique peut aussi être rajoutées pour faciliter la fabrication et/ou optimiser la performance de transduction. Lorsqu'une différence de potentiel est imposée entre les deux électrodes, une contrainte longitudinale apparaît dans la couche piézoélectrique par effet piézoélectrique indirect, générant un moment de flexion d'autant plus important que la couche piézoélectrique se trouve au-dessus ou en-dessous de la fibre neutre de la poutre. A l'inverse, lorsque la poutre se fléchit, la contrainte longitudinale nette dans la couche piézoélectrique engendre des charges électriques aux interfaces électrodes / couche piézoélectrique par effet piézoélectrique direct. Ce mode de transduction présente de nombreux avantages comme son haut niveau d'intégration, sa bonne sensibilité, sa très faible consommation énergétique mais aussi sa robustesse à la miniaturisation. En effet cette transduction est proportionnelle aux contraintes mécaniques dont l'intensité reste constante lorsque l'on miniaturise les dispositifs. Toutefois, si la transduction piézoélectrique a été largement exploitée pour l'actionnement et la détection de micro systèmes, ce n'est que très récemment que sa fonctionnalité a été démontrée puis appliqués dans des dispositifs fonctionnels nanométriques.

L'étude de la transduction piézoélectrique utilisant des couches nanométriques constitue donc l'objectif principal de cette thèse. Pour cela, nous nous attacherons à démontrer, d'un point de vue théorique et pratique, l'intérêt que peut apporter un tel développement technologique pour la mesure de gaz. Nous étudierons donc un modèle analytique prédisant les performances pour la mesure de gaz de poutres encastrées libres piézoélectriques et, suivant les conclusions sur le dimensionnement optimum de tels dispositifs issues du modèle théorique, nous présenterons la fabrication et la caractérisation, depuis les premières mesures électrique jusqu'à l'expérience de preuve de principe de mesure gaz, de micro-poutres résonantes dont la transduction est basée sur des couche de Nitrure d'Aluminium (AlN) de 50 nm d'épaisseur.

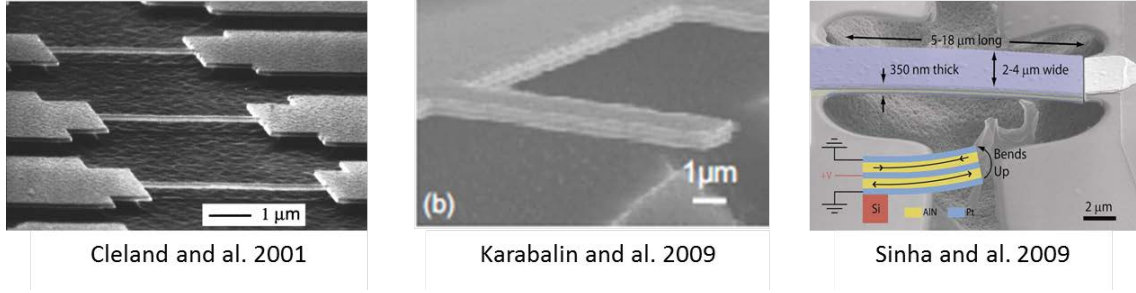


Figure RF- 5 : Etat de l'art antérieur pour la fabrication et la caractérisation de nano-poutres résonantes piézoélectriques

## 2. Etude théorique

La piézoélectricité est la propriété de certains matériaux à accumuler des charges électriques sous l'effet de contraintes mécaniques. C'est un effet réversible, présent dans des alliages appartenant aux 20 classes non centro-symétriques parmi les 32 classes cristallographiques existantes. Si le fonctionnement microscopique de la piézoélectricité fait encore l'objet de nombreux articles théoriques, sa modélisation macroscopique, dans le domaine linéaire, est largement connue et standardisée. Elle repose sur les équations suivantes et utilisant une indexation simplifiée des coefficients, appelées équations constitutives de la piézoélectricité :

$$T_p = c_{pq}^E S_q - e_{kp} E_k$$

$$D_i = e_{iq} S_q + \epsilon_{ik}^S E_k$$

avec  $T_p$ ,  $S_q$ ,  $E_k$  et  $D_k$  les coefficients des vecteurs représentant l'état de contrainte, de déformation, du champ électrique et du déplacement électrique, respectivement. Les coefficients  $c_{ij}^E$ ,  $e_{ik}$  et  $\epsilon_{ij}^S$  représentent les coefficients des matrices d'élasticité, de piézoélectricité et de permittivité, respectivement.

### 2.1. Actionnement des micro-poutres à transduction piézoélectrique

Soit une poutre encastres libre ayant une structure correspondante à la Figure RF- 4 : une première couche, appelée couche élastique, en Nitrure de Silicium (SiN) sur laquelle a été déposé un « stack piézoélectrique » constitué de deux couches métalliques, les électrodes, insérant un couche piézoélectrique en Nitrure d'Aluminium. La modélisation analytique du comportement mécanique d'une telle structure hétérogène peut être obtenue en adaptant l'équation de vibration des poutres d'Euler-Bernoulli :

$$\mu W \frac{\partial^2 w}{\partial t^2} + \mu \Gamma \frac{\partial w}{\partial t} + \langle EI \rangle_{eq} \frac{\partial^4 w}{\partial x^4} = \frac{\partial^2 M_p}{\partial x^2}$$

avec  $\mu = \sum \rho_i t_i$  la densité massique par unité de surface (longueur et largeur) de la poutre ( $\rho_i$  et  $t_i$  étant respectivement la densité massique et l'épaisseur de chaque couche de matériau),  $W$ ,  $\Gamma$ ,  $w$ ,  $x$

et  $M_p$  la largeur de la poutre , le coefficient de dissipation (tous les phénomènes de dissipation étant modélisés par des frottements visqueux), le déplacement dans la direction verticale de la poutre, la coordonnée spatiale dans l'axe de la poutre et enfin le moment d'actionnement piézoélectrique. La rigidité équivalente de la poutre est obtenue en utilisant la méthode de la poutre mono-matériau équivalente pour laquelle la position de la fibre neutre et la rigidité s'expriment par :

$$z_0 = \frac{\sum E_i t_i z_i}{\sum E_i t_i}$$

et

$$\langle EI \rangle_{eq} = \sum E_i I_i$$

Le moment d'actionnement piézoélectrique est donné par :

$$\begin{aligned} M_p(x) &= \left( \int \int_{AIN} (z - z_0) e_{31} \frac{V_{in}}{t_3} dy dz \right) H(L - x) \\ &= W \beta_p V_{in} H(L - x) \end{aligned}$$

avec  $V_{in}$  et  $e_{31}$  la tension électrique d'actionnement et le coefficient piézoélectrique transverse, respectivement. Le coefficient  $\beta_p = e_{31} \left( \frac{t_3}{2} + t_2 + t_1 - z_0 \right)$  dépend de l'asymétrie de l'empilement des matériaux dans le sens de l'épaisseur, comme nous le verrons c'est une figure de mérite importante de l'efficacité de la transduction piézoélectrique. L'équation de vibration peut être résolue en utilisant la méthode de projection sur les modes propres de la poutre conduisant à l'expression suivante du déplacement en bout de poutre :

$$w(L) = \frac{\beta_p}{\langle YI \rangle_{eq}} f(L) V_{in}$$

où  $f(L)$  est une fonction de la longueur et des modes propres de la poutre uniquement.

## 2.2. Détection piézoélectrique de poutres encastées libres

La relation courant / tension électrique aux bornes de la poutre peut être obtenue grâce au théorème de Gauss. Cela conduit à un model électrique équivalent correspond à celui de la Figure RF-6 et comprenant une capacité statique  $C_o = \epsilon_{33} \frac{S}{t_p}$  représentant la structure capacitive de l'empilement électrode / diélectrique (AlN) / électrode, en parallèle avec un circuit résonant (branche motionnelle)  $C_m = \frac{W^2 L \beta_p^2 \gamma_n}{\langle EI \rangle_{eq}}$ ;  $L_m = \frac{1}{C_m \omega_n}$ ;  $R_m = \frac{1}{C_m Q \omega_n}$  modélisant l'excès de charge induit par la piézoélectricité directe et la résonance mécanique de la poutre. Ainsi la relation courant tension aux bornes de la poutre peut s'écrire :

$$i_{out} = j\omega \left( \frac{C_m}{1 + jC_m R_m \omega - C_m L_m \omega^2} + C_o \right) V_{in}$$

Cette dernière équation montre que le signal de courant traversant la poutre est constitué d'un signal de fond passant à travers  $C_o$  et d'un signal utile contenant les informations électriques passant par la branche motionnelle. Numériquement, le signal de fond est au moins un ordre de grandeur supérieur au signal utile imposant l'utilisation d'un détecteur électronique avec une grande gamme

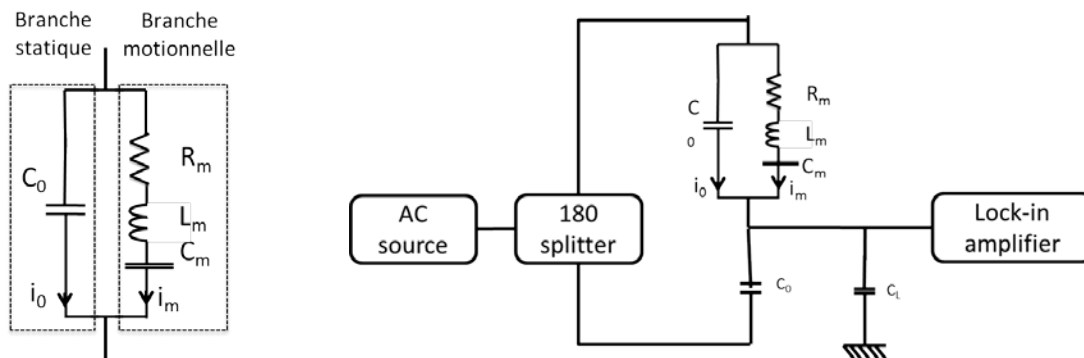


Figure RF- 6 : Circuit électrique équivalent pour une poutre résonante piézoélectrique (gauche). Schéma de mesure en demi-pont capacitif pour annuler le signal de fond passant par la capacité statique de la poutre (droite)

dynamique. Pour résoudre cette difficulté, une architecture en demi-pont peut avantageusement être utilisée (Figure RF- 6). Elle consiste à annuler le signal de fond en l'additionnant à un signal d'amplitude égale mais en opposition de phase. Ce signal peut être facilement obtenu en alimentant une capacité de même valeur que la capacité statique de la poutre avec le même signal d'entrée que celui de la poutre mais en opposition de phase. Dans ce cas le signal utile pour le détecteur électronique (détection synchrone) est donné par :

$$V_{out} = \frac{C_m / (2C_0 + C_L)}{1 + jC_m R_m \omega - C_m L_m \omega^2} V_{in}$$

Cette dernière équation peut-être directement utilisée pour étudier l'influence de l'épaisseur de chaque couche du stack sur l'efficacité de l'actionnement. Comme le montre la Figure RF- 7, réduire l'épaisseur de la couche d'AlN améliore l'efficacité de la transduction, il existe aussi une épaisseur optimum de SiN provenant du compromis à trouver entre la maximisation du bras de levier piézoélectrique (accroître l'épaisseur de SiN) et la rigidité de la poutre (décroître l'épaisseur de SiN).

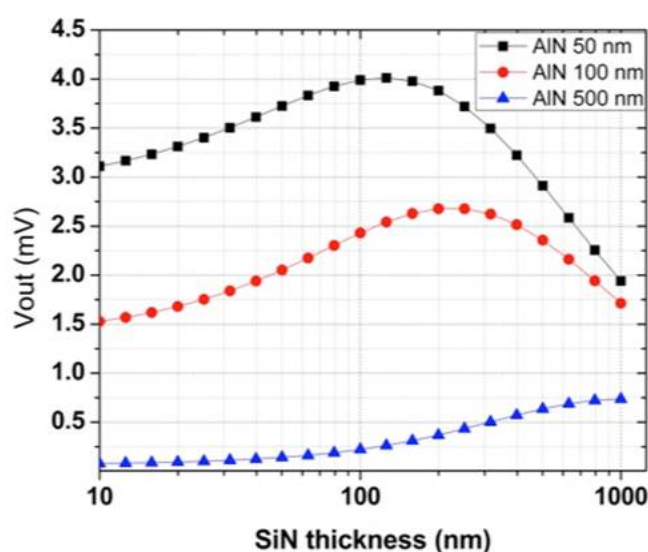


Figure RF- 7 : Signal de sortie en fonction de l'épaisseur de SiN et pour différentes épaisseurs de AlN et dans le cas \$L=100 \mu m\$ et \$C\_L=100\$ nF

### 2.3. SMLOD des poutres piézoélectriques

Dans l'optique de réaliser un capteur de gaz à haute résolution, nous nous proposons de développer plus en détail l'étude d'optimisation du design du résonateur à base de poutres encastrées libres à transduction piézoélectrique. Nous considérons donc un tel résonateur inclus dans une boucle fermée en fréquence de type auto-oscillateur ou boucle à verrouillage de phase permettant de suivre les fluctuations de la fréquence de résonance du résonateur en temps réel. Un tel système est, en pratique, soumis à de nombreuses sources de bruits : bruit blanc et bruit de Flicker des différents étages d'amplification dans la chaîne électronique, bruit thermomécanique, bruit d'absorption / désorption, fluctuation de température, défaut mécanique... mais un rapide calcul de la densité spectral de bruit ramenée à la sortie du résonateur de chacun de ces bruits et selon les formules de la littérature montre que le bruit blanc électronique à l'entrée du premier étage d'amplification électronique domine de plusieurs ordres de grandeurs tous les autres. Ce sera donc le seul que nous considérerons ici.

Dans les hypothèses selon lesquelles le résonateur fonctionne dans le domaine linéaire et exactement à sa fréquence de résonance mécanique, la SMLOD d'un tel système de mesure de gaz est donnée par la formule suivante:

$$SMLOD = \frac{\langle V_{noise} \rangle \mu (2 + C_L/C_0)}{Q^2 V_{in} (C_m/C_0)}$$

avec  $\langle V_{noise} \rangle$  et  $V_{in}$  l'amplitude rms du bruit électronique et la tension d'actionnement de la poutre respectivement. Le terme  $\frac{\langle V_{noise} \rangle}{Q^2 V_{in}}$  est supposé indépendant du design de la poutre. En réalité le facteur de qualité et la tension maximum d'actionnement peuvent être reliés à des paramètres de design : si les phénomènes de dissipation dominants sont dus aux frottements de l'air  $Q \propto W(t/L)^2$  et si la poutre est actionnée à la limite des non-linéarités mécaniques  $V_{in} \propto 6.3L/\sqrt{Q}$ . Toutefois, ces lois de comportement ne correspondent pas aux données expérimentales que nous avons obtenues :  $Q$  varie sensiblement, pour un même design, selon les conditions de fabrication des poutres et la tension maximum d'actionnement expérimentale est bien en deçà de sa valeur théorique. Ainsi seul le terme  $\frac{\rho t(2+C_L/C_0)}{(C_m/C_0)}$  est pris en compte dans l'étude d'optimisation. Ce terme peut être séparé en trois :

- La densité par unité de surface  $\mu = \sum \rho_i t_i$ , ce terme peut être minimiser en diminuant l'épaisseur de toutes les couches de la poutres et plus particulièrement l'épaisseur des électrodes de forte densité.
- La charge capacitive  $2 + C_L/C_0$  constituée de la capacité statique de la poutre résonante en tenant compte des parties non active mécaniquement (pads) et de la capacité d'entrée du premier étage d'amplification. Cette dernière peut être réduite en augmentant le niveau d'intégration du premier étage d'amplification par rapport à la poutre résonante (de façon ultime : co-intégrée sur le même substrat). La capacitance des pads de connexion peut être rendue quasi nulle mais au prix d'étapes supplémentaires dans le procédé de fabrication.

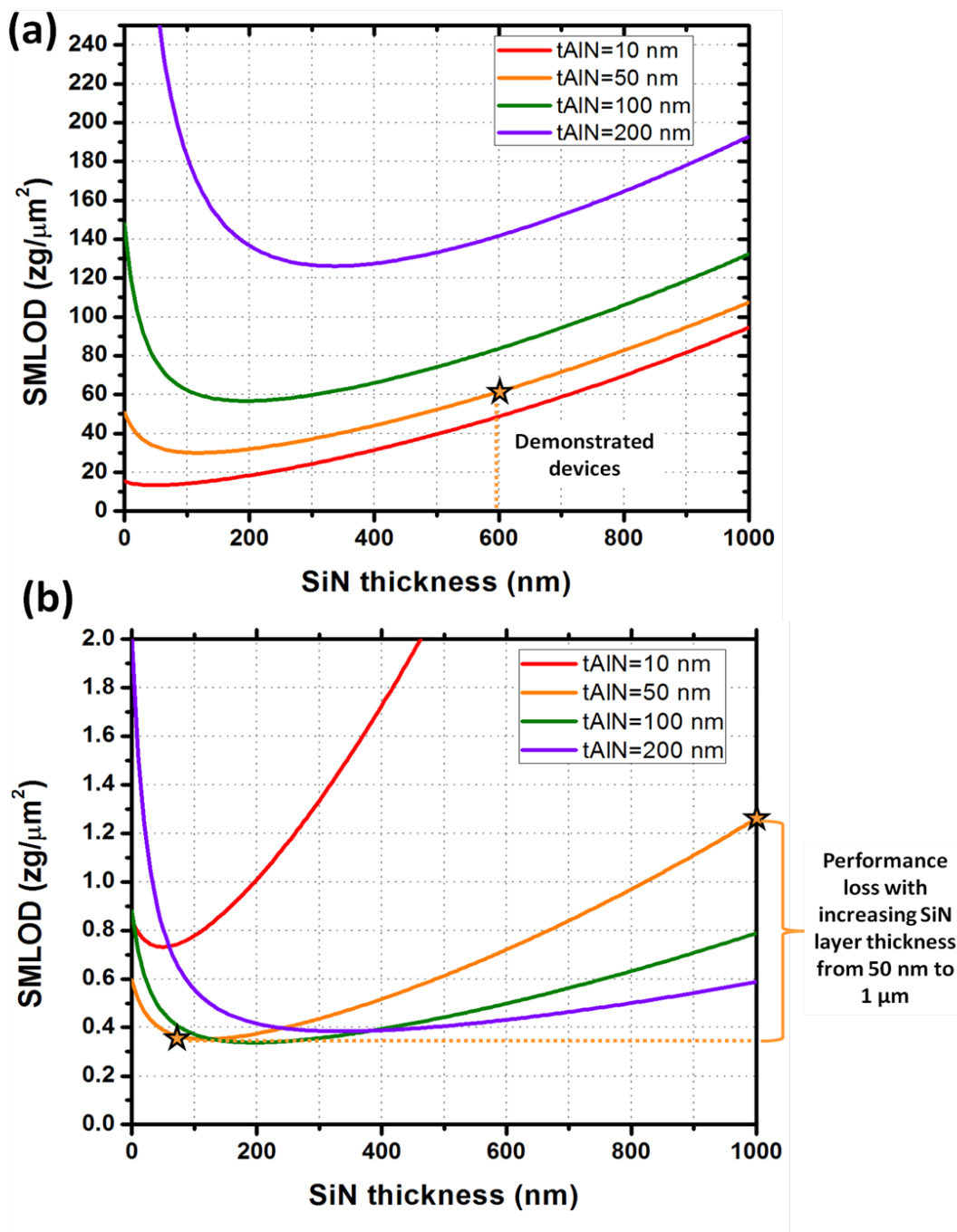


Figure RF- 8 : SMLOD d'une poutre piézoélectrique en fonction de l'épaisseur de SiN et pour différentes épaisseur d'AlN selon deux cas de capacité parasite. (a)  $C_L = 100 \text{ pF} > C_0$  quel que soit l'épaisseur de la couche d'AlN (b)  $C_L = 1 \text{ pF} < C_0$  quel que soit l'épaisseur de la couche d'AlN. De façon à pouvoir comparer ces courbes avec les données expérimentales, tous les autres paramètres de design sont fixés aux valeurs expérimentales : épaisseurs des électrodes 100 nm (inférieure) et 25 nm (supérieur), longueur et largeur de la poutre 80 μm et 40 μm, tension d'actionnement, facteur de qualité, bruit électronique et bande passante : 750 mV, 100, 5 nV/√Hz et 0.1 Hz (respectivement). En fonction de l'épaisseur d'AlN la capacité statique de la poutre varie de 28pF (10 nm) jusqu'à 1.4 pF (200 nm)

Lorsque  $C_L/C_0 \gg 2$ , c'est-à-dire lorsque la capacité parasite de l'électronique ou la capacité des pads domine la SMLOD est proportionnelle au rapport  $\frac{C_L}{C_m} = \frac{\langle EI \rangle_{eq} C_L}{W^2 L \beta_p^2 \gamma_n}$  et donc inversement proportionnelle à la surface de la poutre.

Deplus, comme le montre la Figure RF- 7, diminuer l'épaisseur de la couche d'AIN améliore très rapidement le facteur d'efficacité de transduction  $\beta_p/\langle EI \rangle_{eq}$ . Cela augmente l'intensité du champ électrique (à différence de potentiel fixe), diminue la rigidité totale de la poutre  $\langle EI \rangle_{eq}$ , et place la couche piézoélectrique proche de la surface supérieur de la couche, augmentant ainsi le bras de levier pour l'actionnement et la contrainte mécanique moyenne dans la couche d'AIN pour la détection. Enfin, à épaisseur d'AIN constante, il existe un optimum pour l'épaisseur de SiN provenant du compromis à trouver entre rigidité de la poutre et bras de levier piézoélectrique. Lorsque  $C_L/C_{0min} \ll 2$ , la SMLOD est proportionnelle à  $\frac{C_{0min}}{C_m} = \frac{\langle EI \rangle_{eq} \epsilon_{33}}{W \beta_p^2 \gamma_n t_3}$  donc indépendante de la surface de la poutre.

- *Le rapport capacité motionelle sur capacité statique*  $\frac{C_{0min}}{C_m} = \frac{\langle EI \rangle_{eq} \epsilon_{33}}{W \beta_p^2 \gamma_n t_3}$  ne dépend que des épaisseurs des différentes couches et ce terme doit être pris en compte dans le cas où  $C_L/C_{0min} \ll 2$ . Comme le montre la figure, il existe alors un optimum pour l'épaisseur de la couche d'AIN autour de 100 nm provenant du compromis à trouver entre la minimisation de la masse par unité de surface de la poutre, la maximisation de l'efficacité de transduction, toutes deux obtenues en diminuant l'épaisseur de la couche d'AIN, et la minimisation de la capacité statique de la couche qui tends à augmenter l'épaisseur d'AIN.

En conclusion, dans le domaine de variation des dimensions de la poutre pour lesquelles le facteur de qualité et la limite de non linéarité peuvent être considérés invariants, le design optimum dépend essentiellement des capacités technologiques à travers l'épaisseur minimale d'AIN autorisée et le niveau d'intégration de l'électronique. Lorsque la capacité parasite de l'électronique est grande (faible niveau d'intégration), le design optimal consiste en une poutre de longueur et de largeur maximale et contenant une couche d'AIN d'épaisseur minimale. Lorsque la capacité de l'électronique est faible (haut niveau d'intégration), la longueur et la largeur de la poutre n'influent pas sur les performances tandis que l'épaisseur de la couche d'AIN a une valeur optimale. Ces deux stratégies d'optimisation étant contraires, il existe un optimum global qui est atteint lorsque la capacité statique de la poutre est égale à la capacité parasite du premier étage d'amplification. C'est ainsi que nous pouvons énoncer les règles de design suivantes :

- L'épaisseur d'AIN doit être choisie la plus faible possible en fonction des capacités technologiques.
- La longueur et la largeur doivent être choisies de façon à ce que la capacité statique de la poutre soit égale à la capacité parasite du premier étage d'amplification
- L'épaisseur des électrodes métalliques (denses) doit être choisie minimale en fonction des capacités technologiques
- L'épaisseur de SiN doit être choisie à sa valeur optimale maximisant le rapport  $\beta_p/\langle EI \rangle_{eq}$

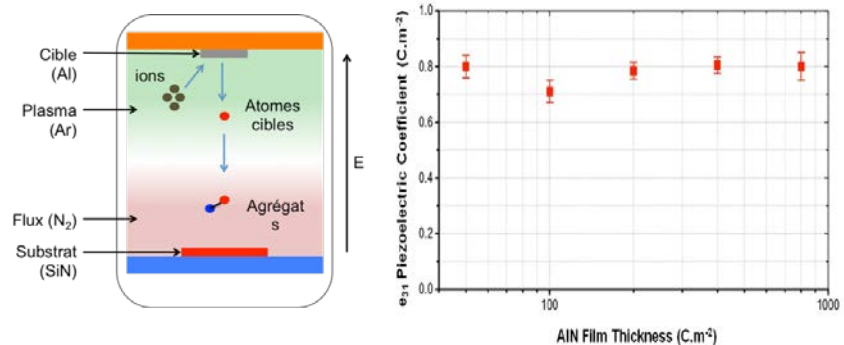


Figure RF-9 : Schéma de principe du procédé de dépôt d'AlN par de la pulvérisation magnétron réactive DC (gauche). Coefficient piézoélectrique  $e_{31}$  en fonction de l'épaisseur d'AlN déposé sur substrat Mo (100 nm) et avec couche de germination AlN (12 nm) (droite).

### 3. Démonstration expérimentale

#### 3.1. Dépôt et caractérisation de couche de 50 nm d'AlN

Suivant les conclusions de l'étude d'optimisation du design, nous avons cherché à investiguer expérimentalement la question de la minimisation de l'épaisseur de la couche d'AlN. Cette activité a fait l'objet du sujet de stage de fin d'étude de J. Abergel. Les recherches bibliographiques dès le début de cette étude montrent que les propriétés piézoélectriques de films minces déposés par pulvérisation magnétron DC réactive se dégradent lorsque l'épaisseur du film diminue. En réalité, les résultats de la littérature concernent des recettes de dépôt optimisées pour la croissance de film relativement épais (>200 nm) c'est-à-dire pour la croissance de film AlN sur un substrat d'AlN. Il était donc nécessaire de repenser la recette pour l'optimiser dans des conditions de croissance d'un film d'AlN sur un substrat métallique.

En partant d'une recette stabilisée de dépôt de film d'AlN pour la fabrication de résonateur BAW (épaisseur 800 nm) sur des wafers de silicium de 200 mm de diamètre, Julie a pu faire varier les tensions d'accélération des ions du plasma, le type de substrat, la température du substrat et l'épaisseur des films d'AlN jusqu'à 50 nm. Les propriétés cristallographiques des films obtenus ont été mesurées par diffraction rayon X (XRD) de façon à déterminer leur orientation dominante et la largeur des pics à hauteur médiane (FWHM) de leur rocking curve. Les contraintes résiduelles des films ont été mesurées grâce à la variation du rayon de courbure hors plan des wafers avant et après dépôt des films. Enfin, le coefficient piézoélectrique  $e_{31,eff}$  des films ont été mesuré selon une procédure décrite dans [7].

Pour les films d'AlN déposés sur des substrats Pt, W ou Mo, les contraintes résiduelles peuvent être compressives ou extensives en fonction de la puissance DC d'accélération des ions du plasma lors du dépôt. Tous ces films montrent une orientation dominante 1000 et la largeur de pic à hauteur médiane de leur rocking curve diminue avec l'épaisseur du film, témoignant d'un alignement des cristallites moins parfait. Malgré cela, le coefficient piézoélectrique  $e_{31,eff}$  reste quasiment constant indépendamment de l'épaisseur et proche de la valeur de l'état de l'art pour les couches plus épaisses :  $0.8 C \cdot m^{-2}$ . En outre cette étude a permis de démontrer l'importance de l'utilisation d'une couche de germination en AlN et de déterminer les épaisseurs minimales accessibles pour les différentes couches : 50 nm pour l'AlN et 150 nm pour le stack complet.

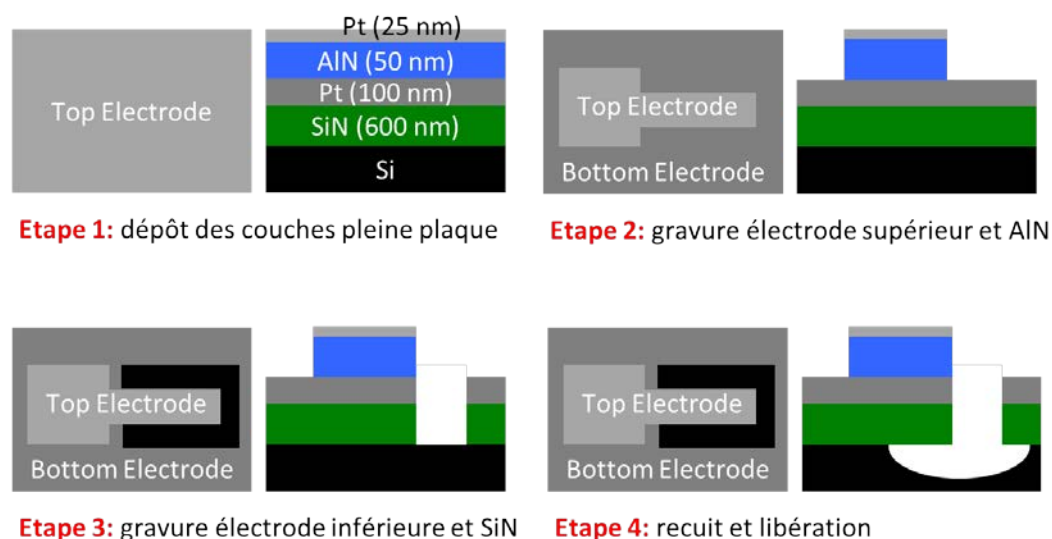


Figure RF- 10 : Procédé de fabrication des poutres encastrées-libres piézoélectriques

### 3.2. Fabrication de poutres piézoélectriques à base de films de 50 nm d'AlN

L'étape suivante des investigations expérimentales réalisées pour cette thèse consiste à fabriquer des poutres encastrées libres incluant une couche d'AlN de 50 nm fonctionnelle pour la transduction des mouvements de flexion. De façon à garantir le succès de la fabrication l'empilement de matériaux choisis ne correspond pas vraiment à l'optimum théorique (Figure RF- 8): la couche élastique de SiN a été volontairement choisie plus épaisse (600 nm) afin de garantir une rigidité suffisante de la poutre et palier au flambage des poutres lors de l'étape de libération due aux contraintes résiduelles dans les différentes couches matériaux. Le procédé de fabrication se fait en deux étapes de lithographie (Figure RF- 10). La première sert à graver l'électrode supérieure et la couche d'AlN tandis que la seconde permet de graver l'électrode inférieure et la couche élastique pour définir des accès au substrat de silicium qui sera finalement gravée en gravure isotrope XeF<sub>2</sub>.

Malgré la forte épaisseur de SiN choisie, l'obtention de structures suspendues droites représente la difficulté majeure de ce procédé de fabrication. Les contraintes résiduelles des différentes couches ont été équilibrées en contrôlant les paramètres de dépôt avec une précision assez médiocre due à l'imprécision de la méthode de mesure des contraintes dans des couches très minces sur wafer entier. Un réglage plus fin de la contrainte résiduelle dans l'électrode supérieur en Platine (dépôt évaporation) a été utilisé grâce à un recuit à 600 °C juste avant l'étape de libération. Avec un recuit à 500 °C, les poutres libérées étaient largement défléchies vers le bas tandis qu'avec un recuit à 700 °C, les poutres étaient défléchies vers le haut. Ainsi, la contrainte résiduelle de l'électrode supérieure peut être suffisamment modifiée pour équilibrer le stack. Toutefois cette méthode n'est pas suffisamment efficace pour éviter des fractures aux points de concentrations des contraintes, par exemple les angles droits à la base des poutres, et ce n'est qu'en minimisant la distance de libération des poutres au plus juste qu'il a été possible d'obtenir des dispositifs fonctionnels. Ainsi, il nous a été possible de stabiliser un procédé de fabrication pour la production de poutres de 90 µm de long 40 µm et contenant un stack matériaux de 775 nm d'épais.

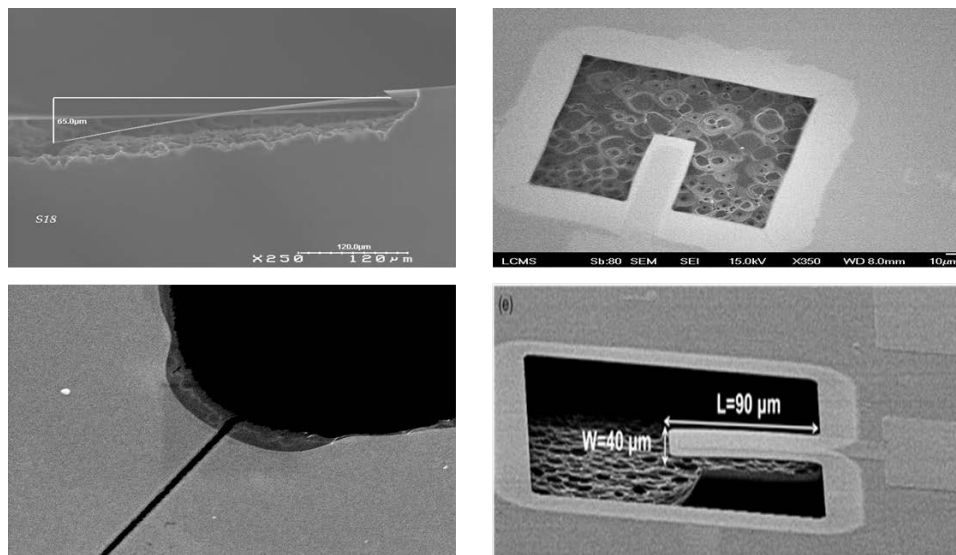


Figure RF- 11 : Micrographes électroniques des poutres piézoélectriques pour différentes étapes d'optimisation du procédé de fabrication. Les contraintes internes des différentes couches entraînent une forte flexion des poutres après libération. Pour remédier à ce problème, différentes stratégies ont été utilisées : contrôle des contraintes internes lors du dépôt des couches, recuit de l'électrode supérieur pour régler sa contrainte interne et minimisation de la distance de libération.

### 3.3. Caractérisation électrique

La fonctionnalité électrique des poutres ainsi fabriquées a logiquement été l'étape suivante des investigations expérimentales. Suivant les résultats de l'étude théorique, les spectres de résonance électrique des poutres ont été mesurés en utilisant un demi pont capacitif pour lequel la capacité d'équilibrage était soit une capacité variable discrète soit une poutre non libérée de même taille et sur le même substrat que la poutre mesurée. L'actionnement et la détection électrique ont été réalisés avec des instruments de laboratoire : source AGILENT 5210 et détection synchrone SR844. Cette configuration de test permet de réduire le signal de fond par un facteur 100 et ainsi de détecter les quatre premiers pics de résonance à 88 kHz, 546 kHz, 1.72 MHz et 3.46 MHz très proches des valeurs théorique de 92 kHz, 578 kHz, 1.62 MHz et 3.17 MHz. D'autres pics, à fréquences jusqu'à 20 MHz, sont aussi visibles dans le spectre mais sont plus difficiles à faire correspondre à des valeurs théoriques à cause de la présence de différents modes possible (torsion, flexion dans le plan, ect...).

Pour le premier mode de résonance, les prédictions théoriques sur l'amplitude du signal sont en parfait accord avec les résultats expérimentaux comme le montre la Figure RF- 12. Pour la poutre ayant servi au mesure présenté dans cette figure le fit analytique expérimental donne un facteur de qualité de  $Q = 125$  et un coefficient piézoélectrique  $e_{31}^{eff} = 0.78 \text{ C. m}^{-2}$  très proche de la valeur mesurée lors du développement du procédé de dépôt des couches d'AlN. Si la valeur de  $e_{31}^{eff}$  varie peu d'une poutre à l'autre ce n'est pas le cas du facteur de qualité qui varie de 75 à 135 selon les poutres et les batchs de fabrication. Force est de constater que de plus amples investigations du sont nécessaires pour comprendre quelle est la source principale de dissipation et en quoi le procédé de fabrication peut l'influencer. Il en va de même pour l'amplitude maximale d'actionnement, qui varie entre 100 et 800 mV soit une amplitude de déflexion entre 110nm et 880 nm bien en dessous de la valeur théorique de 48 µm.

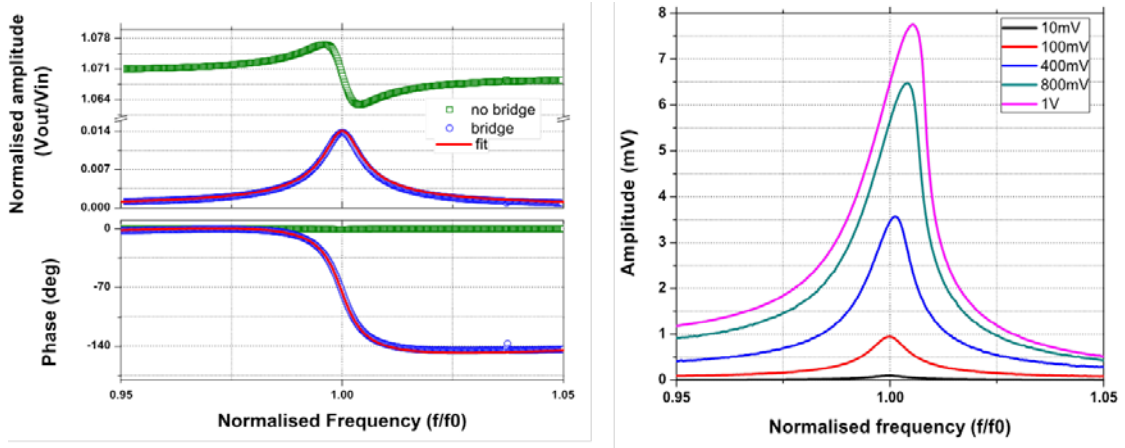


Figure RF- 12 : Spectres de la réponse électrique des poutres encastrees libres piézoélectriques

### 3.4. Caractérisation de la stabilité fréquentielle des poutres

Malgré ces incertitudes et avant de réaliser l'expérience de principe de mesure sous gaz, nous avons choisi de poursuivre l'investigation expérimentale de ces dispositifs pour caractériser leurs performances en termes de stabilité fréquentielle. Pour cela nous avons cherché à mesurer la variance d'Allan des poutres lorsqu'elles fonctionnent au sein d'une boucle fermée en fréquence. La variance d'Allan est un estimateur de la variance (vraie) du signal de fréquence de résonance qui a l'avantage d'être mesurable sur des ensembles finis d'échantillons et de ne pas diverger en présence d'un bruit en  $1/f$ . D'un point de vue mathématique, la variance d'Allan est définie par :

$$\sigma_y^2(\tau) = \frac{1}{N} \sum_{k=0}^{N-1} (\overline{y_{k+1}} - \overline{y_k})^2$$

avec  $y_k = \frac{1}{\tau} \int_{k\tau}^{(k+1)\tau} \frac{\delta f(t)}{f_0} dt$  les échantillons de la variation relative de fréquence mesurés avec un temps d'intégration  $\tau$ . Dans le cadres des hypothèses de notre modèle théorique de bruit (bruit dominant électronique, blanc) la variance d'Allan doit être donnée par :

$$\sigma_y(\tau) = \frac{N_0}{V_{out} \sqrt{\tau}}$$

avec  $N_0$  l'amplitude rms du bruit électronique par racine carré de bande passante de mesure. La mesure de la variance d'Allan une mesure classique pour les base de temps comme les oscillateurs à quartz présent dans de nombreux circuits électroniques d'aujourd'hui, avec des schémas de mesure standardisés. Pour des raisons pratiques liées aux temps de réponse du protocole de communication utilisé pour contrôler les instruments électroniques de laboratoire, nous avons choisi d'utiliser une méthode de mesure différente Figure RF- 13, en boucle ouverte, qui consiste à mesurer non pas le bruit en fréquence mais en phase et à prédire en post-traitement le bruit de fréquence correspondant. Cette méthode nous permet de descendre à des temps d'intégration plus court que ce qui nous serait accessible en boucle fermée et nous avons vérifié que pour les temps d'intégration long, les courbes de variance d'Allan obtenues par cette méthode et en utilisant un schéma de mesure plus classique correspondent exactement.

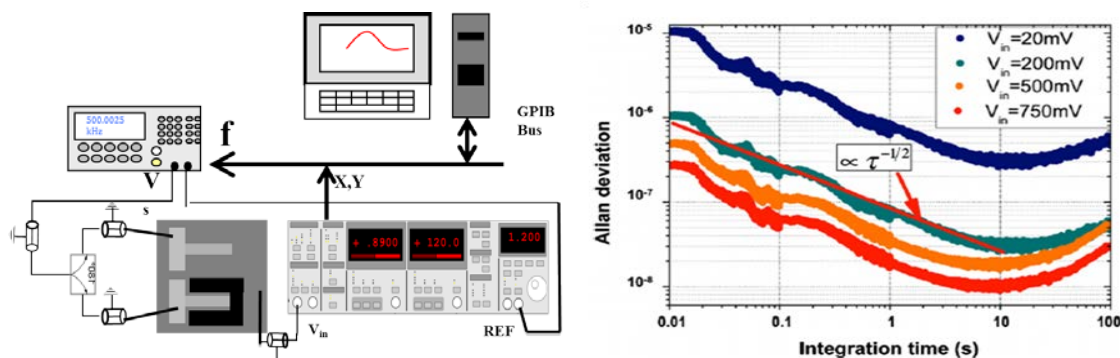


Figure RF- 13 : Schéma de mesure pour la caractérisation de la variance d’Allan des poutres encastrées libres piézoélectrique (gauche). Résultat de la mesure de variance d’Allan des poutres encastrées libres piézoélectriques.

La Figure RF- 13 présente les résultats de mesure de variance d’Allan pour la poutre dont le spectre de résonance est donné dans la Figure RF- 12. En correspondance avec les attentes théoriques, les courbes de variance d’Allan sont proportionnelles à la tension d’actionnement de la poutre et varient en  $\tau^{-1/2}$ . La valeur minimum atteinte est de  $10^{-8}$  pour un temps d’intégration de 10 s. Cela correspond bien à un bruit dominant électronique blanc d’amplitude rms par racine carré de bande passante de mesure de  $5.7 \text{ nV} \cdot \text{Hz}^{-1/2}$  spécifié par le constructeur de la détection synchrone RS844. En utilisant cette valeur nous pouvons estimer la SMLOD d’un tel système de mesure gaz selon la formule selon la formule  $\delta m_{surf} = 2\rho t\sigma_y(\tau) = 53 \text{ zg} \cdot \mu\text{m}^{-2}$  très proche de la valeur théorique prédite dans la Figure RF- 8 de  $57 \text{ zg} \cdot \mu\text{m}^{-2}$ .

Comme le montre le Tableau RF- 1 cela place notre système de mesure de gaz au niveau de l’état de l’art mondial. Il est, de plus, notable que ces poutres résonnantes piézoélectriques fonctionnent à des fréquences bien plus basses que les autres résonateurs de la littérature, cela facilitera le design d’une électronique dédiée. Enfin, le design de ces poutres ne suit pas exactement les règles de design énoncées lors de l’étude théorique. Par conséquent, on peut s’attendre à une amélioration de un à deux ordres de grandeurs des performances du système de mesure gaz en minimisant la capacité parasite de l’électronique de 30 pF à 1 pF et en choisissant une longueur et une largeur de poutre qui matchant cette capacité parasite minimisée.

Résonateur	Fréquence de résonance (MHz)	Déviaton de fréquence minimum	SMLOD (zg.μm <sup>-2</sup> )
FBAR	1100	$3.6 \times 10^{-7}$	10000
SAW	158	$7 \times 10^{-8}$	7000
CMR	180	$1.3 \times 10^{-8}$	60
CMUT	47.7	$1.15 \times 10^{-8}$	80.5
Nano-Poutres	10	$1.5 \times 10^{-7}$	400
Micro-Poutres AlN	0.1	$10^{-8}$	53

Tableau RF- 1 : Comparaison des performances en stabilité de fréquence et SMLOD des différents micro-résonateurs de la littérature.

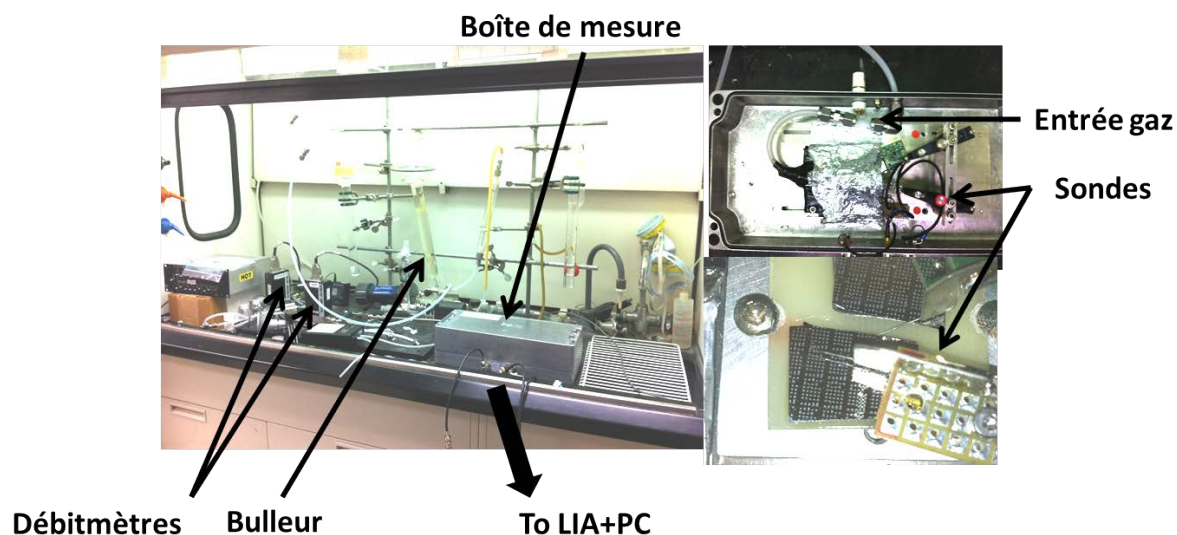


Figure RF- 14 : Photographie du banc de mesure gaz utilisé au California Institute of Technologies pour l'expérience de preuve de principe.

### 3.5. Mesures sous gaz

Fort des résultats très encourageants sur la stabilité en fréquence du système de mesure gaz à base de micro-poutres résonante à transduction piézoélectrique grâce à des films de 50 nm d'AIN, l'étape suivant des travaux expérimentaux consiste à mesurer effectivement la plus petite concentration de gaz possible à l'aide de ce système. Toutes les mesures présentées ici ont été réalisées dans le laboratoire du professeur M.L. Roukes au California Institute of Technologie.

Pour des raisons pratiques, disponibilité sur le banc de mesure et disponibilité de la bonne couche de fonctionnalisation, mais aussi parce qu'il est le plus souvent utilisé dans les publications, nous avons choisi le Di-méthyl-méyle phosphanate (DMMP) comme gaz cible. Il s'agit d'un organo-phosphate précurseur du gaz sarin relativement inoffensif avec une pression de vapeur saturante relativement basse (entre 2.31 et 112 Pa à 25 °C) permettant ainsi de produire facilement des échantillons de faible concentration. La couche de fonctionnalisation de la surface de la poutre résonante utilisée est un polymère développé pour des applications militaires (détection du gaz sarin) par les laboratoires Sandia appelé DKAP. Sa formule chimique exacte est le poly[2-(3-propylène)-3,5 bis (trifluorométhyl) phenol]methyl siloxane et ce polymère présente une forte affinité aux liaisons hydrogène permettant de cibler des groupements fonctionnels tels que les phosphanates (liaison P=O) du DMMP. Dans la littérature, le coefficient de partition du couple DKAP/DMMP est de  $10^7$ , valeur exceptionnellement haute qui justifie d'autant plus notre choix de gaz cible et de couche de fonctionnalisation. La procédure de dépôt du DKAP sur la poutre résonante se fait par « drop coating » : une goutte de solution DKAP-toluène est déposée à la pipette sur la poutre puis séchée à température ambiante pendant 5 min. En mesurant la fréquence de résonance de la poutre avant et après le dépôt, nous pouvons estimer l'épaisseur de couche de DKAP entre 5 et 10 nm.

La délivrance d'échantillon gazeux de DMMP de concentration connue se fait selon le principe de bullage / dissolution. Un gaz neutre ( $N_2$ ) est injecté dans une phase liquide de DMMP pur en équilibre avec sa phase gazeuse de sorte que le gaz sortant du bulleur soit saturé en vapeur de DMMP. La concentration en DMMP de ce flux de gaz est alors précisément connue et il suffit de le

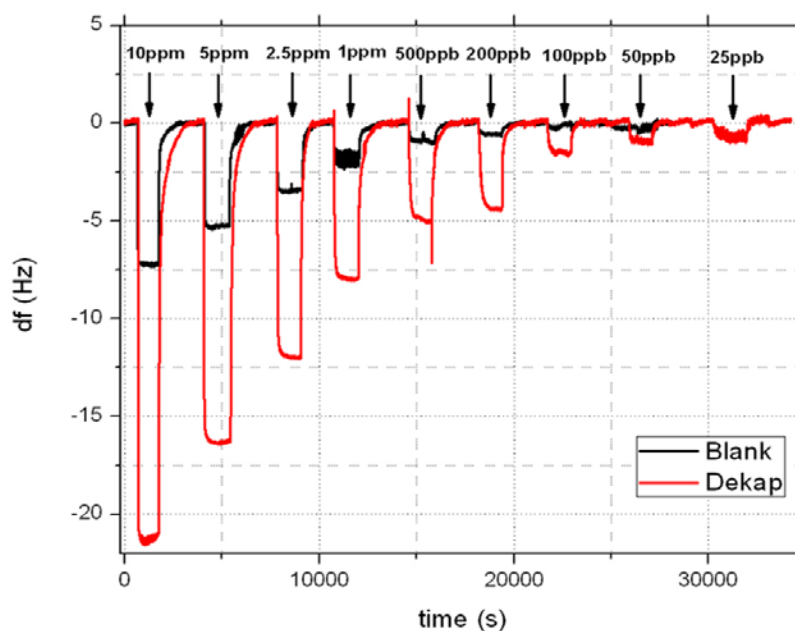


Figure RF- 15 : variation de la fréquence de résonance en fonction du temps lorsque le système de mesure gaz est exposé à des concentrations décroissantes de DMMP.

diluer dans un flux plus important pour obtenir la concentration de DMMP, nécessairement plus basse, désirée. Les différents flux sont contrôlés automatiquement par des débitmètres massiques et le domaine de variation de concentration pour le DMMP sur ce banc s'étend de 12 ppb à 3000 ppm pour un fonctionnement à 25 °C.

La Figure RF- 15 présente les variations de la fréquence de résonance lorsque la poutre est exposée à différentes concentrations de DMMP de 10 ppm à 25 ppb sur un peu plus de 12 heures de mesures. Il est intéressant de voir que la fréquence de résonance retrouve une valeur stable lorsque la poutre n'est plus soumise au flux de DMMP. Toutefois les temps d'absorption (30 secondes) et surtout de désorption (15 minutes) sont très longs par rapport aux résultats de la littérature. Nous pensons que cela est dû au volume important de la chambre de mesure dont les parois dégazent lentement et fournissent ainsi du DMMP à l'environnement de la poutre même après que le flux de DMMP soit coupé. La Figure RF- 16 présente les courbes de sensibilité au DMMP de ce système de mesure gaz. Contrairement à ce qui était attendu, la courbe de la variation de fréquence en fonction de la concentration de DMMP semble saturer pour les fortes concentrations mais reste linéaire aux concentrations plus faibles. Cela peut s'expliquer par la faible épaisseur de la couche de DKAP dont la saturation est atteinte rapidement. Dans le domaine de fonctionnement linéaire, le coefficient de partition du couple DKAP/DMMP peut-être estimé à  $2.10^4$  bien en-dessous de la valeur théorique. Cela peut être expliqué par une exposition trop longue de la solution DKAP à l'air avant le dépôt sur la poutre.

Malgré tout, la concentration minimum de DMMP effectivement mesuré de 25 ppb ainsi que la résolution ultime du système de mesure gaz calculer à partir de la valeur rms du bruit de fréquence (10 ppb) sont déjà parmi les meilleurs de l'état de l'art mondial (c.f. Tableau RF- 2). Considérant toutes les améliorations qui peuvent être apportées par design, en intégrant l'électronique de mesure et en optimisant la couche de fonctionnalisation, nous pensons donc qu'un tel système pourra certainement permettre une résolution de l'ordre du ppt.

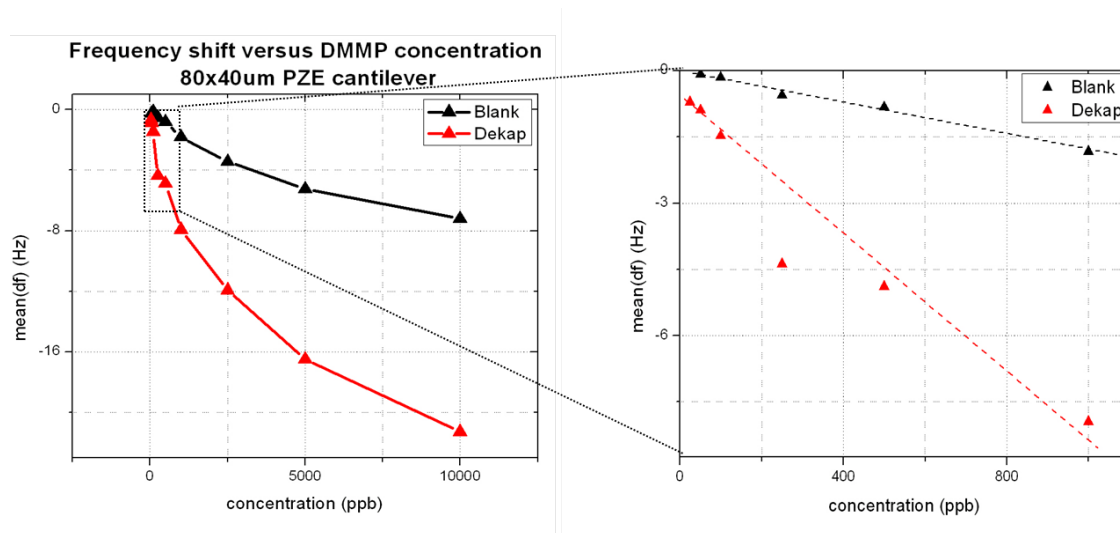


Figure RF- 16 : Courbes de sensibilité du système de mesure gaz à base de micro-poutres piézoélectriques résonantes : variation de la fréquence de résonance en fonction de la concentration de DMMP.

#### 4. Conclusions

Ces travaux de thèse ont été motivés par un objectif double: étudier et démontrer 1) le potentiel des micro/nano poutre résonantes à transduction piézoélectrique pour la réalisation d'un système de mesure de gaz à haute résolution et 2) les avantages de la transduction piézoélectrique basée sur des films d'épaisseur nanométrique. En modélisant le comportement dynamique électromécanique des poutre encastree libre à transduction piézoélectrique ainsi que les performances en terme de bruit en fréquence qui peuvent être obtenus avec de tel composants et une électronique de débouclage en fréquence, nous avons pu extraire des règles de design qui démontrent clairement l'importance de la diminution de l'épaisseur des couches piézoélectrique de transduction. Ce modèle a pu aussi être vérifié expérimentalement grâce à la caractérisation de la variance d'Allan de micro-poutres résonantes utilisant un film d'AlN de 50 nm pour l'actionnement et la détection et inclus dans une boucle à verrouillage de phase. La valeur minimale de variance d'Allan obtenue de  $10^{-8}$  est à l'état de l'art mondial et permet de prédire une résolution en masse par unité de surface de  $53 \text{ zg. } \mu\text{m}^2$  conformément au modèle théorique ( $57 \text{ zg. } \mu\text{m}^2$ ). Cela place ces

Résonateur	Fréquence de résonance (MHz)	Concentration minimum mesurée (ppb)
SAW	158	87
CMR	180	700
CMUT	47.7	15
Micro-poutres AlN	0.1	25

Tableau RF- 2 : Etat de l'art de la résolution en concentration pour la mesure de DMMP avec des micro-systèmes résonants

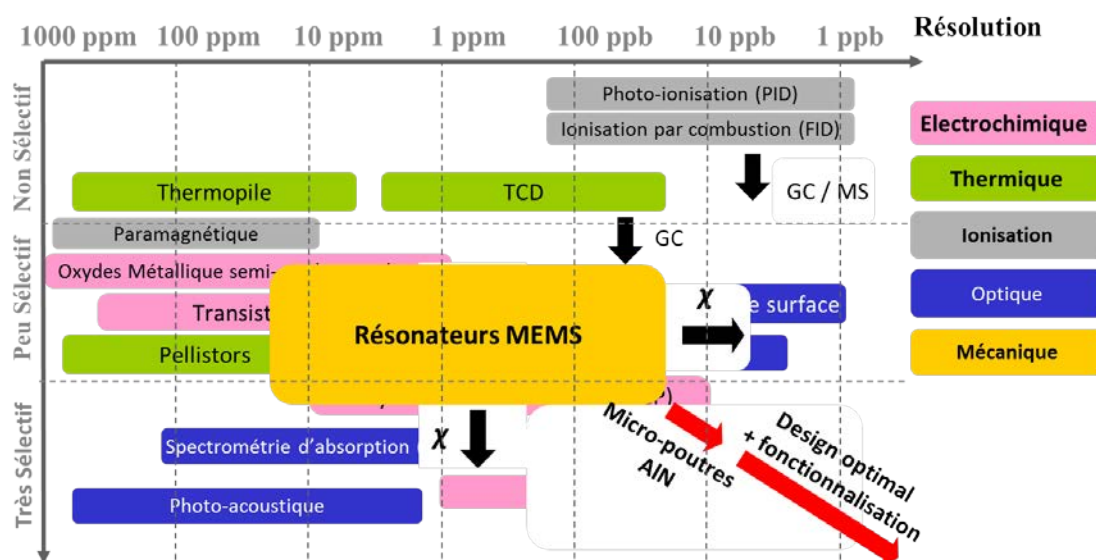


Figure RF- 17 : Comparaison des performances de différentes technologies de mesure de gaz tenant compte des résultats présentés dans ces travaux de thèse

dispositifs parmi les plus prometteurs de la littérature pour la mesure hautement résolue de gaz. Bien que les résultats restent préliminaires nous avons confirmé la possibilité d'obtenir d'excellente performance en mesure gaz avec ces dispositifs en mesurant effectivement la réponse de notre système gaz à des stimuli gazeux. Nous avons donc démontré qu'il était possible de détecter des concentrations de DMMP de 25 ppb, proche de l'état de l'art.

De par les nombreuses sources d'optimisation possible : design, intégration, couche de fonctionnalisation, nous pensons que la limite du ppb pourra être dépassée avec de tels dispositifs. Il s'agit là de la première piste importante pour les travaux futurs sur le sujet. L'autre axe de recherche concerne l'étude de nouveaux design comme par exemple les réseaux de nano-poutres qui ont déjà fournis des résultats intéressant pour la détection de gaz et pourraient largement bénéficier des avantages de la transduction piézoélectrique.

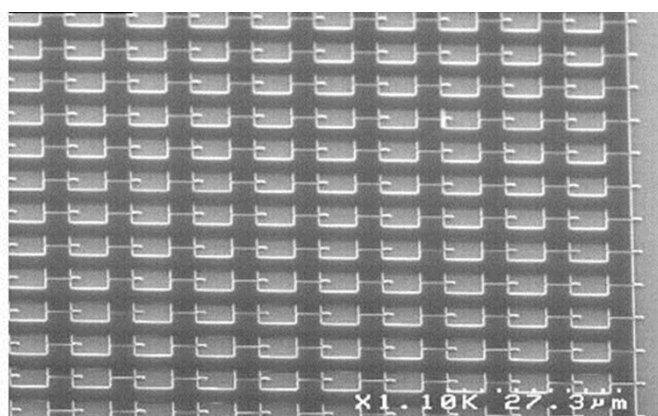


Figure RF- 18 : Micrographie électronique d'un réseau de nano-poutres piézoélectrique adressées collectivement. Ces dispositifs ont été fabriqués au cours de ces travaux de thèses mais restent non fonctionnels, plusieurs améliorations du procédé de fabrication sont proposés pour remédier aux problèmes rencontrés

# General Introduction

---

This dissertation is dedicated to the presentation of the experimental and theoretical progress achieved during this PhD towards the demonstration of high resolution piezoelectric cantilever resonator gas chemo sensor and toward the demonstration of the piezoelectric transduction of nano-scale electro-mechanical devices. This subject is at the meeting point of large and very active fields in today's technological research: gas sensing, resonant Micro and Nano Electro-Mechanical Systems (M/NEMS) and piezoelectric M/NEMS. To understand why it is advantageous to bring these three fields together, we shall follow an application-oriented presentation and start introducing the domain of gas sensing instrumentation. Gas sensing instruments, often abusively called gas sensor (we shall see why) correspond to systems that implement a detection or measurement of the chemical properties of a gaseous sample. First gas sensing systems date back to the late 19<sup>th</sup> century (canaries in a cage that would stop singing in presence of carbon dioxide in coal mines), but the greater part of the development of gas sensing instrumentation has happened during the last two decades. A recent study [1] evaluates the overall market size up to 3.9 billion in 2010 and projects an annual growth of 5-10% per year for the next ten years. However, behind the commercial denomination of gas sensors, hides a great variety of technologies. The market is at such a level of segmentation that prices of gas sensing instruments range over 6-7 orders of magnitude from less than a dollar up to few million dollars (*cf.* Figure 0- 1). This situation can be explained by the wide variety of applications in many different fields such as security (domestic, military and law enforcement), industrial processes, automotive, medicine, biology and environment. For each application, a particular set of specifications concerning targeted gases, concentration range, response time and so on is defined



**Figure 0- 1:** Example of commercial gas analyzer systems with corresponding prices

and it is impossible to address all applications with the same technology. Therefore gas sensors are as diverse as their applications.

We may however make a distinction between gas analyzers and gas chemo sensors. Gas analyzers are complex systems that are able to sample, separate and measure complex gas mixtures. Most compelling examples are mass spectrometers (MS) [2][3], gas chromatographers (GC) [4][5], optical spectrometers [6][7][8], colorimetric strips, human or animal olfactometry trials [9]. Gas chemo-sensors, on the other hand, are simpler systems that detect the presence of one or a small set of gaseous analytes and provide an electrical signal proportional to their concentration. To perform this task a gas chemo sensor must include at least two transduction stages: the so-called chemical and physical transductions (*cf.* Figure 0- 2).

The chemical transduction consists in the adsorption of molecules present in the surrounding gas onto the sensor surface. It results into variation of one or multiple physical properties of the sensor surface. For certain sensors, the chemical transduction happens directly on the surface of the physical transducer material. For others, it relies on a chemically active coating, called functionalization layer (a polymer film, a Self Assembly Monolayer (SAM)... whose chemical properties are designed to target a particular set of chemical species.

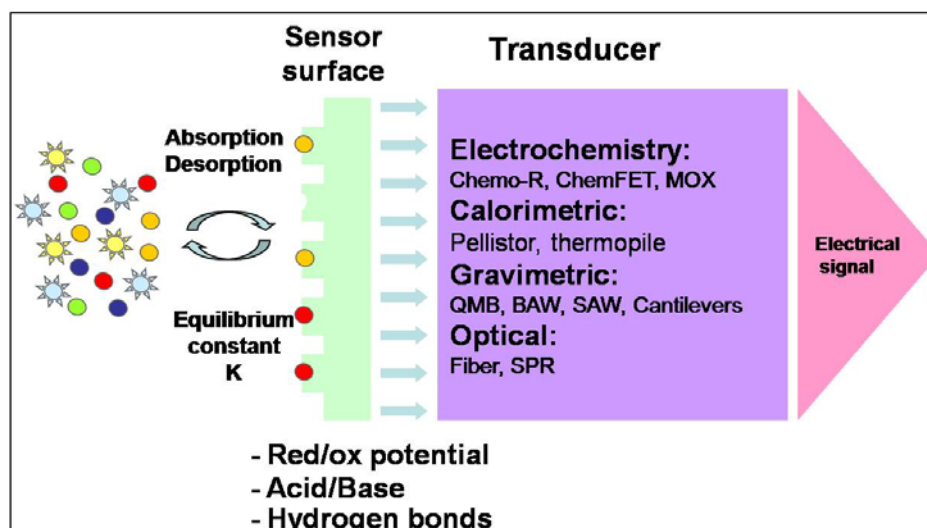


**Figure 0- 2:** General architecture of a gas chemo-sensor

Physical transducers transform the surface physical properties variations into a useful output signal, most of the time, in the electrical domain. Physical transducers may include several sub-transduction stages that are generally categorized according to their main physical domain of operation: electrical, optical, thermal or mechanical.

A gas chemo sensor can be used as a standalone device to monitor the presence of one particular gaseous analyte in mono-gas detectors [10][11] or integrated in arrays of different chemical specialization in systems called electronic noses [9][12] [13]. These bio-inspired multi-gas sensing systems stand in between gas analyzer and gas chemo sensor classes as they include, in addition to the sensitive head, pattern recognition algorithms and pre-analytical modules such as samplers, pre-concentrators or gas chromatographers that improve their analytical power.

With the development of micro and nano technologies in the last three decades, the performances of gas chemo sensors have been improved drastically, paving the way for new applications. Especially, these new devices with provided low fabrication cost, high sensitivity and miniature size are very good candidates for applications where high performances are required and heavy, expensive and slow instruments such as such GC and MS are not viable technically or economically. This is the case, in particular, for on-field detection of warfare agents, monitoring of indoor air pollution and medical diagnosis. For example, the opportunity to detect lung

cancer, which accounts for 25% of cancer deaths worldwide, through the detection of specific breath markers is raising lots of hopes. Dr M. Philips [14] has pioneered this diagnosis technique using GC/MS techniques and listed the candidates Volatile Organic Compounds (VOC) markers and their typical concentration (part per billion (ppb) range). Following this work, the group of Dr H. Haick at the Israel Institute of Technologies has recently published two articles [15][16] demonstrating that less expensive and faster tools based on carbon nanotubes (CNT) or gold nanoparticles chemo-resistor can also be used successfully to detect lung cancers VOC markers. Two companies, NANOMIX Inc [17] and APIX TECHNOLOGY [18], have initiated R&D programs for the development of compact lung cancer diagnostic stations using on breath analysis by the mean of nano sensing components.

Among the new gas chemo-sensors based on micro and nano-technologies, Micro Electro-Mechanical Systems play a peculiar role. They are electronic components with movable parts and typical dimensions in the 1-100 micrometer ( $\mu\text{m}$ ) range. Their development dates back to the seventies and since then one of their main thrusts relies on the use of silicon as structural material [19], exploiting both an exceptional mechanical behavior (high Young's Modulus and large elastic range) and ease and cost effective highly parallel manufacturing processes (lithography, thin film deposition, wet/dry etch methods, wafer bonding...). Since the eighties, MEMS have become ubiquitous with a development driven in three main directions: further miniaturization of components, diversification of the applications and monolithic integration with CMOS circuits for the production of fully integrated systems. As a result, today MEMS market is far from being negligible ( *cf.* Figure 0- 3) with an overall volume of 10 billion USD [20] (against 304 billion USD for the whole semiconductor industry).

Several MEMS based gas chemo-sensors have been developed with different operation principles that we will detail later. The most compelling case concerns resonant MEMS mass sensors. Their working principle is rather simple and relies on the variation of the natural resonance frequency of a mechanical structure, due to the mass of the gas molecules accreting on its surface. In this operation mode, MEMS gas chemo-sensors benefit from two major advantages that enforce high sensing performances 1) frequency is one of the easiest and most accurate physical quantities

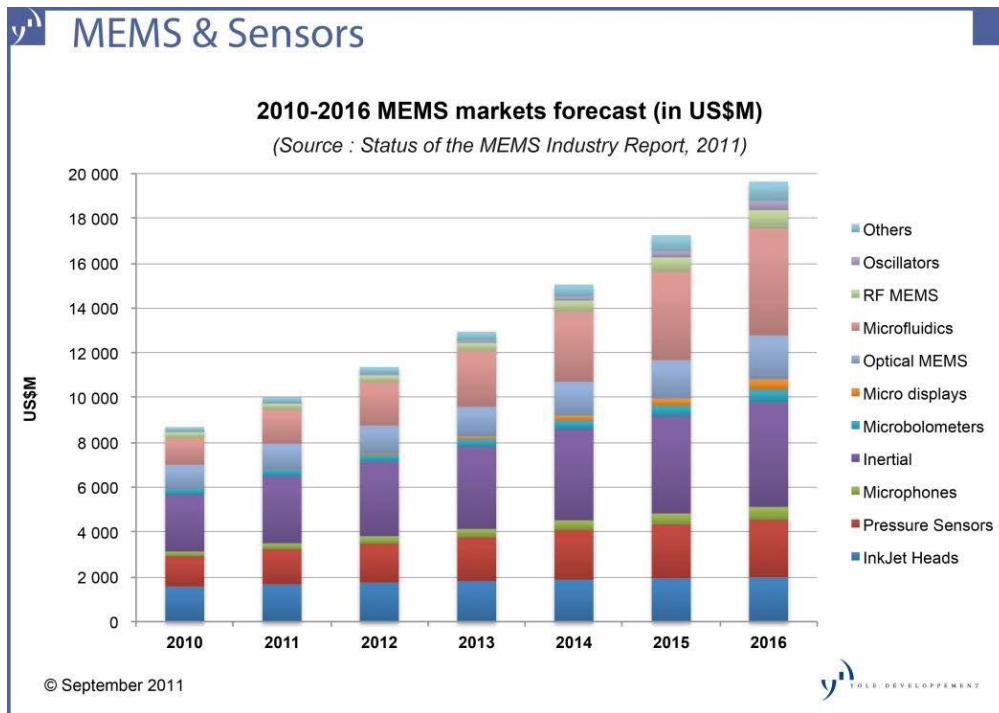


**Figure 0- 3:** Evolution of the MEMS market per applications field, 2010 to 2011: real figures - 2012 to 2016: prospection by Yole Development [20]

to measure and 2) the miniature mass and high resonance frequency of MEMS resonators that make them extremely sensitive to any change in their vibrating mass. Actually, atomic mass resolution [21] [22] has been recently demonstrated with aggressively miniaturized devices called Nano Electro Mechanical Systems (NEMS) and with typical dimensions in the sub-micrometer range.

Nevertheless, gain in mass sensing performance provided by shrinking devices dimensions does neither come without a price nor ensure high gas sensing performance. In addition to the complexity and cost of the nano-scale fabrication techniques, setting up efficient coupling between the nano-scale (the device) and the macro-scale (the operator) is a real scientific challenge and usual transduction techniques in MEMS fail to remain efficient at the NEMS scale. Therefore, it has been a great deal of work to investigate other transduction techniques such as thermo-elastic [23] or magnetic [24] actuation and piezoresistive [25], magnetic [24] or field emission [25] detection. But, despite their proven efficiency, these methods require either too bulky an external setup or consume too much power to be considered for real life applications. Besides, scientists are still debating the advantages of

aggressively shrinking the dimensions of the mechanical resonator for gas sensing application, arguing that a tradeoff must be met between mass sensitivity and large gas molecule capture area [26].

Piezoelectric (PZE) transduction enables on-chip transduction and very low power consumption and thus would be an ideal candidate to overcome the transduction issues of NEMS. However, due to the lack of deposition techniques of PZE films [27] with high PZE performances and dimensions compatible with NEMS design, this transduction method has been hardly ever studied at the nano-scale with only three publications [28][29][30] in the last ten years. In contrast, piezoelectric transduction is well spread among micro scale resonant gas chemo-sensors and has largely demonstrated its efficiency with commercial successes such as Quartz Micro Balance (QMB) [31][32], Surface Acoustic Wave (SAW) [33][34] and Bulk Acoustic Wave (BAW) [35][36]. However, up to now, the gas sensing performances of such devices are barely sufficient to address the aforementioned gas sensing applications.

The main objective of this PhD thesis is thus to investigate the piezoelectric transduction at the nano-scale for the development of high-resolution resonant micro-cantilever based gas sensor and prepare the development of piezoelectric NEMS resonant sensors. To that mean, we have intended to cover the whole prototyping chain from the development of 50 nm thick Aluminum Nitride (AlN) piezoelectric films with good piezoelectric properties to the gas sensing proof of principle experiment using cantilevers resonators actuated and detected piezoelectrically by the mean of these 50 nm thick AlN films. We also have covered the theoretical analysis for sensing performance optimization of these devices and their read-out and control electronic circuits.

This dissertation is structured in four main chapters:

- **Chapter 1** serves as an introduction to the field of gas chemo-sensor based on micro/nano technologies. First, we define figures of merit that can be used to compare the performances of the different gas chemo sensor technologies and present an overview of these technologies. Then, we focus on resonant MEMS based gas chemo-sensors and further develop the analytical modeling of their gas sensing performance. This model can be used to compare the gas sensing

performance of the different type of resonators and will be reused extensively all along this dissertation for design optimization and interpretation of experimental results.

- **Chapter 2** is dedicated to piezoelectric cantilever resonant sensors state of the art, modeling and design optimization. A bibliography review of the different type of transduction techniques commonly encountered in MEMS resonator is exposed first in order to justify our choice towards the piezoelectric transduction. Then, we focus on this technique and present the state of the art of its implementation in piezoelectric cantilever resonators. We establish the analytical formula of the input/output electro-mechanical relationship describing the resonance behavior of a piezoelectric cantilever; and, finally, combine this later model with the one for gas sensing performance of the first chapter in order to look for the optimum cantilever design.
- **Chapter 3** presents the fabrication processes and electrical characterization methods developed in this PhD. Based on the conclusion of the design optimization study, two types of devices have been fabricated: large surface area ultra-thin micro-cantilevers and arrays of nano-cantilevers. Both designs rely on the development of the deposition process of 50 nm thick Aluminum Nitride (AlN) films with high piezoelectric properties (beyond the state of the art).
- **Chapter 4** is dedicated to the demonstration of the high gas sensing performance of our piezoelectric micro-cantilever resonators. To that mean, we will present first our experimental efforts to characterize the frequency stability of such devices and then the results of Di-Methyl-Methyl Phosphonate (DMMP) vapor sensing experiments using a complete gas sensing setup including our devices and their detection and control electronic.

In the Conclusion, we will summarize the presented results, evaluate to which extend the objective of this PhD have been reached and propose future research directions for continuing this work. Finally, Appendix A clusters the details of the bibliographic references used in the dissertation and Appendix B presents our results with Finite Element Modelling (FEM) of piezoelectric cantilevers resonators.

# Chapter 1: Micro technology based gas chemo sensors.

---

**G**as chemo-sensors based on micro / nano technologies have encountered a great success over the last two decade for the development of miniaturized, low cost and high performances gas sensing systems. In this chapter, we intend to give an overview of the different gas chemo sensor technologies and of the Figures Of Merit (FOM) that characterize their gas sensing performances. We will also focus on a particular class of gas chemo-sensor to which belong the devices we have developed during this PhD and which are based on micro/nano mechanical resonators. We will further develop the analytical modeling of their gas sensing performances and compare accordingly the different type of resonator that can be encountered in the literature. This analytical model is at one of the main thrust of this PhD work and will be extensively reused in the next chapters for design optimization and experimental results interpretations.

## 1.1. Micro / Nano Gas chemo-sensors

### 1.1.1. Figures of merit

As stated in the General Introduction, a gas chemo sensor is a device that detects the presence of one or a small set of gaseous analytes and provides an electrical signal proportional to their concentration. To perform this task a gas chemo sensor must include at least two transduction stages: the so-called chemical and physical transductions (*cf.* Figure 0- 2). For optimal operation, a gas chemo-sensor should fulfill many requirements related to the purposes, locations, and conditions of use of the sensor. Sensing performances such as the sensitivity, resolution, dynamic range, selectivity, stability and response time constitute the primary requirements. These are all linked to the sensor design and constitute pertinent Figures Of Merit (FOM). Therefore, they will play a major role in this dissertation and we shall define them mathematically in the following. Second requirements such as continuous operation, power consumption, price, size, and packaging type must not be disregarded as they are equally critical for the commercialization of a sensor. However they come at a later stage of a new sensor development and thus we will not consider here.

- Sensitivity

The sensitivity  $\mathbb{S}$  is defined as the variation of the output signal  $s$  (electrical) for an arbitrarily small variation of the input signal  $c$  (concentration) [37] :

$$\mathbb{S} = \lim_{\Delta c \rightarrow 0} \frac{\Delta s}{\Delta c} = \frac{\partial s}{\partial c} \quad (1.1-1)$$

Assuming linear operation, the sensitivity can be written as the product of the sensitivities of the successive transduction stages, like the gain of cascaded electronic amplifiers [38]. Referring to Figure 0- 2, we may define the chemical and physical sensitivities,  $\mathbb{S}_\chi$  and  $\mathbb{S}_\phi$  respectively, as:

$$\begin{aligned}
 S &= S_\chi \times S_\Phi \\
 S_\chi &= \lim_{\Delta c \rightarrow 0} \frac{\Delta r}{\Delta c} = \frac{\partial r}{\partial c} \\
 S_\Phi &= \lim_{\Delta u \rightarrow 0} \frac{\Delta s}{\Delta r} = \frac{\partial s}{\partial r}
 \end{aligned} \tag{1.1-2}$$

Where  $r$  is the surface physical quantity modified by the adsorption of the targeted molecules and measured by the physical transducer.

- Resolution

The resolution is defined as the minimum measurable variation of the input signal [39][40]. For a linear sensor, it is also assimilated to the smallest measurable input signal variation and called Limit Of Detection (LOD). This FOM is set by the magnitude of noise on the output signal and can be estimated by the ratio  $\frac{\sigma_s}{S}$ ,  $\sigma_s$  being the standard deviation of the output signal:

$$\delta c_{min} \approx \frac{\sigma_s}{S} = S^{-1} \left( \lim_{T \rightarrow +\infty} \left[ \frac{1}{T} \int_{-T}^T |s(t) - \bar{s}|^2 dt \right] \right)^{1/2} \tag{1.1-3}$$

where  $\bar{s} = \lim_{T \rightarrow +\infty} \left[ \frac{1}{T} \int_{-T}^T s(t) dt \right]$  is the output signal average value. In practice, the measurement of  $\sigma_s$  rely on statistical estimators calculated on a finite time interval and on output signal values separated in time by a (constant) sampling period  $T_s$ . This introduces the notion of measurement bandwidth ( $BW_{meas} = \left[ -\frac{2}{T_s}, \frac{2}{T_s} \right]$ ) over which the total noise power is spread and the notion of integration time that defines the noise bandwidth of interest. In the literature, it is often assumed that higher sensitivity sensors provide higher resolution. We will demonstrate later that this is not true as  $\sigma_s$  and  $S$  are actually interdependent.

- Dynamic range

The Dynamic Range (DR) is defined as the ratio between the highest and lowest measurable concentration (LOD). The highest measurable concentration corresponds to the concentration above which the response becomes non-linear. This non-linearity can be related to saturation phenomena, for example when all the adsorption sites on the sensor surface are occupied, or to higher order terms in the

sensor constitutive equation. In general, a sensor DR is defined on several orders of magnitudes and given in dB:

$$DR = 20 \log \left( \frac{\delta c_{max}}{\delta c_{min}} \right) \quad (1.1-4)$$

- Selectivity

The selectivity  $Q$  of a chemo-sensor is defined as the ratio between its sensitivities with respect to two different chemicals [41] and is often expressed as a percentage:

$$Q(\%) = 100 \frac{S_{a1}}{S_{a2}} \quad (1.1-5)$$

It depends almost exclusively on the sensor surface chemical properties and a great deal of work has been dedicated to the development of always more selective chemical coatings [42][43][44][45][46].

- Stability

The stability [41] of a chemo-sensor defines its ability to perform several identical measurements at different times with the same output. Three phenomena are usually considered for this figure of merit: variation of ambient conditions [47] (Temperature, hygrometry... time scale ~ 1hour), aging [48] (time scale ~ year) and reversibility [49] towards the measured chemical. If these effects can be modeled, the output signal can be corrected electronically. In other cases, a dummy device that undergoes the same perturbations as the sensors but protected against the surrounding gas can be used to set up differential measurements.

- Response time

The response or recovery time [41] corresponds to the time taken by the sensor output to reach 90% of its saturation value after switching on (*on time*) or off (*off time*) the exposition of the sensor to the targeted gas. In ideal cases, this FOM is set by the kinetic of the adsorption / diffusion of the gaseous analyte onto the sensor surface. However, it might also be influenced by the physical transduction, especially in the case of thermal transduction, and more frequently by the volume of gas chamber that include the sensors. This is why scientists have put large efforts into the design of specific sensor packages with reduced volume [50][51].

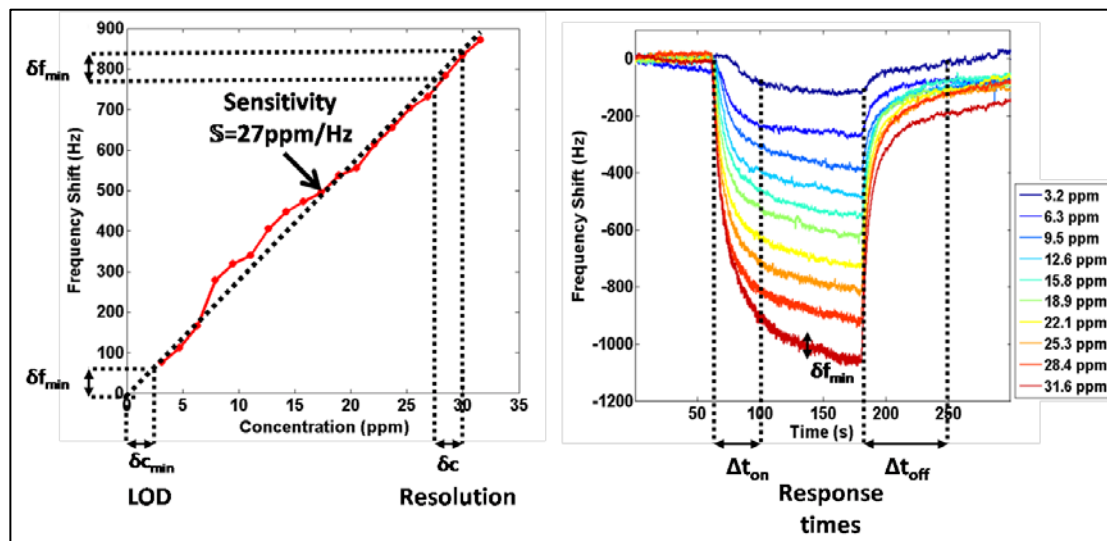


**Figure 1- 1:** Gas sensor characteristic curves and FOM. The figures are reproduced and modified from [52] where the gas chemo-sensor is based on a Capacitive Membrane Ultrasonic Transducer (CMUT) coated with poly-isobutylene (PIB)

### 1.1.2. Chemical functionalization

The optimization of the chemical transduction, despite its tremendous importance, is out of the scope of this dissertation: we focus rather on the physical transduction (piezoelectric cantilever). Therefore, we present here only the few important results that are necessary to understand the rest of the dissertation.

Functionalization layers can be categorized according to their chemical nature: polymers [53], Self Assembly Monolayers (SAM) [54], functionalized carbon nanotubes [55][56] or inorganic films. Polymer coatings offer the greatest variety of functional groups (and thus of chemical affinities), the possibility to engineer their properties at will and a certain ease of processing. This is why they are the most widely spread functionalization layer in the literature. The different techniques for polymeric functionalization are dip coating [57], drop coating [58], ink-jet printing [59], plume deposition [60], grafting (electro- [61] or photo- [62]) and *in-situ* growth.

Self Assembled Monolayers have attracted a certain attention because of their comparable diversity of functional groups with respect to polymer coatings, the

consistency of their surface properties and their high stability under ambient condition. In addition, SAM offer the unique possibility to grow them at defined locations on devices surface using evaporation [63] or electrochemistry [64]. This is particularly advantageous because it allows the fabrication of several gas chemo-sensors with different sensing properties on the same substrate.

Functionalized carbon nanotubes have also been considered recently. They also offer a large diversity of available functional groups, but their main advantage relies on their very high surface over volume ratio that increases the number of adsorption sites at constant functionalization layer volume.

Finally, inorganic films which are much less reported in the literature, present the main advantage of being the most stable functionalization layer compare to carbon based coating (especially at high temperature). Controlling their surface properties can be sometimes cumbersome but they can offer also a higher surface over volume ratio (porous layer). The main deposition techniques are sputtering [65] or evaporation [66] that are now standard and compatible with CMOS process.

Regardless of the type of functionalization layer, the adsorption process can be represented as a complex, so-called *AS*, formation reaction between the targeted gas molecule  $A_{gas}$ , and an adsorption site *S* at the surface of the sensor:



In order to ensure the reversibility of this reaction and thus of the sensor operations, the complex interaction energy  $E_{AS}$  must not exceed 30 kJ. mol<sup>-1</sup>, below chemical bounds energies (40~400 kJ. mol<sup>-1</sup>). This is why adsorption process in gas chemo-sensors are often referred to physisorption as opposed to chemisorption [67] where chemical bounds are established. As a consequence, available solid / gas chemical interactions rely on a restricted number of inter-molecular interactions [44]. Unavoidably, this limits the selectivity of gas chemo-sensors and the extent of information that can be retrieved from the sensor response. More precisely, it has been demonstrated that beyond 6 to 8 different functionalization layers in an array of identical gas chemo-sensors, no additional information on the chemical nature of surrounding gas can be obtained [68][69].

At equilibrium, the mass of adsorbed target analyte in the functionalization layer  $m_g$  is given by:

$$m_g = \rho_g K V_{AS} C_g \quad (1.1-6)$$

where  $\rho_g$ ,  $K$ ,  $V_{AS}$  and  $C_g$  are the gas density of the targeted analyte, the partition coefficient of the couple analyte / functionalization layer that is defined as the ratio of the concentrations of the targeted analyte in the gaseous and the adsorbed phases, the volume of the functionalization layer and the concentration of the targeted analyte, respectively.

Therefore, the partition coefficient and the thickness of the functionalization layer are the two free design parameters for the chemical transduction performances optimization. The lateral dimensions that, along with the thickness, defines the volume of the functionalization layer defines also the whole device design. Using a model called Linear Solvation Energy Relationships [53], it is possible to relate  $K_s$  to different thermodynamic potentials that take into account the solubility, the polarizability, the dipolarity, and hydrogen bond acidity and basicity of the analyte / functionalization layer couple in order to predict and/or engineer the interaction. However, this semi-empiric method has a limited validity as it does not account for the diffusion process or the influence of other analytes in the gas. In the following, we will rely on experimental values of the partition coefficient reported in the literature with values between  $10^2$  and  $10^7$ .

### **1.1.3. Physical transducers overview**

Energy domains are the simplest criteria for categorizing gas chemo-sensors physical transducers and four families can be distinguished: electro-chemical, thermal, optical and mechanical. We will follow this classification and give an overview of the main chemo sensor based on micro/nano technologies.

### 1.1.3.1. Electro-chemical transducers

Gas chemo-sensors based on electrochemistry constitute the most widespread family with, for instance, 500 000 Figaro CMD4160 sensors (*cf.* Figure 0- 1) sold every year. For this type of sensors, the electrical properties of the sensor surface are modified upon the adsorption of the targeted molecules leading to the apparition of an electrical potential (potentiometry) or a current (amperometry) or a modification of the conductivity (conductimetry).

- Semiconducting Metal-Oxide (MOX)

MOX are the most common electrochemical gas sensors. They belong to the conductimetry sub-family [70][71][72]. For n-type sensors based on ZnO<sub>2</sub>, SiO<sub>2</sub> or SnO<sub>2</sub> the exposure to an oxidizing (reducing) gas such as O<sub>2</sub> or NO<sub>2</sub> (H<sub>2</sub>, CH<sub>4</sub> or CO) induces an increase (decrease) of the material resistivity due to the increase (decrease) of the depletion length (*cf.* Figure 1- 2). P-type sensors based on NiO or Co<sub>3</sub>O<sub>4</sub> work reversely and can address the same targeted gases. The success of MOS sensors is due to their low price, very high stability and long lifetime. However the resolution figure obtained with this technology is rather low in the range of 1 part per million (ppm)[73] even though recent introduction of nano-structured material is expected to improve greatly the performances [74][75][76].

- Field Effect Transistors (ChemFET)

ChemFETs [9] are based on the well known Field Effect Transistor architecture with a gate controlling the charge carrier density of a conduction channel between the source and the drain. Two types of operation principle can be encountered based either on potentiometry or either on conductimetry.

For potentiometric ChemFETs, the gate is exposed to the surrounding gas. Its surface potential is modified by the adsorption of targeted gas molecules that modulates the density of carriers in the channel. The gate material can be a catalytic metal such as Pt or Pd [77], a metal oxide [78] or a conductive polymer [79].

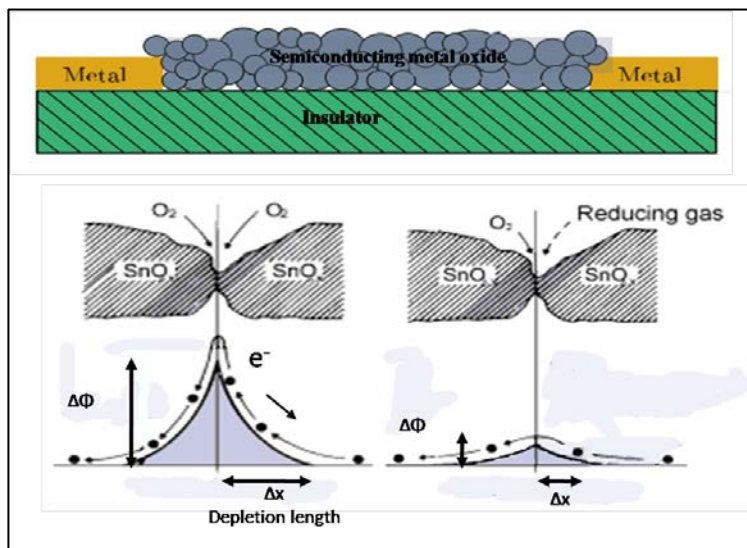


**Figure 1- 2:** Schematic and working principle of a Metal-Oxide gas sensor. In presence of a reducing gas the energy barrier and the depletion layer at two grains boundary is reduced leading to a lower resistivity of the film.

In conductimetric ChemFETs, the channel is exposed to the gaseous environment and its charge carrier density is directly varied by the adsorption of the targeted gas molecules depending on their RedOx activity. In this case, the channel material can be a metal oxide semiconductor [70] or an organic semiconductor [80] or a conductive polymer [79]. Both types of ChemFET provide a resolution and sensitivity comparable to MOS sensors but present the advantage of being sensitive to a much greater number of gas molecules with the possibility to tailor their selectivity. Using semiconductors such as SiC and Ga, they also enable high temperature operation, which makes them ideal candidates for many hostile industrial environment applications [9].

- Conductive Polymer (CP) and Intrinsically Conducting Polymer (ICP)

CP [79][81] and ICP [81] have benefited from the development of organic electronic over the last two decades. Although electronic transport in such material is not yet fully understood, several mechanisms can be exploited for gas sensing such as carriers density variation or modification of the percolation path. The main advantage of CP and ICP sensors is the large number of available materials with different cross-sensitivities and with resolutions in the range of 100 ppb [81][82]. Besides, CP or ICP sensors can be fabricated at very low price and on flexible substrate using ink-jet

printing techniques. The major drawbacks of these sensors are a poor stability and lifetime as a majority of polymers oxidize in air.

- Nano Electro-chemical gas chemo-sensors

These last years, several articles on nano Chemo-resistors or nano ChemFET with carbon nanotubes [83][84][85] (*c.f.* Figure 1- 3(a)), semiconducting nanowires [86][87], or graphene sheets [88] (*c.f.* Figure 1- 3(b)), have been published. Thanks to their miniature size, these sensors achieve the highest level of resolution in the literature: the single molecule resolution is claimed in [88]. More generally, resolution figures in the order of 1 ppb [89] seem readily accessible. In addition, these devices can be easily functionalized and present a very high volume to surface ratio that further enhances their sensitivity. However, reported results show very poor recovery of the sensor response after exposure to the gas sample. This is typical of sensors with low stability and reproducibility. Further developments are thus necessary before proceeding to real life application. One noticeable advance in this sense has been achieved for carbon nanotubes networks based devices that are already marketed for medical applications [90].

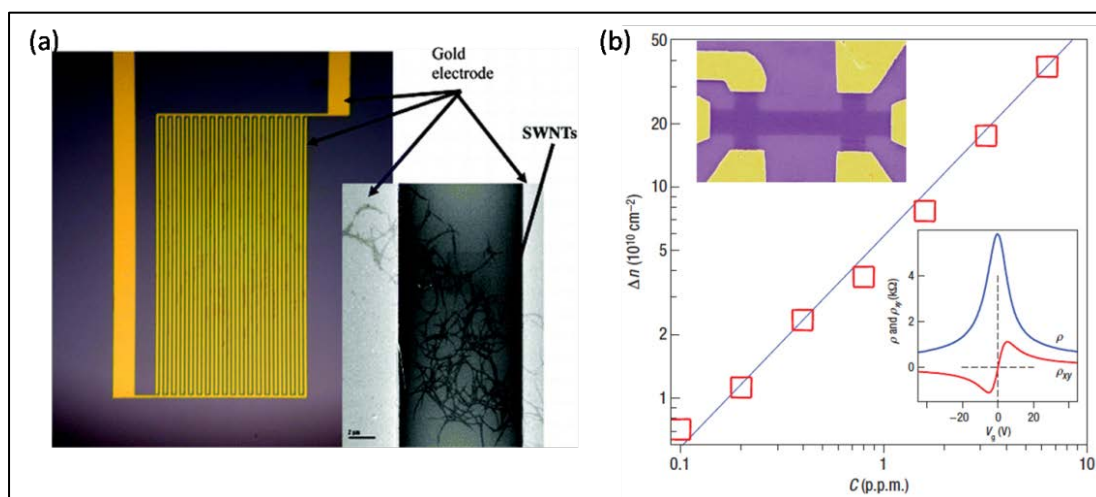


**Figure 1- 3:** Example of (a) Single Wall Carbon Nanotubes and (b) Graphene based gas sensor. Images reproduced from [85] and [88]

### 1.1.3.2. Thermal transducers

Thermal chemo-sensors are divided into two distinct classes: calorimetric sensors that rely on heat exchange during a chemical reaction happening at the surface of the sensor; and Thermal Conductivity Detectors (TCD) that are sensitive to variations of the thermal conductivity of the surrounding gas.

Calorimetric sensors are also divided into Pellistors [91] in which heat is measured through the variations of electrical conductivity of a Pd or Pt resistor, and thermopiles [92] where heat is directly converted into a voltage signal using the Seebeck effect (thermo-couple). The typical resolution of these devices lies in the 1 ppm range [93][94] and due to their non constant temperature during operation their stability and dynamic range is limited. This is why these sensors are almost exclusively reserved for combustible gas detection where highly exothermic reactions can be exploited.

The most widespread TCD architecture [4] includes a Joule heated resistance (W or Pt or Pd) whose equilibrium temperature is fixed by thermal exchanges with the surrounding gas. When exposed to a gas mixture different from a neutral carrier gas (base line response), the cooling of the resistor becomes less (more) efficient, its temperature increases (decreases) and its electrical conductivity drops (rise). The main characteristic of TCDs is their complete un-specificity toward the chemical nature of analytes. But, rather than a drawback, and because of their high sensitivity and stability, they have become the most widespread gas chemo-sensors in GC systems. Beside, thanks to the development of micro GC systems (*c.f.* Figure 1- 4) in the recent years, high performance micro TCDs represent an active research area, resolution down to 100 ppb have been reached [95][96].

### 1.1.3.3. Optical transducers

Micro/Nano optical gas chemo-sensors have been tied to the development of optical fibers in the last thirty years. The first optical fibers based sensors were based on spectroscopy (transmission, fluorescence or Raman) but the difficulty to integrate several light sources or broad-spectrum light sources have limited their integrability. Recently, Surface Plasmon Resonance (SPR) [97] and Photonic Crystal (PR) [98]

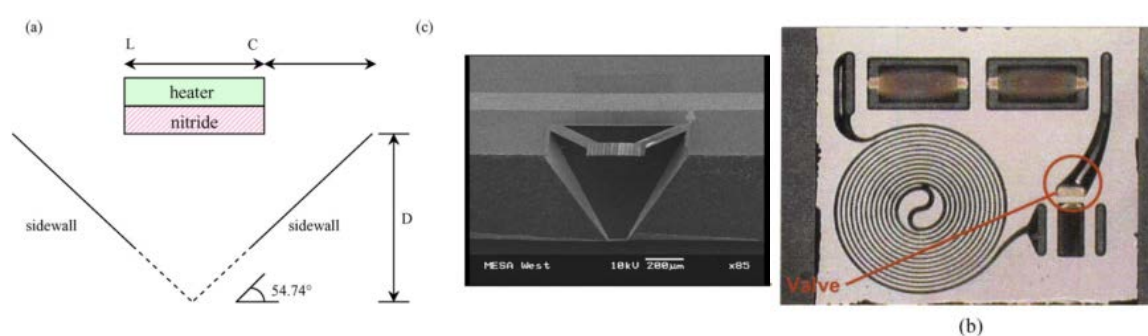


**Figure 1- 4:** Cross sectional and SEM view of a  $\mu$ -TCD detector of the  $\mu$ -ChemLab™. Optical view of the fluidic part of the  $\mu$ -ChemLab™ containing the pumps, the micro-GC and the  $\mu$ -TCD detector. Images reproduced from [95]

optical fibers with integrated LED light sources have shown promising results for gas detections [99]. In both embodiments, the presence of the gaseous analyte is detected through the variations of the optical index of the cladding the fiber. This phenomenon, though highly non linear, is well understood and can be measured with extreme precision, leading to resolution level in the ppb range [97].

#### 1.1.3.4. Mechanical transducers

Mechanical gas chemo-sensors can operate in static or dynamic modes. Dynamic or resonant chemo sensors will be the focus of the next chapter. In static mode, they are usually based on micro beams (cantilevers or bridges) [100][101][102][103] and are sensitive to the mechanical stress induced by the adsorption of the targeted molecule through the induced bending of the structure (*c.f.* Figure 1- 5). This mechanical stress can be caused by the volume expansion of the functionalization layer [104] or by the mechanical interaction between the adsorbed molecules [102]. The detection of the deformation can be based on piezoresistive [100], electrostatic, piezoelectric [103] or optical transduction. Using this type of devices, high performance has been achieved with, for instance, the detection of 1 ppb of DMMP with a silicon cantilever [61]. However, only a small number of functionalization layers with the appropriate properties (sufficient selectivity and mechanical stress build-up) have been identified so far. Therefore these sensors are limited only to a small set of analytes.

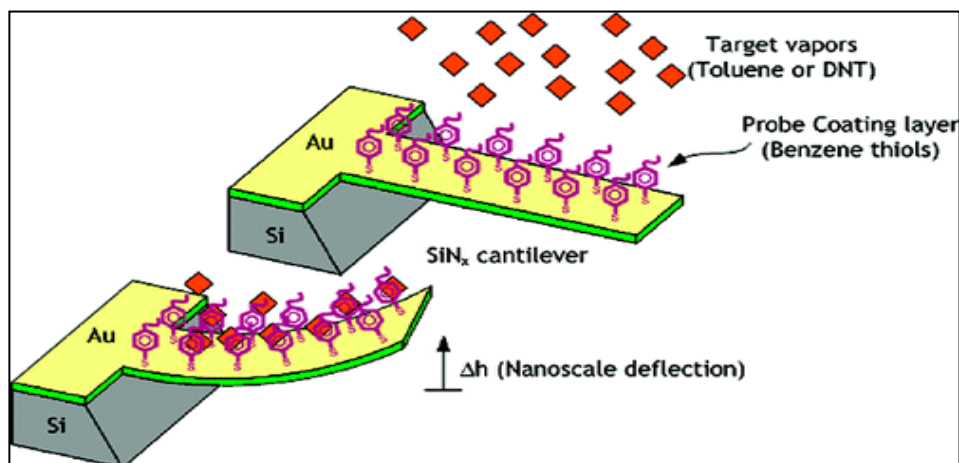


**Figure 1- 5:** Principle of operation of a Toluene of Di Nitro Toluene (DNT) static gas sensor. Upon the adsorption of the targeted molecules, the benzene thiols polarize and start attracting each other, creating a compressive surface stress that bends the cantilever. Image reproduced from [105]

## 1.2. Gravimetric sensors

### 1.2.1. Working principle and architecture

Basically, dynamic mode (or resonant) mechanical chemo sensors are mechanical resonators with one (or several) resonance frequency (ies) that depend(s) on stiffness over mass ratio [106]. Thus, as the adsorption of targeted gas molecules changes the functionalization layer mass density (or stress), it is possible to monitor the amount of adsorbed gas molecules by following the variation of the resonance frequency (*cf* Figure 1- 6).

Figure 1- 7 presents the general architecture of a gravimetric gas chemo sensor from the point of view of automation theory. For continuous operation, the resonator is included in an electronic circuit that implements a frequency feedback loop maintaining the frequency of the actuation signal equal to the (variable) resonance frequency of the resonator. Two feedback topologies are most often used in the literature: the self oscillating loop (represented in Figure 1- 7) and the Phase Locked Loop (PLL). We will describe them in more details in section 2.3.2.

The mechanical resonator is represented in Figure 1- 7 as a 3-ports device: actuation / detection and perturbation ports. At the actuation port the input electric

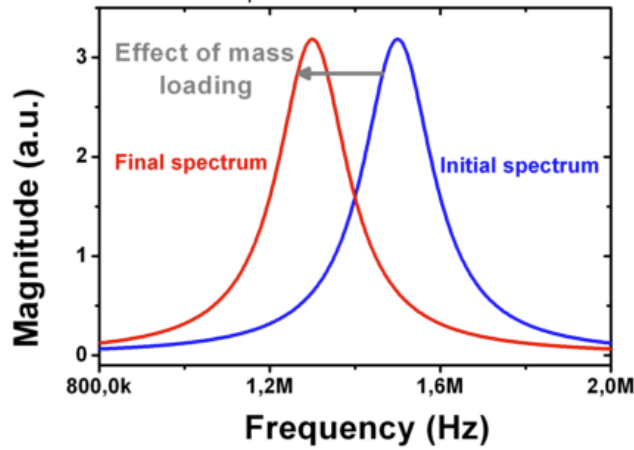


**Figure 1- 6:** Principle of operation of a resonant gas chemo-sensor or gravimetric sensor. Image reproduce from [106]

signal is transduced into a force signal through the transduction gain  $K_a$  (in  $N.V^{-1}$ ) while the displacement of the resonator is converted into an electrical signal at the detection port through the gain  $K_d$  (in  $V.m^{-1}$ ). The perturbation port implements the sensing function of the resonator. It is composed by the chemical transduction that converts the chemical signal into the added mass signal and by the gravimetric (physical) transduction that converts the added mass signal into a resonance frequency shift signal, represented by the gravimetric sensitivity  $S_g$ . As a first order approximation and in the vicinity of a chosen resonance frequency  $\omega_0$ , the mechanical resonator can be modeled as a first order mass + string +damper system with a mechanical transfer function  $H_R(\omega)$  (in  $m.N^{-1}$ ) given by:

$$H_R(\omega) = \frac{w}{F} = \frac{H_0}{1 + j \frac{\omega}{\omega_0 Q} - \left(\frac{\omega}{\omega_0}\right)^2} \quad (1.2-1)$$

where  $w$  and  $F$  are the output displacement and the input excitation force and  $H_0$ ,  $\omega_0$  and  $Q$  the static mechanical gain, the resonance frequency and quality factor, respectively. The resonance frequency  $\omega_0$  can be further related to the resonator effective mass  $M_{eff}$  and spring constant  $k_{eff}$ , as defined in [107], of the resonator:

$$\omega_0 = \sqrt{\frac{k_{eff}}{M_{eff}}} \quad (1.2-2)$$

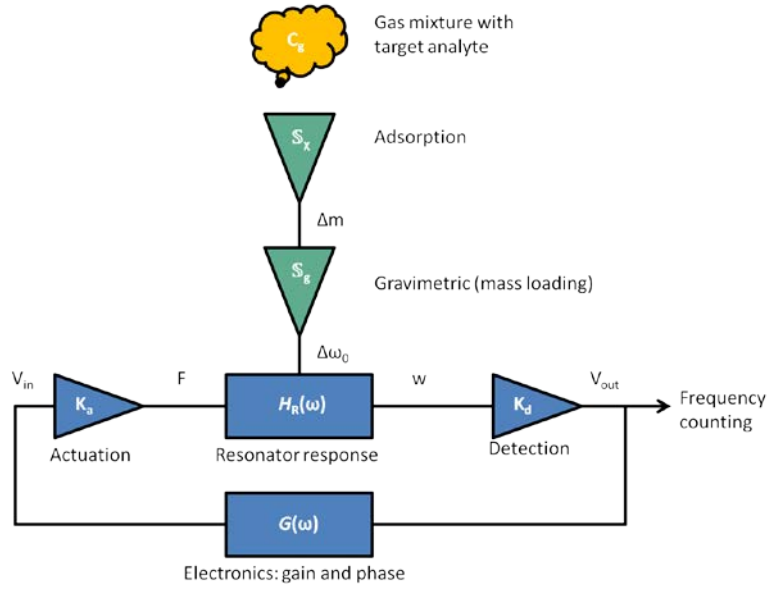


**Figure 1-7:** General architecture of a gravimetric sensor. The mechanical resonator is represented as a 3-ports system: actuation port (electrical signal  $\rightarrow$  force), gravimetric port (mass  $\rightarrow$  frequency shift transduction) and detection port (displacement  $\rightarrow$  electrical). Figure reproduced from [106]

This last equation (1.2-2) can be used to derive an analytical expression of gravimetric sensors sensitivity provided that the concept of the effective mass is exploited with the proper assumptions. For gas sensing application, and according to the model presented in section 1.1.2, we assume that the added mass of gas molecules  $m_g$  is negligible in front of the total mass of the device  $M_{tot}$  and is uniformly adsorbed on the resonator surface. In this framework, the effective mass increase related to the adsorption can be written very simply as  $\delta M_{eff} = \frac{M_{eff}}{M_{tot}} m_g$ . Consequently, the resonance frequency is shifted downward by an amount  $\delta\omega_0$  that can be derived as:

$$\begin{aligned}
 \omega_0 + \delta\omega_0 &= \sqrt{\frac{k_{eff}}{M_{eff} + \delta M_{eff}}} \\
 &= \sqrt{\frac{k_{eff}}{M_{eff}} \left(1 + \frac{m_g}{M_{tot}}\right)^{-\frac{1}{2}}} \\
 &\approx \omega_0 \left(1 - \frac{m_g}{2M_{tot}}\right)
 \end{aligned} \tag{1.2-3}$$

Thus a general expression for the gravimetric sensitivity  $S_g$  is given by:

$$S_g = \frac{\partial \omega_0}{\partial m_g} \approx -\frac{\omega_0}{2M_{tot}} \quad (1.2-4)$$

This equation (1.2-4) is often invoked in articles [37][108][109] to support the idea that smaller resonators provide better gas performances. Indeed, for an homothetic decrease of the device dimension by a factor  $1/\lambda$ , the total mass of the device decreases by a factor  $1/\lambda^3$  and the resonance frequency increases by a factor up to  $\lambda$  (*cf* section 1.2.2). Thus the sensitivity increases by a factor  $\lambda^4$  ! If it is true for the mass sensitivity, we shall demonstrate later this is not necessarily true for gas concentration sensitivity. Indeed, for gas sensing applications shrinking the device dimensions shrinks also the capture area and thus the accreted mass. In short, the sensor becomes more sensitive to added mass but less capable of absorbing gas molecules.

In order to understand what trade-off can be met and optimize the sensitivity and the resolution at the same time, a more precise expression of the resonance frequency is required compared to equation (1.2-2). However this expression depends on the type of the resonator. We shall thus present the main resonator families and their corresponding resonance frequency formula.

### 1.2.2. Mechanical resonators

- Bulk Acoustic Wave (BAW)

BAW resonators consist in a piezoelectric material sandwiched between two metallic electrodes in which a longitudinal or shear acoustic wave propagates [110]. In the case of longitudinal waves, the resonance frequency is given by:

$$f_0 = \frac{1}{2t} \sqrt{\frac{c_{33}^D}{\rho}} \quad (1.2-5)$$

where  $t$ ,  $c_{33}^D$  and  $\rho$  are the thickness of the piezoelectric layer, the elastic constant and the mass density, respectively.

Quartz Cristal Microbalances (QCM), that are already marketed, are the first representatives of this class of gravimetric sensors. They usually operate at frequencies lower than 100 MHz. To improve the sensitivity, Film Bulk Acoustic Resonators (FBAR) with thinner piezoelectric films have been developed recently. Two main architectures can be encountered: suspended membranes [111] or Solid Mounted Resonators (SMR) fixed on an acoustic Bragg mirror [112]. With these devices, resonance frequencies in the GHz range are readily available.

- Surface Acoustic Wave (SAW)

Several types of surface acoustic waves can be generated at the free surface of a piezoelectric material using Inter-Digitated Transducers (IDT): Rayleigh (R), Shear Horizontal Acoustic Plate Modes (SH-APM), Surface Transverse (STW), and Love waves. For all these modes, the resonance frequency is given by:

$$f_0 = \frac{v}{\lambda} \quad (1.2-6)$$

where  $v$  and  $\lambda$  are the velocity of the considered surface acoustic wave and IDT period respectively. As demonstrated in [68][113] and [10] the mass loading effect in SAW resonator results in a decrease of the acoustic velocity, which in turns changes the resonance frequency of the device. The most widespread SAW resonator design consists in one IDT and a metallic reflector separated by few wavelengths such that the acoustic waves travel back and forth. SAW resonators provide, in addition, a possible coupling with RF antenna for remote sensing [10] (*c.f.* Figure 1- 8).

- Lamb Wave Resonator (LWR) and Contour Mode Resonator (CMR)

LWR and CMR share several similitudes with BAW resonators as they are based on the same general equation of vibration. However they do not necessarily include a piezoelectric material for the transductions [114]. They are based on suspended structures such as plates, disks or rings and exploit fundamental acoustic modes with significant contour displacements such as breathing [56] or Lamé modes [115]. The main advantage of these devices relies on the easily accessible high quality factor value in the  $10^3 - 10^5$  range in air, which makes them the best mechanical

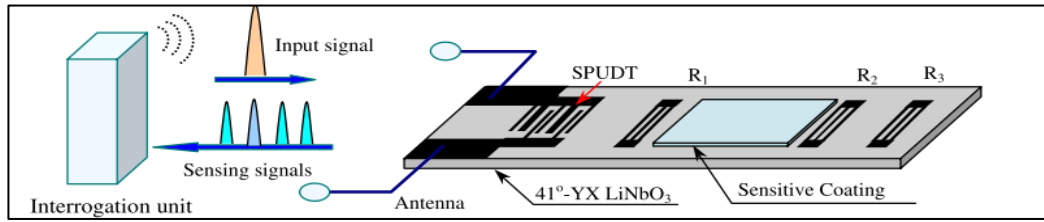


**Figure 1- 8:** Schematic of a wireless SAW sensor. The electromagnetic signal is transformed into a surface acoustic wave thanks to the Single Phase Unidirectional Transducer (SPUDT). Note that the substrate is piezoelectric ( $\text{LiNbO}_3$ ). Once generated, the acoustic signal reflects on three acoustic reflectors  $R_1$ ,  $R_2$  and  $R_3$  before being transduced back into electromagnetic waves. The delay between the different “echoes” depends on the mass loading in the sensitive coating. Figure reproduced from [10].

resonators according to the figure of merit  $Q \times f_0$ . For a square plate in Lamé mode, the resonance frequency is given by:

$$f_0 = \frac{1}{2\pi W} \sqrt{\frac{Y}{\rho(1-\nu)}} \quad (1.2-7)$$

where  $W$ ,  $Y$ ,  $\nu$  and  $\rho$  are the width of the plate, the Young Modulus, the Poisson ratio and the density of the resonator material. Another advantage of these resonators is the dependency of the resonance frequency on the planar dimensions only. This allows to fabricate resonators with different frequencies on the same substrate (impossible, for instance, for a BAW fabrication process with only one piezoelectric material layer deposition step) and, more importantly for sensing operations, to engineer mass sensitivity (set by the thickness) and operation frequency (set by the planar dimensions) independently [116].

- Flexural Mode resonators (FMR)

FMR have encountered a great success in the last decade for gravimetric sensing. The most ubiquitous devices are cantilevers flexural resonators whose resonance frequency is given by:

$$f_0 = \frac{1}{2\pi} \sqrt{\frac{EI}{\rho S}} \left(\frac{\alpha}{L}\right)^2 \quad (1.2-8)$$

where  $E$ ,  $I = \frac{Wt^3}{12}$ ,  $\rho$ ,  $S = Wt$ ,  $\alpha$ ,  $t$ ,  $W$  and  $L$  are the Young's modulus, the second moment of area, the mass density, the cross section surface area, the mode constant and the thickness, the width and the length of the cantilever respectively. Suspended membranes have also achieved high performance such as Capacitive Micro-machined Ultrasonic Transducer (CMUT) [52] (*c.f.* Figure 1- 9), which can be integrated in large arrays architecture with improved Signal Over Noise ratio and thus higher concentration resolution.

### 1.2.3. Performance modeling

#### 1.2.3.1. Sensitivity

The comparison of the gravimetric sensing performance between the different micro-resonators presented in the previous section has been largely debated [37][108][109]. Here we concentrate on a special case of gas sensing where the accreted mass is uniformly spread over the sensor surface. As we will see, this hypothesis leads to a common theoretical formula for the sensitivity and resolution for all the different types of resonators; and to some counter-intuitive conclusions.

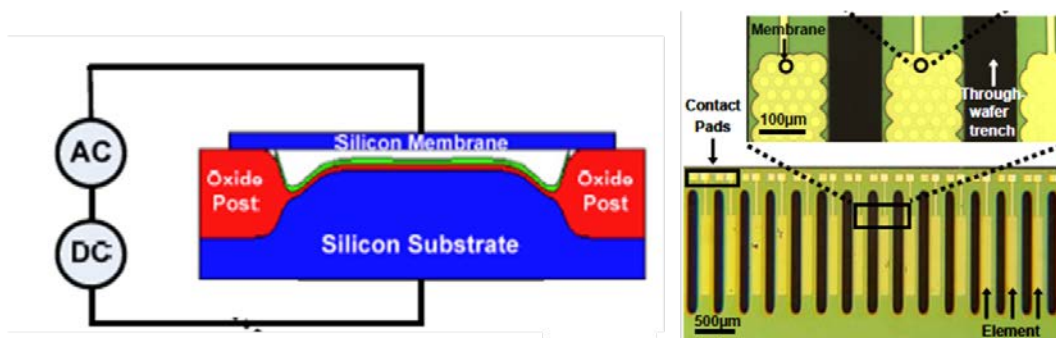


**Figure 1- 9:** (a) Schematics of a Capacitive Membrane Ultrasonic Transducer (CMUT) (b) integration of CMUT in collectively addressed array. Image reproduced from [52]

To begin with, we shall remark that the resonance frequencies of the different types of resonators are spread over not less than five decades. It is clear that measuring a resonance frequency shift of 1 Hz when  $f_0 = 100$  kHz is much easier than when  $f_0 = 1$  GHz. This is why, it is more convenient to think in terms of relative resonant frequency shift  $\Delta f_0/f_0$ . Using equation (1.1-1), the sensitivity of the gas chemo-sensor is given by:

$$S = \frac{\partial}{\partial c} \left( \frac{\Delta f_0}{f_0} \right) \quad (1.2-9)$$

which can be rewritten according to equation (1.1-2) and (1.1-6), as:

$$\begin{aligned} S &= \left( \frac{\partial \Delta m_{tot}}{\partial c} \right) \left( \frac{\partial}{\partial \Delta m_{tot}} \left( \frac{\Delta f_0}{f_0} \right) \right) \\ &= K \rho V_f \left( \frac{\partial}{\partial \Delta m_{tot}} \left( \frac{\Delta f_0}{f_0} \right) \right) \\ &= K \rho t_f \left( \frac{\partial}{\partial \Delta m_s} \left( \frac{\Delta f_0}{f_0} \right) \right) \\ &= S_\chi S_\Phi \end{aligned} \quad (1.2-10)$$

where  $V_f$  and  $t_f$  are the volume and the thickness of the functionalization layer respectively.  $\Delta m_s = \frac{\Delta m_{tot}}{WL}$  is the added mass per unit of surface area of the sensor.

$S_\chi = K \rho_g t_f$  and  $S_\Phi = \left( \frac{\partial}{\partial \Delta m_s} \left( \frac{\Delta f_0}{f_0} \right) \right)$  are the chemical and physical transduction sensitivity respectively and as defined in equation (1.1-2) ( $S_\Phi$  will be referred from now on as the surface mass sensitivity). Using equations (1.2-5), (1.2-7) or (1.2-8),  $S_\Phi$  can be further derived for each type of resonator. As an example, we will consider the flexural cantilever case. Assuming that the total added mass  $\Delta m_{tot}$  is uniformly spread across the cantilever surface and that it remains small compared to the mass of the cantilever, the density of the cantilever per unit length  $\rho S$  in equation 1.2-8 must be replaced by  $\rho S + \frac{\Delta m_{tot}}{L}$  and the resonance frequency after mass loading by  $f_0 + \Delta f_0$ :

$$f_0 + \Delta f_0 = \frac{1}{2\pi} \sqrt{\frac{YI}{\rho S + \frac{\Delta m_{tot}}{L}}} \left( \frac{\alpha}{L} \right)^2 \quad (1.2-11)$$

$$\begin{aligned} &\approx \frac{1}{2\pi} \sqrt{\frac{YI}{\rho S}} \left(\frac{\alpha}{L}\right)^2 \left[1 - \frac{1}{2} \frac{\Delta m_{tot}}{\rho S L}\right] \\ &\approx f_0 \left[1 - \frac{1}{2} \frac{\Delta m_s}{\rho t}\right] \end{aligned}$$

Thus:

$$\mathbb{S}_\Phi = \frac{\partial}{\partial \Delta m_s} \left(\frac{\Delta f_0}{f_0}\right) = -\frac{1}{2} \frac{1}{\rho t} \quad (1.2-12)$$

Interestingly this last expression of the surface mass sensitivity is valid for all mentioned resonator families excepted SAW resonators for which  $\mathbb{S}_\Phi = \frac{K(\nu)}{\rho t}$ ,  $K(\nu)$  being a coefficient that depend only on the Poisson ratio and the acoustic mode only, as demonstrated in [113].

Thus, a first important conclusion is: due the tradeoff to be found between smaller volume (higher mass sensitivity) and larger capture surface area, the thickness of the resonator is the only design parameter whose decrease brings sensitivity gain. In other terms, changing the surface area of the sensors has no effect: the gain in sensitivity is exactly compensated by the loss in capture area. This conclusion is in accordance with reported results in the literature [117]. For instance, [118] and [58] demonstrate, experimentally, similar surface mass sensitivity with 100  $\mu\text{m}$  and 0.6  $\mu\text{m}$  long cantilevers respectively.

### 1.2.3.2. Resolution

To go a step further, and because the real challenge raised by emerging gas sensing applications concerns more the resolution than the sensitivity, we now turn the discussion towards the modeling of gravimetric sensor resolution. According to equation (1.1-3), in the case of gravimetric gas chemo-sensors, the resolution evaluated by the resonance frequency standard deviation  $\sigma_{f_0}$ . However, for the same reasons as before, the relative resonance frequency shift  $\left(\frac{\Delta f_0}{f_0}\right)$  is a more suitable output quantity for performance comparison. Therefore the concentration resolution is given by:

$$\delta c_{min} = \frac{1}{S_{\chi} S_{\Phi}} \left( \frac{\delta f_0}{f_0} \right)_{min} \quad (1.2-13)$$

where  $\left( \frac{\delta f_0}{f_0} \right)_{min}$  is the standard deviation of the relative resonance frequency shift signal  $\left( \frac{\Delta f_0}{f_0} \right)$ . As  $S_{\Phi}$  depends only on the functionalization / analyte couple (ie the chemical transduction), it is more also convenient (as far as the electromechanical part of the sensor is concerned) to concentrate on the so-called Surface Mass Limit of Detection (SMLOD)  $\delta m_{surf} = \frac{1}{S_{\Phi}} \left( \frac{\delta f_0}{f_0} \right)_{min}$  defined as the smallest measurable mass per surface area unit. This FOM is extremely important for the rest of this thesis. We will use it as a basis for the comparison of the intrinsic performances of resonant chemo-sensors, as well as the function to optimize in the design optimization study (*c.f.* section 2.3.3) Using equation (1.2-12) the SMLOD can be expressed as:

$$\delta m_{surf} = 2\rho t \left( \frac{\delta f_0}{f_0} \right)_{min} \quad (1.2-14)$$

Using Parseval theorem,  $\left( \frac{\delta f}{f_0} \right)_{min}$  can be calculated thanks to the relative frequency noise Power Spectral Density (PSD)  $S_{\delta f/f_0}(\omega)$  in the noise bandwidth  $BW$ :

$$\left( \frac{\delta f_0}{f_0} \right)_{min} = \left( \int_{BW} S_{\delta f/f_0}(\omega) d\omega \right)^{1/2} \quad (1.2-15)$$

The derivation of  $S_{\delta f/f_0}(\omega)$  and in a more general fashion the modeling of frequency noise represents a whole branch of today's research in physics, a good overview of the theory can be found in textbook such as [38] and the application of this theory for gravimetric sensor is largely developed in [39][119]. In this dissertation, we may assume that all noise sources are additive, stationary, white and Gaussian. Figure 1- 10 shows how to relate the frequency noise to the amplitude noise. The corresponding analytical formula is very important for the rest of the dissertation as it is at the core of the frequency noise modeling. It is referred in the literature as the Robins formula [120][39][119].

Figure 1- 10 (a) presents the typical representation of a noisy harmonic signal in the so-called phasor space [120] (for the sake of clarity, numerical values have been chosen for computation and plotting convenience). As already state the noise is assumed to be additive, stationary, white and Gaussian such that the noisy signal can be written as  $v(t) = V_0 \cos(2\pi f_r t) + n(t)$ ; where  $V_0$  and  $f_r$  are the amplitude and frequency of the noiseless carrier signal and  $n(t)$  is the random noise function. Each points (crosses) on Figure 1- 10 (a) represents the noisy harmonic signal at a particular time of observation. For each points, the abscissa coordinates is the so-called *in-phase* component of the signal and is defined as  $X_\tau(t) = \int_t^{t+\tau} v(s) \cos(2\pi f_c s) ds$ , while the ordinate coordinate is the so-called *quadratic* signal component defined as  $Y_\tau(t) = \int_t^{t+\tau} v(s) \sin(2\pi f_c s) ds$ . All the points are located inside a disc centered on the noiseless signal phasor with coordinates  $(V_0, 0)$  and with radius the rms amplitude of the noise  $\delta v_{noise} = \left( \lim_{t \rightarrow +\infty} \frac{1}{t} \int_{-t/2}^{t/2} n^2(t) dt \right)$ . In the limit of a high signal over noise ratio  $\left( \frac{V_0}{\delta v_{noise}} \gg 1 \right)$  The RMS phase noise amplitude  $\delta\phi$  of the noisy signal can then be calculated graphically:

$$\delta\phi = \arctan\left(\frac{\delta v_n}{V_{out}}\right) \approx \frac{\delta v_n}{V_{out}} \quad (1.2-16)$$

Using Figure 1- 10 (b) and assuming that the resonator operates in the linear regime of its phase response around its resonance frequency, the phase and frequency noise RMS amplitudes are related by:

$$\delta f / f_0 \approx \delta\phi / 2Q \quad (1.2-17)$$

Where  $Q$  is the quality factor of the resonator. The Robins formula follows directly:

$$\left(\frac{\delta f}{f_0}\right)_{min} = \frac{\langle V_{noise} \rangle}{2Q V_{out}} \quad (1.2-18)$$

And the SMLOD can be written as:

$$\delta m_{surf} = \frac{\rho t \langle V_{noise} \rangle}{Q V_{out}} \quad (1.2-19)$$

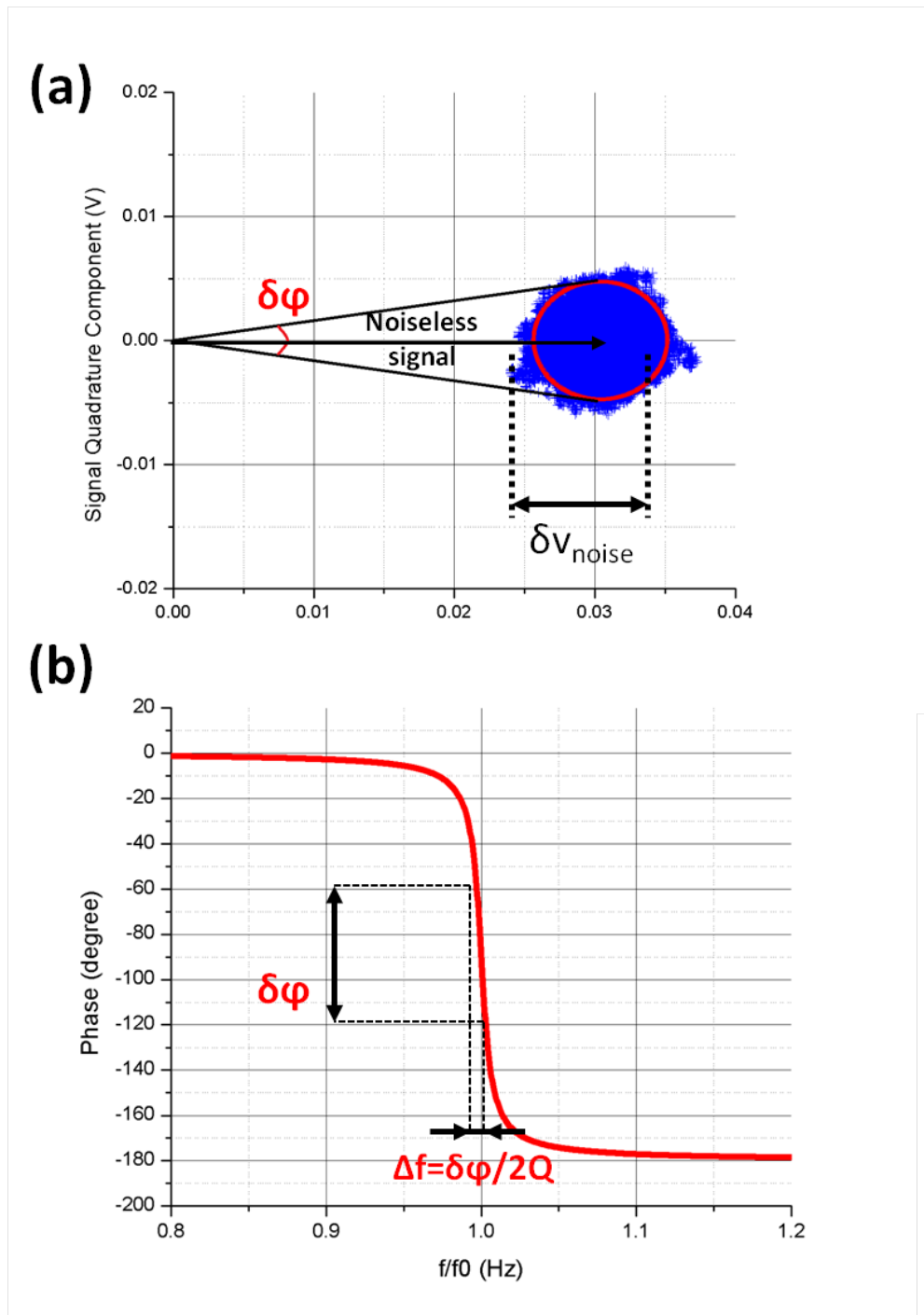


**Figure 1- 10:** Graphical illustration of the relationships between (a) phase noise and amplitude noise and (b) frequency noise and phase noise used in the Robbins formula.

Thus, the second conclusion is that the optimum resonator design for gas sensing is the one that provides, at the same time, small thickness, high quality factor, high output signal and low noise. As it turns out, all these parameters are design dependent and can lead to complicated design optimization trade-off. For instance, equation (1.2-19) suggests that increasing the quality factor improves the SMLOD, however, it also leads to a lower onset of mechanical non linearity [121] and therefore a lower maximum output signal.

Table 1- 1 provides a comparison between selected gravimetric gas chemo-sensors in the literature (1 for each resonator family). In order to remain as consistent as possible, the selection has been made with the following criteria: 1) best gas sensing performances (up to our knowledge), 2) type of detected gas (DMMP only) and 3) measurement of the device frequency stability. One important remark is that the concentration resolution remains in the 1-100ppb range irrespective of the type of resonator. One may wonder if this represents some kind of ultimate limit of gravimetric resonant gas sensor performances. However, concerns about resolution as the main FOM is relatively new in the literature. Thus we think that reported devices can be further optimized and better results will surely be published in a close future.

Table 1- 1 raises two other important remarks. First, the thickness of the resonator seems to be the main design parameter. The thinner the resonator, the better the resolution. Second, micro-cantilever resonators provide an interesting trade-off between resolution performance and not too high operating frequency. In practice, high frequency operation complicates the design of amplifiers (gain vs bandwidth tradeoff, noise) and increases the sensitivity of experimental setups towards parasitic. Hence, clever VHF electronic designs and signal processing techniques must be implemented, increasing the cost and the complexity of the sensor.

Device & Ref	Device area	Resonance Frequency	Quality factor	Surface sensitivity	Minimum Relative Frequency deviation	SMLOD	DMMP Concentration resolution (measured)	DMMP Concentration resolution (estimated)
	( $\mu\text{m}^2$ )	(MHz)		( $\text{cm}^2 \cdot \text{g}^{-1}$ )		( $\text{zg} \cdot \mu\text{m}^{-2}$ )	(ppb)	(ppb)
<b>FBAR</b> [122]	$5 \times 10^4$ <sup>(b)</sup>	1100 <sup>(a)</sup>	210 <sup>(a)</sup>	726 <sup>(a)</sup>	$3.6 \times 10^{-7}$ <sup>(b)</sup>	10000 <sup>(b)</sup>	<sup>(c)</sup>	60 <sup>(e)</sup>
<b>SAW</b> [34]	$5 \times 10^7$ <sup>(b)</sup>	158 <sup>(a)</sup>	<sup>(c)</sup>	100 <sup>(a)</sup>	$7 \times 10^{-8}$ <sup>(a)</sup>	7000 <sup>(b)</sup>	87 <sup>(b)</sup>	42 <sup>(a)</sup>
<b>CMR</b> [123]	$6 \times 10^3$ <sup>(b)</sup>	180 <sup>(a)</sup>	$5 \times 10^4$ <sup>(a)</sup>	$2.3 \times 10^3$ <sup>(b)</sup>	$1.3 \times 10^{-8}$ <sup>(a)</sup>	60 <sup>(a)</sup>	700 <sup>(d)</sup>	0.35 <sup>(e)</sup>
<b>CMUT</b> [124]	$1 \times 10^6$ <sup>(b)</sup>	47.7 <sup>(a)</sup>	140 <sup>(a)</sup>	$4.1 \times 10^3$ <sup>(b)</sup>	$1.15 \times 10^{-8}$ <sup>(a)</sup>	80.5 <sup>(a)</sup>	15 <sup>(d)</sup>	3 <sup>(e)</sup>
<b>Nano-cantilevers</b> [50]	1.5 <sup>(a)</sup>	10 <sup>(a)</sup>	200 <sup>(a)</sup>	$3.75 \times 10^3$ <sup>(b)</sup>	$1.5 \times 10^7$ <sup>(a)</sup>	400 <sup>(b)</sup>	<sup>(c)</sup>	80 <sup>(e)</sup>
<b><math>\mu</math>-cantilevers</b> [125][126]	$3.2 \times 10^3$ <sup>(b)</sup>	0.1 <sup>(a)</sup>	80 <sup>(a)</sup>	$2.8 \times 10^3$ <sup>(b)</sup>	$10^{-8}$ <sup>(a)</sup>	53 <sup>(a)</sup>	25 <sup>(d)</sup>	2 <sup>(e)</sup>

**Table 1- 1:** DMMP sensing performances for different gravimetric gas chemo-sensors in the literature.(a) data provided in the referenced article, (b) data calculated from the informations in the referenced article (c) data not available (d) measured (e) calculated from the SMLOD with a partition coefficient of  $10^5$  and functionalization thickness equal to one tenth of the device thickness.

### 1.3. Conclusion

In this chapter we have presented an overview of gas chemo-sensor based on micro and nano technologies in order to compare their performance and support our choice towards resonant operation. To do so, the first step has consisted in defining mathematically the different Figures of Merit (FOM) for gas sensing applications such as sensitivity, resolution, dynamic range, selectivity, stability and response time. The second step has consisted in looking at the chemical transduction and showing that its performance can be evaluated in terms of partition coefficient and thickness of the functionalization layer (both should be as high as possible). The third step has consisted in classifying, the different micro/nano chemo-sensor technologies according to their energy operation domain (electrical, thermal, optical, mechanical) and identify their advantages and drawbacks. Among them, mechanical resonators-based gas sensors have demonstrated high gas sensing performance and are compatible with the detection of a broad range of targeted gas.

The final step of our analysis has consisted in presenting the modeling of gas sensing performance of such mechanical resonator-based gas sensors. We have shown that the sensitivity is exclusively related to the thickness of the resonator. The resolution depends on the thickness of the resonator but also on the noise, the maximum output signal and the quality factor of the resonator. Among the different resonators design, we have shown that cantilever resonators are interesting candidates for the development of high resolution sensors: high performance has already been demonstrated in the literature and they operate at much lower frequency compared to the other resonator without loss of performance.

## Chapter 2: Piezoelectric micro / nano cantilevers resonators

---

**F**1.2-19) proves that the highest concentration resolution performance is achieved with the thinnest, highest quality factor, lower noise and highest output signal resonator. Consequently, the question of the efficiency of the transduction techniques used to actuate and detect the resonator motion is critical to achieve high performance. From a more general technological point of view, transduction techniques are also at the core of today's NEMS research. We will show, after a brief historical introduction to resonant cantilever based sensors, that all the main transduction techniques in MEMS resonators present drawbacks when applied for nano-scale resonator transduction. We will show that piezoelectric transduction can overcome this difficulty and represent thus an ideal candidate for the development of high resolution resonant cantilever based gas sensors and more generally of nano-scale flexural cantilever resonators. We will then turn towards the analytical modeling of the input/output electromechanical relations for a piezoelectric flexural cantilever resonator and combine it with the analytical models of the gas sensing resolution, presented in the previous chapter. Based on the obtained formulae, we will present finally a design optimization study.

## 2.1. Cantilever resonators for sensing applications

### 2.1.1. Historical overview

The origins of the use of cantilevers as sensing element are to be found in the invention of the Atomic Force Microscopy (AFM) in 1986 [127]. Basically, AFM senses the interactions between the atoms of a sharp tip standing at the free end of a cantilever and the atoms on a surface to be analyzed. Topographic images of the surface can thus be obtained by scanning the AFM probe over the surface and measuring the deflection of the cantilever tip. For optimal operation, AFM probes must have micrometer dimensions (typically 100 x 50 x 0.5  $\mu\text{m}$ ) in order to achieve high resonant frequency (few tenth of kHz) and reduce the sensitivity to external vibrations, and low spring constant in order to improve the force sensitivity of the probe. Thus since the beginning, AFM probes have been produced using micro-fabrication techniques [128] [129].

The presence of unwanted effects such as the instability of AFM set-ups with ambient conditions, has lead scientists to investigate the potential of cantilevers for physical and chemical sensing, such as temperature [130], humidity [131] and mercury vapors [132]. The tremendous gravimetric sensitivity of such micro-cantilevers has then raised a very large interest and opened a race toward the measurement of the lowest possible mass. In 2004, Illic *et al.* achieved a resolution of 0.39 atto-gram ( $10^{-18}\text{g}$ ) [133] with 4  $\mu\text{m}$ -long paddled cantilevers on which gold nanoparticles with 50 nm diameter were deposited. In 2005, Davis and Boisen achieved a similar resolution (2 ag) with 1  $\mu\text{m}$  long in-plane resonating cantilevers. In 2006 Yang *et al.* [21] achieved a resolution of 20 zepto-gram ( $10^{-21}\text{g}$ ) resolution with clamped-clamped 2  $\mu\text{m}$  long beams. In 2008 Jensen *et al.* obtained a resolution of 0.13 zg [22], which corresponds to the weight of 0.4 gold atom using carbon nanotubes based cantilevers. This quest culminated in 2012 with a demonstrated limit of detection of a few yocto-grams ( $1\text{yg}=10^{-24}\text{g}$ , about the mass of one hydrogen atom) by Chaste *et al.*, [134] with a 150nm-long Carbon Nano Tube operating at 2GHz and 4K (in vacuum).

Most of the early cantilever-based sensing works were performed in standard AFM set-ups that present two major drawbacks. First the actuation and detection of the cantilever motion are not integrated on-chip, hence bulky and preventing the

development of compact sensing systems. To address this issue, cantilevers with integrated read-out were developed in the late 1990s based on capacitive [135] or piezoresistive [136] detection and then fully integrated with CMOS circuits [137][138][139]. The second drawback of conventional AFM set-ups is the possibility to perform measurement on only one cantilever at a time. In the electronic nose concept, it is necessary to monitor several cantilevers with different chemical coatings to perform multi-gas analysis [9]. For this reason, the concept of cantilever array was used several times in the 2000s [140][141] with, again, a necessary change of paradigm for the actuation and detection methods. More recently, arrays of identical and commonly addressed cantilever resonators have been proven to be an interesting improvement over single resonators thanks to noise averaging [142] and/or by specific non-linear behaviors of coupled resonators such as mode localization [143].

### 2.1.2. Transduction principles

As stated in the introduction of this chapter, the choice of the transduction technique to actuate and detect cantilever motion has a great impact on system integration and performance. We shall thus overview the main transduction techniques presented so far in the literature and identify their advantage and drawbacks for the development of high resolution cantilever resonator based gas sensor and, more generally, of nano-scale flexural resonators. To do so, we will present the different transduction methods according to the physical domain in which they operate: electrical (electrostatic, magnetic, piezoresistive, piezoelectric), optical and thermal.

- Electrostatic transduction

The electrostatic actuation is the most widely used technique in today's commercial MEMS. Its main advantage relies on its compatibility with silicon-only devices, simplifying thus greatly devices manufacturing process and integration with CMOS circuits. It consists in applying a voltage  $V_0(t)$  between two electrodes (one fixed and one attached to the movable structure) of surface  $S$  and separated by a gap  $g$  so as to create an attractive force  $F_{el}$ :

$$F_{el}(t) = \frac{\epsilon_0 S}{2g^2} V_0^2(t) \quad (2.1-1)$$

Usually  $V_0(t)$  is the sum of a DC voltage  $V_{dc}$  and of an AC voltage  $V_{ac}(t) = V_{ac} \cos(\omega t)$ , yielding:

$$F_{el}(t) = \frac{\epsilon_0 S}{2g^2} \left[ V_{dc}^2 + \frac{V_{ac}^2}{2} + 2V_{dc}V_{ac} \cos(\omega t) + \frac{V_{ac}^2}{2} \cos(2\omega t) \right] \quad (2.1-2)$$

Either harmonics terms in equation (2.1-2) can be used to drive the resonator by setting the signal frequency at the resonator frequency, or half this frequency.

One important feature of the electrostatic actuation method is its inherent non-linearity and the phenomenon of *pull-in*, which both limit the maximum drive voltage to ensure linear and stable operation. In [121], the authors demonstrate a technique to compensate such drawback.

The corresponding detection technique, also called capacitive detection, is also very popular in MEMS. It consists in sensing the capacitance variations between the fixed and movable electrodes due to the gap distance changes. In the parallel plate approximation the capacitance can be written as:

$$C = \frac{\epsilon_0 S}{g - w(t)} \approx C_0 \left( 1 + \frac{w(t)}{g} \right) \quad (2.1-3)$$

where  $w(t)$  is the mechanical displacement of the movable electrode supposed small compared to  $g$ . The two major drawbacks of the capacitive transduction are a poor efficiency as  $\frac{w(t)}{g} \ll 1$  and high sensitivity to parasitic capacitance especially when the device dimensions are shrunk. For this latter matter, sophisticated read-out circuits are often required [144].

- Optical

Laser based actuation using local heating is relatively rare in the literature and restricted to the case where cantilevers can't be connected electrically [145], [146]. On the contrary, optical detection is very common despite its poor integration level. Three main methods can be encountered in the literature: laser beam deflection (inherited from AFM), interferometry and near field coupling. These last two techniques provide the best transduction performances reported in the literature with displacement resolution down to  $10^{-19}$  m/ $\sqrt{\text{Hz}}$  [147] (near field) and  $10^{-21}$  m/ $\sqrt{\text{Hz}}$

[148] (interferometry). These excellent performances are achieved thanks to exceptionally high sensitivities and low detection noise. However, since the minimum size of a laser spot is limited to  $\sim 1 \mu\text{m}$ , interferometry transduction is disturbed by large background signals when resonator dimensions are scaled down and near-field coupling is often preferred for nano-scale devices.

- Magnetic

Magnetic actuation uses Laplace forces that act on a conducting wire in presence of a magnetic field while an electrical current is flowing. The volume force density is given by:

$$\vec{f}_L = \vec{j} \wedge \vec{B} \quad (2.1-4)$$

where  $\vec{j}$  is the electric current density and  $\vec{B}$  the magnetic induction. The associated detection technique, so-called magneto-motive detection, uses the voltage generated in a current loop when the magnetic flux varies. The main drawback of the magnetic transduction techniques lies on the need for large magnetic fields, which are generally created with superconducting solenoids. This is why these techniques are employed almost exclusively at cryogenic temperatures. However, new developments in magnetic thin film technology are paving the way to efficient ambient temperature operations [149]. Interestingly, magnetic actuation remains efficient with scaling down the device dimension and allows for low power operation. Magneto-motive detection, on the other hand, is sensitive to parasitic capacitances that create low pass filters at the device output.

- Thermal / piezoresistive

When two materials with different thermal expansion coefficients are brought together in a cantilevered structure, changes of temperature can induce bending through the so-called bimorph effect [150]. This so-called thermo-elastic transduction technique is widely used in MEMS devices because of its simple implementation and the availability of thin film material with desired properties. The required heat can be

provided by intense light (photothermal actuation) or electrically using Joule heating in a resistive structure integrated on the resonator.

Due to the presence of such resistors, thermo-elastic actuation is often associated with piezoresistive detection, which exploits the variation of a resistance in presence of mechanical strain. Considering, for instance, a conductive material rod, its electrical resistance can be expressed as  $R = \frac{\rho_e l}{S}$ , where  $\rho_e$ ,  $l$  and  $S$  are resistivity, the length and the surface.

Thus, when the rod is strained, the resistance variation can be expressed as:

$$\frac{\delta R}{R} = \frac{\delta \rho_e}{\rho_e} + \frac{\delta l}{l} - \frac{\delta S}{S} = \frac{\delta \rho_e}{\rho_e} + (1 - 2\nu) \frac{\delta l}{l} \quad (2.1-5)$$

where  $\nu$  is the Poisson ration of the rod material. For a metallic resistor the geometric term  $\frac{\delta l}{l}$  dominates leading to small piezoresistive coefficients (1 for Aluminum, up to 10 for Platinum). In semiconducting piezoresistors, the mechanical strain modifies the band-structure and thus the carrier density. Therefore the term  $\frac{\delta \rho_e}{\rho_e}$  becomes preponderant (in the order of 100 for silicon). Both transduction techniques remain efficient at the nano-scale and have enabled the demonstration of the first NEMS cantilevers with fully integrated transduction[25][23]. However, they are dissipative in nature and this drawback limits their use for battery powered systems, large cantilevers arrays or low temperature applications [25][142].

- Piezoelectric

Like thermal transduction, piezoelectric transduction of flexural resonator relies on the so-called bimorph effect [150]. These devices present thus a multi-material structure with at least one piezoelectric layer. For instance, in the most common design, the piezoelectric layer sandwiched between two metallic electrodes (top and bottom) and this three layer stack lies on a non-piezoelectric layer (so-called elastic or structural layer, *cf.* Figure 2- 1 (a)). Other designs can also be considered: beams with several piezoelectric layers in order to separate actuation and detection port (*cf.* Figure 2- 1 (b)) or with a patterned top electrode to enable in-plane flexural motion (*cf.* Figure 2- 1 (c)). For all these devices the working principle remains the same: the stress created in the piezoelectric layer by an externally applied electric

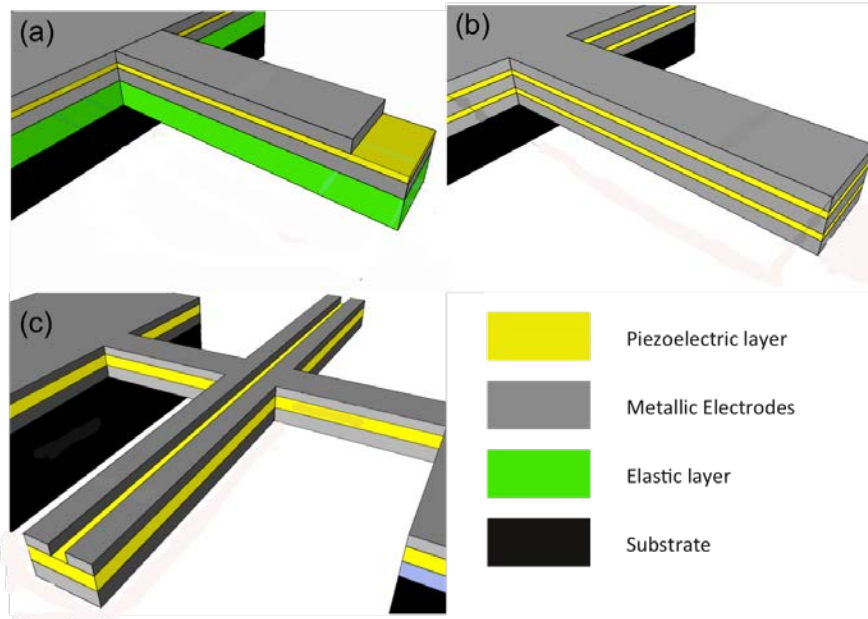


**Figure 2- 1:** Example of piezoelectric flexural cantilever designs (a) single port out of plane flexural cantilever (only one piezoelectric layer is used both for actuation and detection) with additional elastic layer (b) two ports out of plane flexural cantilever (c) two port in-plane cantilever (free free design)

field is compensated by an opposite stress in the other layer and balance can be reached only in a bended state of the whole structure. Conversely, when the device is bent, the piezoelectric layer undergoes a net axial stress which is converted into a charge signal at the interface between the piezoelectric layer and the metallic electrodes.

Table 2- 1 and Table 2- 2 provide a qualitative comparison between the different transduction techniques listed above. Based on these tables, piezoelectric transduction represents the following advantages: it requires neither strong dc biasing nor small gaps like electrostatic / capacitive transduction nor external bulky setups like optical and magnetic transduction and is inherently low power, as opposed to thermo-elastic and piezoresistive transduction. Additionally, piezoelectricity is a stress induced effect and hence its efficiency is unchanged when devices are scaled down.

As we will show in section 2.2.4, the development of piezoelectric micro/nano cantilever resonator is tied to the availability and processing capability of piezoelectric materials. Martin *et al*, [27] have shown that Aluminium Nitride (AlN) films with thickness lower than 100 nm present strongly degraded piezoelectric

properties. More generally, the thickness of piezoelectric films reported in the literature never goes below 100 nm irrespective of the type of material (*c.f.* Table 3-1). This thickness limit is barely compatible with nano-scale device dimensions especially as the overall device thickness is at least twice the piezoelectric layer. Nonetheless, Karabalin *et al.* [29] and Sinha *et al.* [30] have demonstrated the high efficiency of the piezoelectric actuation method in nano-cantilevers ( $6 \mu\text{m} \times 900 \text{ nm} \times 320 \text{ nm}$ ) using 100 nm thick AlN films. No results are actually presented in these two articles on the efficiency of the piezoelectric detection which remains thus to be evaluated experimentally.

Accordingly, sub 100 nm-thick piezoelectric films represent an innovative research area that can benefit both to the development of gravimetric gas sensor and more generally to nano-scale flexural resonators. The main thrusts are fully integrated transduction, low power operation and high gas sensing resolution or high transduction efficiency.

<b>Actuation technique</b>	<b>Advantage</b>	<b>Inconvenient</b>	<b>Scaling</b>
<b>Electrostatic</b>	- Low cost - Low power - Integrated	- Non linear	- Constant
<b>Optical</b>	- Remote	- Low efficiency (for photothermal) - Optical gradient force actuation not yet routine	- Degraded (photothermal) - Improved (optomechanical)
<b>Magnetic</b>	- Efficient	- Bulky setup - Magnetic thin films integration still difficult	- Good
<b>Thermo-elastic</b>	- Low cost - Integrated	- Dissipative	- Good
<b>Piezoelectric</b>	- Low power - Integrated - Efficient	- Multilateral integration	- Good (strain related effect)

**Table 2- 1:** Comparison table between the different actuation techniques for cantilevers.

Detection technique	Advantage	Inconvenient	Scaling
<b>Capacitive</b>	- Low cost - Integrated	- Non linear - Sensitive to parasitic	- Bad
<b>Optical</b>	- Very sensitive - Remote	- Not yet routine in an applied context	- Degraded (interferometry) - Improved (optomechanics)
<b>Magnetic</b>	- Low noise	- Bulky setup - Magnetic thin films integration still difficult	- Good
<b>Piezoresistive</b>	- Low cost - Integrated	- Dissipative - Added noise	- Good
<b>Piezoelectric</b>	- Low power (passive) - Integrated	- Sensitive to parasitic - Multimaterial integration	- Good (strain related effect)

**Table 2- 2:** Comparison table between the different detection techniques of cantilevers

## 2.2. Piezoelectric transduction

### 2.2.1. Generalities

Piezoelectricity corresponds to the property of certain dielectric solids (crystals, ceramics, polymers, DNA...) to accumulate charges on their surface under the effect of a mechanical stress. The word piezoelectricity comes from the Greek *piezein*, which means to squeeze, and *electron* that stands for amber, the first known source of electric charges. It is a reversible effect in the sense that a piezoelectric material does not only respond electrically to a mechanical stimulus (direct effect) but

is also able to expand or shrink under the effect of an external electrical field (converse effect).

Piezoelectricity appears in crystalline materials whose crystallographic cell does not possess any symmetry center, except class 432, which does not exhibit a symmetry center and is however not piezoelectric. There are thus 20 piezoelectric classes out of the 32 existing crystallographic classes. The lack of symmetry center together with the difference of electro-negativity of the atoms in the crystallographic cell allows the non-coincidence of the centroids of the positive and negative charges and thus the presence of a non-null dipolar moment in the material. The magnitude of the dipolar moment depends on the distance between the centroids. Therefore, when the crystallographic cell is strained under the effect of a mechanical stress, the dipolar moment of the material changes and must be compensated by charges on the surface of the material. Reversely, when an external electric field is established across the material, the electrostatic force pushes / pulls the centroids and makes the atoms move from their equilibrium position, which in turn induces a strain. The polarization can be permanent (non null at equilibrium) and in that case the crystal is also pyroelectric: temperature variations induce charges on the surface of the crystal. This is the case in 10 out of the 20 piezoelectric crystallographic classes.

As an example, Aluminum Nitride (AlN) belongs to the P6mm space group (wurtzite). Its crystallographic cell corresponds to a tetrahedron whose summits are occupied by positively charged Aluminum ions and whose centroids is occupied by a negatively charged Nitrogen ion (or vice versa with a reversed tetrahedron (*cf.* Figure 2- 2(a)). This configuration allows a permanent dipole in the [0001] crystallographic direction and confers thus to wurtzite AlN crystals their piezoelectric (and pyroelectric) properties. Figure 2- 2 (b)(c)(d)(e) illustrates the response of the AlN crystallographic cell to a force or an electric potential difference in the same direction (longitudinal) or perpendicular (transversal) as the polarization vector.

Historically, the direct piezoelectric effect was evidenced by Pierre and Jacques Curie [151] using tourmaline crystal in 1880. The converse effect was first predicted theoretically by Lippmann [152] and demonstrated experimentally by the same Curie brothers [153] one year later in 1881. During more than three decades piezoelectricity was essentially a scientific curiosity and it is only during the first world war that real life applications were found with the invention of the sonar by

Paul Langevin [154]. Since then, piezoelectric materials and devices have become an intense field of research and today are ubiquitous in daily life applications such as lighter, miniature RF filters and oscillators, ultrasonic emitter and receivers, industrial sensor, ultra-precise positioning systems (AFM)...

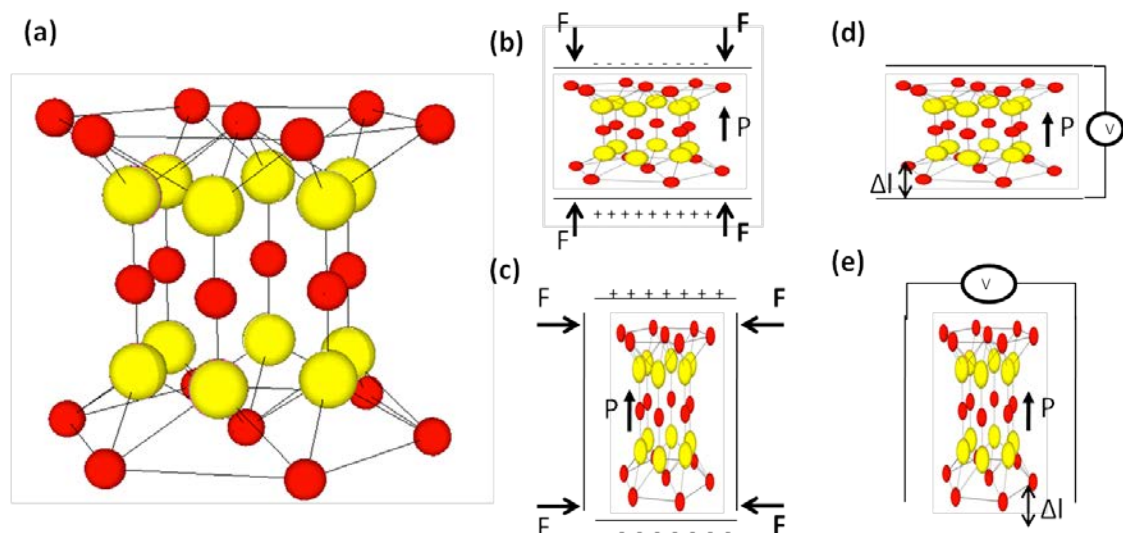


**Figure 2- 2:** (a) 3D view of AlN crystallographic cell. Yellow atoms represent the positively charged Aluminum atoms while the grey atoms represent the negatively charged Nitrogen atoms. The permanent polarization direction is given by the c-axis perpendicular to the hexahedrons planes. 2D piezoelectric crystal (b) direct longitudinal effect, (c) direct transversal (d) reverse longitudinal (e) reverse transversal

### 2.2.2. Piezoelectric materials

Several piezoelectric materials are naturally present on Earth such as quartz, Rochelle Salt or Tourmaline but the development of piezoelectric devices has really been allowed by tailored, human made materials. For sonar systems, emitters and receivers (hydrophone) were based on quartz crystal. This material is still widely used today for time reference applications because of a high stability versus temperature variations (AT-cut).

Materials such as Zinc Oxide (ZnO) and Aluminum Nitride (AlN) present piezoelectric properties about ten times higher than quartz. They are wide band semiconductor and were first developed for optical applications. Their main

advantage is their low dielectric loss and high acoustic quality factor at high frequency making them ideal candidate for RF applications.

When high piezoelectric properties are required, Lead Zirconate Titanate ( $\text{Pb}(\text{Zr},\text{Ti})\text{O}_3$ ) or PZT is undoubtedly the most widely spread material. Its piezoelectric coefficients are about 100 times greater than quartz and it is possible to vary its chemical stoichiometry to tailor its properties and fits one or another particular application. PZT is a ferroelectric material, which means that its remnant polarization is stable and can be reversed under the action of a strong electric field. This phenomenon is exploited in ferroelectric memories. It also presents a Curie temperature above which the material is in paraelectric phase and therefore non piezoelectric.

Today, the development of new piezoelectric materials is motivated by three main trends. The first one is the improvement of the piezoelectric properties and is focused on relaxors derived from PZT such as PZN-PT, PMN-PT... The second trend concerns the development of lead free alternative to PZT. It is largely supported by new regulations limiting the use of lead, even though they have not been applied so far to piezoelectric materials. Barium Titanate ( $\text{BaTiO}_3$ ) and Potassium Sodium Niobate ( $(\text{K},\text{Na})\text{NbO}_3$ ) or KNN are among the most promising candidates and are already available commercially. The last trend concerns the development of alternatives to ZnO and AlN in RF devices with highly coupled materials. Lithium Niobate ( $\text{LiNbO}_3$ ) and Lithium Tantalate ( $\text{LiTaO}_3$ ) would be ideal candidates but their processing techniques remain very complex and expensive.

### 2.2.3. Thermodynamic approach of piezoelectricity

Today, the most advanced theoretical models of piezoelectricity are able to link microscopic properties to macroscopic piezoelectric properties thanks to *ab initio* [155] or first principle [156] calculations. However, it is not necessary to go in such detail here, and we can restrict the presentation of the theoretical modeling of piezoelectricity to the most traditional theoretical framework, called linear theory of piezoelectricity [157], which is based on thermodynamic considerations.

In this model, the equations of linear elasticity are coupled to the charge equation of electrostatics by the means of the piezoelectric constants. According to the first law of thermodynamics, the total differential internal energy  $dU$  for a linear piezoelectric medium neglecting heat can be written as:

$$dU = T_{ij}dS_{ij} + E_i dD_i \quad (2.2-1)$$

where  $T_{ij}$ ,  $S_{ij}$ ,  $E_i$  and  $D_i = \epsilon_0 E_i + P_i$  are the stress, strain, electric field and electric displacement tensor components using the standard notation of piezoelectricity [157].  $\vec{P}(\vec{r}_0) = \frac{1}{V} \int \rho(\vec{r})(\vec{r} - \vec{r}_0) d\vec{r}$  is the polarization vector,  $P_i$  its components and  $\rho(\vec{r})$  the microscopic polarization charge density. The electric enthalpy density  $H$  is defined as:

$$H = U - E_i D_i \quad (2.2-2)$$

Therefore:

$$dH = T_{ij}dS_{ij} - D_i dE_i \quad (2.2-3)$$

and

$$\begin{aligned} T_{ij} &= \left( \frac{\partial H}{\partial S_{ij}} \right)_E \\ D_i &= - \left( \frac{\partial H}{\partial E_i} \right)_S \end{aligned} \quad (2.2-4)$$

In the linear model framework,  $H$  can be expressed as a quadratic function of its state variables  $S_{ij}$  and  $E_i$ :

$$H = \frac{1}{2} c_{ijkl}^E S_{ij} S_{kl} - \frac{1}{2} \epsilon_{ij}^S E_i E_j - e_{kij} E_k S_{ij} \quad (2.2-5)$$

The three terms in the right part of the previous equation represent, respectively, the density of elastic energy, the density of electrostatic energy and the density of linear electromechanical coupling energy. The three sets of coefficients  $c_{ijkl}^E$ ,  $e_{kij}$  and  $\epsilon_{ij}^S$  are the elastic, piezoelectric and dielectric constants respectively. In the general case, there are 21 independent elastic constants, 18 independent piezoelectric constants and 6 independent dielectric constants.

Each group forms a tensor called elastic, piezoelectric and dielectric tensor respectively with dimension 4, 3 and 2 respectively. From equations (2.2-4) and (2.2-5), the constitutive equations of piezoelectricity are:

$$\begin{aligned} T_{ij} &= c_{ijkl}^E S_{kl} - e_{kij} E_k \\ D_i &= e_{ikl} S_{kl} + \epsilon_{ij}^S E_j \end{aligned} \quad (2.2-6)$$

In order to simplify the notations and write the elastic and piezoelectric tensors in the form of a matrix array, let us use the simplified notation[157], which yields

$$\begin{aligned} T_p &= c_{pq}^E S_q - e_{kp} E_k \\ D_i &= e_{iq} S_q + \epsilon_{ik}^S E_k \end{aligned} \quad (2.2-7)$$

Linear piezoelectricity is thus fully described by a set of two coupled linear equations of strain, stress, electric field and displacement components. The following step for the modeling of piezoelectric devices consists in introducing these relations to the equations of mechanics (Newton's laws) and of the conservation of charge. However, in the case of piezoelectric flexural cantilevers, this step is not straightforward as bending is not the natural deformed state of a piezoelectric material which rather expands or compresses. This will be the focus of section 2.3, but first, we shall end this bibliography review by a focus on the already demonstrated piezoelectric resonant cantilevers.

#### **2.2.4. Piezoelectric flexural cantilever resonators**

Based on the literature review in [158], piezoelectric benders have encountered a great success in a broad range of applications but their development is tied to the availability of piezoelectric materials. This is why piezoelectric cantilever technology is relatively young compared to piezoelectricity in general.

Early reports date back to the seventies with Gallantree and Quillam [159] who reported the successful fabrication of 1  $\mu m$  thin polyvinylidene fluoride (PVDF)

films on silicon substrate and the fabrication and characterization of switches and actuators including this material. In 1979 Kino and al. [117] reported the fabrication of ZnO films deposited on Silicon by sputtering and Smits [160] developed a resonant pressure sensor based on these thin films in 1982. The development of PZT thin films is even more recent. Reports on fabrication techniques start in 1977 (Ishida and al. [161]) and cover all the eighties, but the first demonstration of a PZT piezoelectric cantilever dates back to 1991[162].

- AlN based cantilever

First attempts of AlN thin film fabrication date back to the late seventies whereas AlN micro cantilevers were not reported before 2005 [163]. In this article, the devices are micro-bridges 350  $\mu\text{m}$  long and 80  $\mu\text{m}$  wide including a SiN (350nm) / Mo (150nm)/ AlN (500nm)/ Mo (150nm) stack. Released devices exhibit large static bending due to the presence of large residual stresses in the different material layers but operate properly: piezoelectrically-induced deflection can be clearly identified on SEM images. One year later, the same research group [164] demonstrated the possible piezoelectric actuation of the first beam bending modes using optical detection for the displacement transduction.

Mortet *et al.* [165] have reported the first fully electrical actuation and detection of flexural resonance modes of a cantilever 320  $\mu\text{m}$  long and 70  $\mu\text{m}$  wide including a 1  $\mu\text{m}$  thick AlN film. The resonance frequency of these devices has been measured equal to 36.6kHz. This article clearly demonstrated the high efficiency of piezoelectric transduction and its conclusion attracted the attention of several other research groups who initiated then a quickly growing research effort around AlN-based flexural cantilever resonators.

A first research trend has been directed towards the development of more sensitive read-out schemes. Nagano *et al.* [166] have reported the fabrication of a CMOS compatible piezoelectric cantilever embedding two 500nm-thick AlN layer. Static deflection is detected with a balanced low frequency amplifier and is in good agreement with theoretical model. Wang *et al.* [167] have presented the fabrication

and characterization of cantilever resonators for accelerometers application and containing a 1.5  $\mu\text{m}$  thick sputtered AlN film. The detection of the output signal uses a capacitive trans-impedance (charge amplifier) rather than a voltage amplifier. Interestingly, the authors have shown that the noise floor is limited by the amplifier noise and depends strongly on the design of the feedback capacitor.

A second research trend has been directed towards the miniaturization of resonators. Andrei *et al.* [168] have presented the fabrication of 10  $\mu\text{m}$  long, 2  $\mu\text{m}$  wide cantilevers with 1  $\mu\text{m}$  thick sputtered AlN on CrNi or Pt electrodes. Leland *et al.* [169] have reported the fabrication of AlN cantilever with Pt electrodes with similar dimensions. SEM images show a large built-in stress mismatch in the different layers. Unfortunately, only non electrical characterizations are reported and cannot support any conclusions on piezoelectric transduction efficiency. Karabalin *et al.* [29] have reported the first fabrication and characterization of nano-scale piezoelectric with dimensions 6  $\mu\text{m}$  x 900nm x 320 nm for cantilevers and 4  $\mu\text{m}$  x 900nm x 320 nm for bridges. These devices exploit a 100 nm thick AlN piezoelectric active layer with piezoelectric properties comparable to thicker films. The efficiency of the piezoelectric actuation is clearly demonstrated in this article where the limit of non linearity is reached for an actuation voltage of only few volts. On the other hand, the mechanical transduction was not efficient enough and optical transduction were preferred for the motion detection. The same year, Sinha *et al.* [30] presented the fabrication of 5  $\mu\text{m}$  x 2  $\mu\text{m}$  x 340 nm cantilevers with two 100 nm thick active AlN layers. The high efficiency of the piezoelectric actuation is again demonstrated but, this time, only for static deflection.

- Piezoelectric cantilever flexural resonator for mass sensing applications

Finally the last research trend concerned the demonstration of the sensing capability of piezoelectric cantilever resonators. Focusing first on mass sensing, Ferrari *et al.* [170] have been the first to report on the mass sensitivity of 1 mm long alumina beam with PZT thin film for piezoelectric actuation and detection. The cantilever operates in a self-oscillating loop close to its resonance frequency of 12

kHz. The sensitivity is measured by depositing a known quantity of silicone grease on the cantilever and found to be equal to  $0.9 \mu\text{g}/\text{Hz}$ . The mass resolution is also evaluated through mercury vapor adsorption and found to be equal to  $0.17 \mu\text{g}$ . Shin *et al.* [171] have reported better mass sensitivity with  $200 \mu\text{m}$  long cantilevers including  $500 \text{ nm}$  thick PZT thin films with resonance frequencies ranging from  $18.6$  to  $24.2 \text{ kHz}$ . The sensitivity has been measured by depositing thin copper films on cantilever and found to be in the  $30 \text{ pg}/\text{Hz}$  range. Park *et al.* [172] have reported similar results with  $380$ ,  $480$  and  $580 \mu\text{m}$  long and  $400 \mu\text{m}$  wide cantilevers containing  $2 \mu\text{m}$  thick PZT films. The mass sensitivity has been measured there by depositing a thin gold film on the cantilever tip and found to be  $152$ ,  $57.1$  and  $30.7 \text{ pg}/\text{Hz}$ , respectively. In a very recent paper, Olivares *et al.* [173] have studied the mass sensing performance of cantilevers and bridges fabricated with the same process as in [164]. The mass sensitivity has been measured by depositing thin  $\text{SiO}_2$  films on the cantilever and found to be in the range of  $300 \text{ ag}/\text{Hz}$ .

Focusing now on gas sensing, very few articles presenting the gas sensing performance of piezoelectric cantilevers can be found. Roger *et al.* [174] have reported a resonating piezoelectric cantilever based set-up for mercury vapor detection. The authors do not describe the design of the cantilever but claim to have measured concentration level as low as  $92 \text{ ppb}$  with an estimated resolution limit down to  $20 \text{ ppb}$ . Adams *et al.* [175] have presented the detection of ethanol and water vapor in the part per thousand range with three piezoelectric cantilevers wired in series and coated with different polymers. The most interesting point of this article is the demonstration of the ultra low power operation in the range of a tenth of  $\text{nW}$ .

Piezoelectric cantilever resonators are the object of the research activities of several groups in the world. Larger devices have demonstrated high transduction efficiency for both actuation and detection of the resonator motion. Very few nano-scale devices have been reported so far and while the piezoelectric actuation seems to be working very well, the piezoelectric detection seems to be more problematic. We will show that the electronic detection setup required for better piezoelectric detection efficiency is actually very constrained. To demonstrate this point and to continue our evaluation of the potential of the piezoelectric transduction in cantilevers flexural resonator, we shall now turn the discussion towards the analytical modeling of the resonant behavior of these devices. This is the topic of the next section.

## 2.3. Analytical Modeling and design optimization

### 2.3.1. Analytical input/output relationship for a piezoelectric cantilever

In order to be consistent with our processing capability, we will focus on the cantilever structure depicted in Figure 2- 3(a) with a Silicon Nitride (SiN) so-called elastic layer on top of which an Aluminium Nitride (AlN) piezoelectric layer, sandwiched between two Platinum (Pt) electrodes, is deposited. The electromechanical modeling of such heterogeneous multi-morph system is largely reported in the literature [150], [159], [176], [177], therefore we will only recall here the derivation method and the useful results. Under the classical Euler-Bernoulli theory, the bending vibration equation can be written as:

$$\mu W \frac{\partial^2 w}{\partial t^2} + \mu \Gamma \frac{\partial w}{\partial t} + \langle EI \rangle_{eq} \frac{\partial^4 w}{\partial x^4} = \frac{\partial^2 M_p}{\partial x^2}(x) \quad (2.3-1)$$

where  $\mu = \sum \rho_i t_i$  is the surface mass density of the resonator (mass per unit length and width),  $\rho_i$  and  $t_i$  being the mass density and thickness of each material layer (from bottom to top) that constitute the cantilever, respectively.  $W$ ,  $\Gamma$ ,  $w$ ,  $x$  and  $M_p$  are the width of the cantilever, the damping coefficient, the vertical displacement of the neutral plane, the special coordinate in the longitudinal direction of the cantilever and the piezoelectric bending momentum, respectively. The neutral plane position at rest with respect to the bottom surface of the cantilever and the equivalent beam rigidity  $\langle EI \rangle_{eq}$ , can be expressed using the equivalent beam approach [107]:

$$z_0 = \frac{\sum E_i t_i z_i}{\sum E_i t_i} \quad (2.3-2)$$

$$\langle EI \rangle_{eq} = \sum E_i I_i$$

where  $E_i$ ,  $z_i$  and  $I_i$  are the Young's modulus, the mid-plane position with respect to the cantilever bottom surface and the quadratic momentum with respect to  $z_0$  of the  $i^{\text{th}}$  material layer. As  $M_p$  is constant over the length of the beam, the driving term in equation 2.3-1 is zero except at the boundaries. We will use the Heaviside function  $H$  to express the piezoelectric momentum:

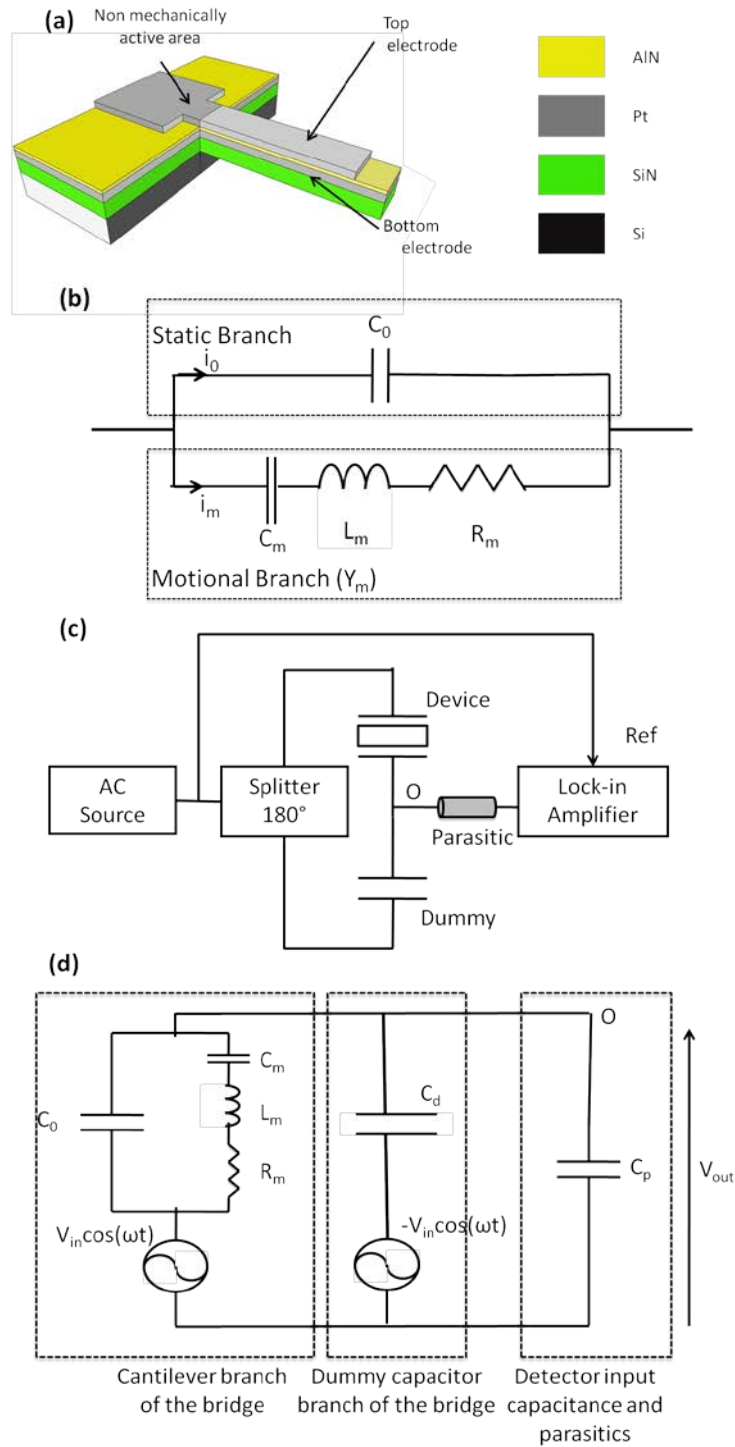


**Figure 2- 3:** (a) Schematic of the cantilever structure under study (b) Butterworth-Van Dyke equivalent circuit of the piezoelectric bimorph; (c) Capacitive half bridge architecture: out of phase signals are applied to the cantilever and a dummy capacitor with capacitance equal to the cantilever static capacitance. The output signal is taken at the common port of the cantilever and dummy capacitor where the background signal is cancelled out. (d) Equivalent circuit of the half bridge setup, the output signal can be derived by applying Kirshoff's laws at point O.

$$M_p(x) = \left( \int \int_{AIN} (z - z_0) e_{31} \frac{V_{in}}{t_3} dydz \right) H(L - x) \quad (2.3-3)$$

$$= W\beta_p V_{in} H(L - x)$$

where  $V_{in}$  and  $e_{31}$  are the input actuation voltage and the effective transverse piezoelectric coefficient, respectively.  $\beta_p = e_{31} \left( \frac{t_3}{2} + t_2 + t_1 - z_0 \right)$  depends on the multilayer stack asymmetry and is a figure of merit of the actuation gain. Assuming small dissipation, equation (2.3-1) can be solved using Galerkin's method where the general solution is given by:

$$w(x, t) = \sum_n \lambda_n(t) \Phi_n(x) \quad (2.3-4)$$

where  $\lambda_n$  in equation are the time varying amplitudes the contribution of the  $n^{\text{th}}$  undamped eigen modes of the cantilever  $\Phi_n$  [107],  $\Phi_n$  are given by:

$$\Phi_n(x) = A_n \left[ \cosh\left(\frac{\alpha_n x}{L}\right) - \cos\left(\frac{\alpha_n x}{L}\right) + \sigma_n \left( \sin\left(\frac{\alpha_n x}{L}\right) - \sinh\left(\frac{\alpha_n x}{L}\right) \right) \right] \quad (2.3-5)$$

where  $A_n = \sqrt{\frac{L^3}{\int_0^L \left[ \cosh\left(\frac{\alpha_n x}{L}\right) - \cos\left(\frac{\alpha_n x}{L}\right) + \sigma_n \left( \sin\left(\frac{\alpha_n x}{L}\right) - \sinh\left(\frac{\alpha_n x}{L}\right) \right) \right]^2 dx}}$  is the normalized mode amplitude,  $\alpha_n$  is the  $n^{\text{th}}$  roots of  $1 + \cos(\alpha_n L) \cosh(\alpha_n L) = 0$  ( $\alpha_1 = 1.875, \alpha_2 = 4.694, \alpha_3 = 7.854 \dots$ ); finally  $\sigma_n = \frac{\cosh\left(\frac{\alpha_n x}{L}\right) + \cos\left(\frac{\alpha_n x}{L}\right)}{\sinh\left(\frac{\alpha_n x}{L}\right) + \sin\left(\frac{\alpha_n x}{L}\right)}$ .

Substituting equation (2.3-4) in equation (2.3-1) and using the orthogonality of  $\Phi_n$ , we obtain:

$$\lambda_n(\omega) = \frac{WL\beta_p \frac{d\Phi_n}{dx}(L)}{\langle EI \rangle_{eq} \alpha_n^4} \frac{V_{in}}{1 + j \left( \frac{\omega}{Q_n \omega_n} \right) - \left( \frac{\omega}{\omega_n} \right)^2} \quad (2.3-6)$$

where,  $\omega_n = \left( \frac{\alpha_n}{L} \right)^2 \sqrt{\frac{\langle EI \rangle_{eq}}{\mu}}$  and  $Q_n$  are, respectively, the  $n^{\text{th}}$  mode resonance frequency and quality factor.

Assuming a sine wave actuation voltage at a frequency  $\omega$  close to the  $n^{\text{th}}$  resonance frequency, the input voltage / output current relation can be derived from Gauss theorem over one electrode area: S

$$\begin{aligned} i_{out} &= j\omega \int \int \int_{AIN} \left( e_{31} (z - z_0) \frac{\partial^2 w}{\partial x^2} - \epsilon_{33} \frac{V_{in}}{t_3} \right) dx dy dz \\ &= j\omega \left( \frac{\frac{W^2 L \beta_p^2 \gamma_n}{\langle EI \rangle_{eq}}}{1 + j \left( \frac{\omega}{Q_n \omega_n} \right) - \left( \frac{\omega}{\omega_n} \right)^2} - C_0 \right) V_{in} \end{aligned} \quad (2.3-7)$$

where  $\gamma_n = \frac{|\Phi'_n(L)|^2}{\alpha_n^4}$  is a constant which only depends on the considered mode shape, and  $C_0 = \epsilon_{33} \left( \frac{WL + S_{pads}}{t_3} \right)$  is the static capacitance arising from the metal/insulator/metal structure, taking into account the mechanically not active areas of surface  $S_{pads}$  (c.f. Figure 2- 3(a)). Equation (2.3-7) is interpreted in terms of Butterworth-Van Dyke (BVD) lump elements circuit [176] where the cantilever is modeled as a capacitance  $C_0$  in parallel with a resonant  $R_m, L_m, C_m$  motional branch (c.f. Figure 2- 3 (b)) with:

$$C_m = \frac{W^2 L \beta_p^2 \gamma_n}{\langle EI \rangle_{eq}}; \quad L_m = \frac{1}{C_m \omega_n}; \quad R_m = \frac{1}{C_m Q \omega_n} \quad (2.3-8)$$

It is possible to get rid of the current flowing through  $C_0$  via a balancing measurement. Several electronic circuits can be considered [178], [179], theoretically providing the same output signal. In practice, the circuit depicted in Figure 2- 3 (c) and (d) presents the simplest and yet efficient and robust method, avoiding time consuming tuning of variable component and gain. In this configuration the output voltage signal seen by the lock-in amplifier is given by:

$$V_{out} = \frac{Y_m(\omega) + j\omega(C_0 - C_d)}{Y_m(\omega) + j\omega(C_0 + C_d + C_p)} V_{in} \quad (2.3-9)$$

where  $Y_m(\omega) = \frac{j\omega C_m}{1 + j\omega C_m R_m - \omega^2 C_m L_m} = \frac{j\omega C_m}{1 + j(\omega/Q_n \omega_n) - (\omega/\omega_n)^2}$  is the admittance of the motional branch (c.f. Figure 2- 3 (b)) and  $C_d$  and  $C_p$  are the capacitance of the dummy capacitor of the bridge and the input capacitor of the lock-in amplifier accounting for all parasitics (cables). Assuming a perfect balance of the bridge (i.e.

$C_d = C_0$ ) and considering that  $QC_m \ll 2C_0 + C_p$ ; the input / output electromechanical transfer function can be written as:

$$V_{out} = \left( \frac{C_m}{2C_0 + C_p} \right) \frac{V_{in}}{1 + j(\omega/Q_n\omega_n) - (\omega/\omega_n)^2} \quad (2.3-10)$$

### 2.3.2. Frequency loops

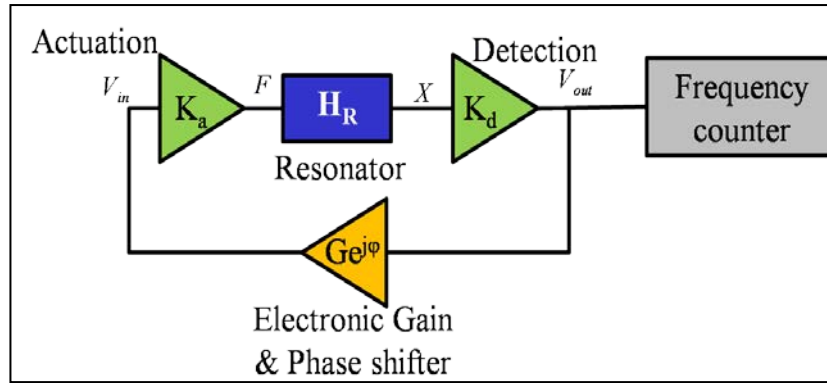
Gravimetric resonant sensors are based on the variation of the resonance frequency of a mechanical structure with the addition of mass due to the accretion of gas molecule on the sensor surface. Therefore these devices must be integrated in an electronic circuit architecture that allows the tracking of the resonance frequency changes, preferably in real time. Several architectures can be considered such as self oscillation loops [38], Phase Lock Loop (PLL) [38], Frequency Lock Loop (FLL) [38] (require accordable resonators); frequency sweep; or thermal noise-based method [180]. The two first methods are by far the most common in the literature and we will focus only on these two in the following.

Figure 2- 4 presents the general architecture of the self-oscillation loop architecture. The output signal of the resonator is fed back to its input after amplification and phase shifting such that the signal loss and dephasing in the resonator is exactly compensated by the feedback amplifier. In these conditions and without any other power sources than the DC power of the amplifier, a steady state oscillating signal at the resonance frequency of the resonator can settle in the loop.

More precisely, oscillation appears in the loop when the following conditions, called Barkhausen conditions, are verified at a particular frequency  $\omega_R$ :

$$|H_{OL}(\omega_R)| = 1 \text{ and } \arg(H_{BO}(\omega_R)) = 0 \quad (2.3-11)$$

where  $H_{OL}(\omega) = Ge^{j\varphi}K_aK_dH_R(\omega)$  is the open loop gain. In these conditions, the closed loop gain  $H_{CL}(\omega) = \frac{H_{OL}(\omega)}{1+H_{OL}(\omega)}$  diverges at  $\omega = \omega_R$ , which can be interpreted as the possible existence of a non null AC signal in the loop with no input signal. In practice, as we want to track the variation of the resonance frequency, the different electronic components in the loop are designed such that  $\omega_R = \omega_0$ . Beside, a slightly higher amplifier gain  $G$  is chosen such that  $|H_{BO}(\omega_R)| > 1$ . Therefore, any



**Figure 2- 4:** Architecture of a self oscillating loop. The gain and phase shift of the electronic amplifier are adjusted such that the open loop transfer function  $G=1$ . In this case the electronic amplifier compensates exactly for the different signal loss in the loop and the whole system oscillates naturally. The frequency counter measures the frequency of the signal in the loop using another time reference

noise signal with frequency component at  $\omega_R$  will be amplified and re-injected into the loop with a growing amplitude lap after lap. After several cycles, a non linearity in one of the loop components (for example the saturation voltage of the amplifier) or an Automatic Gain Controller (AGC) can be used to regulate the oscillation amplitude at a constant level.

Figure 2- 5 presents the general architecture of a Phase Locked Loop resonance frequency measurement setup. The frequency phase characteristic of the resonator  $\arg(H_R(\omega))$  is exploited in order to lock the cantilever output signal phase to its value at the resonance frequency ( $\frac{\pi}{2}$  in general). The feedback process consists in adjusting the frequency of the signal of the Voltage Controlled Oscillator (VCO) proportionally to the measured phase difference between the input and output signals of the resonator.

The self-oscillating architecture requires a simpler electronic circuit and therefore, is easier to implement than the PLL. However, this architecture is very sensitive to the mechanical resonator characteristics, which varies with the fabrication technology, the environment and the presence of non linear phenomena in the different loop components. Therefore the choice of one of these architectures is essentially a tradeoff between costs, ease of implementation, robustness, ease of integration and performance and will depend on the targeted application.

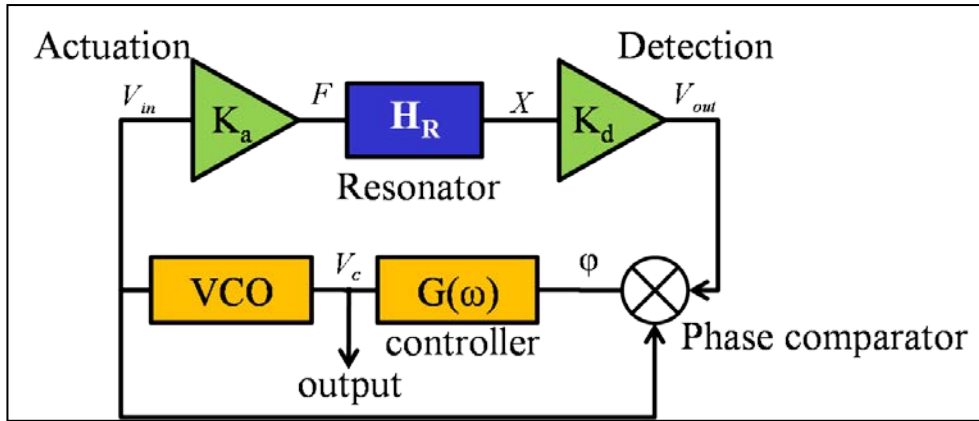


**Figure 2- 5:** Architecture of a Phase Locked Loop resonance frequency measurement setup. The Voltage Control Oscillator (VCO) delivers a signal to the device with a frequency fixed by the controlling signal  $V_c$  which, in turn, is fixed by the phase difference between the VCO signal and the output signal from the cantilever and the controller transfer function

### 2.3.3. Design optimization

#### 2.3.3.1. Preliminaries

Regardless of the chosen type of resonance frequency tracking loop, it is important to make the distinction between the resonance frequency of the resonator and the frequency of the signal in the loop. This last one is supposed to be equal to the resonance frequency of the resonator by design of the frequency loop, but it can be slightly different and more importantly it is always fluctuating due to noise.

Following the noise model presented in [39] and [119], each noise source in the frequency loop corresponds to a frequency deviation whose magnitude can be related to the noise source Power Spectral Density (PSD). Thus, prior to a design optimization study, it is necessary to find out which noise source dominates depending on the design parameters. In [39] and [119], identified noise sources are:

- The amplifier white noise arising from several noise sources inside the amplifier circuit. This noise depends on the amplifier circuit topology and its transistor technology. State of the art low noise MOSFET amplifier achieves a PSD  $S_{amp} = 0.9 \text{ nV}/\sqrt{\text{Hz}}$ .

- The thermo-mechanical noise arising from the Brownian motion of the cantilever. It is best represented as a random force acting on the resonator with a PSD  $S_f = \frac{4k_b T M_{eff} \omega_0}{Q}$  (in  $N^2/\text{rad} \cdot s^1$ ) where  $k_b$ ,  $T$ ,  $M_{eff}$ ,  $f_0$  and  $Q$  are the Boltzmann constant, the temperature, the effective mass resonance, resonance frequency and quality factor of the resonator, respectively
- The adsorption/desorption noise due to the random arrival/departure of molecule on/from the resonator surface. A complete derivation of its PSD can be found in [181][182] and [183].
- The temperature fluctuation noise due to the fluctuation of the temperature of the resonator and consequently of its material parameters and geometric dimensions.

For the sake of completeness we shall add the Flicker noise of the amplifier and potential resistive element in the measurement loop [38]. However, it turns out that, for piezoelectric cantilever resonators with length between 1 and 100  $\mu\text{m}$ , the white amplifier noise is largely dominant. For instance, considering a small measurement bandwidth, the thermo-mechanical noise PSD referred at the output of the resonator  $S_{V,th} = \frac{k_b T Q}{4\pi^4 L f_0^3} \left( \frac{\beta_p \Phi_n'(L)}{C_p + 2C_0} \right)$  gives values between 0.1 and 10  $\text{fV}/\sqrt{\text{Hz}}$  at least one order of magnitude below state of the art low noise amplifiers white noise PSD. Accordingly, we consider that the SMLOD of a piezoelectric cantilever resonator depends only on the amplifier noise. Recalling equation (2.3-10) the output signal at the resonance frequency of a piezoelectric cantilever is given by:

$$V_{out} = \left( \frac{C_m}{2C_0 + C_p} \right) Q V_{in} \quad (2.3-12)$$

Where  $C_m$ ,  $C_0$ ,  $C_p$ ,  $Q$  and  $V_{in}$  are the motional capacitance, the static capacitance, the input capacitance of the electronic detector, the quality factor and the input signal respectively. Recalling that  $C_0 = \epsilon_{33} \left( \frac{WL + S_{pads}}{t_3} \right) = C_{0min} + C_{pads}$  and defining  $C_L = C_p + 2C_{pads}$  ( $L$  stands for load), the output signal on resonance can be rewritten as:

$$V_{out} = \left( \frac{C_m}{2C_{0,min} + C_L} \right) Q V_{in} \quad (2.3-13)$$

1.2-19), the SMLOD of a piezoelectric cantilever resonator with dominant white amplifier noise can finally be expressed as:

$$\delta m_{surf} = \frac{\rho t \langle V_{noise} \rangle}{Q V_{out}} = \frac{\sqrt{S_{amp} BW}}{Q^2 V_{in}} \frac{\mu(2 + C_L/C_{0,min})}{(C_m/C_{0,min})} \quad (2.3-14)$$

where  $S_{amp}$ , and  $BW$  are the amplifier white noise PSD and the measurement bandwidth.  $\mu = \sum \rho_i t_i$  is the cantilever mass per surface area where  $\rho_i$  and  $t_i$  are the density and thickness of each layer in the cantilever.

### 2.3.3.2. Optimization without constraints

The term  $\frac{\sqrt{S_{amp} BW}}{Q^2 V_{in}}$  in equation (2.3-14) can be considered as independent on the geometrical properties of the cantilever. Theoretically, the quality factor  $Q$  in air should be dominated by viscous damping and should scale like  $W \left(\frac{t}{L}\right)^2$  [184]. Also, the optimum voltage  $V_{in}$  should be limited by the onset of mechanical nonlinearity, equal to  $\frac{6.3L}{\sqrt{Q}}$  [121]. However, these theoretical formulae do not account for our experimental results:  $Q$  varies significantly from one cantilever to another and the maximum input voltage is found to be much lower than expected. As a detailed study of  $Q$  and  $V_{in,max}$  is out of the scope of this dissertation we thus exclude them from this design optimization and use their typical experimental values for numerical calculations (100 and 750 mV, respectively).

The second term in equation (2.3-14) can be further split into three parts.

- *The surface mass density*  $\mu = \sum \rho_i t_i$  where  $\rho_i$  stands for the mass density of each layer. This term is minimized when the total thickness of the beam is minimized, and especially when the dense metallic electrodes are chosen to be as thin as possible.
- *The capacitive load*  $2 + C_L/C_{0,min}$ . The parasitic capacitance  $C_p$  can be reduced by bringing the first amplifier stage as close as possible to the cantilever. This can be done, for example by integrating the resonator and its

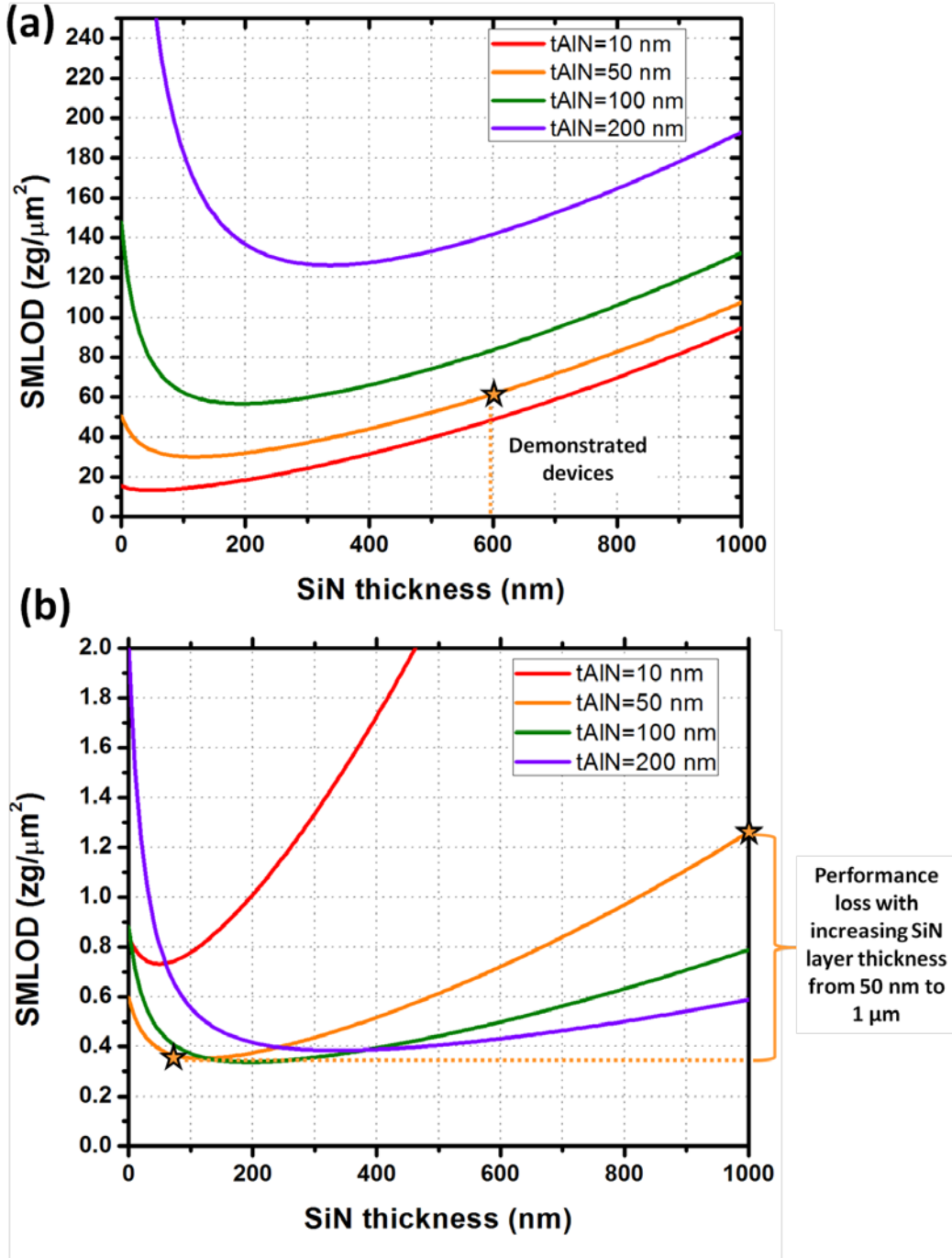


**Figure 2- 6:** SMLOD as a function of the SiN layer thickness and for different AlN layer thicknesses and for two capacitance matching cases: (a)  $C_L = 100 \text{ pF} > C_0$  for all AlN thicknesses (b)  $C_L = 1 \text{ pF} < C_0$  for all AlN thicknesses. For comparison with experimental results, the remaining parameters are common for the two figures: bottom and top electrode thickness : 100 nm and 25 nm (respectively), length and width:  $80 \mu\text{m}$  and  $40 \mu\text{m}$  (respectively), the actuation voltage, quality factor, measurement bandwidth and amplifier white noise are 750 mV, 100, 0.1 Hz and  $5 \text{ nV}/\sqrt{\text{Hz}}$  (respectively). The static capacitance of the cantilever  $C_0$  varies from 28 pF for 10 nm thick AlN film down to 1.4 pF for 200 nm thick AlN films

electronic on the same chip, taking advantage of the compatibility of AlN with CMOS processing [185].  $C_{pads}$  can be reduced by reducing the surface of the non-mechanically active areas but at the cost of additional process steps as in [29]. When  $C_L/C_0 \gg 2$  i.e. when  $C_p$  or the non-mechanically active parts of  $C_0$  dominates, the SMLOD is proportional to the ratio  $\frac{C_L}{C_m} = \frac{\langle EI \rangle_{eq} C_L}{W^2 L \beta_p^2 \gamma_n}$  and thus inversely proportional to the device surface area. Beside, as illustrated in Figure 2- 6(a), decreasing the AlN layer improves drastically the transduction efficiency ratio  $\beta_p / \langle EI \rangle_{eq}$ . It increases the actuation electric field for a given voltage, decreases the equivalent rigidity  $\langle EI \rangle_{eq}$  and puts the active AlN layer where the bending stress is maximum maximizing thus the piezoelectrically induced charges. Finally, for a given thickness of AlN and electrodes layers, a tradeoff exists for the thickness of the SiN layer. Indeed, if it is too thin,  $\beta_p$  approaches zero and only in-plane motion can be actuated, while if it is too thick the cantilever becomes too rigid to be deflected. When  $C_L/C_{0min} \ll 2$  the SMLOD is proportional to  $\frac{C_{0min}}{C_m} = \frac{\langle EI \rangle_{eq} \epsilon_{33}}{W \beta_p^2 \gamma_n t_3}$  and independent from the cantilever surface area ( $\langle EI \rangle_{eq}$  is proportional to  $W$ ).

- *The static capacitance over motional capacitance ratio*  $\frac{C_{0min}}{C_m} = \frac{\langle EI \rangle_{eq} \epsilon_{33}}{W \beta_p^2 \gamma_n t_3}$  depends only on the thickness of the different layers relative to each other. Figure 2- 6(b). Presents the SMLOD curves as function of SiN thickness and for different AlN thicknesses, in the case  $C_L/C_{0min} \ll 2$ ; i.e. when SMLOD is dominated by  $\frac{C_{0min}}{C_m}$  ratio. As opposed to Figure 2- 6(a), the curves are now intersecting and minimum SMLOD is reached for  $t_{AlN} = 100$  nm, instead of 10 nm. The existence of such optimum for the AlN layer thickness is related to the competition, when this layer thickness is decreased, between, on one side, the decrease of the linear mass density  $\mu$  and the improvement of the transduction efficiency  $\beta_p / \langle EI \rangle_{eq}$ , versus, on the second side, the increase of the static capacitance  $C_{0min}$  of the cantilever.

As a conclusion, within the dimension range where the product quality factor by the limit of non linearity does not scale, the optimum performance depends not only on the cantilever design but also on the input capacitance of the detection electronic.

When the input capacitance of the electronic amplifier (accounting for the parasitic capacitance of cables and the capacitance of the cantilever pads) is large, the optimum design consists in increasing the length and width of the cantilever and decreasing the thickness of the AlN layer. When the input capacitance of the electronic amplifier is low, the SMLOD is independent on the length and width of the cantilever and an optimum exists for the AlN layer thickness. As these two optimization strategies are opposite, the ultimate optimum is reached at the meeting point of the two cases: when the input (parasitic) capacitance of the electronic detector matches the static capacitance of the cantilever.

Therefore, given the electronic detector input capacitance and the minimum thickness of the AlN layer allowed by the fabrication process, the optimum design is defined as follow:

- The AlN layer must be chosen as thin as possible ( $t_{AlN,min}$ )
- The length and width must be chosen such that  $C_{Omin} = \frac{WL\epsilon_{33}}{t_{AlN,min}} = \frac{C_L}{2}$
- The dense metallic electrodes should be chosen as thin as possible in order to minimize the mass density per unit length of the cantilever
- The thickness of the SiN elastic layer should be chosen equal to its optimum value given by  $\left. \frac{\partial \delta m_{surf}}{\partial t_{SiN}} \right|_{t_{2min}, t_{3min}, t_{4min}} = 0$  (c.f. Figure 2- 7 )

When all of these design rules are validated, the SMLOD value depends only on the minimum AlN thickness allowed by the technology and not on the electronic detector input capacitance value: it is cancelled out in the SMLOD formula. Figure 2- 8 gives ultimate SMLOD values as a function of the AlN thickness assuming a length over width ratio  $L/W = 10$ . As the length, the width and the different layers thicknesses are fully defined in these design rules, the cantilever resonance frequency is also defined and depends on both the minimum AlN thickness allowed by the technology and the input (parasitic) capacitance of the electronic detector. Figure 2- 9(a) and (b), gives the optimum length (assuming  $L/W = 10$ ) and optimum resonance frequency, respectively, as a function of the input capacitance of the electronic detector and for different minimum AlN thicknesses.

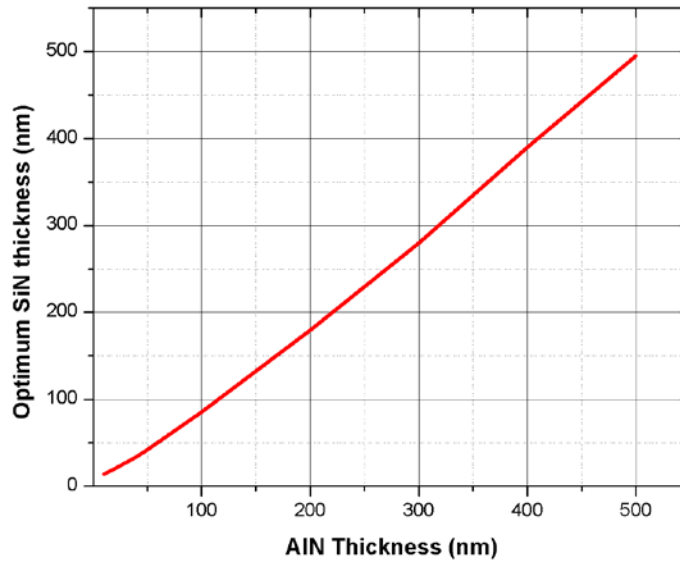


**Figure 2- 7:** Optimum SiN thickness as a function of the AlN thickness defined by the equation  $\frac{\partial \delta m_{surf}}{\partial t_{SiN}} = 0$  and calculated, for this graph, with a bottom and top Pt electrode of thickness equal to 10 nm.

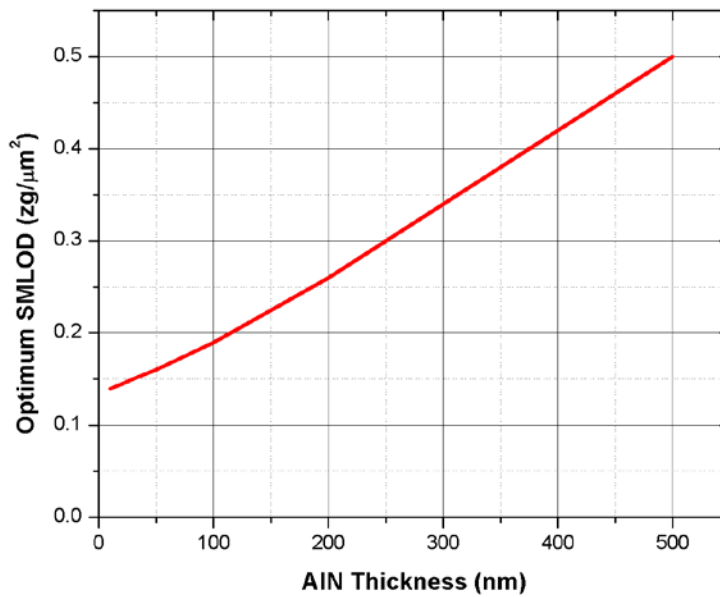


**Figure 2- 8:** Ultimate SMLOD reached thanks to our design rules as a function of the minimum AlN thickness allowed by the technology. For this graph parameters are: actuation voltage, quality factor, measurement bandwidth and amplifier white noise equal to 750 mV, 100, 0.1 Hz and  $5 \text{ nV}/\sqrt{\text{Hz}}$  (respectively). Minimum Pt layer thickness (top and bottom): 10 nm. The length and width are chosen such that  $C_{0min} = \frac{C_L}{2}$  and  $L/W = 10$  (this eliminates  $W, L$  and  $C_L$  from the SMLOD formula), the SiN layer thickness is taken at its optimum value (*c.f.* Figure 2- 7)

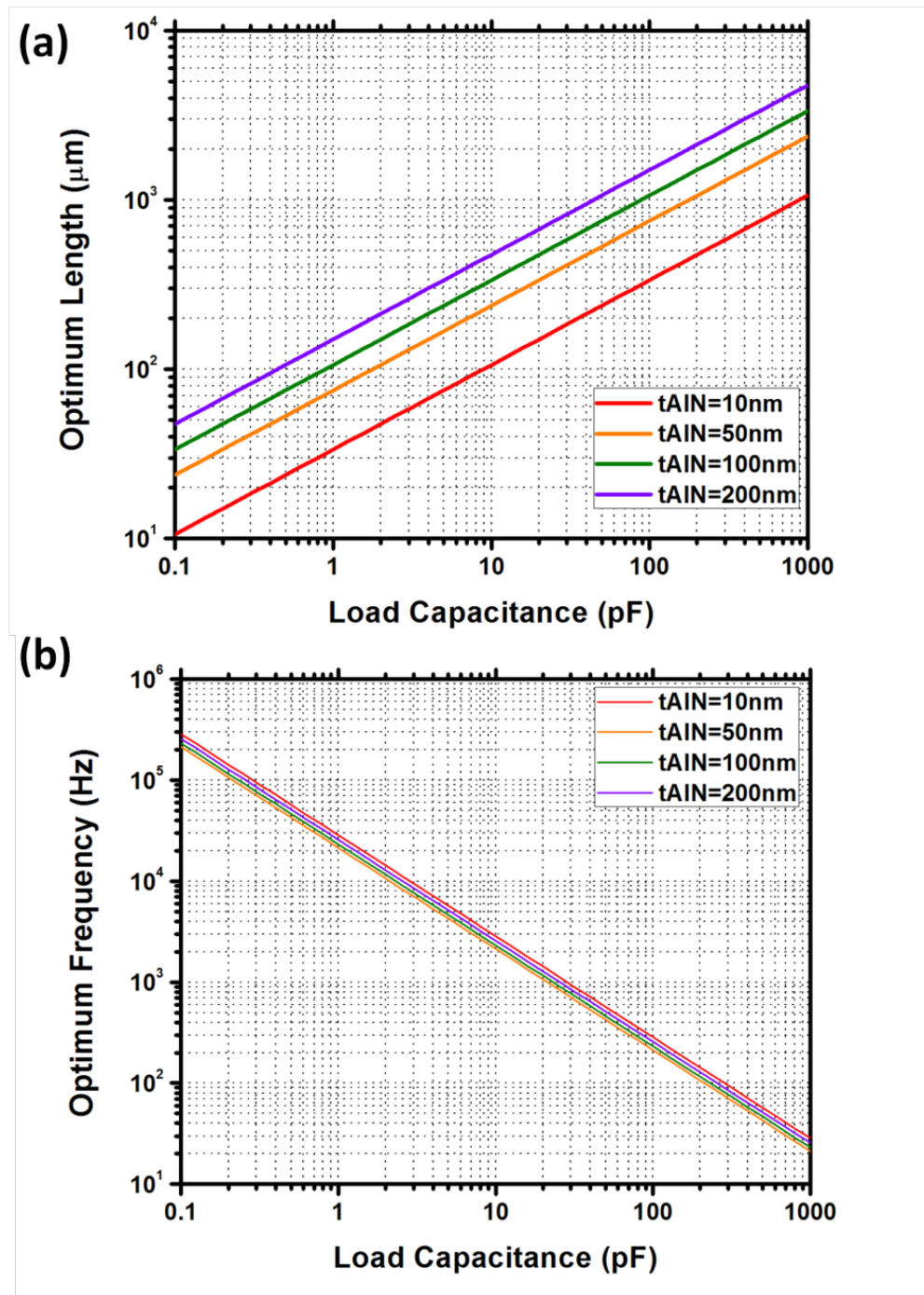


**Figure 2- 9:** Optimum length and optimum resonance frequency according to our design rules. Parameters for this graph are the same as in Figure 2- 8

### 2.3.3.3. Optimization with constraints

- **Case 1: Matched capacitance**

Following the design rules, for an input capacitance of the electronic detector of  $C_L = 100$  pF and a minimum AlN layer thickness of 50 nm, as per our fabrication and characterization capabilities, the ultimate SMLOD is equal to  $0.21$  zg/ $\mu\text{m}^2$ . The corresponding length, width, SiN and Pt electrodes thickness are: 760  $\mu\text{m}$ , 76  $\mu\text{m}$ , 48 nm and 10 nm (hence a total thickness of 118 nm). The corresponding resonance frequency is 212 Hz.

- **Case 2: Stiffness limited**

Such design is clearly not practical: long and thin cantilevers are very flexible and therefore very sensitive to built-in stress of the different material layer, temperature fluctuations and ambient vibrations. It is thus necessary to stiffen the cantilever.

The first course of action consists in choosing a smaller  $L/W$  ratio. The length can thus be decreased and the width increased maintaining the cantilever surface area constant and thus the SMLOD value. Our analytical model and the conclusions we have drawn will become less valid with respect to Euler Bernoulli theory of flexural beam, but as demonstrated by our experimental results (*c.f.* section 3.3.2) and FEM simulation results (*c.f.* appendix B.1) a ratio  $L/W = 2$  does not bring significant numerical errors. With this correction the optimum design is now:  $L = 340$   $\mu\text{m}$   $W = 170$   $\mu\text{m}$  and the corresponding resonance frequency is 1.14 kHz.

The second course of action consists in increasing the SiN layer thickness and decreasing the length and the width of the cantilever. Increasing the SiN thickness is however less penalizing for the sensing performance. Same SMLOD values as in Figure 2- 6(b) are accessible with an input capacitance of the electronic detector of  $C_L = 100$  pF provided that the static capacitance of the cantilever matches  $C_L$ . In this case, the increase of the SMLOD due to an increase of the SiN thickness from 50 nm to 1  $\mu\text{m}$  is limited: from  $0.38$  zg/ $\mu\text{m}^2$  to  $1.2$  zg/ $\mu\text{m}^2$  (*c.f.* Figure 2- 6 (b)) whereas a decrease of the length by only a factor of 2 results in an increase of the SMLOD by a factor of 4.

- **Case 3: Quality factor and onset of non-linearity limited**

As a last comment on this design optimization study, we shall come back on our hypothesis of constant quality factor and cantilever tip displacement amplitude at the onset of non-linearity. As already stated, if this last parameter is limited by mechanical non linearity it must be equal to  $\frac{6.3L}{\sqrt{Q}}$  [121]. In this case the maximum output signal will be given by:

$$V_{out} = \frac{6.3WL\beta_p \Phi'_n(L)}{\sqrt{Q}\Phi_n(L)(C_L + 2C_0)} \quad (2.3-15)$$

And the SMLOD:

$$\delta m_{surf} = \sqrt{\frac{S_{amp} BW}{Q} \frac{\Phi_n(L)(C_L + 2C_0)}{12.6WL\beta_p \Phi'_n(L)}} \quad (2.3-16)$$

If the quality factor  $Q$  in air is dominated by viscous damping, it should scale like  $W \left(\frac{t}{L}\right)^2$  [184].  $\Phi_n(L)$  scales as  $L$ ,  $\Phi'_n(L)$  does not scale,  $\beta_p$  scales as  $t$  and  $C_L + 2C_0$  scales as  $\frac{WL}{t}$  assuming that the criteria for optimum output signal detection  $C_0 = C_L$  is met. Thus, considering the variation of the onset of non linearity and quality factor with device geometry, the SMLOD scales as:

$$\delta m_{surf} \propto \frac{L^2}{\sqrt{W}t^3} \quad (2.3-17)$$

This theoretical estimation of the SMLOD variations is contradictory to the previous design rules and we must expect an optimum design “somewhere in between”. It turns out that, to the extent of our characterization capabilities, the viscous damping model fails to predict measured quality factors that vary significantly from one cantilever to another. Also it has been observe that the onset of non-linearity is reached at a much lower driving power than expected with the mechanical non-linearity model. These two observations leads to the conclusion that other phenomena limits both the quality factor and on-set of non-linearity, a detail study is thus required to draw a complete conclusion on the optimum design.

## 2.4. Conclusion

In this chapter we have compared the different transduction methods available in M/NEMS resonators and shown that the piezoelectric transduction offers several advantages: it requires neither strong dc biasing nor small gaps like electrostatic / capacitive transduction, or external bulky setup like optical and magnetic transduction, and is inherently low power, as opposed to thermo-elastic and piezoresistive transduction. Additionally, piezoelectricity is a stress induced effect, as opposed to capacitive displacement transduction, and hence its efficiency is unchanged when devices are scaled down.

After an overview of linear piezoelectricity theory and available piezoelectric material thin films, we have focused the discussion on the implementation of the piezoelectric transduction in cantilever resonators. We have shown that although it is widely used in micro-scale cantilever, it has been rarely studied at the nano-scale because of the difficulties to fabricate, with current processing technologies, piezoelectric film with thickness lower than 100nm and high piezoelectric performance.

We have then focused on the analytical modeling and the design optimization of piezoelectric cantilever resonators. Following section 1.2.3.2, where we have shown that the SMLOD is the most pertinent figure of merit to carry out a design optimization study. We have shown that the theoretical SMLOD of a piezoelectric cantilever resonator depends not only on the design of the cantilever (thickness of the different layers in the cantilever, length and width) but also on the way the cantilever is integrated with the detection electronic (input capacitance of the first amplifier stage, connection pads capacitance). The optimum design reached when the smallest AlN thickness allowed by the fabrication technology is used and when the cantilever capacitance is matched to the load capacitance. In this way, the transduction efficiency is maximized and the total thickness of the cantilever minimized.

We can thus conclude that the development of sub-100 nm thick AlN films for the transduction of cantilever resonator is the key technological aspect for development of high resolution piezoelectric cantilever resonator based gas sensors.

# Chapter 3: Sensing Devices Fabrication and Characterization

---

This chapter is dedicated to the technological developments achieved during this PhD towards the demonstration of high resolution piezoelectric cantilever gravimetric gas sensors. Following the conclusion of the previous chapter, reducing the thickness of the piezoelectric layer used to actuate and detect cantilever motion is critical to improve gravimetric sensing performances. Therefore, the first part of this chapter is dedicated to the development of 50 nm thick AlN films, with high piezoelectric performances achieved during the master thesis project of Julie Abergel.

The second part of the chapter is dedicated to the integration of these AlN piezoelectric thin films within real device fabrication processes. Based on the second conclusion of the previous chapter, and considering that the integration of a device in a fully optimized electronic circuit will come at a later stage of the development, we have chosen to focus on two types of design: micro-cantilevers and arrays of nano-cantilevers. The first design follows entirely the philosophy of the design optimization strategy presented in the previous chapter: if the input capacitance of the electronic detector is large, long and wide cantilevers provide higher performances. The second design intends to overcome the decrease of the efficiency of the piezoelectric transduction in nano-scale device with high input capacitance detector by summing up the signal of a large number of identical nano-scale resonators.

To shorten the development time, we have chosen to fabricate first micro-cantilevers and take advantage of 1) the full-custom processing facilities of the Plateforme des Technologies Avancées clean room and 2) the experience gained about manufacturing similar devices in a previous project [186]. The obtained devices are functional and their electrical response will be presented and compared to analytical modeling. Our attempt for the fabrication of large array of nano-scale cantilever resonators using Very Large Scale fabrication technique will be presented at the end of this chapter along with the required technological development to overcome encountered difficulties.

## 3.1. Sub-100 nm piezoelectric films

### 3.1.1. Choice of the piezoelectric material

As presented in the introduction, the first step towards the development of ultra-thin piezoelectric cantilever is to investigate the possibility of fabricating materials stacks (bottom electrode / piezoelectric material / top electrode) with thicknesses below 500 nm and sufficiently high piezoelectric coefficients. This requirement on the thickness range is very different from what is currently used for piezoelectric devices [187][188]. However, several PZE materials thin films with thickness around 100 nm have already been demonstrated in the literature (*cf.* Table 3- 1). All these films have different material properties and deposition techniques that should be considered to make the proper choice.

Quartz and LiTaO<sub>3</sub> present a low effective  $e_{31}$  piezoelectric coefficient that limits their use in extensional bimorph operation. ZnO provides several advantages such as low Young's modulus and electric permittivity and compatibility with CMOS processing. However in the literature ZnO thin films have not been investigated in the low thickness range [189]. Beside, slightly thicker films as in [190] exhibit high leakage currents, which is not desired in our final device. PZT provides high  $e_{31}$  piezoelectric coefficient but also a too high permittivity and therefore too high a static capacitance to be used for detection. LiNbO<sub>3</sub> can provide a high  $e_{31}$  coefficient at the level of PZT. However it can be cumbersome to obtain thin LiNbO<sub>3</sub> films with optimum crystalline orientation with classical thin film deposition such as sputtering. Recently, the now famous SMART CUT™ films transfer technique has been used to obtain the right film orientation [191]. Sputtered LiNbO<sub>3</sub> provides large  $e_{41}$  and  $e_{51}$  coefficients that could be exploited in shear bimorph [192] but this bending motion actuation method is far less effective than extensional bimorph.

AlN provides a good trade-off among these piezoelectric materials with a low density and permittivity, moderate  $e_{31}$  piezoelectric coefficient and relatively high Young's modulus. In addition, AlN has already encountered commercial successes with FBAR resonators and is known to provide high chemical and thermal stability and compatibility with CMOS processing [185]. To date, the first report on AlN thin films deposition dates from the early seventies [193] for application in optics. Since

Mat.	PZE Coeff. $e_{31}$ (C. m <sup>-2</sup> )	Perm. $\epsilon_{33}$	Young's Modulus $Y^E$ ? (MPa)	Density $\rho$ (kg. m <sup>-3</sup> )	Thickness (nm)	Deposition Technique
PZT	-5	1400	100	7000	130 160	Sol gel [200] Sputtering [200] [186]
LiNbO <sub>3</sub>	0.2	27.7	293	4650	< 1000	Sputtering [201]
LiTaO <sub>3</sub>	-0.38	43	282	7490	160	Transfer [202][203]
ZnO	-1.7	11	123	5700	200	Sputtering [190]
AlN	-0.74	10	343	3300	100	Sputtering [29][30]

**Table 3- 1:** Relevant material properties for ultrathin piezoelectric films in the literature

then, several other deposition techniques have been investigated such as Chemical Vapor Deposition (CVD / MOCVD / PECVD) [194] Molecular Beam Epitaxy (MBE) [195][196], Laser Pulse Ablation (LPA)[197] and different sputtering techniques [198][199]. Today, the latter ones, and more especially DC pulsed reactive magnetron sputtering, have become the mainstream technique thanks to a low process temperature that limits the built-in stress and the widespread availability of sputtering facilities in CMOS foundries. However, as demonstrated in [27], further optimizations of this process are required to fabricate sub-100 nm AlN films with good piezoelectric properties.

### 3.1.2. 50 nm AlN films development

#### 3.1.2.1. DC pulsed Reactive Magnetron Sputtering

Growth mechanisms determine the microstructure and the morphology of thin films, which ultimately determine their physical properties such as residual stress, surface roughness, mass density, elastic and piezoelectric constants. It is thus critical to understand their influence in view of optimizing material properties. Sputtering is a physical deposition process that uses ions generated in glow discharge plasmas and accelerated by an electric field to physically eject atoms from a target surface. These

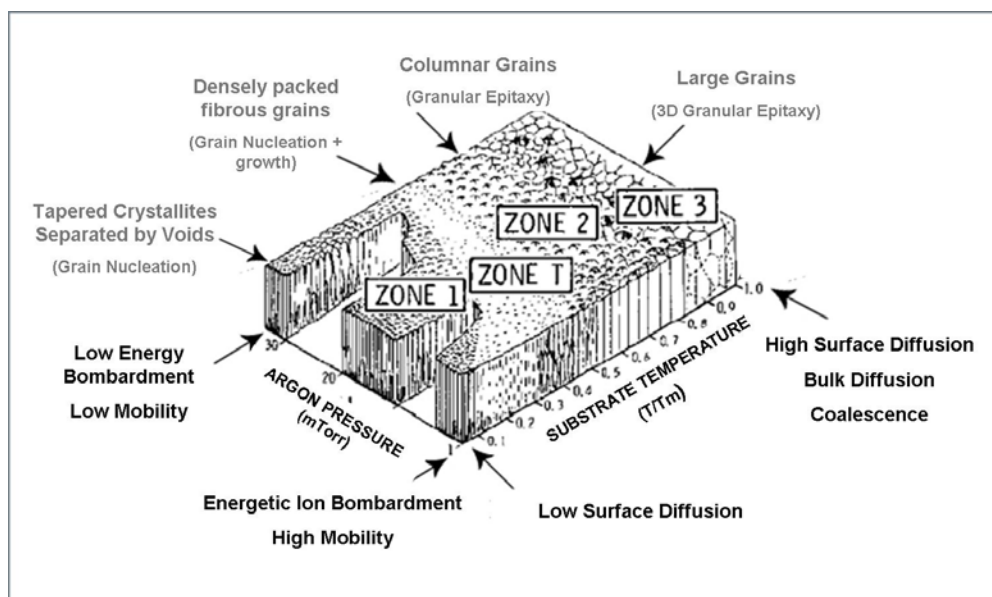


**Figure 3- 1:** Growth mode and corresponding crystalline structure. Image reproduced and modified from [204]

so-called sputtered atoms travel through the vacuum chamber and land on the sample surface where they diffuse to find an energy-favorable site and establish bounds. In the case of AlN, sputtered films present a crystalline structure in T zone [204] (*cf.* Figure 3- 1) with small grains at the interface between the substrate and the film, which evolve into columnar grains through the film thickness.

In the literature, the quality of AlN sputtered film is evaluated in terms of grain size, crystal orientation, intrinsic stress and uniformity across the wafer. Process parameters such as the distance between target and substrate [205], pressure, RF discharge power [206] and DC bias [207] influence the bombardment energy and should be optimized to find a trade-off between surface mobility and defects density. In addition, these process parameters influence the built-in stress and a second trade-off should be found between good structural properties and reasonable stress [198].

Finally, a third optimization should be carried out for the piezoelectric properties [208]. Actually, the piezoelectric response is the average response of each crystallite. Thus, good piezoelectric properties can be obtained in small grains polycrystalline films providing that each grain presents the same crystallographic orientation (*c*-axis in our case) and polarization direction. The quality of the crystal

orientation is characterized by the Full Width at Half Maximum (FWHM) of the x-ray rocking curve. Better-oriented films possess lower FWHM values. However, FWHM is insensitive to the presence of inversion domains that leads to the cancellation of the piezoelectric macroscopic response of inversely polarized grains [209][210]. Therefore, the chemical and physical properties of substrate for the growth of AlN are also of prime importance. This is why, as reported in [198] and [211], Platinum (Pt) is an efficient substrate for the growth of AlN thanks to its hexagonal symmetry and chemical stability with respect to plasma ions.

In [27], all AlN films are deposited with the same process conditions and without optimization with respect to the targeted thickness. The authors observe that AlN first starts growing by local epitaxy with a precision of alignment defined by a low textured (rocking curve FWHM between  $3.7^\circ$  and  $3.9^\circ$ ) underlying Pt layer. It is only after the growth of the first 100 nm that the crystalline planes alignment improves. Therefore, their process should be considered satisfactory for the growth of AlN films with thicknesses above 100 nm where AlN – AlN epitaxy dominates but not for the fabrication of thinner films where the Pt / AlN interface properties dominate. Based on these observations, the fabrication of 100 nm AlN films with good piezoelectric properties requires thus a special optimization that focuses on the nucleation process. It has been the main objective of Julie Abergel's master thesis who studied the influence of the substrate properties and DC bias on the uniformity, crystallite orientation, stress and piezoelectric properties of AlN films in the low thickness regime. The results shown in the next section stem from her work.

### 3.1.2.2. Results

Starting from a well-stabilized AlN deposition process for BAW resonators with usual thicknesses of 800 nm, AlN films were deposited on 200 mm silicon wafers with thickness from 50 nm up to 800 nm, different DC bias and different metal electrodes on the top of the Si substrates (Platinum, Molybdenum, Tungsten and  $p^{++}$  doped silicon). The residual stress is extracted from wafer curvatures (measured with a KLA-Tencor Flexus 2320) before and after the deposition of each layer with the help of Stoney formula [198]. XRD patterns are collected in both  $\theta - 2\theta$  and  $\omega$

scans, respectively, for dominant orientation and rocking curve FWHM quantification [198]. Finally, the effective transverse PZE coefficient  $e_{31,eff}$  is measured thanks to the method reported in [212]. A squared capacitor containing the piezoelectric stack (bottom electrode / AlN / top electrode) with millimeter size is deposited and patterned on the top of a silicon wafer, which is in turn cleaved into  $\sim 4 \times 1 \text{ cm}^2$  cantilevers. During the experiment, the cantilever is clamped at one end and brought into oscillation by imposing and releasing a known displacement on its free end. The electric discharge in a resistor of the piezoelectric capacitor belonging to the cantilever is then recorded.  $e_{31,eff}$  is extracted from the integral of the obtained curve.

For AlN films deposited on Pt and Mo, the residual stress can be switched from tensile to compressive by reducing the DC power in agreement with the results reported in [213][208]. XRD measurements show that all fabricated films are fully c-axis oriented. Besides, the rocking curve FWHM increases with decreasing thickness from  $1.4^\circ$  to  $2.4^\circ$ , in agreement with the results reported in [27][30][214] but  $e_{31,eff}$  remains constant and equals  $0.8 \text{ C} \cdot \text{m}^{-2}$  close to the state of the art value for thicker films [27](*cf.* Figure 3- 2).

Table 3- 2 presents  $e_{31,eff}$  values obtained on different stacks. It demonstrates that Mo, Pt and W can be used as a growth bottom electrode (stacks **Ref**, **B1** and **B2**) without loss of performance. Also, the presence of a seed layer that improves the texture of the growth substrate is critical (stacks **S1** and **S2**). In the same fashion, the thickness of the bottom electrode cannot be decreased below 50 nm (stacks **BT1** and **BT2**).

Following our objective of fabricating piezoelectric cantilever gravimetric gas chemo-sensors, these first experimental developments are very encouraging as they demonstrate that the limitation presented in [27] can be overcome. Besides, they provide useful information for device design such as the viability of complete material stacks with minimum thickness of 150 nm.

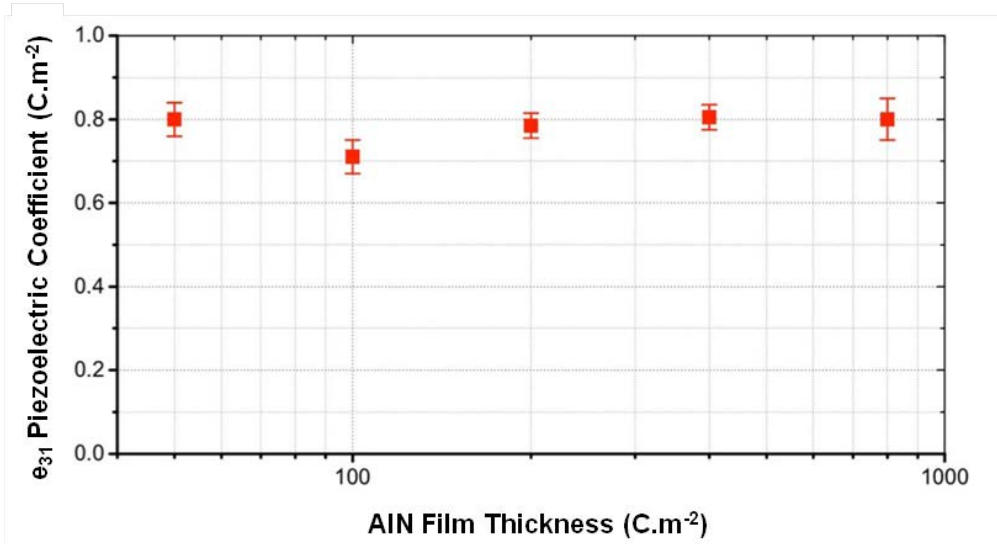


**Figure 3- 2:** Variation of AlN  $e_{31,eff}$  with film thickness

Sample	Seed layer	Bottom Electrode	Top Electrode	$e_{31}$
Ref	AlN	Mo 100 nm	Pt 80 nm	0.8 C. m <sup>-2</sup>
B1	TiO <sub>2</sub>	Pt 100 nm	Pt 25 nm	0.8 C. m <sup>-2</sup>
B2	AlN	W 100 nm	Pt 80 nm	0.8 C. m <sup>-2</sup>
S1	None	Mo 100 nm	Pt 100 nm	0.24 C. m <sup>-2</sup>
S2	None	Si p <sup>++</sup> (wafer)	Pt 100 nm	0.11 C. m <sup>-2</sup>
BT1	AlN	Mo 50 nm	Pt 80 nm	0.73 C. m <sup>-2</sup>
BT2	AlN	Mo 25 nm	Pt 80 nm	0.46 C. m <sup>-2</sup>

**Table 3- 2:** Influence of the type and thickness of the bottom electrode and of the presence of a seed layer on  $e_{31,eff}$  of 50 nm thick AlN films

## 3.2. Micro-cantilevers fabrication

### 3.2.1. Process

Following the success of the development of 50 nm thick AlN films with satisfactory piezoelectric properties and controllable stress, the following step consists in fabricating real cantilevers. Although we wish to benefit from the VLSI integration capability of micro-technologies, we have decided to work first at the sample level exploiting the customizable clean room facilities of the Plateforme des Technologies Avancées (PTA) and develop a reliable fabrication process that could be scaled up

later on in LETI's industrial clean rooms. In order to remain compatible with VLSI processes, we have decided to use optical lithography rather than e-beam lithography, as the latter is expensive and time consuming, even though very powerful for the fabrication of nano-scale devices.

Optical lithography steppers available in PTA clean room facilities are limited to 2  $\mu\text{m}$  for lateral dimensions. Therefore, we decided to reuse an existing set of masks for the fabrication of 80 – 400  $\mu\text{m}$  long cantilevers (*cf.* Figure 3- 3). Although this strategy is supposed to simplify the fabrication process, one peculiar difficulty lies in the fact that hundreds of micrometers long cantilevers are very sensitive to built-in stress. It induces static bending of released structures and even, in the worst cases, breaking the cantilevers.

To avoid this unwanted effect, chosen material stacks include a thicker structural layer (in Si or  $\text{Si}_3\text{N}_4$ ) in order to stiffen the whole structure. These films have the additional advantage of almost null built-in stress. Figure 3- 4 presents the two selected stacks. The first one is composed of  $\text{Si}_3\text{N}_4$  (600 nm) / AlN seed / Pt (100 nm) / AlN (50 nm) / Pt (25 nm). It is compatible with  $\text{XeF}_2$  isotropic etch of the Si substrate for the release step. The choice of  $\text{Si}_3\text{N}_4$  as a structural layer is motivated by

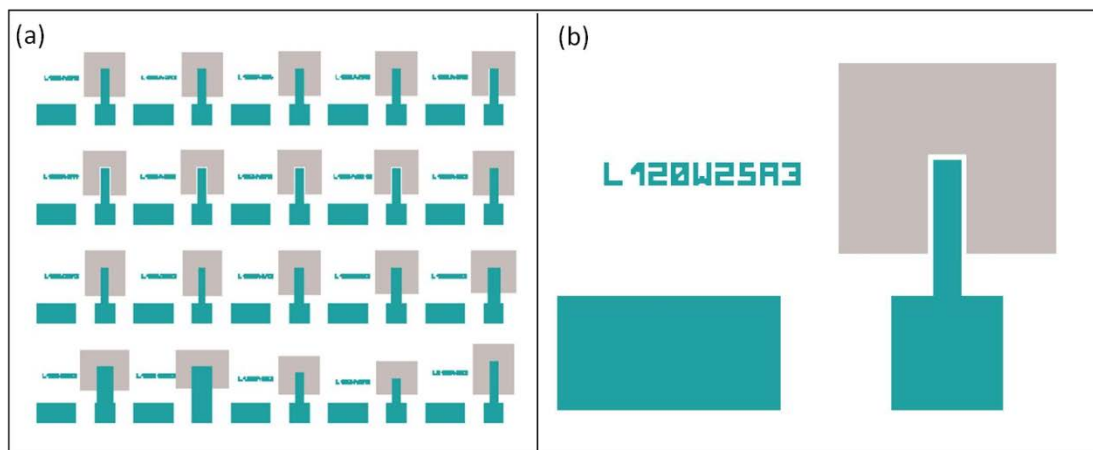


**Figure 3- 3:** Micro-cantilevers mask layout (a) view of the complete patterns containing all the cantilever designs (b) details of one particular cantilever. The first mask level in green is used to pattern the top electrode and the **AlN** layer. The second mask is the negative of the grey patterns and is used to etch an access to the Si substrate through the bottom electrode and the  **$\text{Si}_3\text{N}_4$**  structural layer.

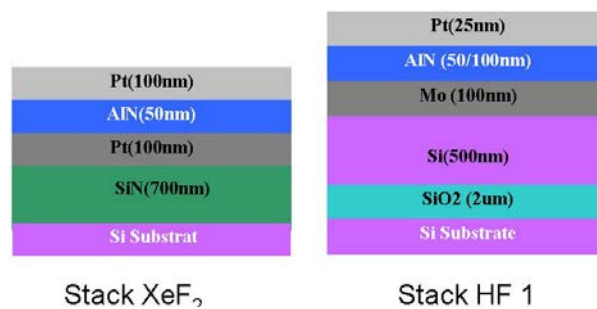


**Figure 3- 4:** Chosen material stacks for micro-cantilevers fabrication

the experience gained in a previous project [186] and the choice of Pt is motivated by its compatibility with the deposition of 50 nm thick AlN films as presented in the previous section. The second stack is based on a Silicon On Insulator (SOI) wafer with a 2  $\mu\text{m}$  thick buried oxide (BOX) and a 500 nm thick epi-Si layer. In this case, the piezoelectric stack is AlN seed / Mo (100 nm) / AlN (50 nm) / Pt (25 nm). The  $\text{SiO}_2$  sacrificial layer can be etched away with liquid hydrofluoric acid (HF) solution. This technique is closer to the vapor HF technique usually used in VLSI processes.

Figure 3- 5 presents the two lithographic steps process flow for the fabrication of the micro-cantilevers. After the full sheet deposition of the stack on 200 mm performed in LETI's CMOS clean room, the next step consists in cutting 4  $\text{cm}^2$  samples in order to perform the following steps in PTA clean room facilities:

- Lithography

The two lithography steps are performed using a UV-mask aligner *Karl Suss* MJB 4 and a 2  $\mu\text{m}$  thick positive photoresist AZ5212. Soft and hard bake times correspond to the standard recipe provided by the photoresist manufacturer (*Microchemicals GmbH*): 60 seconds @ 90  $^\circ\text{C}$  and 90 seconds @ 100  $^\circ\text{C}$  respectively. For the first step, a minority of the surface area of the mask blocks the UV beam, hence the exposure time is reduced to 12 seconds. On the contrary, for the second step the majority of the surface area of the mask blocks the UV beam and the exposure time is increased up to 17 seconds.

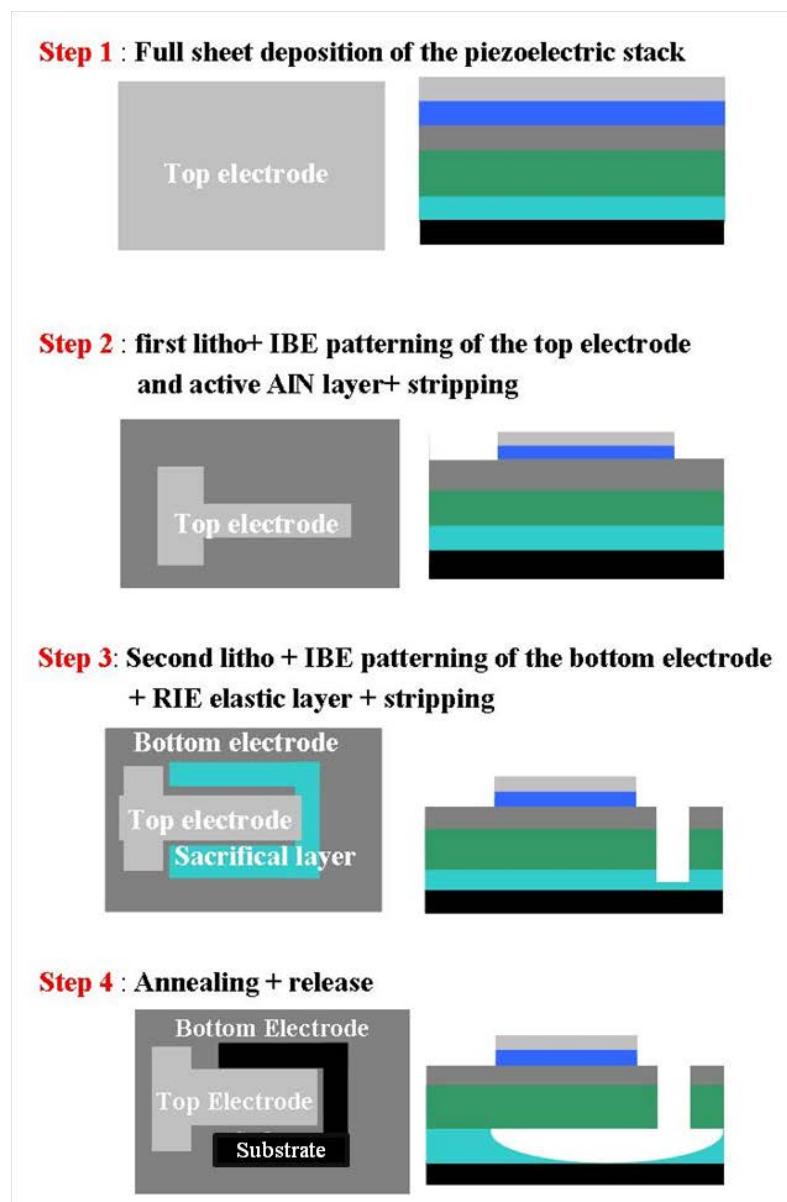


**Figure 3- 5:** Micro-cantilevers fabrication process flow

- Ion Beam Etching

Ion Beam Etching, or ion milling, is used to pattern the Pt or Mo electrodes and AlN films. This etching technique is purely physical and provides relatively low etching rate: 10 nm/min for Pt and Mo and 4 nm/min for AlN. A Secondary Ion Mass Spectrometer (SIMS) records the type of ions ejected from the samples and allows stopping the etching process when proper etching depth is reached. The etching time is variable for each run and varies of about  $\pm 1$  minute depending on the previous utilization of the IBE setup. The maximum etching time is achieved during the second

step for patterning the bottom electrode. To avoid solidification of the photoresist due to overheating, we split the process in 7 minutes steps followed by a 30 seconds oxygen plasma and 1 minute thermalization.

- Structural layer Reactive Ion Etching

A chemically enhanced dry etch process is used to pattern the thicker  $\text{Si}_3\text{N}_4$  (600 nm) and Si (500 nm) layers. The standard recipe for  $\text{SF}_6$  anisotropic Inductively Coupled Plasma (ICP) etch has been modified by increasing the bias power in order to improve patterns steepness. A small amount of oxygen is also introduced in the plasma in order to avoid solidification of the resist. In this way, we achieved etching rates of 30 nm/min for  $\text{Si}_3\text{N}_4$  and 100 nm/min for Si for a total process time of 20 minutes and 5 minutes respectively.

- Stripping

Due to the unavoidable partial solidification, the photoresist is not removed easily especially after the second lithography step. Sonication in successive baths of AZ remover, Acetone, Alcohol and de-ionized water is usually not sufficient and leaves residues over the sample surface. Exposing the sample to  $\text{O}_2$  plasma during 30 seconds, prior to the sonication provides some improvement. But the most efficient technique is to wipe the sample surface with a clean cloth soaked in acetone.

- Thermal Annealing and Release

These last two steps are critical for the control of the built-in stress induced deflection of the beam and requires equipment that is not available in the PTA clean room. They are thus realized with the LETI MEMS 200 clean room facility. Thermal annealing is performed in a UV Rapid Thermal Annealing (RTA) oven in three steps: 5 minutes ramp up to the targeted temperature, 3 minutes stabilization and 30 minutes cooling. As mentioned above,  $\text{XeF}_2$  vapor and wet HF processes are employed for the release steps of the first and second stacks respectively. The etching depth with  $\text{XeF}_2$  is defined by the number of cycles (2 minutes exposure to gas followed by chamber cleaning and purging). For wet HF, etching time and solution concentration are the two control parameters. But, due to the too thin  $\text{SiO}_2$  thickness chosen for stack 2, we have never managed to fully release these cantilevers and only the  $\text{XeF}_2$  process produced working cantilevers.

### 3.2.2. Static deflection control

In the same fashion as we intend to actuate the flexural modes of our piezoelectric bimorph cantilever, internal in-plane stress in the different layers produces a static bending of the cantilevers. Let us consider a cantilever beam with  $n$  material layers each undergoing an in-plane stress  $\sigma_i$ . The static deflection at the free end of the beam can be obtained using the equivalent beam approach (*cf.* section 2.3.1) leading to the following equation for vertical displacement of the free end of the cantilever:

$$w(L) = \frac{M}{2\langle EI \rangle_{eq}} L^2 \quad (3.2.1)$$

where the bending moment due to the built-in stress is:

$$\begin{aligned} M &= \int_0^{\sum t_i} (z - z_0) \sigma_i dy dz \\ &= W \sum_{i=1}^n \sigma_i t_i \left( \frac{t_i}{2} + t_{i-1} + \dots + t_1 - z_0 \right) \end{aligned} \quad (3.2.2)$$

Equation (3.2-1) indicates that longer beams are more sensitive to the static bending, but also that the deflection can be cancelled by balancing the stress of the different layers. Our first idea consists thus in tuning the stress of the top 25 nm thick Pt electrode through thermal annealing. Indeed sputtered Pt films exhibit the very interesting properties of a variable built-in stress depending on the maximum temperature experienced during the whole process. These stress variations cover a large range of values: from -800 MPa for room temperature deposition up to 1 GPa for 700 °C deposition. Prior to the fabrication and using the measurements of the stresses of the other layers obtained during the development of the sub-100 nm AlN films (*cf.* Table 3- 3), we have calculated the required in plane built-in stress of the top Pt layer in order to obtain a small upward deflection (10 nm for a 100  $\mu$ m long beam). The corresponding annealing temperature has been identified from experimental abacus available for our Pt sputtering deposition process.

However for such small film thicknesses, available stress characterization technique [198] is not really accurate ( $\pm 100$  MPa precision) and, for the first micro-cantilevers fabrication batch, a broader range of temperature has been tested. For the first stack with Si<sub>3</sub>N<sub>4</sub> as structural layer, the theoretical annealing temperature is 500

°C but as illustrated on Figure 3- 6(a), for this temperature the cantilevers are still largely bent downward. It is only for annealing temperature of 700 °C that the cantilevers are bent upwards (*cf.* Figure 3- 6(b)).

The differences with respect to the theoretical predictions can be explained by the fact that the Si<sub>3</sub>N<sub>4</sub> layer is partly etched during XeF<sub>2</sub> step. As a consequence, it is thinner at the free end of the cantilever than at its clamped end. In addition, for all tested annealing temperatures, each right angle at the clamping of the cantilever or other corners in the layout present cracks (*cf.* Figure 3- 6(c)): as the Si<sub>3</sub>N<sub>4</sub> gets suspended it relaxes its stress and breaks at these points where stress concentrates. Based on these two observations, the release depth is therefore another very important control parameter. We thus decided to limit the number of XeF<sub>2</sub> etching cycles and targeted to release only cantilevers with the smallest width on the mask (40 μm).

Due to lithography process variations, the width of the cantilevers varies significantly: ±1 μm over a sample and ±3 μm in between samples, in average. Hence, for each fabrication batch, a first sample is used for test. It undergoes a series of 5 XeF<sub>2</sub> cycles in between which the presence of cracks and the number of released cantilevers is determined with SEM images. For the other samples of the batch, the number of cycles is set to the number of XeF<sub>2</sub> cycles required to release 80% of the cantilevers on the test sample. This approximation method has been proven to be the most efficient way to produce straight cantilevers with increasing quality factors batch after batch.

<b>Stack</b>	<b>Structural layer</b>	<b>Bottom Electrode</b>	<b>AlN</b>	<b>Stress of the top electrode for 10 nm upward deflection (L=100 μm)</b>	<b>Corresponding annealing temperature</b>
<b>1</b>	Si <sub>3</sub> N <sub>4</sub> 600 nm -300 MPa	Pt 100 nm 600 MPa	50 nm 300 MPa	800 MPa	500 °C
<b>2</b>	Si 500 nm 0 MPa	Mo 100 nm 100 MPa	50 nm 300 MPa	-300 MPa	0 °C

**Table 3- 3:** Calculated stress and corresponding annealing temperature for null static deflection

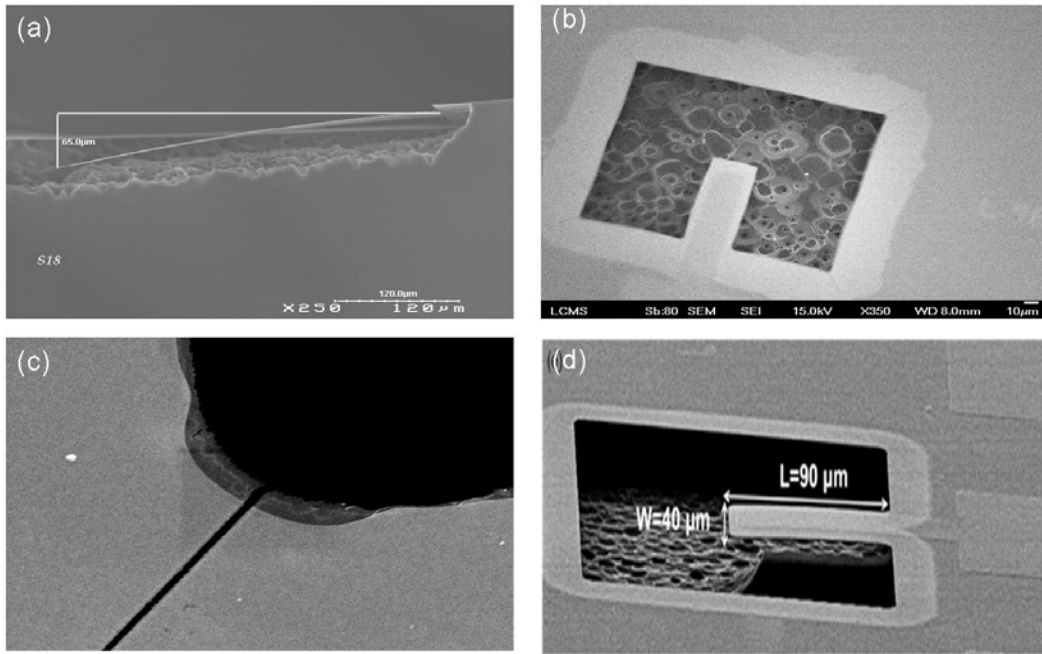


**Figure 3- 6:** Optimization of the annealing and release process steps. (a) downward deflected cantilever annealed at 500 °C, (b) slightly upward deflected cantilever annealed at 700 °C, (c) zoom on a crack of the **Pt** bottom electrode at the cantilever anchor, (d) fully optimized cantilever.

### 3.3. Electrical Characterization

#### 3.3.1. Electrical setup: active probes

Along with the optimization of the fabrication process, it is critical to verify the proper electrical and mechanical operations of our micro-cantilevers. Applying equation (2.3-7) for this geometry, the static current flowing through the static capacitance  $C_0$  is about ten times greater than the motional current. Thus as mentioned in section 2.3.1, a bridge- based background cancellation scheme is required to properly measure the resonance frequency. Several bridge configurations can be considered, theoretically providing the same output signal. The chosen circuit presents the simplest, yet efficient and robust solution. It avoids time consuming tuning of multiple variable components as in [178] and [170].

Ceramic variable capacitors with capacitance values of few pico-Farads and precision of tenth of femto-Farads are commercially available. In practice, bridge setups including these variable capacitors can be rapidly balanced and are compatible

with all cantilevers on the sample. However, when several resonance modes have to be characterized at once as in Figure 3- 7, this setup does not provide a perfect balance over the entire frequency range. Actually, the dielectric properties of AlN vary with the frequency, which in turn changes the static capacitance value.

In [215], the authors demonstrate that an identical but immobilized device can be used as dummy capacitor. In our case, we can take advantage of the presence of the bottom electrode on the majority of the sample surface area and use an unreleased cantilever as dummy device (obtained by misaligning, on purpose, the second mask during the fabrication). But the matching of the static capacitance (24 pF theoretically) depends on the fabrication process and variations of  $\pm 1$  pF are obtained in our case. This variation is far too large in order to ensure a signal-over-background ratio greater than one. Therefore, the use of such integrated dummy capacitor requires a time consuming search for the compatible couple cantilever / dummy capacitor prior to each electrical characterization in order to match both static capacitances.

Finally, in this configuration, the output signal is limited by the different shunt capacitances arising from the cables and detector input. To minimize this effect, one solution consists in bringing the first amplification stage as close as possible to the device and ultimately co-integrate them on the same substrate. In our case, the best solution would be to integrate our samples on a PCB-circuit board. But this would require bonding wires on connection pads. For our devices, this process has a very low success rate because the pressure required to solder the wire is too large to avoid failure (cracks) of the top Pt electrode and of the AlN layer. It results most of the time in short circuits between the top and bottom electrode. In the most favorable cases, the leakage resistance between top and bottom electrode remains high enough to sustain an electric field across the AlN layer. But electric performance is strongly degraded.

To address this connection issue, one possibility is to use a similar process as in [29] where the top electrode is connected to isolated island of bottom electrodes thanks to suspended metallic bridges. This technique has the additional advantage of reducing the total static capacitance close to its minimum corresponding to the surface area of the cantilever. However, it requires at least five lithography steps and

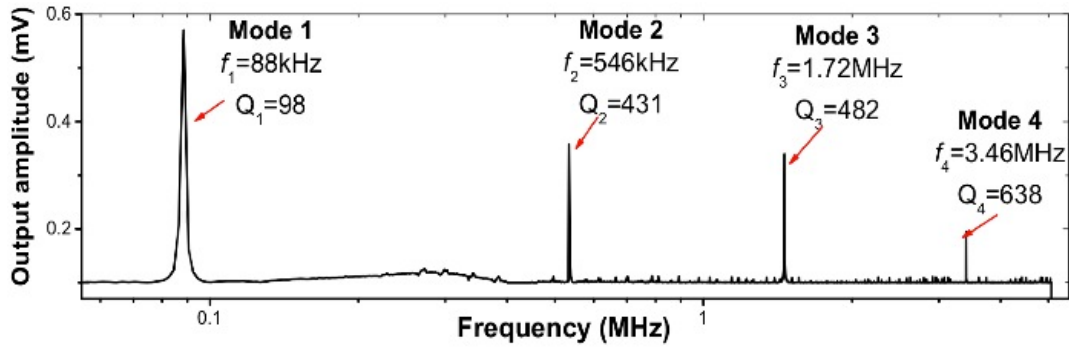


**Figure 3- 7:** Frequency response of 80  $\mu\text{m}$  long PZE cantilever resonator. The observed four resonance peaks correspond to the first four flexural modes of the cantilever. Theoretical resonance frequencies are 92 kHz, 578 kHz, 1.62 MHz and 3.17 MHz.

the corresponding masks are not available to us. Thus our solution consisted in developing a compact probe setup with a double stage amplifier PCB circuit board directly mounted on the probes (*cf.* Figure 3- 8). This setup exhibits a great mechanical stability and more importantly the increase of total static capacitance while connecting the probe to the cantilever is very reproducible (0.4 pF).

The whole setup is anchored in an Aluminum box that acts as a Faraday cage. Tungsten probes visible on the right inset picture are soldered onto the PCB circuit board held by manual micro-positioners. The circuit design has been realized in collaboration with G. Arndt, PhD student at CEA-LETI. The circuit has two amplification stages. The first one is based on a trans-impedance scheme with feedback resistance  $R_f = 1 \text{ M}\Omega$  and capacitor  $C_p = 1 \text{ pF}$  in order to insure low input impedance (1 k $\Omega$ ) and a large trans-impedance gain of 0.5 M $\Omega$ . The second stage is based on an inverting voltage amplifier with a gain of 50.

Unfortunately, the robustness and the noise performances of the circuit were found very poor due to a fabrication defect that has been identified too late. Thus, for all the following electrical characterizations, this circuit has been by-passed. Nevertheless, thanks to the compactness of the setup, the parasitic capacitance never exceeds 100 pF which is in the order of magnitude of the unavoidable 30 pF input capacitance of the lock-in amplifier used for the electrical measurements.

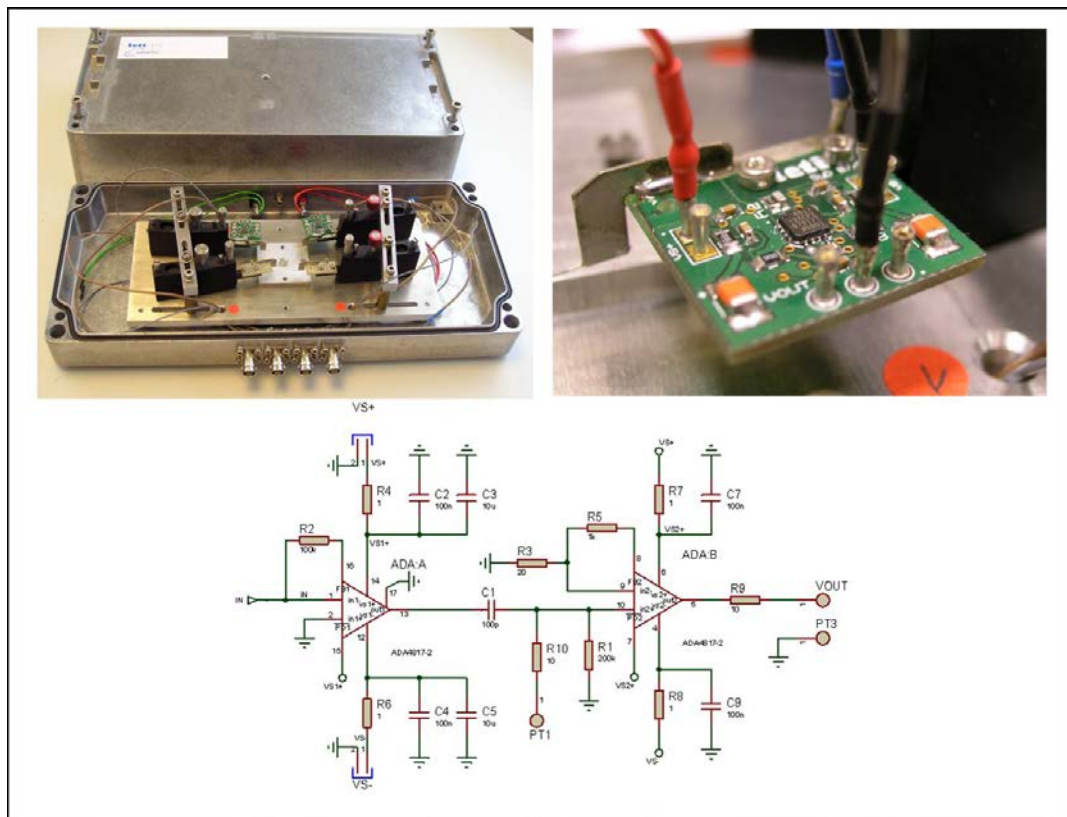


**Figure 3- 8:** Custom made set-up for micro-cantilever characterization.

### 3.3.2. Results and analytical fit

All measurements were performed in air with a SR844 lock-in amplifier in order to minimize the detection noise at the operating frequency (80 kHz – 200 MHz). Figure 3- 9 shows the frequency response of one of the tested cantilevers with four resonance peaks at 88 kHz, 546 kHz, 1.72 MHz and 3.46 MHz in good agreement with the analytical / FEM predictions for the flexural mode resonance frequencies: 92 kHz, 578 kHz, 1.62 MHz and 3.17 MHz. Several other peaks can be observed up to 20 MHz but their identification with FEM / analytical results is not practical due to the great number of possible candidates. It is also worth noticing that the quality factor of the four identified flexural modes increases while the maximum amplitude decreases. This decay is the result of the faster decrease of the efficiency of the piezoelectric transduction at higher resonance modes compared to the increase of the quality factor. Actually, the piezoelectric detection is sensitive to the average

stress along the cantilever and therefore for modes with several nodes, positive and negative stress regions along the cantilever cancel out in the electrical response.

As illustrated in Figure 3- 9 the analytical model is in excellent agreement with the experimental results. Thanks to the bridge operation, the background signal is reduced by two orders of magnitude. In order to properly fit theoretical and experimental results, the static capacitance mismatch between the cantilever and the dummy capacitor as well as the parasitic capacitance are first measured with an HP4815 vector impedance meter. With these experimental values, the residual background signal is subtracted numerically from the experimental data. Finally, the fitting procedure consists in finding the values of  $Q$  and  $e_{31}^{eff}$  that best fit the amplitude and phase curves (least square algorithm).

For the cantilever used in Figure 3- 10 we obtain  $Q = 125$  and  $e_{31}^{eff} = 0.78 \text{ C.m}^{-2}$ . This fitted effective  $e_{31}$  value is very consistent with the value obtained during the development of the 50 nm thick AlN films (*cf.* Figure 3- 2) and varies by  $\pm 0.2 \text{ C.m}^{-2}$  over the different fabricated cantilevers and samples. On the contrary, the quality factor varies greatly from one fabrication batch to another and values from 75 up to 135 have been obtained. For our cantilever design, we expect the viscous losses to be the dominant dissipation mechanism. But such variations of the quality factor suggest that the fabrication process also plays an important role, especially for the performance of the clamping area. In order to investigate rigorously the sources of dissipation in our cantilever, a study on the frequency response in vacuum must be carried out but could not be done as the custom probe setup is not designed for that.

Finally, the maximum actuation voltage has been found to be equal to 750 mV above which stiffening non-linearity occurs (*cf.* Figure 3- 10). Using our analytical model, this input voltage corresponds to a displacement amplitude of 110 nm, which is well below the theoretical limit of the mechanically-induced nonlinearity  $w_{max} = \frac{6.3L}{\sqrt{Q}} \approx 48 \mu\text{m}$  [121].

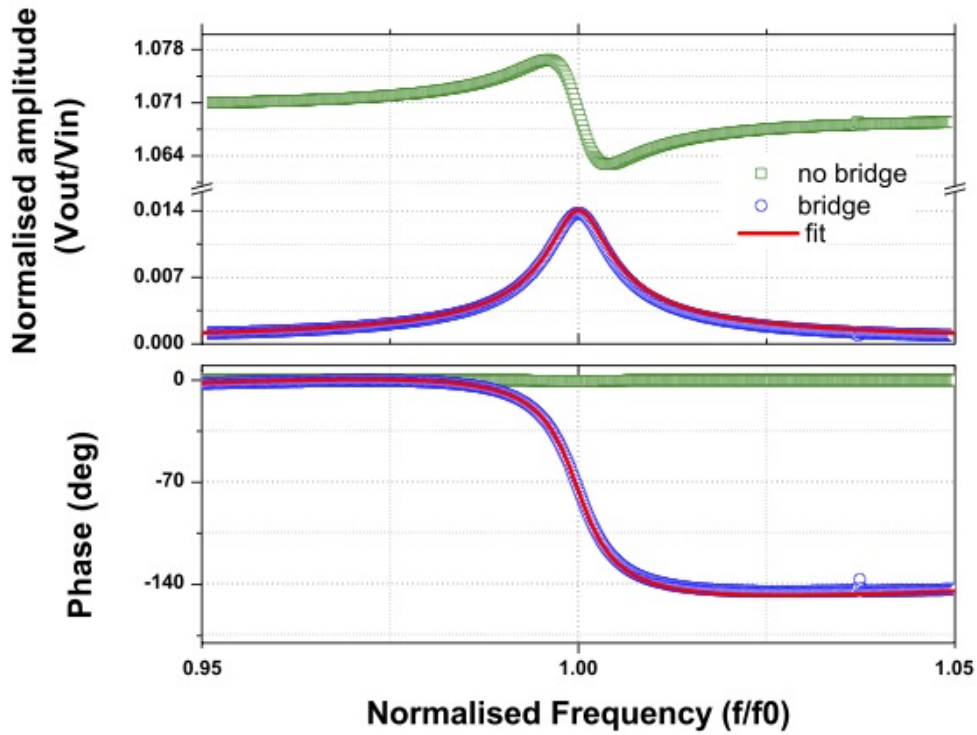


**Figure 3- 9:** First flexural mode electrical response and analytical fit.

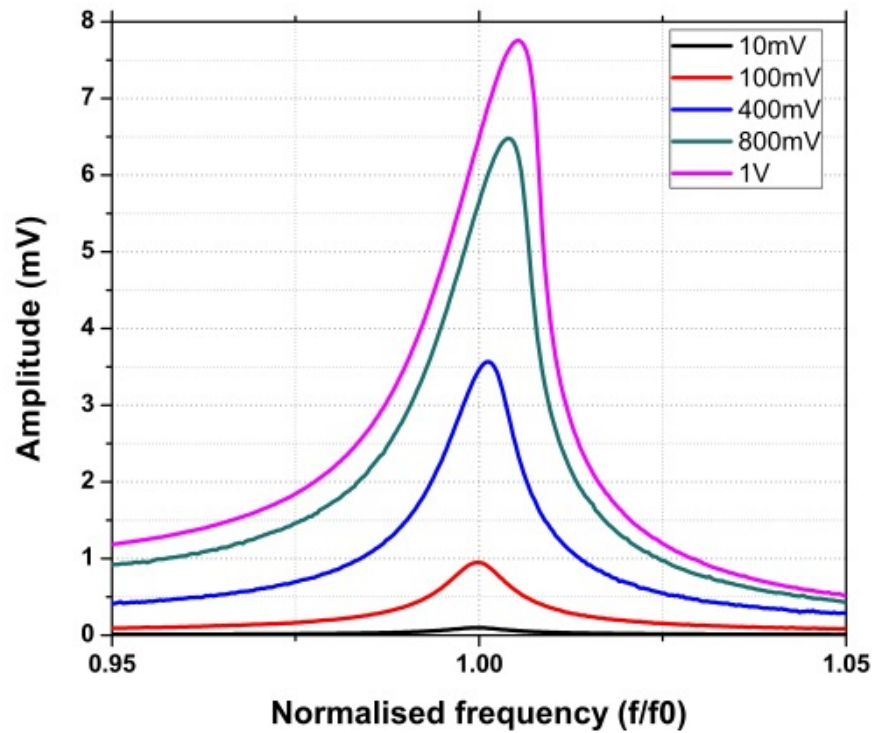


**Figure 3- 10:** Non linear electrical response of the first resonant mode for different driving voltage

## 3.4. Nano-cantilevers arrays

### 3.4.1. Process

Following the successful fabrication and characterization of micro-cantilevers, we have decided to carry on the fabrication of nano-cantilevers and more especially arrays of nano-cantilevers. Such devices presents can bring several advantage with respect to single micro-cantilever resonator. Connected in parallel, all cantilevers participate equally to the output signal, thus for a constant total vibrating surface we can expect similar signal level but at much higher frequency and thus with a much higher mass sensitivity. These devices have been fabricated using LETI's 200 nm deep-UV lithography tools with critical dimension of 0.2  $\mu\text{m}$  and a compatible set of masks that has been primarily developed for the fabrication of nano-cantilevers and nano-cantilever arrays with thermoelastic (Th) and piezoresistive (PZR) transductions. In particular, it contains 17 design variations of arrays of 2800, 5016 or 6800 nano-cantilevers all based on the so-called two-legged design (*cf.* Figure 3-11) compatible with piezoelectric transduction. By etching in one step the whole piezoelectric stack, the array patterns define arrays of piezoelectric cantilevers with common top and bottom electrodes and therefore connected electrically in parallel.

In addition, this mask set allows the fabrication of stand-alone cantilevers with the two-legged design that can be operated with PZE actuation and PZR detection. This will help to overcome the efficiency loss of the PZE detection at the nano-scale (*cf.* section 2.4). Especially because Mo and Pt, the two possible materials for AlN PZE cantilever electrodes, have a large PZR coefficients, respectively 7 and 10.

The fabrication process has thus been established by combining the experience gained during the fabrication of PZE micro-cantilever and of the Th /PZR nano-cantilevers. The chosen material stack consists of AlN (50 nm) / Mo (50 nm) / AlN (50 nm) / Mo (25 nm) deposited on a Si wafer with a thermally grown 2  $\mu\text{m}$  thick silicon oxide. According to section 2.3.3 it corresponds to the optimum thickness distribution in terms of transduction efficiency. The use of Mo as metallic material for the electrodes has been motivated by the good piezoelectric properties that can be obtained with 50 nm thick AlN films grown on Mo (*cf.* Table 3- 2), by its lower mass

density compared to Pt and finally by the contamination issues that forbids the use of Pt in LETI's 200 mm clean room facilities.

Figure 3- 12 presents the chosen two lithography steps process. As opposed to the micro-cantilever process, the whole stack is patterned during the first step. A 700 nm thick SiO<sub>2</sub> hard mask is deposited and patterned prior to the IBE in order to improve patterns conformation and avoid the solidification of the photoresist. The second lithography step is used to provide an access to the bottom electrode by removing the top electrode and AlN on the large leads that connect the different devices. This second lithography and IBE steps are performed at the sample level in PTA clean room with a custom flexible mask. Finally, samples are released using vapor HF isotropic etch of the underlying SiO<sub>2</sub> layer.

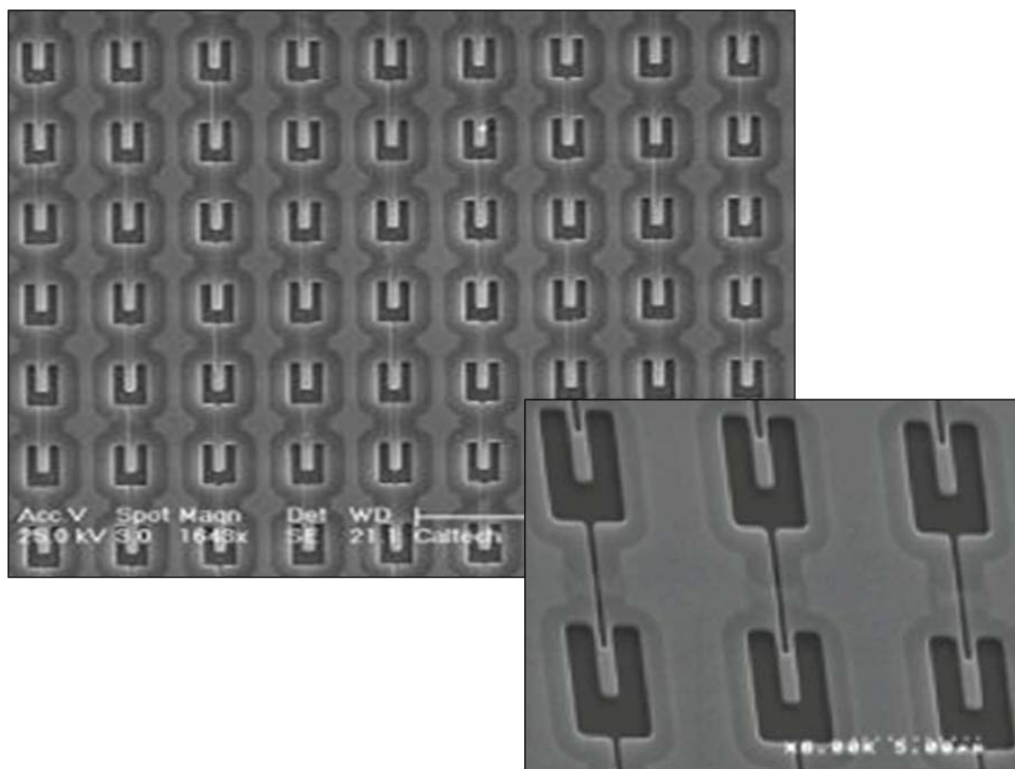


**Figure 3- 11:** SEM image of an array of Th/PZR nano-cantilever array. The cantilevers are 2.8  $\mu\text{m}$  long 1  $\mu\text{m}$  wide, include a stack Si (160 nm) / AlSi (25 nm) and are distributed over 20 rows and 140 column.

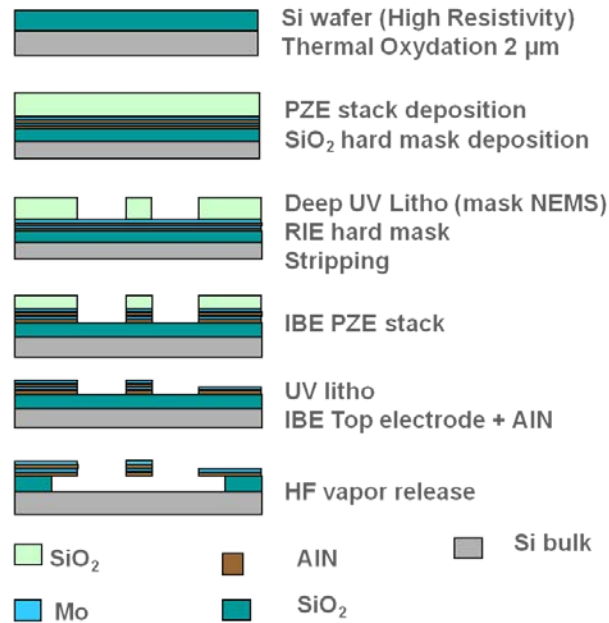


**Figure 3- 12:** Nano-cantilevers fabrication process flow

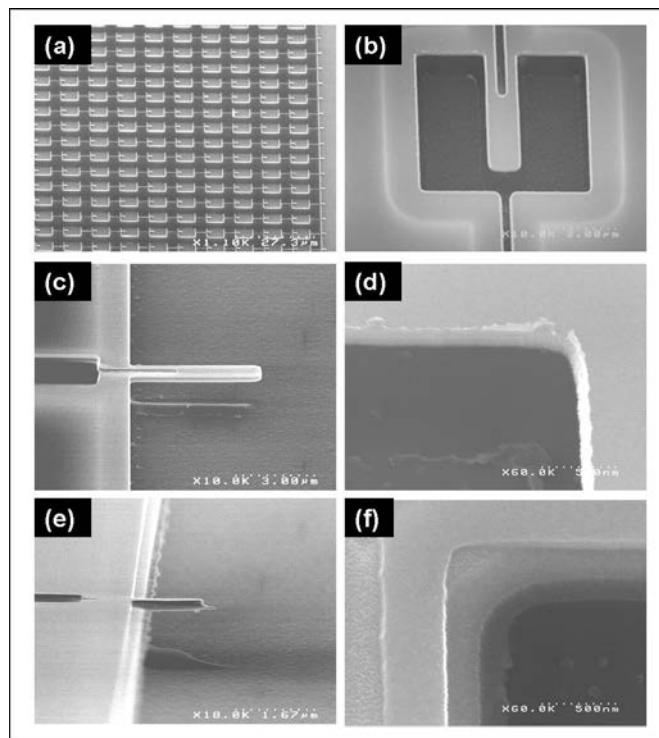


**Figure 3- 13:** SEM micrograph of the PZE fabricated nano-cantilevers.(a) array of nano-cantilever (b) zoom on a single cantilever in the array (c) tilted view of a single cantilever IBE etched with an angle of  $90^\circ$  revealing the presence of etching residues on the cantilever sides (d) zoom on the residues (e) tilted view of a single nano-cantilever IBE etched with an angle of  $45^\circ$  (f) zoomed on an edge with a large slope of  $40^\circ$  with respect to the substrate.

### 3.4.2. Results

Figure 3- 13 presents different SEM images of the fabricated nano-cantilevers, Two etching angles have been tested for the first IBE step. For the 45° etching angle (*cf.* Figure 3- 13(e) and (f)), the sharpness of the walls is very poor with a slope of 40° with respect to the substrate surface. As a consequence, the pattern conformation is also poor and none of the legs have been completely patterned. On the contrary, with an etching angle of 90°, critical dimensions of 0.4 μm are accessible with steep walls (81° with respect to the substrate). Unfortunately, etched materials have re-deposited on the sides of the walls and form visible residues after the release step. It is worth noting that all fabricated cantilevers are straight and fully released even though no particular effort has been dedicated to the control built-in stress related cantilever bending. Indeed, applying equation (3.2-1) for a cantilever 2.8 μm long, and with a built in stress of 300 MPa for the top AlN and Mo layers and of -300 MPa for the bottom AlN and Mo layers, one obtains a built-in bending displacement of the cantilever tip of 5 nm. It is also worth noticing that neither AlN nor Mo have been etched during the HF vapor process while the SiO<sub>2</sub> hard mask has been completely removed.

Samples etched with a 90° etch angle have been tested electrically. Unfortunately, all of them exhibit a very low leakage resistance. More precisely, values in the 100 Ω range were (higher in the case of single cantilevers and lower in the case of arrays) measured when several MΩ were expected. Hence, no electric field can be sustained across the devices electrodes with a reasonable input power. Such leakage resistance levels are however too high to be explained by local electrical breakdowns in the AlN layer and are most certainly due to short circuit paths coming from the presence of the IBE residues.

This issue must be carefully addressed for the design of the next PZE nano-cantilever generation. The IBE etch can be further optimized, for example by looking for the etching angle that insures proper patterns conformation and limits material re-deposition. Rapid SF<sub>6</sub> plasma treatment might also be investigated for residues removal. Finally, the use of an additional deep-UV lithography step for etching the bottom electrode and with slightly enlarged patterns (avoiding the re-deposition on

AlN and top electrode layers and thus eliminate short circuit paths), is certainly an efficient strategy.

### **3.5. Conclusion**

This chapter presents the different results of the technological development towards the demonstration of high resolution cantilever-based gravimetric gas chemosensors. The first step has been to choose the proper piezoelectric material and the corresponding deposition technique compatible with the reduction of the thickness of the cantilever. Thanks to the optimization of an already existing AlN DC pulsed reactive magnetron sputtering processes we have successfully demonstrated that 50 nm thick films can exhibit high piezoelectric properties. The key for such optimization relies on the use of a proper growth substrate (Mo, Pt, or W) and a seed AlN layer underneath to promote the growth substrate texture.

The integration in real devices of these ultra-thin AlN films has been first performed in few hundreds of  $\mu\text{m}$  long cantilevers. For such devices, the control of the stress in the different layers of the material stack is of critical importance. Eventually, we have opened a suitable process window using thermal annealing and precise control of the released depth. The fabricated cantilevers have also been tested electrically thanks to a custom made active probes setup and using a bridge configuration that allows the reduction of the influence of the parasitic capacitance at the input of the first amplification stage and of the static capacitance of the cantilever, respectively. Thanks to this setup, we are able to observe several resonance peaks in the 50 kHz - 20MHz frequency range. The first four correspond to the out-of plane resonance frequency calculated theoretically and exhibit increasing quality factors around 100 for the first mode up around 600 for the fourth mode. Concentrating on the first mode only, the bridge setup enables an increase of the signal over background ratio from 0.1 up to 10 and phase shift before and after the resonance from  $1-3^\circ$  up to  $175-178^\circ$  that will facilitate the implementation of feedback loops. Finally, the electrical response on a frequency range close to the first resonance mode is in very good agreement with the analytical modeling using material and geometrical parameter value from other experiments.

Using a process flow inspired from the successful micro-cantilever fabrication, we have finally fabricated nano-cantilevers and nano-cantilevers arrays. Unfortunately, all these devices present a too low leakage resistance to be investigated electrically. Several strategies can be implemented to overcome this issue: further investigation of the IBE step using different etch angles, development of an etching residue removal step and / or a modification of the mask layout. Nonetheless, as we have seen in the previous chapter, the design of the fabricated micro-cantilevers is expected to provide very high gas sensing performance. Thus, we have decided to concentrate our efforts on the experimental demonstration of this performance and have left the development of nano-cantilever array fabrication for later on.

# Chapter 4: Sensing Performances Characterization

---

**T**his chapter is dedicated to the characterization of the gas sensing performance of the resonant piezoelectric micro-cantilever whose fabrication and electrical characterization has been presented in the previous chapter. As a first step, we will present our experimental efforts to quantify the frequency stability of these devices. We will show results obtained with actual frequency loops (PLL and self-oscillating loop) but also with an open loop setup that allows the measurement of the frequency stability on a broader integration time scale. These results will allow us to estimate the SMLOD of our device and compare them with the other resonators reported in the literature.

In the last part of this chapter, we will present a proof of principle experiment that demonstrates the very high performances of these piezoelectric cantilever resonators for gas sensing application. To that mean, we have exposed our devices to Di-Methyl-Methyl-Phosphonate (DMMP) vapors with decreasing concentration. Although a great deal of work remains for the complete characterization of the gas sensing performance of our resonant piezoelectric gas sensor, these results clearly demonstrate that our piezoelectric cantilevers have a sensitivity and a resolution among the best ever reported in the literature.

## 4.1. Noise Characterization

### 4.1.1. Allan deviation

In order to obtain experimentally the minimum measurable relative frequency variation, equation (1.2-15), based on Parseval theorem, states that:

$$\left(\frac{\delta f}{f}\right)_{min} = \int_{-\infty}^{+\infty} S_y(\Omega) d\Omega \quad (4.1.1)$$

where  $y = \frac{\delta f}{f}$  is the relative frequency noise signal and  $S_y(\Omega)$  is noise Power Spectral Density (PSD). Therefore to determine experimentally the minimum measurable relative variation, an experimental mean to measure the frequency noise PSD is required. This measurement in the frequency domain is commonly used for time reference applications in order to obtain frequency stability informations on long time scales. The measurement of the variance of the resonator's frequency is the equivalent in the time domain and is more dedicated to long time scales, more appropriate to sensing. Actually, the *true variance*  $\sigma_y^2$  of the relative frequency signal  $y(t)$ , is:

$$\sigma_y^2 = \lim_{T \rightarrow +\infty} \left[ \frac{1}{T} \int_{-T}^T |y(t)|^2 dt \right] = \int_{-\infty}^{+\infty} S_y(\Omega) d\Omega \quad (4.1.2)$$

In practice, the knowledge of  $|y(t)|^2$  over an infinite time is of course impossible and we can only rely on an estimator  $\sigma_{y,e}^2$  defined over a finite experimental time  $T_e$ , which converges towards  $\sigma^2$  when  $T_e \rightarrow +\infty$ :

$$\sigma_{y,e}^2 = \frac{1}{T_e} \int_{-T_e/2}^{T_e/2} |y(t)|^2 dt \quad (4.1.3)$$

However,  $\sigma_e^2$  is still not practical as it is divergent for frequency noise spectral density with negative exponents in  $f$ . To overcome this issue several other estimators of the true variance have been introduced over the years and the most commonly used is the so-called Allan deviation [24], [38], [39]. This latter quantity is defined as:

$$\sigma_y^2(\tau) = \frac{1}{N} \sum_{k=0}^{N-1} (\overline{y_{k+1}} - \overline{y_k})^2 \quad (4.1.4)$$

where  $y_k = \frac{1}{\tau} \int_k^{(k+1)\tau} y(t)dt$  are N consecutive measurements of the relative frequency shift averaged over the integration (measurement) time  $\tau$ . It is related to the relative frequency noise PSD by the relation [38]:

$$\sigma_y^2(\tau) = 2 \int_0^{+\infty} S_y(\Omega) \frac{\sin^4(\tau\Omega/2)}{(\tau\Omega/2)^2} d\Omega \approx 2 \int_0^{1/\tau} S_y(\Omega) d\Omega \quad (4.1.5)$$

Using this latter equation it can be demonstrated that the Allan deviation converges towards the true variance for random walk FM, flicker FM and white FM noises but not for flicker and phase noise. Table 4- 1 gives the correspondence between phase noise and frequency noise PSD and Allan deviation for noise with different asymptotic behavior with respect to Fourier frequencies. Measurements of Allan deviation will thus not only determine the minimum measurable resonance frequency variation but also provide information on the type of dominant noise in the measurement bandwidth.

Noise type	Phase noise $S_\varphi(f)$	Frequency noise $S_y(f)$	Allan deviation $\sigma_y^2(\tau)$
White PM	$b_0$	$\frac{b_0}{f_0^2} f^2$	$\frac{3f_H b_0}{(2\pi f_0)^2} \tau^{-2}$
Flicker PM	$b_{-1} f^{-1}$	$\frac{b_{-1}}{f_0^2} f$	$[1.038 + 3 \ln(2\pi f_H \tau)] \frac{b_{-1}}{(2\pi f_0)^2} \tau^{-2}$
White FM	$b_{-2} f^{-2}$	$\frac{b_{-2}}{f_0^2}$	$\frac{1}{2} \frac{b_{-2}}{f_0^2} \tau^{-1}$
Flicker FM	$b_{-3} f^{-3}$	$\frac{b_{-3}}{f_0^2} f^{-1}$	$2 \ln(2) \frac{b_{-3}}{f_0^2}$
Random walk FM	$b_{-4} f^{-4}$	$\frac{b_{-4}}{f_0^2} f^{-2}$	$\frac{(2\pi)^2 b_{-4}}{6 f_0^2} \tau$

**Table 4- 1:** Links between the power law models for phase and frequency noise and Allan deviation. This table is reproduced from [38]. In this frequency law model phase noises are categorized according to their asymptotic behavior with respect to frequency:  $f^0, f^{-1}, f^{-2}$  and so on. The coefficients  $b_0, b_{-1}, b_{-2}, b_{-3}$  and  $b_{-4}$  give the asymptotic noise PSD level. PM and FM stand for Phase Modulation and Frequency Modulation respectively.  $f_H$  is the low pass filter cut-off frequency of the required filter to avoid the Allan deviation to diverge in white PM and Flicker PM noises cases.

### 4.1.2. Open Loop Characterization

Measurement techniques for the Allan deviation are standardized in [216]. All implement a phase comparison with another, more “trustworthy”, frequency source in PLL setups and involve high precision electronic setups that we did not reproduce in our laboratory. Precisely, electrical mixers with sufficient noise performances in the frequency range of our micro cantilever are actually very rare on the market and we have considered that developing our own was a loss of time. However, we do possess the required equipment for high precision phase measurements with Lock-in Amplifiers (LIA) such as Stanford Research 830 and 844 (SR830 and SR844) models. These LIA can be (and will be) use as phase analyzer for digital PLL but in such setup, the loop response time is restricted by GPIB based communication protocols to 100 ms, which is barely sufficient to assess the optimum Allan deviation integration time.

To overcome this difficulty, we have implemented a method previously developed by G. Jourdan [217][218]. It consists in measuring the phase noise of a circuit identical to a PLL setup but with the loop opened after the phase comparator (*c.f.* Figure 4- 1). The cantilever is driven at a fixed frequency close to the first mode resonance frequency and the phase variations of the output signal are recorded. The Allan deviation is then computed from the measured phase noise assuming closed loop architecture with ideal feedback. The validity of this method is supported experimentally by the superposition of the Allan deviations curves obtained using this method and a PLL for higher integration times between 1s and 100 s (*cf.* Figure 4- 3)

The corresponding electrical setup is depicted in Figure 4- 1. A frequency source HP33250 delivers a sinusoidal signal at a fixed frequency as close as possible to the cantilever resonance frequency. The output signal  $V_{out}(t) = X(t) \cos(\omega t) + Y(t) \sin(\omega t)$  is measured with a LIA SR488 and the two *in phase* and *quadrature* component,  $X(t)$  and  $Y(t)$  respectively (*c.f.* section 1.2.3.2), are recorded from the SR488 with an A/D converter (a digital oscilloscope with 2.5 Msamples). Prior to the measurement, the phase reference of the LIA is tuned such that the mean value of the output signal phase is null. In these conditions, the signal  $X(t)$  corresponds to the carrier signal plus the *in-phase* noises component while  $Y(t)$  carries only the

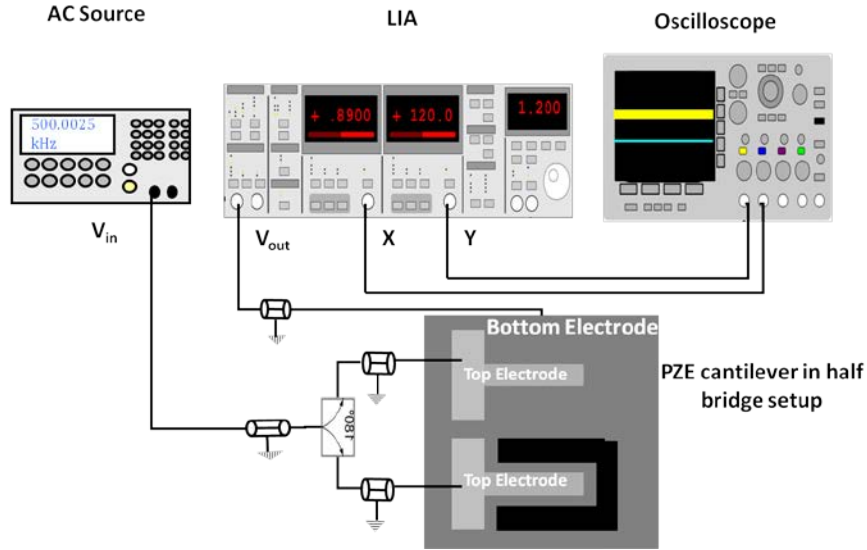


**Figure 4- 1:** Electrical setup schematic for Open loop Allan deviation measurement method.

*quadrature* noises signal. Assuming small noise PSD, the phase noise signal during an experiment is therefore:

$$\varphi(t) = \arctan \left[ \frac{Y(t)}{X(t)} \right] \approx \frac{Y(t)}{X(t)} \quad (4.1.6)$$

Assuming that the setup operates in closed loop with an ideal controller the relative frequency noise signal corresponding to this phase signal noise follows the Robbins formula:

$$y(t) = \frac{\delta f_0}{f_0}(t) = \frac{\varphi(t)}{2Q} \quad (4.1.7)$$

where  $Q$  is the quality factor of the piezoelectric cantilever. This relative frequency noise signal can then be used for the computation of the Allan deviation.

For a precise and reliable measurement, great care must be taken in the choice of the LIA sensitivity and sampling rate. Also, in order to cover integration time of Allan deviation from 10 ms to 100 s with at least 100 signal samples, we perform the measurements in three steps with  $\tau_{LIA} = 100 \mu\text{s}$ , 1 ms and 10 ms and with corresponding total measurement time  $T_{exp} = 10 \text{ s}$ , 100 and 1000 s.

Figure 4- 2 presents the results of such experiment for time constants between 10 ms and 100 s and input voltage between 50 mV and 750 mV. In the lower integration time range (0.01 to 1 s), the Allan deviation is proportional to the input voltage and scales like  $\tau^{-1/2}$  which is consistent with a dominant additive white amplitude noise [119]. The minimum value of  $10^{-8}$  obtained for an integration time of 10 s is also consistent with a dominant electronic noise with a PSD of  $5.7 \text{ nV} \cdot \text{Hz}^{-1/2}$  corresponding satisfactorily to the LIA manufacturer specifications. Based on this measurement, we can calculate an expected SMLOD equals to  $53 \text{ zg} \cdot \mu\text{m}^{-2}$  close to the value predicted in Figure 2- 6. Compared to previously reported results in the literature (*cf.* Table 1- 1 ), these values of SMLOD and Allan deviation place our cantilever among the best gravimetric sensors. It should also be reminded that the current cantilever design does not exactly satisfy the design rules of section 2.3.3.2 and thus further improvements of up to two orders of magnitude can be expected by minimizing the input capacitance of the LIA down to a few pF and choosing the proper cantilever length and width to match the static capacitance of the cantilever to the input capacitance of the LIA as explained in section 2.3.3.

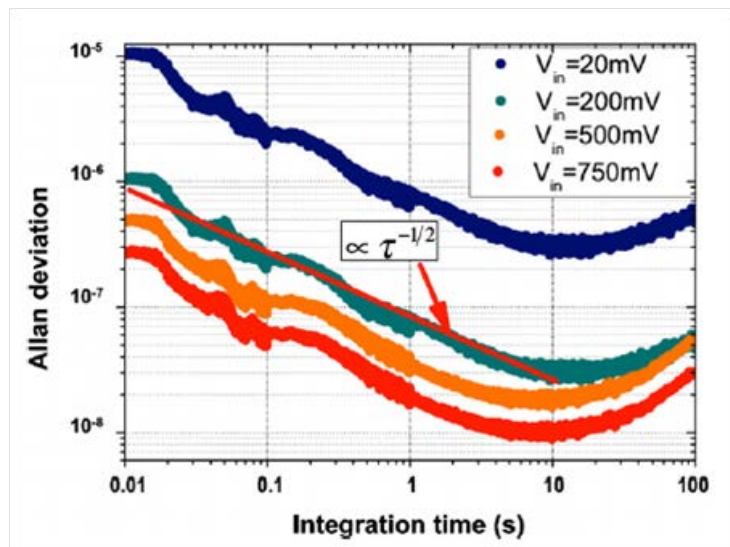


**Figure 4- 2:** Open loop Allan deviation results. As expected the dominant noise source is the electronic noise, which creates  $\tau^{-1/2}$  asymptotes that shift downwards with increasing input power. The minimum Allan deviation value is  $10^{-8}$  for  $\tau = 10 \text{ s}$  and fits well with the analytically predicted value of  $1.6 \cdot 10^{-8}$  using equation (1.2-18) .

### 4.1.3. Frequency loops

In order to proceed towards real gas sensing experiments, it is necessary to implement a resonance frequency measurement loop and characterize its frequency noise performance. In this section we will present both the digital PLL and a self-oscillating loop developed for our piezoelectric micro-cantilevers and their Allan deviation measurement result.

#### 4.1.3.1. Phase Locked Loop

The electrical setup for our digital PLL is similar to the one used for open loop Allan deviation characterization. A frequency source drives a half capacitive bridge including the cantilever and a LIA is used to record the *in-phase* and *quadratic* components of the output signal of the bridge (*cf.* Figure 4- 3(a)). The only difference is that a custom SIMULINK (MATLAB) software records this signal, computes the corresponding phase signal (*cf.* equation (4.1-6)) and controls the frequency of the signal generator *in real time* in order to maintain the phase signal at its resonance frequency value.

The custom controller that computes the frequency correction signal has been developed previously at LETI by C. Kharrat [219]. It is based on an eighth degree transfer function whose coefficients are calculated thanks to an  $H_\infty$  optimization algorithm. Compared to a proportional or a Proportional-Integral-Derivative (PID) controller, this  $H_\infty$  controller ensures an optimal robustness and noise rejection but at the expense of a lower response time which is not critical in our case as we are limited for the PLL integration time by the GPIB communication protocol time above 100 ms. Figure 4- 3(b) presents the Allan deviation curves obtained with this setup. The cantilevers used here belong to the latest fabrication batch, which showed a critical input power of 100 mV lower than the cantilever used in Figure 4- 2. Beside, these characterizations were performed with long cables and thus larger parasitic capacitances. In these conditions the maximum output signal amplitude was around 1 mV, about 8 times lower than the maximum output signal of the cantilever used in Figure 4- 2. According to equation (1.2-18), this loss of output signal strength induces an increase of the frequency deviation by the same factor if the noise level of the LIA

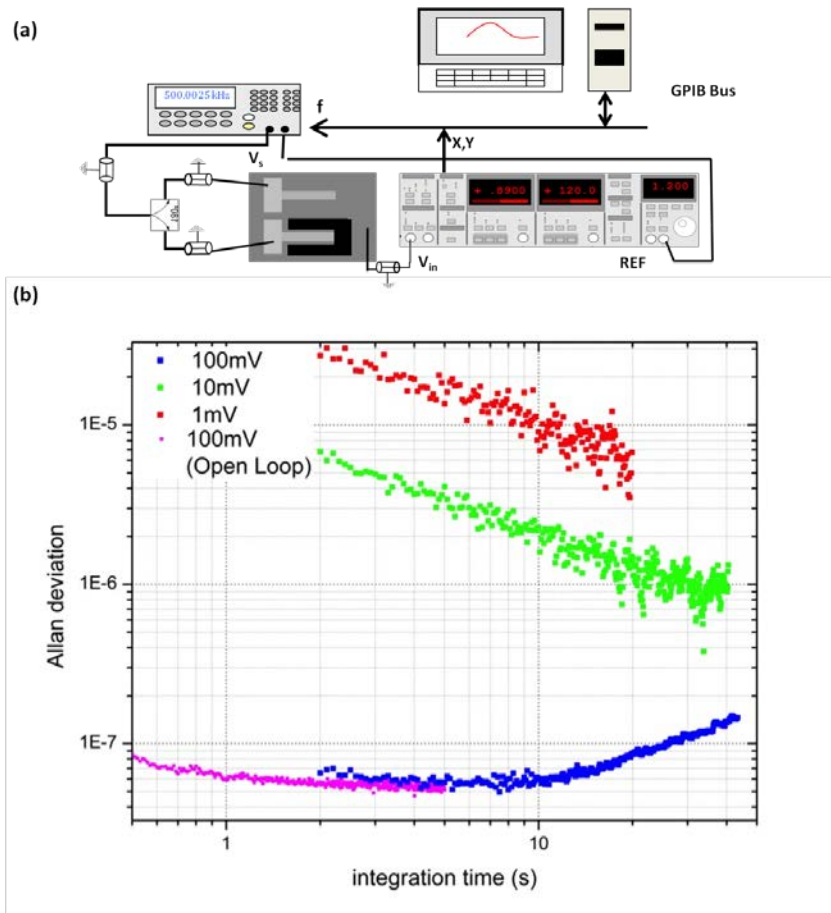


**Figure 4- 3:** (a) Digital PLL Allan deviation measurement and setup. (b) Allan deviation curves of the digital PLL setup. This figure further supports the validity of the open loop Allan deviation measurement method thanks to the superposition of the violet (open loop) and blue (closed loop) curves obtained respectively with the open loop setup and the PLL setup for the same cantilever and the same input signal amplitude  $V_{in} = 100$  mV.

remains constant. This is exactly what we observe experimentally with a minimum Allan deviation of only  $8 \cdot 10^{-8}$  measured on the PLL setup with these 100mV maximum drive power cantilevers. These results further support our noise model. Identically to Figure 4- 2, the Allan deviation curves are proportional to the input voltage and reach a minimum when the input voltage is at the onset of non linearity.

#### 4.1.3.2. Self Oscillating loop

The self oscillating loop setup for our piezoelectric cantilever has been developed in collaboration with G. Arndt using a discrete components electronic circuit on a PCB board. For practical reasons, cantilevers were connected to the circuit with wire-bonding. As already discussed in section 3.3.1, this contact technique has a low yield for our cantilever and results most of the time in a short circuit between the top and bottom electrode. In the most favorable cases, the leakage resistance is large enough to sustain an electrical field but a variable resistance is now required to balance the bridge and the signal-to-background ratio is strongly degraded. The first consequence of the use of wire bonded cantilevers is that the frequency loop is very unstable as the bridge balance is limited to a small frequency range and oscillation can thus be initiated by the background signal at frequencies far from the resonance frequency of the cantilever. The second consequence is that the maximum input signal must be limited to 25 mV in order to avoid electrical breakdown.

Figure 4- 4(a) presents the developed electronic circuit. The first electronic amplification stage is based on a standard inverter amplifier scheme with an ADA4817 as active component that theoretically provides both low noise level ( $2.4 \text{ nV} \cdot \text{Hz}^{-1/2}$ ) and a large bandwidth (200 MHz). The Barkhausen condition on the phase is obtained by tuning the cutoff frequency of a first order high pass filter (tunability of the phase in open loop  $0 - 90^\circ$ ) while the amplitude condition is obtained by tuning the saturation level of an amplifier with unit gain (clamped amplifier).

With maximum input voltage amplitude of 25 mV the cantilever output signal amplitude is 0.3 mV. Moreover, the amplifier input noise was estimated from open loop measurement in the order of  $40 \text{ nV}/\sqrt{\text{Hz}}$ . In these conditions, equation (1.2-18) predicts a frequency deviation for a 1 Hz bandwidth of  $7 \times 10^{-7}$ . Figure 4- 4 (b)

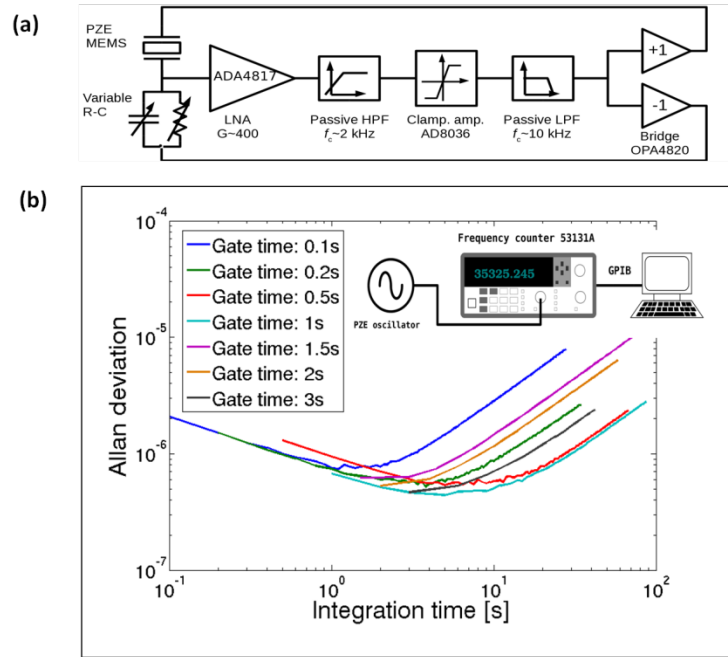


**Figure 4- 4:** (a) Self oscillating loop setup schematics, (b) Allan deviation curves using the open loop setup

shows Allan deviation curves of our self oscillation setup with a minimum value of  $4.10^{-7}$  consistent with our noise model.

As a conclusion, the PLL setup is much more robust, insensitive to background signal and more importantly allows reaching better frequency noise performances. We have thus naturally selected this setup for gas sensing experiment whose results are presented in the following.

## 4.2. Gas sensing experiments

All the experiments we present in this part have been performed at M.L. Roukes laboratory at Caltech with a gas delivery bench that was used in [58] and [50]. For reasons detailed later, results presented here remain insufficient to claim a complete characterization of the gas sensing performance of our piezoelectric resonator. Nevertheless, the comparison of our results with those obtained in previous experiments demonstrated the great advantage of these devices for gas sensing application.

### 4.2.1. Experimental setup

- Choice of the test gas.

Detection of warfare agent, such as Sarin gas, has been listed in the possible application for high resolution gas sensor. Only minute quantity of such gas can have disastrous effect of human health and military and security agencies are constantly

looking for the most reliable and sensitive technology to detect such gas. Besides, the choice of Dimethyl methylphosphonate (DMMP), a simulant/precursor of the Sarin gas, as test gas to evaluate the gas sensing performances of our piezoelectric cantilever was also motivated by other reasons:

- DMMP is relatively safe: it is toxic but less carcinogenic than most of the other possible test gas: formaldehyde, Tetrahydrofuran (THF) and hexane.
- DMMP is commercially available and compatible with Caltech gas test bench
- A specific polymer for the functionalization layer called DKAP with partition coefficient in the order of  $10^6 - 10^7$  for DMMP was available at Caltech (thanks to collaborations with SANDIA Laboratories).
- DMMP has a very low vapor pressure (between 2.31 to 112 Pa at 25 °C) and a slightly higher molar mass ( $124 \text{ g}\cdot\text{mol}^{-1}$ ) compared to the other possible test gas (formaldehyde: 173 Pa and  $30 \text{ g}\cdot\text{mol}^{-1}$ , hexane: 14480 Pa and  $88 \text{ g}\cdot\text{mol}^{-1}$ , THF: 17530 Pa and  $72 \text{ g}\cdot\text{mol}^{-1}$ ). This allows very low vapor concentration level with a gas delivery system based on bubbler. The corresponding adsorbed mass on the cantilever remains also in the same order of magnitude as with other test gas.
- DMMP is very often used in the literature as a test gas allowing a comparison of our device with respect to those reported in the literature.

DMMP is an organophosphorus compound with the chemical formula  $\text{C}_3\text{H}_9\text{O}_3\text{P}$  or  $\text{CH}_3\text{PO}(\text{OCH}_3)_2$ . It is a colourless liquid that is primarily used as flame retardant. Its chemical properties are summed up in Table 4- 2. The saturation vapor pressure is the pressure exerted by a vapor in thermodynamic equilibrium with its

condensed phases (solid or liquid) at a given temperature and in a closed volume. In our gas experiment, we will exploit this thermodynamic equilibrium between DMMP liquid and vapor phase in order to obtain a gas stream of  $N_2$  and DMMP with a known DMMP concentration. However, values of DMMP saturation vapor pressure at room temperature can vary from 2.31 Pa [220] to 160 Pa [221] depending on the literature reference. Such spreading of reference values can induce large experimental error. The commonly accepted model for the saturation vapor pressure  $P_{sat}$  of a chemical species is the so-called Antoine model [222] that states:

$$\log\left(\frac{P_{sat}}{P_0}\right) = A - \frac{B}{T + C} \quad (4.2.1)$$

4.2-1

where  $P_0 = 10^5$  Pa is the reference pressure and  $A$ ,  $B$  and  $C$  are three experimental constants. According to this formula and using values of [220] (*c.f.* Table 4- 2), one finds  $P_{sat} = 6.3$  Pa at room temperature (25 °C) with an uncertainty of 38% for an uncertainty of  $\pm 1^\circ\text{C}$  on the temperature.

For our experiments and the interpretation of the results, we have taken  $P_{sat} = 61$  Pa which is the value used by Caltech scientists that built up the test bench ([58] [50]). In this way, the nominal value of the DMMP vapor concentration delivered to the cantilever might be off by an order of magnitude (positive or negative). In addition, the variation of the temperature of the DMMP solution and of the  $N_2$  stream around  $\pm 2^\circ\text{C}$  over the 12 hours of experiments adds a further 50% uncertainty on  $P_{sat}$ .

<b>DMMP Properties</b>		
<b>Molecular formula</b>		$C_3H_9O_3P$
<b>Molar Mass</b>		124.08 <sup>(a)</sup>
<b>Antoine equation coefficient</b>	<b>A</b>	1.82 <sup>(a)</sup>
	<b>B</b>	445 <sup>(a)</sup>
	<b>C</b>	-224 <sup>(a)</sup>
<b>Vapor pressure</b>		6.3 Pa @ 25 °C <sup>(a)</sup>
		61 Pa @ 25 °C <sup>(b)</sup>

**Table 4- 2:** Chemical properties of DMMP <sup>(a)</sup> data taken from [220]. <sup>(b)</sup> data used by Caltech scientist and in our experiments

- Functionalization layer

As already stated, we have chosen to use a polymer coating called “DKAP” available at Caltech thanks to a collaboration with Sandia Laboratories. It is a poly[2-(3-propylene)-3,5 bis (trifluoromethyl) phenol]methyl siloxane and has a glass transition temperature of ~20°C in ambient conditions. The strong affinity of DKAP towards DMMP relies on its strong hydrogen bound acidity that interacts with the phosphanate (P=O) group of DMMP [142]. No activation energy value has been, up to our knowledge, reported so far.

The coating procedure consists in drop-depositing 100 mL of a solution of 5 mg.cm<sup>-3</sup> of DKAP in toluene followed by drying in ambient air for several minutes. By measuring the cantilever resonance frequency shift before and after the deposition, the DKAP thickness is evaluated around 5 nm. Recalling equation (1.2-13), the Limit Of Detection (LOD) in terms of concentration is given by:

$$\delta c_{min} = \frac{\delta m_{surf}}{K \rho_g t_f} \quad (4.2.2)$$

4.2-2

where  $K$ ,  $\rho_g$  and  $t_f$  are the partition coefficient of the couple analyte / functionalization layer, the mass density of the analyte, and the thickness of the functionalization layer. Therefore increasing the thickness of the functionalization layer is beneficial for sensing performances as it increases the amount of adsorbed mass. This optimization is, of course, limited by the influence of the functionalization layer on the mechanical behavior of the cantilever. We have considered it negligible up to now but it is clear that this assumption will not be valid anymore with polymer films thicker than the cantilever. The second limit for the use of thick functionalization layers relies on the competition between adsorption, desorption and diffusion of targeted analyte in the functionalization layer and thus on the response time of the sensor.

As our cantilevers are 800 nm thick, there is still a lot of room for increasing the DKAP functionalization layer thickness and compare to the result we will present in the following using a very thin DKAP layer (5 nm), at least one order of magnitude improvement of the concentration LOD can be expected by optimizing the DKAP layer thickness

- Gas Test Bench

Figure 4- 5 shows a picture and a schematic of the gas test bench. Its operating principle is based on the stability of the saturation vapor pressure of DMMP in  $N_2$  at a given temperature and on a subsequent dilution step to obtain the desired concentration. A small stream of  $N_2$  is injected in a gas bubbler containing a high purity solution of DMMP. As the headspace between the liquid DMMP solution and the outlet of the bubbler is saturated in DMMP vapors, the gas mixture exiting the gas bubbler has a constant DMMP vapor concentration set by DMMP saturation vapor pressure  $P_{vp}$ :

$$c_{DMMP,sat} = \frac{P_{vp}}{P_{tot}} \times 10^9 \text{ (in ppb)} \quad (4.2.3)$$

4.2-3

where  $P_{tot} \sim 1 \text{ atm}$  is the total pressure in the bubbler headspace. The saturated DMMP- $N_2$  stream is then diluted in a large flow rate stream of  $N_2$  and delivered to the cantilever. A bi-stable valve is used to expose the cantilever either to the diluted DMMP stream or to a pure  $N_2$  stream with same total flow rate. In the on-state of the valve, the concentration of DMMP experienced by the cantilever is given by the ratio of mass flow rates between the saturated flow  $Q_{sat}$  and total output flow  $Q_{tot}$ , called dilution ratio  $d_R = \frac{Q_{sat}}{Q_{tot}}$ :

$$c_{DMMP} = d_R c_{DMMP,sat} = d_R \frac{P_{vp}}{P_{tot}} \times 10^9 \text{ (in ppb)} \quad (4.2.4)$$

4.2-4

The Mass Flow Controller (MFC) used to control the saturated flow ( $F_c$ ) can be varied between 0.001 and 1 l/min while the one used to control the dilution flow  $F_d$  can be varied from 0.1 to 10 l/min. In this way, the gas delivery system can deliver a  $N_2$ -DMMP gas mixture with a vapor concentration of DMMP between 3000 ppm and 12 ppb. However, it was observed that the higher total flow rates (above 5 l/min) that are required to reach the lowest DMMP concentration (below 50 ppb) also induce an increase in the frequency noise on the PLL frequency signal. We attributed this increase of noise to the difficulty to obtain a laminar flow in the sensor chamber and to the subsequent turbulences that disturb the cantilever motion and the electrical probes connected to the cantilever pad.

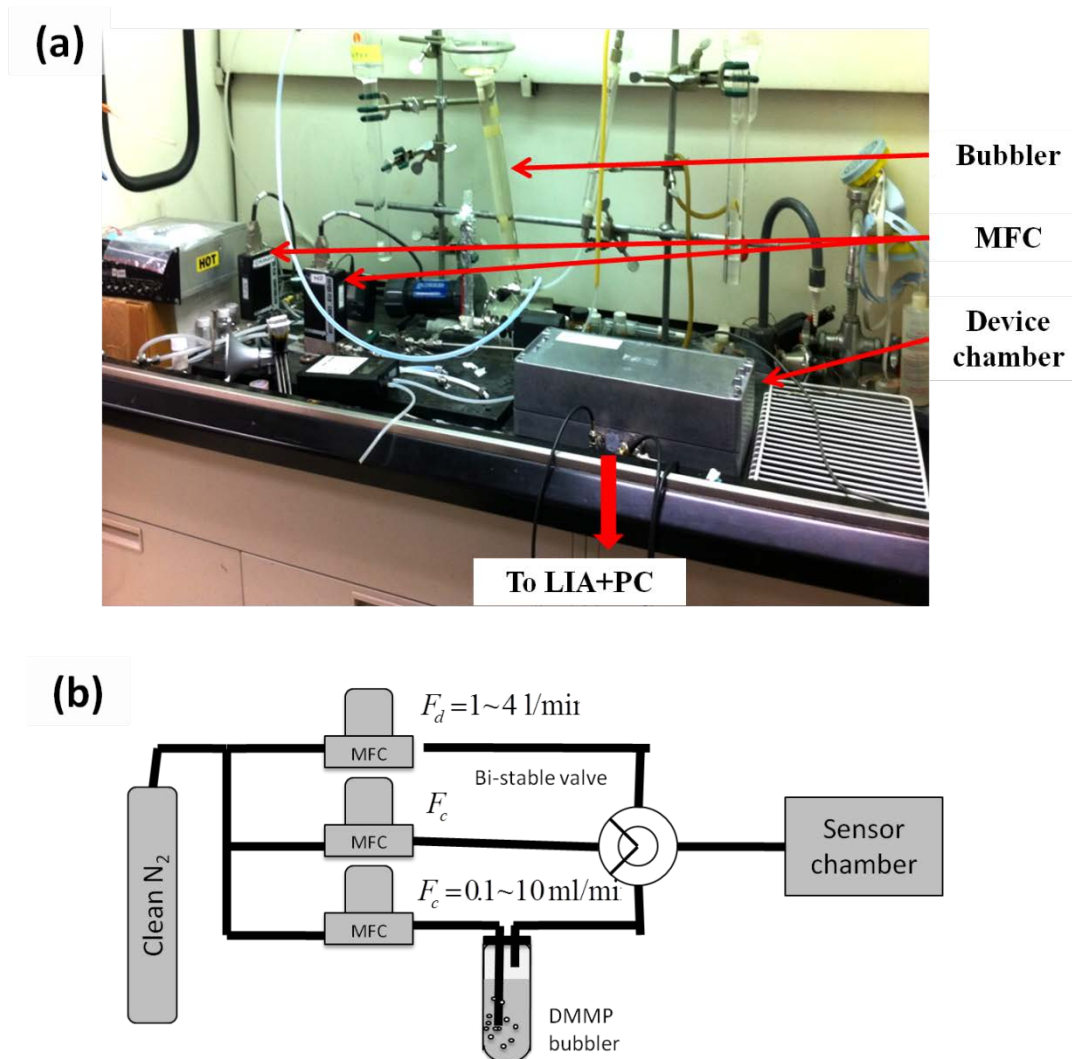


**Figure 4- 5:** Gas sensing experiment setup: (a) picture of the gas test bench at Caltech with the device chamber (b) Schematic of the operating principle (MFC stands for Mass Flow Meter).

Some attempts to confine the gas stream in a small flow path have been performed without real success. Laminar flow conditions for these flow rates require very small flow radius. Encapsulation of the cantilever in a micro flow channel, for example a PMMA capillary as in [142] seem to be the best solution. Unfortunately the layout of our devices and their electrical leads as is is not compatible with such encapsulation.

Also, there is some uncertainty on the DMMP concentration obtained as its vapor pressure depends on temperature and humidity, and the temperature and humidity of the N<sub>2</sub> stream was not extremely well controlled.

## 4.2.2. Results

### 4.2.2.1. First experiments on blank devices

As a conservative approach, an uncoated cantilever of the third fabrication batch was exposed to DMMP concentration of 5.7, 11.4 and 114 ppm. The results of this experiment are illustrated in Figure 4- 6 where the corresponding resonance frequency shifts of 1.5, 2.7 and 7Hz can be observed. In operation (i.e. in the presence of gas flow) the Root Mean Square (RMS) frequency deviation is 0.12Hz demonstrating a concentration resolution around 500ppb.

This first experiment mostly serves as a preparation for a more complete investigation of the gas sensing performance of our piezoelectric cantilevers. We have therefore identified the following important parameters that should be controlled later:

- The frequency stability of this cantilever is relatively poor with an Allan deviation of  $8 \times 10^{-8}$ . This is due to the low onset of non linearity observed for an input drive of 50 mV only. As a consequence, in the real experiment, a pre-selection of the cantilevers with respect to their onset of non linearity will be performed. 20 devices were fabricated in the fourth fabrication batch used for the gas experiment. Out of these 20, 16 showed a maximum input drive in the range of 100 mV (maximum 120mV) corresponding to a minimum Allan deviation of  $3 \times 10^{-8}$ .
- Absorption and desorption times are very long, 10 minutes and 20 minutes respectively, most certainly due to the large volume of the gas chamber. For the real experiment an enclosure made of plastic and aluminum foil must be used to reduce the gas chamber volume. This helps with reducing the adsorption time down to 30 seconds but had little impact on the desorption time (15 min). As a consequence no dynamic studies (study of the response time) of our sensor can be performed with this setup. Conclusion can only be drawn in the steady-state regime.

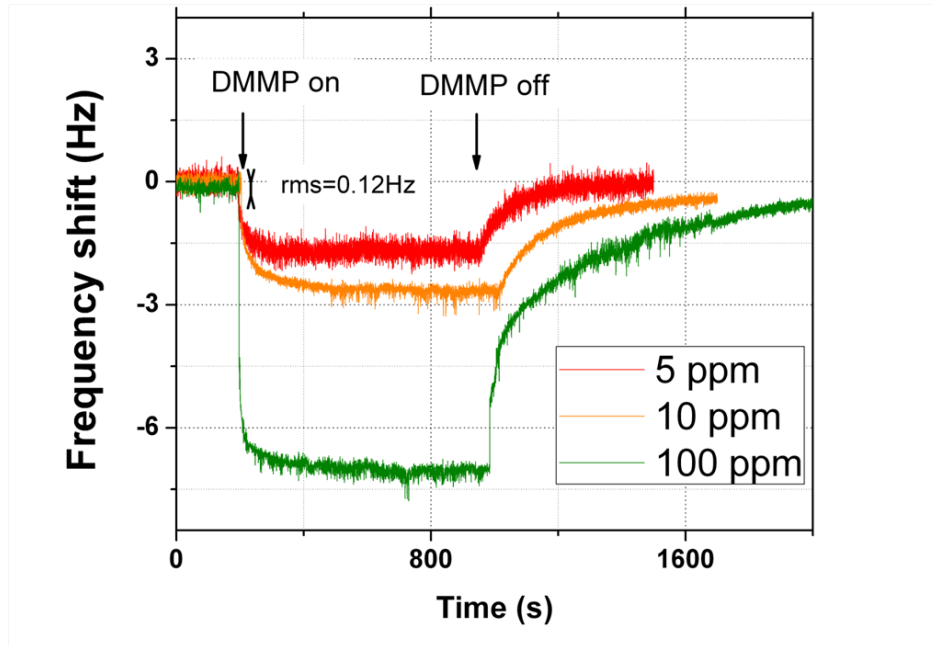


**Figure 4- 6:** First DMMP vapor detection measurement with an uncoated cantilever and un-optimized setup.

- With a total flow rate of 1 l/min required to deliver the 5 ppm DMMP flow , the frequency noise of the red curve in Figure 4- 6 is already five times larger than the frequency noise obtained with the lower flow rate used for the two other concentrations. To avoid this issue, a new mass flow meter and a flow splitter have been added to the test bench after the switching valve. This allows a better control of the actual flow delivered to the sensor without changing the DMMP concentration. However the available mass flow controller had a range of 0.1-10 l/min and thus in the real experiment the flow delivered to the cantilever was kept constant to 500 ml/min for DMMP concentration above 50ppb and equal to 1 l/min for the 25 ppb concentration.

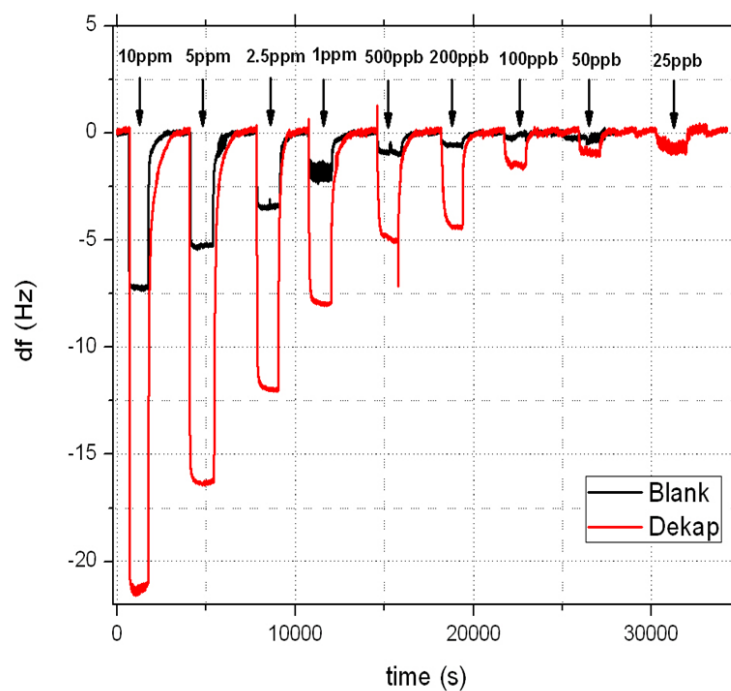
#### 4.2.2.2. DMMP sensing

Figure 4- 7 presents the response of our DMMP vapor detection system to a DMMP vapor concentration ranging from 10 ppm down to 25 ppb. This concentration level corresponds to the lowest DMMP concentration allowed by the gas delivery test bench without too large increase of frequency noise. It is also the lowest measured

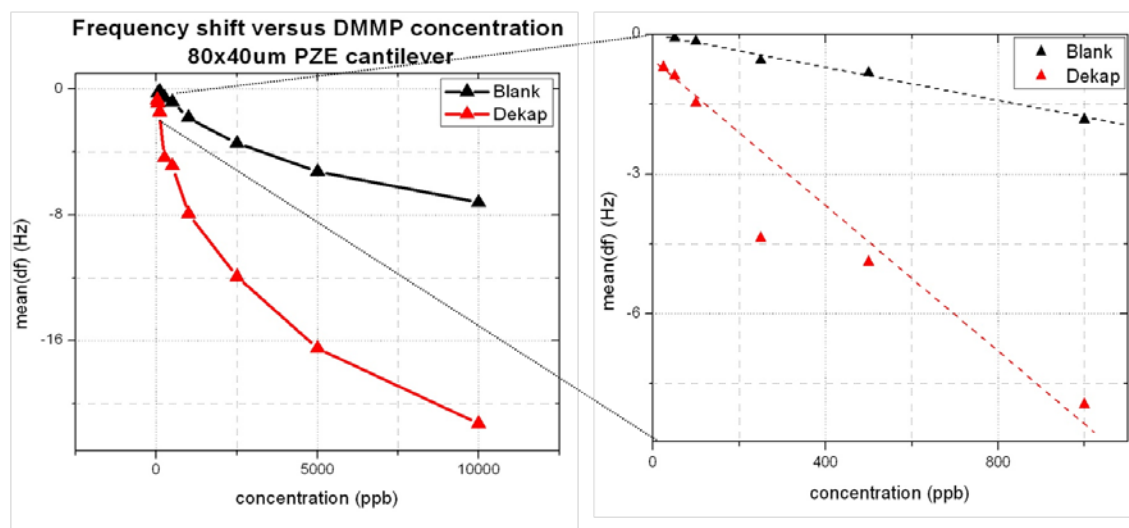
concentration of DMMP reported so far in the literature (Table 4- 3). It should be noted that the device frequency is fairly stable over the non-stop 12-hour measurement and recovers its initial value when the exposure to DMMP vapor is turned off (no significant drift over time). However an important difference between the fall (~ 30s) and rise time (up to 15 min) can be observed. Such large desorption time is uncommon in the literature and have not been observed during experiments with NEMS devices on the same bench and same functionalization layer [58] and [50]. Thus, we think it is not related to a very low desorption rate  $k_{off}$  but rather to the desorption of DMMP molecules from the sensor chamber walls when the DMMP flow is switched off.

Figure 4- 8 presents frequency shift versus DMMP vapor concentration. It is linear for low DMMP concentration and saturates for concentration higher than 1 ppm. This saturation is most likely linked to the extremely low thickness of the DKAP: the concentration range of our DMMP sensor can be extended by orders of magnitude by increasing the DKAP thickness. In the linear regime, the concentration sensitivity is 28 mHz/ppb, which allows us to calculate a moderate value of the partition coefficient for DKAP/DMMP couple of  $2.10^4$ . This is more than 2 orders of magnitude smaller than values reported in [50]. This can be explained by the use in our experiments of an DKAP solution that was already strongly degraded due to a too long exposure to ambient air (2-4 month).

In spite of this surprisingly poor partition coefficient, the minimum measured DMMP concentration (25 ppb) and the ultimate concentration resolution calculated from the RMS frequency noise (10 ppb) are at the level of the state of the art (Table 4- 3). As two to three orders of magnitude improvement can be reasonably expected with the use of a newer DKAP solution for the functionalization of the cantilever, we are confident that DMMP concentration in the ppt levels can be reached, and even outstripped if the design of the cantilever is optimum as presented in section 2.3.3.3.



**Figure 4- 7:** DMMP vapor detection experiment with an uncoated and a DKAP coated cantilever and for DMMP vapors concentration from 10 ppm down to 25 ppb



**Figure 4- 8:** Frequency shift versus DMMP concentration (sensitivity graph) for our cantilever resonator gas sensing setup for an un-coated (blank) and a DKAP coated cantilever

Device & Ref	Resonance Frequency (MHz)	DMMP Concentration resolution (measured) (ppb)	DMMP Concentration resolution (estimated) (ppb)
FBAR [122]	1100 <sup>(a)</sup>	<sup>(c)</sup>	60 <sup>(e)</sup>
SAW [34]	158 <sup>(a)</sup>	87 <sup>(b)</sup>	42 <sup>(a)</sup>
CMR [123]	180 <sup>(a)</sup>	700 <sup>(d)</sup>	0.35 <sup>(e)</sup>
CMUT [124]	47.7 <sup>(a)</sup>	15 <sup>(d)</sup>	3 <sup>(e)</sup>
Nano-cantilevers [50]	10 <sup>(a)</sup>	100 <sup>(d)</sup>	80 <sup>(e)</sup>
$\mu$ -cantilevers [125][126]	0.1 <sup>(a)</sup>	25 <sup>(d)</sup>	2 <sup>(e)</sup>

**Table 4- 3:** Comparison of our piezoelectric cantilever resonator based gas sensor performances with other micro/nano resonator based gas sensor. (a) data provided in the referenced article, (b) data calculated from the informations in the referenced article (c) data not available (d) measured (e) calculated from the SMLOD with a partition coefficient of  $10^5$  and functionalization thickness equal to one tenth of the device thickness.

### 4.3. Conclusion

With the results presented in this chapter, we have validated the theoretical method we have followed to obtain a high resolution sensor based on piezoelectric cantilevers resonator. More precisely, the theoretically analysis has shown that the most important parameter to estimate the gas sensing performance is the frequency stability of the resonator that determines the minimum measurable resonance frequency shift. We have thus measured the Allan Deviation, a particular estimator of the frequency noise variance, of our piezoelectric cantilever. These experiments have

been performed using a custom open loop setup, a digital PLL and a self-oscillating scheme. In all cases results are consistent with analytical predictions under the hypothesis of a dominant electronic noise (white). In the best configuration and even though our cantilever design is far from being optimal, the minimum obtained Allan deviation is  $10^{-8}$ , at the level of the state of the art of micro/nano resonator. This sets the SMLOD of our cantilever to  $53 \text{ zg}/\mu\text{m}$  among the best ever reported values. To confirm the potentially high gas sensing resolution of these devices, we have also experimentally studied the response of our cantilevers under DMMP vapor. Although these experiments provide only preliminary results, we have been able to detect the presence of DMMP down to 25 ppb concentration and estimate our Limit Of Detection (LOD) down to 10 ppb. This resolution figures are among the best ever reported in the literature.

Thinner cantilevers with a lower static capacitance, higher quality factor and onset of non-linearity, read-out circuits with lower input capacitance and more efficient functionalization layer will surely enable even better performances. Before that, the experimental setup and procedure for gas sensing experiment must be improved especially for what concerns the temperature stability, the precision on the nominal DMMP vapor concentration delivered to the cantilevers and the encapsulation of the cantilever in a low volume gas chamber. Other types of gas should also be tested.

# General Conclusion

---

The goal of this PhD work was twofold: investigating the potential of piezoelectric cantilevers for the realization of high resolution resonant gas chemo sensor and progressing toward the demonstration of the piezoelectric transduction at the nano-scale. These two questions represent an important technological challenge in today's research. Several gas sensing applications such as on-field detection of warfare agents, monitoring of indoor air pollution and medical diagnosis (like lung cancer) require the development of always faster, more sensitive and more selective gas sensing systems. Actually, current gas sensing technologies offer either bulky and expensive but highly reliable instruments (gas chromatographer or mass spectrometer) or either low performance, low-cost but miniaturized components. In the meantime, several new and very promising sensor paradigms are being investigated especially thanks to the development of micro and nano-technologies over the last three decades. Among them, Micro and Nano Electro Mechanical (M/NEMS) resonator-based gas sensors offer particularly interesting perspectives.

Their working principle is rather simple and relies on the variation of the natural resonance frequency of a mechanical structure, due to the mass of the gas molecules accreting on its surface. In this operation mode, MEMS gas chemo-sensors benefit from two major advantages providing high sensing performances: 1) frequency is one of most accurate physical quantities to measure and 2) the miniscule mass and high resonance frequency of MEMS resonators make them extremely sensitive to changes in their vibrating mass. Nevertheless, in the race for always smaller devices, the question of the efficiency of the transduction techniques used to actuate and/or detect the device motion has become a key issue. It turns out that the smaller the device, the lower the output signal, the higher the sensitivity to parasitics and thus the harder the measurement.

In order to investigate these two questions, we have begun our analysis in Chapter 1 by an overview existing gas chemo sensors technologies and the possible Figures of Merit that can be used to compare their performance. These devices are single components that deliver an electrical output signal proportional to the concentration of one (or several) gas analyte(s) in the surrounding gas mixture. Their

architecture is composed of two main parts: the chemical transduction that transforms the concentration signal into a physical one at the sensor surface; and the physical transduction that transforms the surface physical signal into an electrical one. These sensors can be classified and compared according to a few set of figure of merit namely: the sensitivity, the resolution or Limit Of Detection (LOD), the dynamic range, the selectivity, the stability and the response time. The chemical transduction plays a very important role but is not in the focus of this PhD, we have thus quickly presented its working principle and introduced useful notions such as the partition coefficient. We have then given an overview of the different physical transduction principles that can be encountered in gas chemo sensors: electrical, thermal, optical and mechanical. M/NEMS resonator-based gas chemo sensors belong to a subclass of mechanical resonators. With respect to other gas chemo sensors technologies, they offer high sensitivity and resolution performances at the ppb level. They allow the detection of a large panel of analytes with short response time. Finally they benefit from the use of highly parallelized Top Down micro and nano fabrication techniques and are thus very versatile in terms of design and system integration.

Among these devices, several types of mechanical resonators have already been tested: BAW, SAW, CMR, FMR. An analysis of their sensitivity and limit of detection has shown that, as opposed to what is often claimed in the literature, scaling down the device dimensions is not always beneficial. For gas sensing application, the accreted mass of targeted molecules is uniformly spread over the sensor surface, therefore the smaller the surface area of the sensor the smaller is the total accreted mass. There is thus room for engineering tradeoff. We have shown that two resonator characteristics matter most: the overall thickness and the resonance frequency stability.

This latter parameter depends on the resonator design and on the type of transduction used to actuate and detect device motion. In chapter 2, we have given an overview of the different transductions techniques available for cantilever flexural resonator.

Piezoelectric (PZE) transduction has several advantages compared to more conventional techniques in M/NEMS, namely electrostatic, capacitive, thermo-elastic, piezoresistive and optical. It enables on-chip transduction, very low power operation and most importantly it scales down without loss of efficiency as it is a stress/strain-

related transduction (as opposed to displacement-related transductions). Nonetheless, this transduction technique has been very little studied at the nanoscale; probably due to the lack of piezoelectric films deposition techniques compatible with the nano-scale dimensions of the device and with high piezoelectric performance.

Following this remark, we have look for more quantitative argument in favor of ultra-thin piezoelectric films. We have thus focused on the analytical modeling of piezoelectric transduction in cantilever resonators and use it for a design optimization study. We have shown that, under the hypothesis of a dominant electronic noise, constant quality factor and onset of non-linearity, the gravimetric performance is sensitive to the cantilever design but also to its integration level with its detection electronic. We have shown that the optimum performance is reached when the minimum AlN thickness allowed by the fabrication technologies is used and when the capacitance of the cantilever is matched to the so-called load capacitance constituted by the input capacitance of the electronic detector, the capacitance of the cable between the cantilever and the electronic detector and finally by the capacitance of the cantilever connection pads.

Following these conclusions, we have presented in chapter 3 the development of sub-100 nm thick AlN films using DC pulse reactive magnetron sputtering with high piezoelectric properties and the integration of these films in properly working devices. We have shown that the residual stress of the AlN layer can be switched from tensile to compressive by reducing the DC power, that the rocking curve FWHM increases with reducing the AlN layer thickness and finally that the  $e_{31}$  piezoelectric coefficient remains constant and equal to  $0.8 \text{ C} \cdot \text{m}^{-2}$  at the level of state of the art for AlN thin films even down to 50 nm. The obtained 50 nm thick AlN films are the thinnest-ever demonstrated piezoelectric films with high piezoelectric performance in the literature.

As a conservative approach and in order to reduce development time, we have reused an pre-existing set of masks at LETI that allows the fabrication of cantilevers 80  $\mu\text{m}$  long and 40  $\mu\text{m}$  wide. We have also decided to use a SiN elastic layer with a high-enough thickness to stiffen the cantilever and reduce its sensitivity to built-in stress in the different layers. An annealing step at the end of the process has also been used to tune the built-in stress of a low temperature-deposited Pt top electrode in order to balance built-in stresses of the other material layers. Of course the fabricated

cantilever embeds the developed 50 nm thick AlN film for the actuation and detection. The obtained cantilevers have a first flexural mode resonance frequency slightly below 100 kHz corresponding to the analytically predicted value. The electrical response of these cantilevers fits also very well with the analytical model presented in Chapter 2. The output signal level on resonance is in the order of a few mV which is already satisfactory considering that the design of the cantilever is far from being optimum.

In the last part of chapter 3, we have presented our attempt to fabricate large arrays of nano cantilevers with a single lithography step VLSI compatible process and an optimum material stack. These devices should overcome the efficiency decrease of the piezoelectric transduction with table-top electronic detector by summing up the response of a large number of identical nano-scale resonators. Due to a lack of time and resources, only one fabrication run has been performed and all the fabricated devices were short circuited. This is most likely due to the re-deposition of metallic material on the edge of the cantilever. Further process developments are required in order to optimize the stack etching process.

Having in hands properly operating micro cantilevers, we have then investigated their use for gas sensing and all results are presented in Chapter 4. We have first investigated the frequency stability of these devices using a custom open loop setup and the two classical resonance frequency tracking loops (self-oscillation and PLL). These experiments proved that the setup is mainly limited by the input noise of the electronic detector and are always consistent with our analytical prediction. With the open loop setup, we have managed to measure Allan deviation in air of the order of  $10^{-8}$ , among the lowest value ever reported in the literature and corresponding to a Surface Mass Limit of Detection (SMLOD) of  $53 \frac{\text{zg}}{\mu\text{m}}$ . This ranks our cantilever among the best resonant gas sensing platforms. However, the optimum integration time where the Allan deviation is minimum has been found to be around 1 second which is slower than other higher frequency resonator based gas sensor but fully compatible with our PLL setup.

Finally, this setup was used to investigate the behavior of our piezoelectric cantilever resonators to Di-methylmethylphosphonate (DMMP) vapors. These experiments were performed in a large gas chamber and in the steady-state regime

after a very long transient times (~15 min). The polymer functionalization layer was not optimal: too thin and not sensitive enough to DMMP. Nonetheless, we have demonstrated that our piezoelectric cantilever resonators are able to detect DMMP concentration level down to 25 ppb with a limit of detection down to 10 ppb; once again among the best performance ever reported in the literature.

As a summary, we have managed to develop a high resolution gas sensor based on AlN thin film cantilever resonators with performance at the level of the state of the art. We have developed the theoretical and technological framework to demonstrate devices with even better performance. As for the demonstration of the piezoelectric transduction at the nano-scale, progresses brought by this work might seem less important but are for sure not negligible. Based on the results presented here, manufacturing few micron-long 200 nm thick piezoelectric cantilevers are clearly at hand. The active material layer, 50 nm thick AlN films, is ready and well known in terms of characteristic and deposition capability, patterning techniques must be further optimized but already show interesting results. As importantly, this thesis gives the theoretical basis to predict the output signal and gas sensing performance of any cantilever design. It can be also reused for more exotic design and thus it is a very efficient tool for the designer of future devices.

The following of this work, in our opinion, should first concentrate of the continuation of the gas sensing performance of our micro-cantilever. Different types of functionalization and targeted gas must be tested and procedure and test bench must be improved. As importantly, the possibility to encapsulate the cantilever in micro-fluidic package will surely bring much improvement on the way gas sensing experiment will be performed. In the meantime, new resonator design could be investigated. The current cantilever process can be reused to produce even thinner cantilevers, ultimately embedding the optimum material stack. This will result in higher transduction efficiency and thus higher output signal, lower Allan deviation and hopefully better gas sensing performance. Nevertheless, this will require checking and understanding how the quality factor and the onset of non-linearity vary with material stack thickness. Other types of resonators can also be investigated; our preference goes to two ports, in plane, free-free beams (*c.f.* Figure 2- 1). These

devices have a material stack that can be chosen fully symmetrical and thus insensitive to built-in stress. They do not require any elastic layers and thus can be designed thinner. They are anchored to the substrate at the middle of the beam, and have a patterned top electrode split in two along the beam length and defining thus two electrical ports. One port can be used for the actuation and the other one for the detection of the in-plane flexural motion reducing thus the so-called background signal. They have the following advantages: low thickness, large surface area, two electrical ports, and potentially a very high quality factor: anchor loss should be minimized thanks to the free-free setup and the in-plane motion should be less sensitive to viscous damping. These two research directions (improvement of gas sensing experiment and new design) might very well lead to the demonstration of gas sensing performance in the ppt range, 3-4 orders of magnitude better than what has been demonstrated in this thesis.

# Bibliography

---

- [1] BCC Research Market forecasting, “Gas Sensors and Gas Metering: Applications and Markets,” 2010.
- [2] R. Botter and G. Bouchoux, “Spectrometrie de masse,” *Techniques de l’ingenieur*, 2008.
- [3] E. Hoffmann and V. Stoobant, *Mass Spectrometry: Principles and Applications*. London: Wiley-Interscience Publication, 2007.
- [4] H. M. McNair and J. M. Miller, *Basic Gas Chromatography*. Bonston: Wiley & Sons, 2009.
- [5] M. Caude and A. Jardy, “Methodes chromatographiques,” *Techniques de l’ingenieur*, pp. 1–6, 2008.
- [6] P. Werle, “Near- and mid-infrared laser-optical sensors for gas analysis,” *Optics and Lasers in Engineering*, vol. 37, no. 2–3, pp. 101–114, Mar. 2002.
- [7] G. Dooly, E. Lewis, C. Fitzpatrick, and P. Chambers, “Low Concentration Monitoring of Exhaust Gases Using a UV-Based Optical Sensor,” *IEEE Sensors Journal*, vol. 7, no. 5, pp. 685–691, May 2007.
- [8] J. Li, W. Chen, and B. Yu, “Recent Progress on Infrared Photoacoustic Spectroscopy Techniques,” *Applied Spectroscopy Reviews*, vol. 46, no. 6, pp. 440–471, Aug. 2011.
- [9] T. C. Pearce, S. S. Schiffman, H. T. Nagle, and W. Gardner, J, Eds., *Handbook of Machine Olfaction*. Wienheim: Wiley-VCH, 2003.
- [10] W. Wang, K. Lee, T. Kim, I. Park, and S. Yang, “A novel wireless, passive CO<sub>2</sub> sensor incorporating a surface acoustic wave reflective delay line,” *Smart Materials and Structures*, vol. 16, no. 4, pp. 1382–1389, Aug. 2007.
- [11] FIGARO, “CDM4160 - Pre-calibrated module for carbon dioxide detection.”
- [12] C. Di Natale, “Electronic nose and sensorial analysis: comparison of performances in selected cases,” *Sensors and Actuators B: Chemical*, vol. 50, no. 3, pp. 246–252, Aug. 1998.
- [13] A. V Shevade, M. L. Homer, H. Zhou, A. D. Jewell, A. K. Kisor, K. S. Manatt, J. Torres, J. Soler, S. S. Yen, M. A. Ryan, M. Blanco, and W. A. Goddard, “Development of the Third Generation JPL Electronic Nose for International

- Space Station Technology Demonstration,” *37th International Conference on Environmental Systems (SAE)*,, 2007.
- [14] M. Phillips, R. N. Cataneo, A. R. C. Cummin, A. J. Gagliardi, K. Gleeson, and J. Greenberg, “preliminary report Detection of Lung Cancer With Volatile Markers in the Breath \*,” *Chest*, vol. 123, pp. 2115–2123, 2003.
- [15] G. Peng, E. Trock, and H. Haick, “Detecting simulated patterns of lung cancer biomarkers by random network of single-walled carbon nanotubes coated with nonpolymeric organic materials.,” *Nano letters*, vol. 8, no. 11, pp. 3631–5, Nov. 2008.
- [16] G. Peng, U. Tisch, O. Adams, M. Hakim, N. Shehada, Y. Y. Broza, S. Billan, R. Abdah-Bortnyak, A. Kuten, and H. Haick, “Diagnosing lung cancer in exhaled breath using gold nanoparticles.,” *Nature nanotechnology*, vol. 4, no. 10, pp. 669–73, Oct. 2009.
- [17] “Nanomix Inc.” [Online]. Available: [www.nano.com](http://www.nano.com).
- [18] “APIX TECHNOLOGY.” [Online]. Available: <http://apixtechnology.com/>.
- [19] K. E. Petersen, “Silicon as a mechanical material,” *Proceedings of the IEEE*, vol. 70, no. 5, pp. 420–457, 1982.
- [20] Yole development, “MEMS Market,” 2009.
- [21] Y. T. Yang, C. Callegari, X. L. Feng, K. L. Ekinici, and M. L. Roukes, “Zeptogram-scale nanomechanical mass sensing.,” *Nano letters*, vol. 6, no. 4, pp. 583–6, Apr. 2006.
- [22] K. Jensen, K. Kim, and a Zettl, “An atomic-resolution nanomechanical mass sensor.,” *Nature nanotechnology*, vol. 3, no. 9, pp. 533–7, Sep. 2008.
- [23] I. Bargatin, I. Kozinsky, and M. L. Roukes, “Efficient electrothermal actuation of multiple modes of high-frequency nanoelectromechanical resonators,” *Applied Physics Letters*, vol. 90, no. 9, p. 93116, 2007.
- [24] K. L. Ekinici and M. L. Roukes, “Nanoelectromechanical systems,” *Review of Scientific Instruments*, vol. 76, no. 6, p. 61101, 2005.
- [25] I. Bargatin, E. B. Myers, J. Arlett, B. Gudlewski, and M. L. Roukes, “Sensitive detection of nanomechanical motion using piezoresistive signal downmixing,” *Applied Physics Letters*, vol. 86, no. 13, p. 133109, 2005.
- [26] A. Boisen, S. Dohn, S. S. Keller, S. Schmid, and M. Tenje, “Cantilever-like micromechanical sensors,” *Reports on Progress in Physics*, vol. 74, no. 3, p. 36101, Mar. 2011.
- [27] F. Martin, P. Murali, M.-A. Dubois, and A. Pezous, “Thickness dependence of the properties of highly c-axis textured AlN thin films,” *Journal of Vacuum*

- Science & Technology A: Vacuum, Surfaces, and Films*, vol. 22, no. 2, p. 361, 2004.
- [28] A. N. Cleland, M. Pophristic, and I. Ferguson, “Single-crystal aluminum nitride nanomechanical resonators,” *Applied Physics Letters*, vol. 79, no. 13, p. 2070, 2001.
- [29] R. B. Karabalin, M. H. Matheny, X. L. Feng, E. Defay, G. Le Rhun, C. Marcoux, S. Hentz, P. Andreucci, and M. L. Roukes, “Piezoelectric nanoelectromechanical resonators based on aluminum nitride thin films,” *Applied Physics Letters*, vol. 95, no. 10, p. 103111, 2009.
- [30] N. Sinha, G. E. Wabiszewski, R. Mahameed, V. V. Felmetger, S. M. Tanner, R. W. Carpick, and G. Piazza, “Piezoelectric aluminum nitride nanoelectromechanical actuators,” *Applied Physics Letters*, vol. 95, no. 5, p. 053106, 2009.
- [31] “Quartz Microbalance Sensors - AppliedSensor,” 2012.
- [32] X. Du, Z. Wang, J. Huang, S. Tao, X. Tang, and Y. Jiang, “A new polysiloxane coating on QCM sensor for DMMP vapor detection,” *Journal of Materials Science*, vol. 44, no. 21, pp. 5872–5876, 2009.
- [33] “zNose Model 4500 - Electronic Sensor Technology,” 2012.
- [34] W. Wang, S. He, S. Li, and Y. Pan, “High frequency stability oscillator for surface acoustic wave-based gas sensor,” *Smart Materials and Structures*, vol. 15, no. 6, pp. 1525–1530, Dec. 2006.
- [35] E. S. Kim, “Piezoelectric MEMS for audio signal transduction, microfluidic management, resonant mass sensing, and movable surface micromachined structures,” *2008 IEEE Ultrasonics Symposium*, pp. 924–929, Nov. 2008.
- [36] D. Chen, Y. Xu, J. Wang, and L. Zhang, “Chemical Nerve gas sensor using film bulk acoustic resonator modified with a self-assembled Cu<sub>2</sub>S/11-mercaptopundecanoic acid bilayer,” *Sensors & Actuators: B. Chemical*, vol. 150, no. 1, pp. 483–486, 2010.
- [37] S. Wenzel and R. M. White, “Analytic comparison of the sensitivities of bulk-wave, surface-wave and flexural plate-wave ultrasonic gravimetric sensors,” *Applied Physics Letters*, vol. 54, no. 20, pp. 1976–1978, 1989.
- [38] E. Rubiola, *Phase noise and Frequency stability in Oscillators*. Cambridge University Press, 2009.
- [39] a. N. Cleland and M. L. Roukes, “Noise processes in nanomechanical resonators,” *Journal of Applied Physics*, vol. 92, no. 5, p. 2758, 2002.
- [40] K. L. Ekinici and M. L. Roukes, “Nanoelectromechanical systems,” *Review of Scientific Instruments*, vol. 76, no. 6, p. 061101, 2005.

- [41] M. E. Franke, T. J. Koplín, and U. Simon, "Metal and metal oxide nanoparticles in chemiresistors: does the nanoscale matter?," *Small*, vol. 2, no. 1, pp. 36–50, Jan. 2006.
- [42] J. W. Grate, S. N. Kaganove, and V. R. Bhethanabotla, "Examination of mass and modulus contributions to thickness shear mode and surface acoustic wave vapour sensor responses using partition coefficients," *Faraday Discussions*, vol. 107, pp. 259–283, 1997.
- [43] M. R. Jarrett and H. O. Finklea, "Detection of Nonpolar Vapors on Quartz Crystal Microbalances with Ni(SCN)<sub>2</sub> (4-picoline)<sub>4</sub> Coatings," *Analytical Chemistry*, vol. 71, no. 2, pp. 353–357, Jan. 1999.
- [44] A. Hierlemann, E. T. Zellers, and A. J. Ricco, "Use of Linear Solvation Energy Relationships for Modeling Responses from Polymer-Coated Acoustic-Wave Vapor Sensors energy relationships (LSERs) as models of responses from," *Analytical Chemistry*, vol. 73, no. 14, pp. 3458–3466, 2001.
- [45] Y. K. Jones, M. M. Johnson, F. Josse, and J. M. Hossenlopp, "ATR-FTIR spectroscopic analysis of sorption of aqueous analytes into polymer coatings used with guided SH-SAW sensors," *IEEE Sensors Journal*, vol. 5, no. 6, pp. 1175–1184, Dec. 2005.
- [46] E. Garcia-Berrios, T. Gao, M. D. Woodka, S. Maldonado, B. S. Brunshwig, M. W. Ellsworth, and N. S. Lewis, "Response versus Chain Length of Alkanethiol-Capped Au Nanoparticle Chemiresistive Chemical Vapor Sensors," *Journal of Physical Chemistry*, vol. 114, pp. 21914–21920, 2010.
- [47] N. Dewan, S. P. Singh, K. Sreenivas, and V. Gupta, "Influence of temperature stability on the sensing properties of SAW NO<sub>x</sub> sensor," *Sensors and Actuators B: Chemical*, vol. 124, no. 2, pp. 329–335, Jun. 2007.
- [48] Y. Ozaki, S. Suzuki, M. Morimitsu, and M. Matsunaga, "Enhanced long-term stability of SnO<sub>2</sub>-based CO gas sensors modified by sulfuric acid treatment," *Sensors and Actuators B: Chemical*, vol. 62, pp. 220–225, 2000.
- [49] Z. Cao, Y. Zheng, F. Gong, S. Long, P. Chen, and X. He, "Recognition of alkyl ketone molecules based on thickness-shear-mode acoustic sensors with calixarene derivatives," *Microchemical Journal*, vol. 86, no. 1, pp. 71–79, Jun. 2007.
- [50] M. Li, E. B. Myers, H. X. Tang, S. J. Aldridge, H. C. McCaig, J. J. Whiting, R. J. Simonson, N. S. Lewis, and M. L. Roukes, "Nanoelectromechanical resonator arrays for ultrafast, gas-phase chromatographic chemical analysis.," *Nano letters*, vol. 10, no. 10, pp. 3899–903, Oct. 2010.
- [51] X. Chen, M. Cao, Y. Li, W. Hu, P. Wang, K. Ying, and H. Pan, "A study of an electronic nose for detection of lung cancer based on a virtual SAW gas sensors array and imaging recognition method," *Measurement Science and Technology*, vol. 16, no. 8, pp. 1535–1546, Aug. 2005.

- [52] H. J. Lee, K. K. Park, O. Oralkan, M. Kupnik, and B. T. Khuri-Yakub, "CMUT as a chemical sensor for DMMP detection," *2008 IEEE International Frequency Control Symposium*, pp. 434–439, May 2008.
- [53] J. W. Grate, S. J. Patrash, and M. H. Abraham, "Method for Estimating Polymer-Coated Wave Vapor Sensor Responses," *Analytical Chemistry*, vol. 67, no. 73, pp. 2162–2169, 1995.
- [54] L. a. Pinnaduwege, D. L. Hedden, a. Gehl, V. I. Boiadjev, J. E. Hawk, R. H. Farahi, T. Thundat, E. J. Houser, S. Stepnowski, R. a. McGill, L. Deel, and R. T. Lareau, "A sensitive, handheld vapor sensor based on microcantilevers," *Review of Scientific Instruments*, vol. 75, no. 11, p. 4554, 2004.
- [55] P. Xu, X. Li, H. Yu, M. Liu, and J. Li, "Self-assembly and sensing-group graft of pre-modified CNTs on resonant micro-cantilevers for specific detection of volatile organic compound vapors," *Journal of Micromechanics and Microengineering*, vol. 20, no. 11, p. 115003, Nov. 2010.
- [56] C. Zuniga, M. Rinaldi, S. M. Khamis, T. S. Jones, A. T. Johnson, and G. Piazza, "DNA-Decorated Carbon Nanotubes as Sensitive Layer for AlN Contour-Mode Resonant-MEMS Gravimetric Sensor," *2009 IEEE 22nd International Conference on Micro Electro Mechanical Systems*, pp. 320–323, Jan. 2009.
- [57] E. J. Houser, T. E. Mlsna, V. K. Nguyen, R. Chung, R. L. Mowery, and R. Andrew McGill, "Rational materials design of sorbent coatings for explosives: applications with chemical sensors.," *Talanta*, vol. 54, no. 3, pp. 469–85, May 2001.
- [58] M. Li, H. X. Tang, and M. L. Roukes, "Ultra-sensitive NEMS-based cantilevers for sensing, scanned probe and very high-frequency applications.," *Nature nanotechnology*, vol. 2, no. 2, pp. 114–20, Feb. 2007.
- [59] I. Voiculescu, M. E. Zaghoul, R. a. McGill, E. J. Houser, and G. K. Fedder, "Electrostatically actuated resonant microcantilever beam in CMOS technology for the detection of chemical weapons," *IEEE Sensors Journal*, vol. 5, no. 4, pp. 641–647, Aug. 2005.
- [60] C. Ayela, F. Vandevelde, D. Lagrange, K. Haupt, and L. Nicu, "Combining resonant piezoelectric micromembranes with molecularly imprinted polymers.," *Angewandte Chemie (International ed. in English)*, vol. 46, no. 48, pp. 9271–4, Jan. 2007.
- [61] P. S. Waggoner and H. G. Craighead, "Micro- and nanomechanical sensors for environmental, chemical, and biological detection.," *Lab on a chip*, vol. 7, no. 10, pp. 1238–55, Oct. 2007.
- [62] D. James, S. M. Scott, Z. Ali, and W. T. O'Hare, "Chemical Sensors for Electronic Nose Systems," *Microchimica Acta*, vol. 149, no. 1–2, pp. 1–17, Dec. 2004.

- [63] G. Zuo, X. Li, Z. Zhang, T. Yang, Y. Wang, Z. Cheng, and S. Feng, "Dual-SAM functionalization on integrated cantilevers for specific trace-explosive sensing and non-specific adsorption suppression," *Nanotechnology*, vol. 18, no. 25, p. 255501, Jun. 2007.
- [64] F. Le Floch, J.-P. Simonato, and G. Bidan, "Electrochemical signature of the grafting of diazonium salts: A probing parameter for monitoring the electro-addressed functionalization of devices," *Electrochimica Acta*, vol. 54, no. 11, pp. 3078–3085, Apr. 2009.
- [65] S. J. Ippolito, S. Kandasamy, K. Kalantar-zadeh, W. Wlodarski, and A. Holland, "Comparison between conductometric and layered surface acoustic wave hydrogen gas sensors," *Smart Materials and Structures*, vol. 15, no. 1, pp. S131–S136, Feb. 2006.
- [66] C. Cantalini, H. T. Sun, M. Faccio, M. Pelino, S. Santucci, L. Lozzi, and M. Passacantando, "NO<sub>2</sub> sensitivity of WO<sub>3</sub> thin film obtained by high vacuum thermal evaporation," *Sensors and Actuators B: Chemical*, vol. 31, no. 1–2, pp. 81–87, Feb. 1996.
- [67] A. W. Adamson and A. P. Gast, *Physical chemistry of surfaces*. Wiley-Interscience Publication, 1958.
- [68] J. W. Grate, B. M. Wise, and M. H. Abraham, "Method for Unknown Vapor Characterization and Classification Using a Multivariate Sorption Detector. Initial Derivation and Modeling Based on Polymer-Coated Acoustic Wave Sensor Arrays and Linear Solvation Energy Relationships," *Analytical Chemistry*, vol. 71, no. 20, pp. 4544–4553, Oct. 1999.
- [69] M. C. Burl, B. C. Sisk, T. P. Vaid, and N. S. Lewis, "Classification performance of carbon black-polymer composite vapor detector arrays as a function of array size and detector composition," *Sensors and Actuators B: Chemical*, vol. 87, no. 1, pp. 130–149, Nov. 2002.
- [70] D. M. Wilson, S. Hoyt, J. Janata, K. Booksh, and L. Obando, "Chemical sensors for portable, handheld field instruments," *IEEE Sensors Journal*, vol. 1, no. 4, pp. 256–274, 2001.
- [71] G. Eranna, B. C. Joshi, D. P. Runthala, and R. P. Gupta, "Oxide Materials for Development of Integrated Gas Sensors: A Comprehensive Review," *Critical Reviews in Solid State and Materials Sciences*, vol. 29, no. 3, pp. 111–188, Jul. 2004.
- [72] N. Yamazoe, "Toward innovations of gas sensor technology," *Sensors and Actuators B: Chemical*, vol. 108, no. 1–2, pp. 2–14, Jul. 2005.
- [73] N. Barsan, D. Koziej, and U. Weimar, "Metal oxide-based gas sensor research: How to?," *Sensors and Actuators B: Chemical*, vol. 121, no. 1, pp. 18–35, Jan. 2007.

- [74] A. Ponzoni, E. Comini, G. Sberveglieri, J. Zhou, S. Z. Deng, N. S. Xu, Y. Ding, and Z. L. Wang, "Ultrasensitive and highly selective gas sensors using three-dimensional tungsten oxide nanowire networks," *Applied Physics Letters*, vol. 88, no. 20, p. 203101, 2006.
- [75] I.-D. Kim, A. Rothschild, B. H. Lee, D. Y. Kim, S. M. Jo, and H. L. Tuller, "Ultrasensitive chemiresistors based on electrospun TiO<sub>2</sub> nanofibers," *Nano Letters*, vol. 6, no. 9, pp. 2009–2013, 2006.
- [76] Z. L. Wang, "Nanobelts, Nanowires, and Nanodiskettes of Semiconducting Oxides From Materials to Nanodevices," *Advanced Materials*, vol. 15, no. 5, pp. 432–436, Mar. 2003.
- [77] C.-W. Hung, H.-L. Lin, H.-I. Chen, Y.-Y. Tsai, P.-H. Lai, S.-I. Fu, H.-M. Chuang, and W.-C. Liu, "Comprehensive study of a Pd-GaAs high electron mobility transistor (HEMT)-based hydrogen sensor," *Sensors and Actuators B: Chemical*, vol. 122, no. 1, pp. 81–88, Mar. 2007.
- [78] Y. Cheng, P. Xiong, L. Fields, J. P. Zheng, R. S. Yang, and Z. L. Wang, "Intrinsic characteristics of semiconducting oxide nanobelt field-effect transistors," *Applied Physics Letters*, vol. 89, no. 9, p. 093114, 2006.
- [79] J. Janata and M. Josowicz, "Conducting polymers in electronic chemical sensors.," *Nature materials*, vol. 2, no. 1, pp. 19–24, Jan. 2003.
- [80] J. Janata and M. Josowicz, "Organic semiconductors in potentiometric gas sensors," *Journal of Solid State Electrochemistry*, vol. 13, no. 1, pp. 41–49, Jun. 2008.
- [81] K. J. Albert, N. S. Lewis, C. L. Schauer, G. a Sotzing, S. E. Stitzel, T. P. Vaid, and D. R. Walt, "Cross-reactive chemical sensor arrays.," *Chemical reviews*, vol. 100, no. 7, pp. 2595–626, Jul. 2000.
- [82] J. T. English, B. a. Deore, and M. S. Freund, "Biogenic amine vapour detection using poly(anilineboronic acid) films," *Sensors and Actuators B: Chemical*, vol. 115, no. 2, pp. 666–671, Jun. 2006.
- [83] T. Zhang, S. Mubeen, N. V Myung, and M. a Deshusses, "Recent progress in carbon nanotube-based gas sensors.," *Nanotechnology*, vol. 19, no. 33, p. 332001, Aug. 2008.
- [84] P. Bondavalli, P. Legagneux, and D. Pribat, "Carbon nanotubes based transistors as gas sensors: State of the art and critical review," *Sensors and Actuators B: Chemical*, vol. 140, no. 1, pp. 304–318, Jun. 2009.
- [85] J. Li, Y. Lu, Q. Ye, M. Cinke, J. Han, and M. Meyyappan, "Carbon Nanotube Sensors for Gas and Organic Vapor Detection," *Nano Letters*, vol. 3, no. 7, pp. 929–933, Jul. 2003.

- [86] F. Patolsky, G. Zheng, and C. M. Lieber, "Nanowire based sensors," *Analytical chemistry*, pp. 4261–4269, 2006.
- [87] J. Jie, W. Zhang, K. Peng, G. Yuan, C. S. Lee, and S.-T. Lee, "Surface-Dominated Transport Properties of Silicon Nanowires," *Advanced Functional Materials*, vol. 18, no. 20, pp. 3251–3257, Oct. 2008.
- [88] F. Schedin, a K. Geim, S. V Morozov, E. W. Hill, P. Blake, M. I. Katsnelson, and K. S. Novoselov, "Detection of individual gas molecules adsorbed on graphene.," *Nature materials*, vol. 6, no. 9, pp. 652–5, Sep. 2007.
- [89] J. P. Novak, E. S. Snow, E. J. Houser, D. Park, J. L. Stepnowski, and R. a. McGill, "Nerve agent detection using networks of single-walled carbon nanotubes," *Applied Physics Letters*, vol. 83, no. 19, p. 4026, 2003.
- [90] "Nanōmix - Breakthrough Detection Solutions with the Nanoelectronic Sensation Technology." [Online]. Available: <http://nano.com/index.html>. [Accessed: 12-Nov-2011].
- [91] P. Furjes, Z. Vizvary, M. Adam, A. Morrissey, C. Ducso, and I. Barsony, "Thermal investigation of micro-filament heaters," *Sensors and Actuators A: Physical*, vol. 99, no. 1–2, pp. 98–103, Apr. 2002.
- [92] A. Hierlemann, "Application-specific sensor systems based on CMOS chemical microsensors," *Sensors and Actuators B: Chemical*, vol. 70, no. 1–3, pp. 2–11, Nov. 2000.
- [93] P. Krebs and A. Grisel, "A low power integrated catalytic gas sensor," *Sensors and Actuators B: Chemical*, vol. 13, no. 1–3, pp. 155–158, May 1993.
- [94] R. E. Cavicchi, G. E. Poirier, N. H. Tea, M. Afridi, D. Berning, A. Hefner, J. Suehle, M. Gaitan, S. Semancik, and C. Montgomery, "Micro-differential scanning calorimeter for combustible gas sensing," *Sensors and Actuators B: Chemical*, vol. 97, no. 1, pp. 22–30, Jan. 2004.
- [95] D. Cruz, J. Chang, S. Showalter, F. Gelbard, R. Manginell, and M. Blain, "Microfabricated thermal conductivity detector for the micro-ChemLab," *Sensors and Actuators B: Chemical*, vol. 121, no. 2, pp. 414–422, Feb. 2007.
- [96] K. Chen and E. Wu, Y, "Thermal analysis and simulation of the microchannel flow in miniature thermal conductivity detectors," *Sensors and Actuators A: Physical*, vol. 79, no. 3, pp. 211–218, Feb. 2000.
- [97] S. M. Daly, M. Grassi, D. K. Shenoy, F. Ugozzoli, and E. Dalcanale, "Supramolecular surface plasmon resonance (SPR) sensors for organophosphorus vapor detection," *Journal of Materials Chemistry*, vol. 17, no. 18, p. 1809, 2007.
- [98] O. S. Wolfbeis, "Fiber-optic chemical sensors and biosensors.," *Analytical chemistry*, vol. 80, no. 12, pp. 4269–83, Jun. 2008.

- [99] B. Lee, S. Roh, and J. Park, "Current status of micro- and nano-structured optical fiber sensors," *Optical Fiber Technology*, vol. 15, no. 3, pp. 209–221, Jun. 2009.
- [100] H. P. Lang, M. Hegner, E. Meyer, and C. Gerber, "Nanomechanics from atomic resolution to molecular recognition based on atomic force microscopy technology," *Nanotechnology*, vol. 13, pp. 29–36, 2002.
- [101] S. Okumaya, Y. Mitobe, K. Okuyama, and K. Matstsushita, "Hydrogene Gas Sensing Using Pd-Coated Cantilever," *Japanese Journal of Applied Physics*, vol. 39, no. 6, pp. 3584–3590, 2000.
- [102] Z. Hu, T. Thundat, and R. J. Warmack, "Investigation of adsorption and absorption-induced stresses using microcantilever sensors," *Journal of Applied Physics*, vol. 90, no. 1, p. 427, 2001.
- [103] J. D. Adams, B. Rogers, L. Manning, Z. Hu, T. Thundat, H. Cavazos, and S. C. Minne, "Piezoelectric self-sensing of adsorption-induced microcantilever bending," *Sensors and Actuators A: Physical*, vol. 121, no. 2, pp. 457–461, Jun. 2005.
- [104] T. Kiefer, L. G. Villanueva, F. Fargier, F. Favier, and J. Brugger, "The transition in hydrogen sensing behavior in noncontinuous palladium films," *Applied Physics Letters*, vol. 97, no. 12, p. 121911, 2010.
- [105] D. Raorane, S.-H. "Shawn" Lim, and A. Majumdar, "Nanomechanical Assay to Investigate the Selectivity of Binding Interactions between Volatile Benzene Derivatives," *Nano Letters*, vol. 8, no. 8, pp. 2229–2235, Jul. 2008.
- [106] S. Fanget, S. Hentz, P. Puget, J. Arcamone, M. Matheron, E. Colinet, P. Andreucci, L. Duraffourg, E. Meyers, and M. L. Roukes, "Gas sensors based on gravimetric detection: A Review," *Sensors and Actuators B: Chemical*, no. 0, p. -, 2011.
- [107] A. Ugural and S. K. Fenster, *Advanced strength and applied elasticity*, vol. 4, no. 3. Elsevier Science Publishing Company Inc., 1987.
- [108] D. Then, a. Vidic, and C. Ziegler, "A highly sensitive self-oscillating cantilever array for the quantitative and qualitative analysis of organic vapor mixtures," *Sensors and Actuators B: Chemical*, vol. 117, no. 1, pp. 1–9, Sep. 2006.
- [109] I. Dufour and L. Fadel, "Resonant microcantilever type chemical sensors: analytical modeling in view of optimization," *Sensors and Actuators B: Chemical*, vol. 91, no. 1–3, pp. 353–361, Jun. 2003.
- [110] J. F. Rosenbaum, *Bulk Acoustic Wave Theory and Devices*. Boston-London: Artech, 1998.
- [111] M. Pijolat, S. Loubriat, S. Queste, D. Mercier, a. Reinhardt, E. Defaÿ, C. Deguet, L. Clavelier, H. Moriceau, M. Aïd, and S. Ballandras, "Large

- electromechanical coupling factor film bulk acoustic resonator with X-cut LiNbO<sub>3</sub> layer transfer,” *Applied Physics Letters*, vol. 95, no. 18, p. 182106, 2009.
- [112] I. Koné, F. Domingue, a. Reinhardt, H. Jacquinet, M. Borel, M. Gorisse, G. Parat, F. Casset, D. Pellissier-Tanon, J. F. Carpentier, L. Buchailot, and B. Dubus, “Guided acoustic wave resonators using an acoustic Bragg mirror,” *Applied Physics Letters*, vol. 96, no. 22, p. 223504, 2010.
- [113] M. Vellekoop, “Acoustic wave sensors and their technology,” *Ultrasonics*, vol. 36, no. 1–5, pp. 7–14, Feb. 1998.
- [114] V. Agache, M. Cochet, R. Blanc, F. Baleras, and P. Caillat, “High Q factor plate resonators for ultrasensitive mass sensing applications,” *TRANSDUCERS 2009 - 2009 International Solid-State Sensors, Actuators and Microsystems Conference*, vol. i, pp. 1630–1633, Jun. 2009.
- [115] E. Colinet, J. Arcamone, A. Niel, E. Lorent, S. Hentz, and E. Ollier, “100 MHz oscillator based on a low polarization voltage capacitive Lamé-mode MEMS resonator,” in *2010 IEEE International Frequency Control Symposium*, 2010, pp. 174–178.
- [116] M. Rinaldi and G. Piazza, “Effects of volume and frequency scaling in AlN contour mode NEMS resonators on oscillator phase noise,” in *2011 Joint Conference of the IEEE International Frequency Control and the European Frequency and Time Forum (FCS) Proceedings*, 2011, pp. 1–5.
- [117] J. E. Bowers, B. T. Khuri-Yakub, R. L. Jungerman, and G. S. Kino, “Effect of nonuniform piezoelectric films on monolithic surface acoustic wave devices,” *Applied Physics Letters*, vol. 41, no. 9, pp. 805–807, 1982.
- [118] N. V. Lavrik and P. G. Datskos, “Femtogram mass detection using photothermally actuated nanomechanical resonators,” *Applied Physics Letters*, vol. 82, no. 16, p. 2697, Apr. 2003.
- [119] K. L. Ekinci, Y. T. Yang, M. L. Roukes, and I. Introduction, “Ultimate limits to inertial mass sensing based upon nanoelectromechanical systems,” *Journal of Applied Physics*, vol. 95, no. 5, pp. 2682–2689, 2004.
- [120] W. P. Robins, *Phase Noise in Signal Sources*. Peter Pergrinus, 1982.
- [121] N. Kacem, J. Arcamone, F. Perez-Murano, and S. Hentz, “Dynamic range enhancement of nonlinear nanomechanical resonant cantilevers for highly sensitive NEMS gas/mass sensor applications,” *Journal of Micromechanics and Microengineering*, vol. 20, no. 4, p. 45023, Apr. 2010.
- [122] H. Zhang and E. S. Kim, “Vapor and liquid mass sensing by micromachined acoustic resonator,” *IEEE MEMS 2003*, pp. 1–2, 2003.

- [123] M. Rinaldi, C. Zuniga, and G. Piazza, "SS-DNA functionalized array of AlN contour mode NEMS resonant sensors with single CMOS multiplexed oscillator for sub-ppb detection of volatile organic chemicals," *IEEE MEMS 2011*, no. Figure 2, pp. 976–979, 2011.
- [124] H. J. Lee, K. K. Park, and M. Kupnik, "Chemical Vapor Detection Using a Capacitive Micromachined Ultrasonic Transducer," *Analytical chemistry*, vol. 83, no. 24, pp. 9314–20, 2011.
- [125] P. Ivaldi, J. Abergel, M. H. Matheny, L. G. Villanueva, R. B. Karabalin, M. L. Roukes, P. Andreucci, S. Hentz, and E. Defay, "50 nm thick AlN film-based piezoelectric cantilevers for gravimetric detection," *Journal of Micromechanics and Microengineering*, vol. 21, no. 8, p. 85023, Aug. 2011.
- [126] P. Ivaldi, J. Abergel, H. Blanc, E. Colinet, E. B. Myers, M. L. Roukes, P. Robert, P. Andreucci, S. Hentz, and E. Defay, "DMMP vapor detection with 50nm thick AlN films based microcantilevers," *TRANSDUCERS 2011 - 2011 International Solid-State Sensors, Actuators and Microsystems Conference*, vol. 1, no. 2, pp. 162–165, 2011.
- [127] G. Binnig, C. Quate, and C. Gerber, "Atomic force microscope.," *Physical review letters*, vol. 56, no. 9, pp. 930–933, Mar. 1986.
- [128] T. R. Albrecht, "Microfabrication of cantilever styli for the atomic force microscope," *Journal of Vacuum Science & Technology A: Vacuum, Surfaces, and Films*, vol. 8, no. 4, p. 3386, Jul. 1990.
- [129] O. Wolter, "Micromachined silicon sensors for scanning force microscopy," *Journal of Vacuum Science & Technology B: Microelectronics and Nanometer Structures*, vol. 9, no. 2, p. 1353, Mar. 1991.
- [130] J. R. Barnes, R. J. Stephenson, C. N. Woodburn, S. J. O'Shea, M. E. Welland, T. Rayment, J. K. Gimzewski, and C. Gerber, "A femtojoule calorimeter using micromechanical sensors," *Review of Scientific Instruments*, vol. 65, no. 12, p. 3793, Dec. 1994.
- [131] T. Thundat, R. J. Warmack, G. Y. Chen, and D. P. Allison, "Thermal and ambient-induced deflections of scanning force microscope cantilevers," *Applied Physics Letters*, vol. 64, no. 21, p. 2894, May 1994.
- [132] T. Thundat, E. A. Wachter, S. L. Sharp, and R. J. Warmack, "Detection of mercury vapor using resonating microcantilevers," *Applied Physics Letters*, vol. 66, no. 13, p. 1695, Mar. 1995.
- [133] B. Ilic, "Attogram detection using nanoelectromechanical oscillators," *Journal of Applied Physics*, vol. 95, no. 7, p. 3694, 2004.
- [134] J. Chaste, a Eichler, J. Moser, G. Ceballos, R. Rurali, and a Bachtold, "A nanomechanical mass sensor with yoctogram resolution.," *Nature nanotechnology*, vol. 7, no. 5, pp. 301–4, May 2012.

- [135] J. Brugger, N. Blanc, P. Renaud, and N. F. de Rooij, "Microlever with combined integrated sensor/actuator functions for scanning force microscopy," *Sensors and Actuators A: Physical*, vol. 43, no. 1–3, pp. 339–345, May 1994.
- [136] S. C. Minne, S. R. Manalis, and C. F. Quate, "Parallel atomic force microscopy using cantilevers with integrated piezoresistive sensors and integrated piezoelectric actuators," *Applied Physics Letters*, vol. 67, no. 26, p. 3918, 1995.
- [137] D. Lange, C. Hagleitner, A. Hierlemann, O. Brand, and H. Baltes, "Complementary Metal Oxide Semiconductor Cantilever Arrays on a Single Chip: Mass-Sensitive Detection of Volatile Organic Compounds," *Analytical Chemistry*, vol. 74, no. 13, pp. 3084–3095, Jul. 2002.
- [138] S. Ghatnekar-Nilsson, E. Forsén, G. Abadal, J. Verd, F. Campabadal, F. Pérez-Murano, J. Esteve, N. Barniol, a Boisen, and L. Montelius, "Resonators with integrated CMOS circuitry for mass sensing applications, fabricated by electron beam lithography," *Nanotechnology*, vol. 16, no. 1, pp. 98–102, Jan. 2005.
- [139] J. Arcamone, M. a F. van den Boogaart, F. Serra-Graells, J. Fraxedas, J. Brugger, and F. Pérez-Murano, "Full-wafer fabrication by nanostencil lithography of micro/nanomechanical mass sensors monolithically integrated with CMOS," *Nanotechnology*, vol. 19, no. 30, p. 305302, Jul. 2008.
- [140] A. Boisen, J. Thaysen, H. Jensenius, and O. Hansen, "Environmental sensors based on micromachined cantilevers with integrated read-out," *Ultramicroscopy*, vol. 82, no. 1–4, pp. 11–16, Feb. 2000.
- [141] G. Yoshikawa, H.-P. Lang, T. Akiyama, L. Aeschimann, U. Staufer, P. Vettiger, M. Aono, T. Sakurai, and C. Gerber, "Sub-ppm detection of vapors using piezoresistive microcantilever array sensors.," *Nanotechnology*, vol. 20, no. 1, p. 015501, Jan. 2009.
- [142] I. Bargatin, E. B. Myers, J. S. Aldridge, C. Marcoux, P. Brianceau, L. Duraffourg, E. Colinet, S. Hentz, P. Andreucci, and M. L. Roukes, "Large-scale integration of nanoelectromechanical systems for gas sensing applications.," *Nano letters*, vol. 12, no. 3, pp. 1269–74, Mar. 2012.
- [143] M. Spletzer, A. Raman, A. Q. Wu, X. Xu, and R. Reifenberger, "Ultrasensitive mass sensing using mode localization in coupled microcantilevers," *Applied Physics Letters*, vol. 88, no. 25, p. 254102, 2006.
- [144] P. a Truitt, J. B. Hertzberg, C. C. Huang, K. L. Ekinici, and K. C. Schwab, "Efficient and sensitive capacitive readout of nanomechanical resonator arrays.," *Nano letters*, vol. 7, no. 1, pp. 120–6, Jan. 2007.
- [145] S. W. Stahl, E. M. Puchner, and H. E. Gaub, "Photothermal cantilever actuation for fast single-molecule force spectroscopy.," *The Review of scientific instruments*, vol. 80, no. 7, p. 073702, Jul. 2009.

- [146] C. Hall and N. York, "Optical excitation of nanoelectromechanical oscillators," *Applied Physics Letters*, vol. 86, no. May, pp. 3–5, 2005.
- [147] A. Schliesser, G. Anetsberger, R. Rivière, O. Arcizet, and T. J. Kippenberg, "High-sensitivity monitoring of micromechanical vibration using optical whispering gallery mode resonators," *New Journal of Physics*, vol. 10, no. 9, p. 095015, Sep. 2008.
- [148] V. B. Braginsky, F. Y. Khalili, and K. S. Thorne, *Quantum Measurement*. Cambridge University Press, 1995.
- [149] L. Bilhaut, "Actionnement magnétique à l' échelle nanométrique," 2009.
- [150] S. Timoshenko, "ANALYSIS OF BI-METAL THERMOSTATS," *Journal of the American Optical Society*, vol. 11, pp. 233–255, 1925.
- [151] J. Curie and P. Curie, "Developpement, par pression, de l'electricite polaire dans les cristaux hemiedres a faces inclinees," *Compte Rendus de l'Academie des Sciences*, vol. 91, pp. 294–295, 1880.
- [152] M. G. Lippman, "Principe de la conservation de l'electricite," *Anales de Chimie et de Physique*, vol. 5, p. 159, 1881.
- [153] J. Curie and P. Curie, "Contractions et dilatations produites par des tensions electrique dans les cristaux herniedres a faces inclinees," *Compte Rendus de l'Academie des Sciences*, vol. 93, pp. 1137–1140, 1881.
- [154] C. Chilowsky and P. Langevin, "Production of submarine signals and the location of submarine objects," US14715471917.
- [155] M. Majdoub, P. Sharma, and T. Cagin, "Enhanced size-dependent piezoelectricity and elasticity in nanostructures due to the flexoelectric effect," *Physical Review B*, vol. 77, no. 12, pp. 1–9, Mar. 2008.
- [156] W. Heywang, K. Lubitz, and W. Wersing, *Piezoelectricity: Evolution and Future of a technology*. Springer, 2008.
- [157] *IEEE Standard on Piezoelectricity*. National Institute of Standards and Technology (NIST), Institute of Electrical and Electronics Engineers (IEEE), 1988.
- [158] R. Ballas, H. Schlaak, and a Schmid, "The constituent equations of piezoelectric multilayer bending actuators in closed analytical form and experimental results," *Sensors and Actuators A: Physical*, vol. 130–131, pp. 91–98, Aug. 2006.
- [159] J. G. Smits and A. Ballato, "Dynamic admittance matrix of piezoelectric cantilever bimorphs," *Journal of Microelectromechanical Systems*, vol. 3, no. 3, 1994.

- [160] J. G. Smits, "Resonant diaphragm pressure gauge," *Proc. Symp Force, displacement Pressure and Flow*, 1982.
- [161] M. Ishida, H. Matsunami, and T. Tanaka, "Preparation and properties of ferroelectric PZT thin films by rf sputtering," *Journal of Applied Physics*, vol. 48, no. 3, pp. 951–953, 1977.
- [162] K. G. Brooks, D. Damjanovic, N. Setter, P. Luginbuhl, G. A. Racine, and N. F. de Rooij, "Piezoelectric response of PZT thin film actuated micromachined silicon cantilever beams," in *Proceedings of 1994 IEEE International Symposium on Applications of Ferroelectrics*, 1991, pp. 520–522.
- [163] J. Olivares, E. Iborra, M. Clement, L. Vergara, and J. Sangrador, "Piezoelectric actuation of microbridges using AlN," *Sensors and Actuators A: Physical*, vol. 123–124, pp. 590–595, Sep. 2005.
- [164] S. González-Castilla, J. Olivares, M. Clement, E. Iborra, J. Sangrador, J. Malo, and J. I. Izpura, "Electrical detection of the mechanical resonances in AlN-actuated microbridges for mass sensing applications," *Applied Physics Letters*, vol. 92, no. 18, p. 183506, 2008.
- [165] V. Mortet, K. Haenen, J. Potmesil, M. Vanecek, and M. D'Olieslaeger, "Diamond - Application to piezoelectric bimorph cantilever sensors," *Physica Status Solidi (a)*, vol. 203, no. 12, pp. 3185–3190, Sep. 2006.
- [166] T. Nagano, M. Nishigaki, K. Abe, K. Itaya, and T. Kawakubo, "Fabrication and Performance of Piezoelectric MEMS Tunable Capacitors Constructed with AlN Bimorph Structure," *2006 IEEE MTT-S International Microwave Symposium Digest*, pp. 1285–1288, 2006.
- [167] L.-P. Wang, E. Ginsburg, F. Gerfers, D. Samara-Rubio, B. Weinfeld, Q. Ma, V. Rao, and M. Y. He, "Sputtered AlN Thin Films for Piezoelectric MEMS Devices," *2006 5th IEEE Conference on Sensors*, pp. 10–13, Oct. 2007.
- [168] K. Krupa, M. Jozwik, C. Gorecki, a Andrei, L. Nieradko, P. Delobelle, and L. Hirsinger, "Static and dynamic characterization of AlN-driven microcantilevers using optical interference microscopy," *Optics and Lasers in Engineering*, vol. 47, no. 2, pp. 211–216, Feb. 2009.
- [169] E. S. Leland, P. K. Wright, and R. M. White, "A MEMS AC current sensor for residential and commercial electricity end-use monitoring," *Journal of Micromechanics and Microengineering*, vol. 19, no. 9, p. 094018, Sep. 2009.
- [170] V. Ferrari, D. Marioli, a. Taroni, E. Ranucci, and P. Ferruti, "Development and application of mass sensors based on flexural resonances in alumina beams," *IEEE Transactions on Ultrasonics, Ferroelectrics and Frequency Control*, vol. 43, no. 4, pp. 601–608, Jul. 1996.
- [171] S. Shin, S. Song, Y. Lee, N. Lee, J. Park, H. Park, and J. Lee, "Fabrication and Sensing Behavior of Piezoelectric Microcantilever for Nanobalance," *Japanese*

- Journal of Applied Physics*, vol. 42, no. Part 1, No. 9B, pp. 6139–6142, Sep. 2003.
- [172] J. H. Park, T. Y. Kwon, H. J. Kim, S. R. Kim, D. S. Yoon, C.-I. Cheon, H. Kim, and T. S. Kim, “Resonance properties and mass sensitivity of monolithic microcantilever sensors actuated by piezoelectric PZT thick film,” *Journal of Electroceramics*, vol. 17, no. 2–4, pp. 565–572, Dec. 2006.
- [173] S. Gonzalez-Castilla, J. Olivares, E. Iborra, M. Clement, J. Sangrador, J. Malo, and I. Izpura, “Piezoelectric microresonators based on aluminum Nitride for mass sensing applications,” *2008 IEEE Sensors*, pp. 486–489, Oct. 2008.
- [174] B. Rogers, L. Manning, M. Jones, T. Sulchek, K. Murray, B. Beneschott, J. D. Adams, Z. Hu, T. Thundat, H. Cavazos, and S. C. Minne, “Mercury vapor detection with a self-sensing, resonating piezoelectric cantilever,” *Review of Scientific Instruments*, vol. 74, no. 11, p. 4899, 2003.
- [175] J. D. Adams, G. Parrott, C. Bauer, T. Sant, L. Manning, M. Jones, B. Rogers, D. McCorkle, and T. L. Ferrell, “Nanowatt chemical vapor detection with a self-sensing, piezoelectric microcantilever array,” *Applied Physics Letters*, vol. 83, no. 16, p. 3428, 2003.
- [176] M. Brissaud, “Modelling of non-symmetric piezoelectric bimorphs,” *Journal of Micromechanics and Microengineering*, vol. 14, no. 11, pp. 1507–1518, Nov. 2004.
- [177] S. N. Mahmoodi, N. Jalili, and M. F. Daqaq, “Modeling, Nonlinear Dynamics, and Identification of a Piezoelectrically Actuated Microcantilever Sensor,” *IEEE/ASME Transactions on Mechatronics*, vol. 13, no. 1, pp. 58–65, Feb. 2008.
- [178] J. Adams, L. Manning, B. Rogers, M. Jones, and S. Minne, “Self-sensing tapping mode atomic force microscopy,” *Sensors and Actuators A: Physical*, vol. 121, no. 1, pp. 262–266, May 2005.
- [179] V. Ferrari, D. Marioli, and A. Taroni, “Improving the accuracy and operating range of quartz microbalance sensors by a purposely designed oscillator circuit,” *IEEE Transactions on Instrumentation and Measurement*, vol. 50, no. 5, pp. 1119–1122, 2001.
- [180] G. Arndt, “System architecture and circuit design for micro and nanoresonators-based mass sensing arrays,” 2011.
- [181] Y. K. Yong and J. R. Vig, “Modeling resonator frequency fluctuations induced by adsorbing and desorbing surface molecules.,” *IEEE transactions on ultrasonics, ferroelectrics, and frequency control*, vol. 37, no. 6, pp. 543–50, Jan. 1990.

- [182] J. R. Vig and Y. Kim, "Noise in microelectromechanical system resonators.," *IEEE transactions on ultrasonics, ferroelectrics, and frequency control*, vol. 46, no. 6, pp. 1558–65, Jan. 1999.
- [183] O. Jaks and Z. Djuric, "Adsorption  $\pm$  desorption noise in micromechanical resonant structures," *Sensors And Actuators*, vol. 96, pp. 244–251, 2002.
- [184] S. Bianco, M. Cocuzza, S. Ferrero, E. Giuri, G. Piacenza, C. F. Pirri, A. Ricci, L. Scaltrito, D. Bich, A. Merialdo, P. Schina, and R. Correale, "Silicon resonant microcantilevers for absolute pressure measurement," *Journal of Vacuum Science & Technology B: Microelectronics and Nanometer Structures*, vol. 24, no. 4, p. 1803, 2006.
- [185] M. Aissi, E. Tournier, M. a. Dubois, C. Billard, H. Ziad, and R. Plana, "A 5 GHz above-IC FBAR Low Phase Noise Balanced Oscillator," *IEEE Radio Frequency Integrated Circuits (RFIC) Symposium, 2006*, pp. 25–28, 2006.
- [186] G. Arndt, E. Defay, G. Le Rhun, P. Rey, F. Perruchot, M. Aid, L. Liu, and M. Miller, "Dynamic analytical modelling and piezoelectric characterization of a Pb(Zr, Ti)O<sub>3</sub>/SiN cantilever with losses," *Journal of Micromechanics and Microengineering*, vol. 20, no. 11, p. 115019, Nov. 2010.
- [187] P. Muralt, "Recent Progress in Materials Issues for Piezoelectric MEMS," *Journal of the American Ceramic Society*, vol. 91, no. 5, pp. 1385–1396, May 2008.
- [188] G. Piazza, "Integrated aluminum nitride piezoelectric microelectromechanical system for radio front ends," *Journal of Vacuum Science & Technology A: Vacuum, Surfaces, and Films*, vol. 27, no. 4, p. 776, 2009.
- [189] S. Xu, Y. Qin, C. Xu, Y. Wei, R. Yang, and Z. L. Wang, "Self-powered nanowire devices.," *Nature nanotechnology*, vol. 5, no. 5, pp. 366–73, May 2010.
- [190] S. J. Kang, J. Y. Choi, D. H. Chang, and Y. Y. Yoon, "A Study on the Growth and Piezoelectric Characteristics of ZnO Thin Film Using a RF Magnetron Sputtering Method," *Journal of the Korean Physical Society*, vol. 47, pp. 589–594, 2005.
- [191] J.-S. Moulet, M. Pijolat, J. Dechamp, F. Mazen, A. Tauzin, F. Rieutord, A. Reinhardt, E. Defay, C. Deguet, B. Ghyselen, L. Clavelier, M. Aid, S. Ballandras, and C. Mazure, "High piezoelectric properties in LiNbO<sub>3</sub> transferred layer by the Smart Cut technology for ultra wide band BAW filter applications," *2008 IEEE International Electron Devices Meeting*, pp. 1–4, Dec. 2008.
- [192] C. Poizat and a Benjeddou, "On analytical and finite element modelling of piezoelectric extension and shear bimorphs," *Computers & Structures*, vol. 84, no. 22–23, pp. 1426–1437, Sep. 2006.

- [193] R. F. Rutz, E. P. Harris, and J. J. Cuomo, "An AlN Switchable Memory Resistor Capable of a 20-MHz Cycling Rate and 500-picosecond Switching Time," *IBM Journal of Research and Development*, vol. 17, no. 1, pp. 61–65, 1973.
- [194] K. Uehara, Y. Aota, S. Kameda, H. Nakase, Y. Isota, and K. Tsubouchi, "Growth of Atomically Flat-Surface Aluminum Nitride Epitaxial Film by Metalorganic Chemical Vapor Deposition," *Japanese Journal of Applied Physics*, vol. 44, no. No. 5A, pp. 2987–2992, May 2005.
- [195] T. Palacios, F. Calle, E. Monroy, J. Grajal, M. Eickhoff, O. Ambacher, and C. Prieto, "Nanotechnology for SAW devices on AlN epilayers," *MATERIALS SCIENCE AND ENGINEERING B-SOLID STATE MATERIALS FOR ADVANCED TECHNOLOGY*, vol. 93, no. 1–3, pp. 154–158, 2002.
- [196] O. Ambacher, "Growth and applications of Group III nitrides," *JOURNAL OF PHYSICS D-APPLIED PHYSICS*, vol. 31, no. 20, pp. 2653–2710, 1998.
- [197] S. Six and B. Rauschenbach, "Stress generation during ion beam-assisted pulsed laser deposition of thin AlN films," *THIN SOLID FILMS*, vol. 415, no. 1–2, pp. 285–289, 2002.
- [198] M.-A. Dubois and P. Muralt, "Stress and piezoelectric properties of aluminum nitride thin films deposited onto metal electrodes by pulsed direct current reactive sputtering," *Journal of Applied Physics*, vol. 89, no. 11, p. 6389, 2001.
- [199] V. V Felmetger, P. N. Laptev, and S. M. Tanner, "Crystal orientation and stress in AC reactively sputtered AlN films on Mo electrodes for electro-acoustic devices," *2008 IEEE Ultrasonics Symposium*, pp. 2146–2149, Nov. 2008.
- [200] E. Defay, G. Le Rhun, F. Perruchot, P. Reiy, A. Suhm, M. Aid, L. I. Liu, S. Pacheco, and M. Miller, "Piezoelectric PZT thin films in the 100nm range: a solution for actuators embedded in low voltage devices," *Young*, pp. 619–622, 2009.
- [201] K. K. Wong, *Properties of Lithium Niobate*, EMIS Data. (INSPEC, London, 1989.
- [202] Epcos, "Lithium Niobate / Lithium Tantalate."
- [203] A. Brugere, J. S. Moulet, S. Gidon, A. Tchelnokov, C. Deguet, L. Clavelier, and B. Ghyselen, "Piezoresponse Force Microscopy study of a single-crystal LiTaO<sub>3</sub> thin film obtained by the Smart Cut TM technology," *IEEE INTERNATIONAL SYMPOSIUM ON THE APPLICATIONS OF FERROELECTRICS*, pp. 3–6, 2010.
- [204] J. A. Thornton, "The microstructure of sputter-deposited coatings," *Journal of Vacuum Science & Technology A: Vacuum, Surfaces, and Films*, vol. 4, no. 6, pp. 3059–3065, 1986.

- [205] X. Xu, "Morphological properties of AlN piezoelectric thin films deposited by DC reactive magnetron sputtering," *Thin Solid Films*, vol. 388, no. 1–2, pp. 62–67, Jun. 2001.
- [206] F. Engelmark, G. Fucntes, I. V. Katardjiev, a. Harsta, U. Smith, and S. Berg, "Synthesis of highly oriented piezoelectric AlN films by reactive sputter deposition," *Journal of Vacuum Science & Technology A: Vacuum, Surfaces, and Films*, vol. 18, no. 4, p. 1609, 2000.
- [207] L. Vergara, "Influence of oxygen and argon on the crystal quality and piezoelectric response of AlN sputtered thin films," *Diamond and Related Materials*, vol. 13, no. 4–8, pp. 839–842, Aug. 2004.
- [208] E. Iborra, "Piezoelectric properties and residual stress of sputtered AlN thin films for MEMS applications," *Sensors and Actuators A: Physical*, vol. 115, no. 2–3, pp. 501–507, Sep. 2004.
- [209] J. Ruffner, "Effect of substrate composition on the piezoelectric response of reactively sputtered AlN thin films," *Thin Solid Films*, vol. 354, no. 1–2, pp. 256–261, Oct. 1999.
- [210] S. Mishin, D. R. Marx, B. Sylvia, V. Lugh, K. L. Turner, and D. R. Clarke, "Sputtered AlN thin films on Si and electrodes for MEMS resonators: relationship between surface quality microstructure and film properties," *IEEE Symposium on Ultrasonics, 2003*, vol. 00, no. c, pp. 2028–2032, 2003.
- [211] A. Artieda, M. Barbieri, C. S. Sandu, and P. Mural, "Effect of substrate roughness on c-oriented AlN thin films," *Journal of Applied Physics*, vol. 105, no. 2, p. 24504, 2009.
- [212] E. Defay, C. Zinck, C. Malhaire, N. Baboux, and D. Barbier, "Modified free vibrating beam method for characterization of effective  $e_{31}$  coefficient and leakage resistance of piezoelectric thin films," *Review of Scientific Instruments*, vol. 77, no. 10, p. 103903, 2006.
- [213] M. Dubois, "Measurement of the effective transverse piezoelectric coefficient  $e_{31}$  of AlN and Pb(Zr,Ti)O<sub>3</sub> thin films," *Sensors and Actuators A: Physical*, vol. 77, no. 2, pp. 106–112, Oct. 1999.
- [214] V. V. Felmetger, P. N. Laptev, and R. J. Graham, "Deposition of ultrathin AlN films for high frequency electroacoustic devices," *Journal of Vacuum Science & Technology A: Vacuum, Surfaces, and Films*, vol. 29, no. 2, p. 021014, 2011.
- [215] J. E.-Y. Lee and A. a. Seshia, "Parasitic feedthrough cancellation techniques for enhanced electrical characterization of electrostatic microresonators," *Sensors and Actuators A: Physical*, vol. 156, no. 1, pp. 36–42, Nov. 2009.
- [216] D. W. Allan, D. A. Howe, and E. L. Walls, *Characterization of Clocks and Oscillators Edited by*. National Institute of Standards and Technology, 1990.

- [217] G. Jourdan, “Vers un microscope de force de Casimir, mesure quantitative de forces faible et nanositionnement absolu,” CNRS-L. Neel UJF, 2007.
- [218] E. Mile, G. Jourdan, I. Bargatin, S. Labarthe, C. Marcoux, P. Andreucci, S. Hentz, C. Kharrat, E. Colinet, and L. Duraffourg, “In-plane nanoelectromechanical resonators based on silicon nanowire piezoresistive detection.,” *Nanotechnology*, vol. 21, no. 16, p. 165504, Apr. 2010.
- [219] C. Kharrat, E. Colinet, and A. Voda, “H infinity Loop shaping control for PLL-based mechanical resonance tracking in NEMS resonant mass sensors,” *2008 IEEE Sensors*, pp. 1135–1138, Oct. 2008.
- [220] “Dimethyl methylphosphonate.” [Online]. Available: <http://webbook.nist.gov/cgi/cbook.cgi?ID=C756796&Units=SI&Mask=4&Type=ANTOINE&Plot=on#ANTOINE>.
- [221] “Nerve Agent Precursor: Dimethyl Methyl Phosphonate.” [Online]. Available: <http://cbwinfo.com/Chemical/Precursors/p3.html>.
- [222] Y. Wang, Z. Zhou, Z. Yang, X. Chen, D. Xu, and Y. Zhang, “Gas sensors based on deposited single-walled carbon nanotube networks for DMMP detection.,” *Nanotechnology*, vol. 20, no. 34, p. 345502, Aug. 2009.
- [223] Comsol, “MEMS MODULE model library.”
- [224] A. Greenbaum, *Iterative Methods for Solving Linear Systems*. SIAM, 1997, p. 220.
- [225] “MUMPS : a parallel sparse direct solver.” [Online]. Available: <http://graal.ens-lyon.fr/MUMPS/index.php?page=home>. [Accessed: 05-Mar-2012].

# Appendix A: FEM modeling of piezoelectric cantilever

---

As a complement to analytical modeling, Finite Element Models (FEM) represents a time-effective method to validate hypothesis and verify numerical predictions while taking into account complex bodies shapes and boundary conditions. In this appendix, we will present our effort on FEM modeling of piezoelectric cantilevers using the commercial software COMSOL. We will use a cantilever design that reproduces as closely as possible the geometry of our real device (see section 3.2.1 and Figure 3- 5) in order to understand the possible difference between analytical predictions and experimental results. For instance, the analytical model developed in the second chapter of the dissertation does not take into account the over-etching of the sacrificial layer at the clamped end of the cantilever which has for sure an influence on the resonance behavior of the cantilever. Beside, our analytical model is based on Euler Bernoulli theory of beams which is valid for small width over length ratio (typically 0.1) which is not the case for our real cantilever where  $W/L=0.5$ .

## A.1 Model description

COMSOL Multiphysics (Version 3.5) provides a module dedicated to the modeling of piezoelectric devices as a particular case of multi-physic domains coupling (mechanical and electrical domains). More precisely, it enables solving the fundamental equation of mechanics (Newton law) and electrostatics (Charge conservation) coupled through the constituent equation of piezoelectricity [157]. Using standard tensor notations, these equations can be written as:

$$\begin{aligned} \nabla \cdot \hat{c}(\nabla_s \mathbf{u}) + \nabla \cdot \hat{e}^T(\nabla V) - \hat{\xi} \dot{\mathbf{u}} - \hat{\rho} \ddot{\mathbf{u}} &= \mathbf{F}_V \\ \nabla \cdot (\hat{e} \nabla V + \hat{\sigma}_e \int \nabla V dt) + \nabla \cdot \hat{e}(\nabla_s \mathbf{u}) &= \rho_V \end{aligned} \quad (2.3-18)$$

where  $\mathbf{u} = \begin{bmatrix} u \\ v \\ w \end{bmatrix}$ ,  $V$  are the four unknown functions of the special coordinates

and represent the displacement field (x-y-z direction respectively) and the electric

potential.  $\mathbf{F}_V = \begin{bmatrix} f_x \\ f_y \\ f_z \end{bmatrix}$  and  $\rho_V$  are the external mechanical forces and electrical charges

volume density. The matrix  $\hat{c}$ ,  $\hat{e}$ ,  $\hat{\xi}$ ,  $\hat{\rho}$ ,  $\hat{\epsilon}$  and  $\hat{\sigma}_e$  are the elastic, piezoelectric, damping, mass density, permittivity and conductivity coefficient matrix respectively whose value for the different materials used in our simulation is given in Table B- 1. Note that for non-piezoelectric materials  $\hat{e} = [0]_{i,j}$  and the two equations in B.1-1 are decoupled.

In addition to the electrical / mechanical domain coupling, COMSOL Multiphysics provides the possibility link the FEM variable with the global variable of a SPICE model of an electrical circuit. This feature is particularly interesting because it enables simulating a complete device + detection electronic system. To do so, boundary surfaces in the FEM model are set as “*electrical ports*” with a constant potential that is computed by the SPICE model. Reciprocally, the FEM model is included in the SPICE model as discrete components with a current vs voltage characteristic computed from the FEM model. An example of such FEM-SPICE coupled model is described in a tutorial in [223] and has been adapted to meet our simulation needs. This FEM-SPICE coupling adds only few degrees of freedom (DOF) to the total number of DOF (typically three out of a couple of hundred of thousands) and has thus almost no influence on the computation time.

In correspondence with the colorized boundaries on Figure B- 1(b); the boundary conditions used in our model are:

- Mechanical domain:

Free:  $\nabla \cdot \hat{c}(\nabla_s \mathbf{u}) + \nabla \cdot \hat{e}^T(\nabla V) = 0$

Fixed:  $\mathbf{u} = \begin{bmatrix} u \\ v \\ w \end{bmatrix} = \mathbf{0},$

- Electrical domain (restricted to piezoelectric material domain boundaries):

Insulated:  $\mathbf{n} \cdot \left( \hat{\epsilon} \nabla V + \hat{\sigma}_e \int \nabla V dt + \hat{e}(\nabla_s \mathbf{u}) \right) = 0$  ( $\mathbf{n}$  boundary normal vector)

Electrical port:  $V = V_{circ}$

A typical SPICE netlist for the half bridge setup connected electronic circuit to the FEM model is:

```

Vin1 1 0 AC      1 0
X1  1 0 top_elec
Vin2 2 0 AC      1 180
C0  2 3 10 pF
X2  3 0 bot_elec
Cp  3 0 100 pF
.SUBCKT top_elec V_pzd_term1 I_pzd_term1 COMSOL: *
.SUBCKT bot_elec V_pzd_term2 I_pzd_term2 COMSOL: *
.ENDS

```

Where Vin1 and Vin2 are two AC voltage sources in phase opposition feeding the top electrode component X1 and the dummy capacitor C0 respectively. The bottom electrode component X2, the dummy capacitor C0 and the parasitic capacitor Cp are all connected to the node 3 or “bridge middle point”. The two instances starting by .SUBCKT are used to define sub-circuits path link to the FEM model.

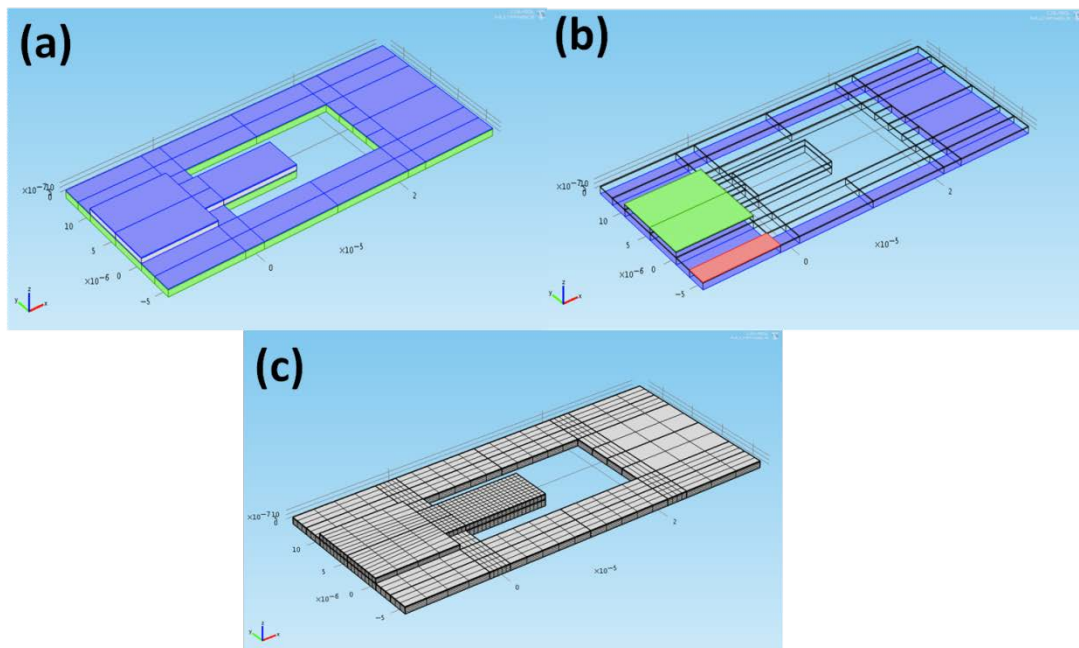


**Figure A- 1:** FEM problem definition (a) Materials: blue Pt, grey AlN and green SiN (b) Boundaries conditions: blue mechanically fixed, green electrical port “top electrode”, red electrical port “bottom electrode”, all other boundary are mechanically free and electrically insulated (c) Typical mesh with medium density obtained by extruding a rectangular mesh of the bottom SiN boundary through the thickness of the different layers.

	AlN	SiN	Pt
<b>Elastic Matrix / Young Modulus (MPa)</b>	$\begin{bmatrix} 360 & 122 & 162 & 0 & 0 \\ 122 & 360 & 162 & 0 & 0 \\ 162 & 162 & 377 & 0 & 0 \\ 0 & 0 & 0 & 113 & 0 \\ 0 & 0 & 0 & 0 & 113 \\ 0 & 0 & 0 & 0 & 0 \end{bmatrix}$	250	168
<b>Piezoelectric matrix (C.m<sup>-2</sup>) / Poisson Ratio</b>	$\begin{bmatrix} 0 & 0 & 0 & 0 & -0.4 \\ 0 & 0 & 0 & -0.4 & 0 \\ -0.8 & -0.8 & 1.48 & 0 & 0 \end{bmatrix}$	0.23	0.38
<b>Relative permittivity Matrix</b>	9 (isotropic)	9.5 (isotropic)	0
<b>Density (kg.m<sup>-3</sup>)</b>	2770	3100	21450
<b>Damping</b>	0.08 (isotropic)	0.08 (isotropic)	0.08 (isotropic)
<b>Conductivity</b>	0	0	1.36.10 <sup>6</sup>

**Table A- 1:** Numerical value of the material parameters used for the FEM simulations. The damping coefficient is chosen such that the quality factor of the first mode is 100 as per the typical value obtained on real devices.

The hexahedron mesh on Figure B- 1(c) is obtained by extruding a 2D rectangular mesh of the bottom surface of the SiN layer, through the thickness of the different material layers. This meshing technique allows a perfect control of the size and homogeneity of the elements that is critical to find a good tradeoff between computation time and results accuracy. Accuracy can be evaluated with residuals that COMSOL solvers compute either while solving (for iterative solvers such as GMRES [224]) or at the end of the resolution (for direct solvers such as MUMPS [225]). As a rule of thumb, we set a relative residue objective to  $10^{-3}$  in order to obtain with certitude three digit precision on the numerical values of the different variable. However in practice, in order to the number of DOF below 300000 for reasonable computation time, we start each FEM study with a convergence study that consists in looking at the stability of output values (resonance frequencies, tip deflection, electrical field, stress components) while increasing the mesh density (*c.f.* Figure B- 2). As a result we have found that, for the precision objective up to the third digit, the length of the cantilever must be meshed by at least 50 elements, the width by at least  $5 \cdot W/L$  elements and each layer thickness by at least 4 elements (5 for the AlN layer).

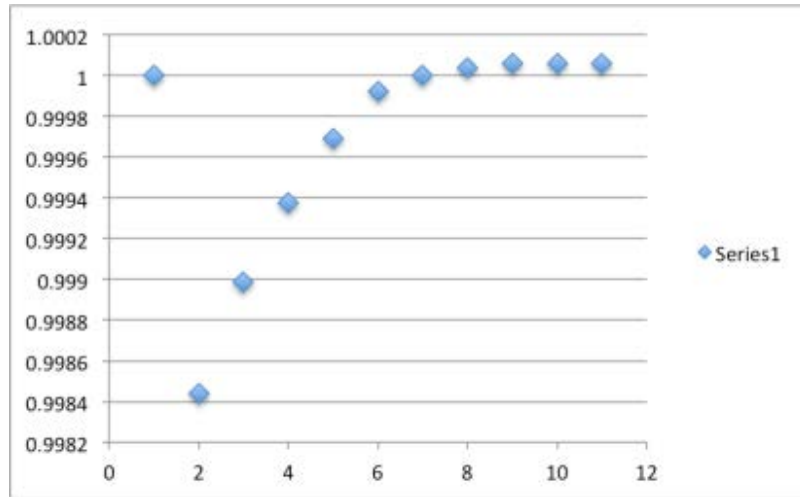


**Figure A- 2:** Results of FEM convergence study for first resonance mode frequency

## A.2 Results

Figure B- 3 shows the output result of a FEM harmonic simulation for the amplitude of output voltage of the capacitive bridge. For this simulation, the design of the cantilever is chosen in the domain of validity of Euler Bernoulli hypothesis with a length  $L = 80 \mu\text{m}$ , a width  $W = 8 \mu\text{m}$  and a material stack SiN (700 nm) / Pt (100 nm) / AlN (50 nm) / Pt (25nm). The seven visible peaks correspond to the six first flexural modes and the first extensional mode (*cf* inset Figure B- 3) and the corresponding resonance frequencies are in excellent agreement with the analytical values (*cf*. Table B- 1).

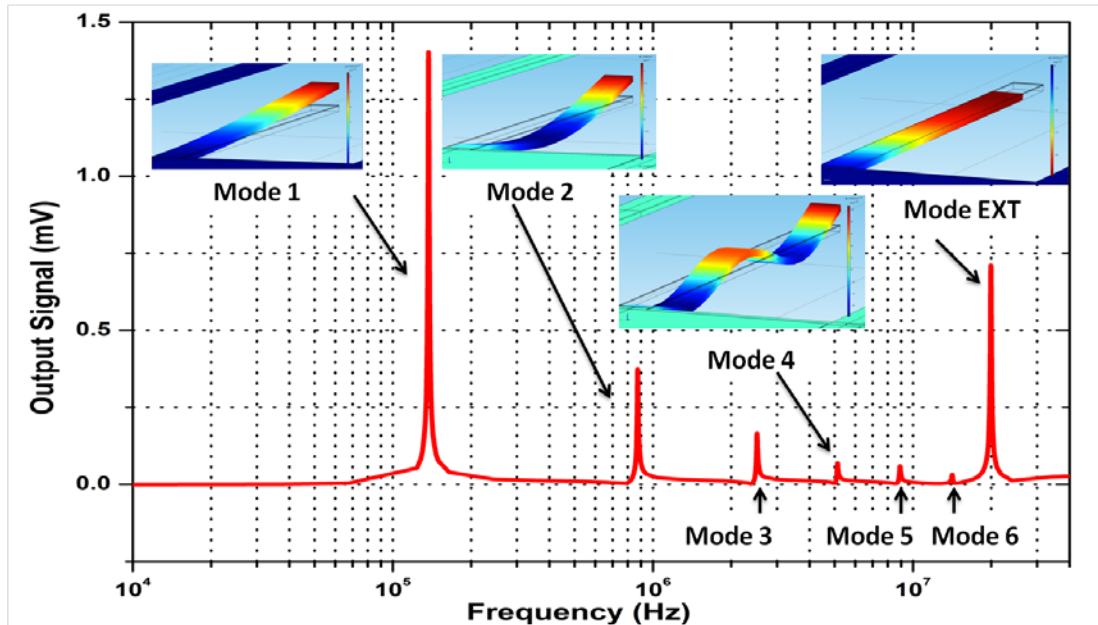


**Figure A- 3:** FEM harmonic analysis: output voltage of the capacitive bridge vs frequency.

	<b>FEM</b>	<b>Analytical</b>
<b>Flexural mode 1</b>	137.2 kHz	141.9 kHz
<b>Flexural mode 2</b>	873.8 kHz	900.4 kHz
<b>Flexural mode 3</b>	2.514 MHz	2.52 MHz
<b>Flexural mode 4</b>	5.126 MHz	4.972 MHz
<b>Flexural mode 5</b>	8.92 MHz	8.55 MHz
<b>Flexural mode 6</b>	14.15 MHz	13.3 MHz
<b>Extentional mode 1</b>	19.9 MHz	20.3 MHz

**Table A- 2:** Comparison between the predicted resonance frequency values of the first seventh flexural modes and the first extentional with FEM and analytical model respectively.

Figure B- 4 shows the same FEM simulation results as in Figure B- 3 but for a cantilever geometry that corresponds closely to the one of the cantilever whose fabrication is detailed in Chapter 3: same length and stack than for the previous case but with a width  $W = 40 \mu\text{m}$  and under-etch length  $u = 20 \mu\text{m}$ . Consequently to the width increase, new resonance modes corresponding to the out of plane lateral flexure of the beam appear on Figure B- 4. In addition, the variations of the z-direction displacement  $w$  along the width of the cantilever for out of plane longitudinal flexural modes are not negligible for mode order superior than 2 (insets figure Figure B- 4).

The resonance frequencies of the out of plane flexural modes are also considerably lower than the analytically predicted values (*cf.* Table B- 2). The main reason for such a difference is of course the presence of the over-etched region below the cantilever clamps. But even when the presence of suspended clamping region is neglected, the FEM resonance frequencies values are 10% lower than the analytical one. This difference can be explained by the assumption in Euler-Bernoulli theoretical framework of a negligible lateral stress ( $\sigma_{yy} = 0$ ) which is not valid in large width devices. However, these differences affect majorly higher resonance modes and our uni-axial analytical model remains valid and efficient for design studies restricted to the first flexural resonant mode.

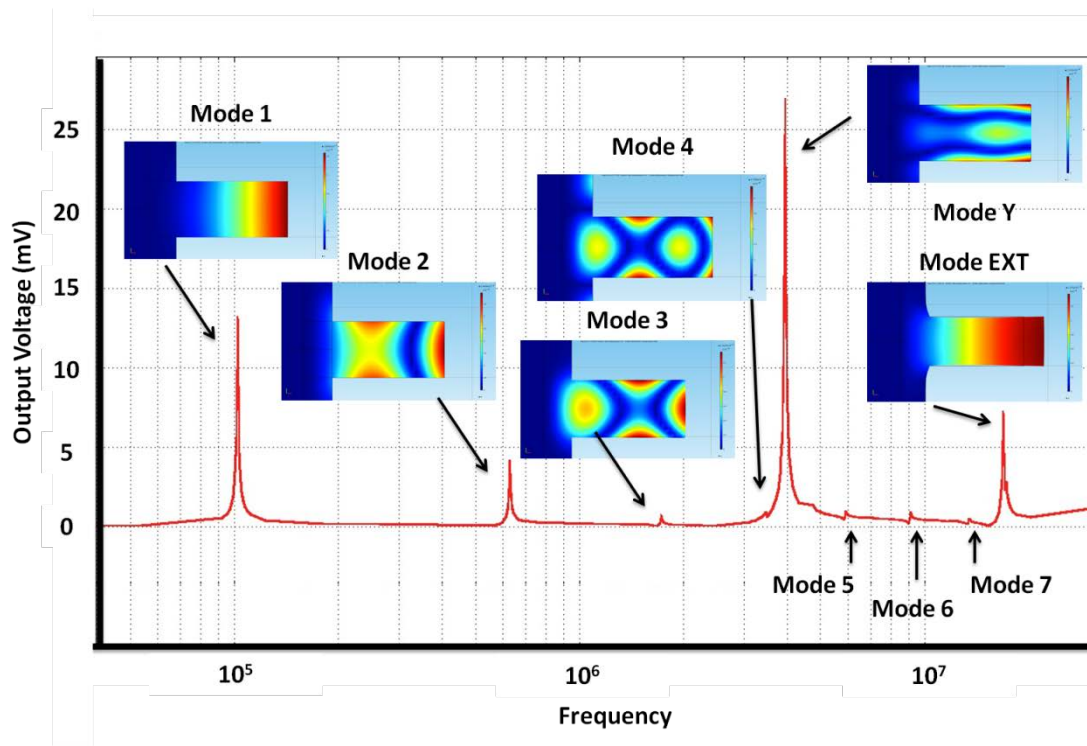


**Figure A- 4:** FEM harmonic analysis: output voltage of the capacitive bridge vs frequency.